AN INVESTIGATION ON THE POTENTIAL OF COVALENT ORGANIC FRAMEWORKS (COFs) TO BE USED AS NANOCARRIERS IN DRUG DELIVERY SYSTEMS

A thesis submitted to the Faculty of Science
for the degree of Doctor of Philosophy at the University of Malta

Supervisor: Prof. Dr. Liana Vella-Żarb Ph.D. (Birmingham)

Marie Christine Scicluna

2021

The research work disclosed in this publication
is funded by the Tertiary Education Scholarships Scheme.

Statement of Authenticity

The undersigned declare that this thesis is based on work carried out by ***Marie Christine Scicluna*** candidate for the Ph.D. degree under the supervision of ***Prof. Dr. Liana Vella-Żarb*** within the Department of Chemistry.

Marie Christine Scicluna	Prof. Dr. Liana Vella-Żarb
Candidate	*Supervisor*

To my parents,
Mary Rose and Anthony

Acknowledgements

It is my utmost pleasure and privilege to express my deepest gratitude and profound appreciation to my supervisor Prof. Dr. Liana Vella-Żarb, for accepting me into the CrEMa research group, and for introducing me to this exciting area of study and the world of crystallography. I am deeply grateful for her invaluable guidance and support, continuous encouragement, patience and tutelage throughout my research, without which this project would not have been possible. Special thanks go to Prof. Dr. Ulrich Baisch for his patience in training me to use the glovebox, and for his collaboration, expertise and helpful advice along this journey. I would also like to thank all the staff at the Department of Chemistry and the main office at the Faculty of Science, especially Prof. Dr. Emmanuel Sinagra and Ms. Marie Stella Grima, for their valued assistance during the last four years. I am thankful to my fellow CrEMa colleagues, Dr. Duncan Micallef, Mr. Luke Frendo, Ms. Lynn Marie Barbara and Ms. Lorella Spiteri, for their helpful support, friendship and motivation. I especially appreciate Ms. Spiteri's collaboration in carrying out geometry optimisation and Mr. Gabriel Gauci's training on how to use the UV-Vis spectrophotometer.

I acknowledge the European Synchrotron Radiation Facility (ESRF) for provision of synchrotron radiation, and would like to thank Dr. Diadkin Vadim and Dr. Dmitry Chernyshov for their assistance in using beamline BM01. I would also like to thank our collaborators in Kiel, Germany, for their cooperation in collecting laboratory powder X-ray diffraction data. Special recognition goes to the Tertiary Education Scholarships Scheme for funding my research and allowing me to further my studies.

Last but not least, I thank my family for their unmeasurable love, positivity and reassurance, and for their financial support, allowing me to pursue this research opportunity. To my beloved mum for reading through all of these pages and my dear dad for his level-headed approach and sound advice. Most of all, I praise God Almighty for watching over me and giving me the strength to persevere.

This was one of the most challenging and formative experiences of my life. The COVID-19 pandemic brought about great uncertainty and numerous delays in the last year and a half of my Ph.D. However, in spite of this, the publication of my first review in 2020 [1], which has already been significantly cited, was very motivating. A heartfelt thank you to all, who have contributed towards this rewarding doctoral experience.

Abstract

Covalent organic frameworks (COFs) are intrinsically designed to accommodate guest molecules in their tuneable, structurally regular pores, which are characterised by high surface areas and large pore volumes. The design of COFs with unique chemical and physical properties, can be extended to the incorporation of active pharmaceutical ingredients (APIs) as guests, to create COF drug carriers. This novel application of COFs to the field of therapeutics, provides an alternative route to (i) enhance the loading capacity of nanoparticle drug delivery systems, (ii) effectively increase drug solubility and protection from degradation in biological environments, and (iii) provide additional control on the distribution and release of the entrapped drug molecules. To date, the development of COF networks, conjugated with smart stimuli-responsive polymers, for use as drug carriers is very limited and unexplored, leaving a significant gap in literature.

The aim of this project was to address this gap by structurally engineering new smart COF materials loaded with pharmaceutical molecules, and determining their sensitivity and release response to target stimuli, in simulated physiological conditions. Twelve distinctive diffraction patterns were obtained from four monomer combinations, indicating the formation of new potential COFs, which are currently at different stages of crystal structure determination. FTIR and hot stage microscopy results further confirmed new linkage formation. A fully characterised new cage-based imine and ester linked COF structure, synthesised from the 4 + 2 + 9 condensation of 2-amino-2-(hydroxymethyl)propane-1,3-diol, **C6**, with terephthalaldehyde, **C7**, and with pyridine-2,5-dicarboxylic acid, **C8**, using LAG and catalytic amounts of 1:1 1,4-dioxane:1,3,5-trimethylbenzene, was used as the core of the nanocarrier system. Modification of its unit cell parameters and atomic coordinates upon loading of 5-fluoro-1H-pyrimidine-2,4-dione, **C14**, and conjugation of pH sensitive pyridine-2,6-dicarbaldehyde, **C9**, electro sensitive 1,1'-ferrocenedicarboxaldehyde, **C10**, and UV sensitive 4-[(4-aminophenyl)diazenyl]aniline, **C11**, indicated the physical adsorption of the molecules into the pores and onto the surface of the framework. Control on the release of the loaded API molecules was confirmed *in vitro* for the three final complexes, through an enhanced release at the target stimuli, with the biggest increase exhibited by the **C9** conjugated complex, and a sustained release for the **C10** conjugated complex. This demonstrates the application of COFs as stimuli-responsive nanocarriers in drug delivery systems, which by proof of concept can be extended to other frameworks, and API and smart molecules.

Table of Contents

List of Tables

List of Figures

List of Schemes

List of Abbreviations

API(s)	Active Pharmaceutical Ingredient(s)
BET	Brunauer-Emmett-Teller
CIF	Crystallographic Information File
CNT(s)	Carbon Nanotube(s)
COF(s)	Covalent Organic Framework(s)
CON(s)	Covalent Organic Nanosheet(s)
CRT	Controlled-Release Technology
CSD	Cambridge Structural Database
CTF(s)	Covalent Triazine-based Framework(s)
DCC	Dynamic Covalent Chemistry
DFT	Density Functional Theory
EPR	Enhanced Permeability and Retention
ESRF	European Synchrotron Radiation Facility
FRET	Fluorescence Resonance Energy Transfer
GRASE	Generally Recognised As Safe and Effective
LAG	Liquid-Assisted Grinding
LCST	Lower Critical Solution Temperature
MIL	Materials of Institut Lavoisier
MOF(s)	Metal Organic Framework(s)
MRI	Magnetic Resonance Imaging
MSN(s)	Mesoporous Silica Nanoparticle(s)
MWCO	Molecular Weight Cut-Off
NCOF(s)	Nanoscale Covalent Organic Framework(s)
NCTF(s)	Nanoscale Covalent Triazine-based Framework(s)
NMOF(s)	Nanoscale Metal Organic Framework(s)
PAF(s)	Porous Aromatic Framework(s)
PBS	Phosphate Buffer Solution
PDT	Photodynamic Therapy
PEG	Polyethylene glycol
PNP(s)	Polymeric nanoparticle(s)
PXRD	Powder X-Ray Diffraction

SCXRD	Single Crystal X-Ray Diffraction
SEM	Scanning Electron Microscopy
STA	Simultaneous Thermal Analysis
TGA	Thermogravimetric analysis
XRD	X-Ray Diffraction
XRM	X-Ray Microscopy
ZIF(s)	Zeolitic Imidazolate Framework(s)

1. Literature Review

1.1. An Introduction to Nanotechnology

Nanotechnology is a science involving the manipulation of matter on an atomic, molecular and supra-molecular scale, in the size range of a few to several hundred nanometres. Over the past two decades, nanotechnology has been actively employed in the development of drug delivery systems, overcoming the limitations of conventional carriers.

Nanoparticles range from 1 to 100 nanometres, making them 10,000 to 1,000 times smaller than human cells, which on average measure a few micrometres in diameter. In nanomedicine, size is often restricted to less than 200 nm. Any nanotechnology smaller than 50 nm can easily enter any tissue and cell at a molecular level, while those smaller than 20 nm can move out of blood vessels as they circulate through the body. [2]

The potential of nanotechnology for drug delivery, which has been extensively reported and referred to in both scientific literature and the press, has been translated into tangible outcomes. Different nanoparticles are currently used to benefit patients, including liposomes, dendrimers, nanoshells, quantum dots and carbon nanotubes (Figure 1.1).

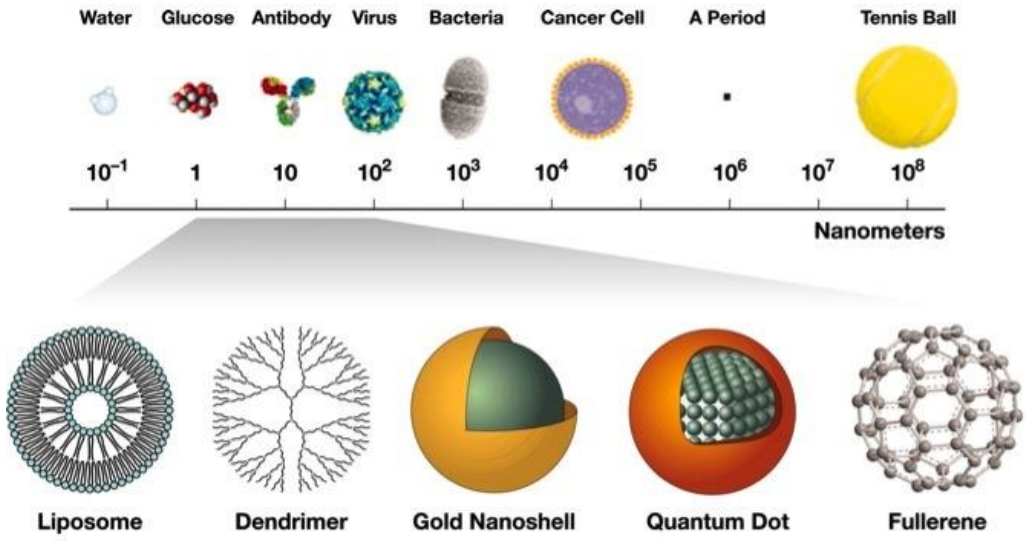

Figure 1.1. Nanometre scale comparison of nanoparticles with other materials. [3]

1.2. The History of Controlled-Release Drug Delivery Systems

The first generation of controlled-release drug delivery systems was developed for oral and transdermal administration back in the 1950s. These systems used a basic mechanism of controlled-release, whereby the drug is released more efficiently at a slow predetermined rate for an extended period of time. These formulations were developed based on dissolution-, diffusion-, osmosis- and ion-exchange mechanisms. In the 1980s, the second generation of controlled-release drug delivery systems was not as successful, due to the limitations and difficulties of creating a closed self-regulating system that can sense and evaluate its environment and adapt its release controlling abilities in response to internal triggers.

It was at the beginning of the 21st century that the ongoing 'nanotechnology fever' started, on the assumption that nanosized materials would present different characteristics than larger materials. This led to the application of nanotechnology in medicine (nanomedicine) for diagnostic, therapeutic and prognostic purposes, and was later extended for the improved treatment of cancerous tissues. The enhanced permeability and retention (EPR) effect on nanoparticles increases their delivery and hence the concentration of a drug around a tumour by 100 – 400 %, when compared with solution formations. However, in spite of this, the majority of the total amount of administered nanoparticles ends up in non-target sites. [4]

This has led to the exploitation of their distinct properties while overcoming their challenges and limitations, including immunologic response, toxicity, target site accumulation, and solubility amongst others. The ultimate goal in drug delivery is to develop a system for the prevention, control and treatment of debilitating diseases, delivering drugs more effectively to a target area. In spite of all the hype surrounding nanotechnology, it is significantly difficult to physically achieve an efficient and uncomplicated system to replace traditional non-nanoparticle systems.

1.3. From Non-Specific Targeting to Selective Targeting

Conventional drug delivery systems make use of systemic administration, i.e. blood circulation, to distribute a drug throughout the body. This type of drug delivery is classified under non-specific targeting because the whole body is exposed to the drug.

Such systems are also potentially accompanied by serious side effects and poor drug delivery to desired cells, depending on the nature of the drug being delivered.

The development of new selective therapeutic agents involves advanced polymer chemistry and electronic engineering, to aid in the differentiation of specific parts of the body. The main challenge is to differentiate the diseased cells from normal healthy cells. The key objective in designing and developing new drug delivery systems is to engineer the active pharmaceutical ingredient (API) in such a way as to (i) provide selective access to target areas, (ii) provide an increased and accurate cellular uptake of the API, (iii) effectively protect unstable drugs from degradation and/or denaturation, and (iv) minimise systemic exposure, i.e. interaction with parts of the body that are not the target of the API. [5, 6]

Nanotechnology has made selective targeting possible. Nanoparticles can be designed and programmed to have unique chemical and physical properties, e.g. size, shape, and surface characteristics, to assist therapeutic agents to pass through biologic barriers, mediate molecular interactions and identify the desired cells. [7, 8, 9, 10, 11, 12, 13, 14] Selective targeting can be classified as either passive or active.

In passive targeting, nanoparticles make use of the physiological characteristics of tumour biology to selectively accumulate there via the EPR effect. Tumour-derived blood vessels (labelled as angiogenic vessels in Figure 1.2), are wide and leaky due to abnormalities in their membranes. Pores between endothelial cells of their membranes range between 100 and 780 nm, making it possible for nanoparticles to easily pass through. Limited lymphatic drainage concentrates the nanoparticles at the site for an extended period, further promoting the passive diffusion process by which the drug enters the cells. [15, 16] The first nanocarrier-forms of passive targeting, marketed in the 1990s, were based on liposomes. In fact, most of the currently approved liposomal drug delivery systems are classified under passive targeting. As blood circulates the body, nanoparticles are transported to target sites where, unlike drug solutions, they accumulate without diffusion back into the bloodstream. When they reach tissues, they are simply subjected to enzymatic degradation in order to release the drug which is then internalised by the cells. [17]

Due to their high surface-area-to-volume ratio, most nanoparticles have an encapsulation efficiency of around 10 %. [18] Increasing their loading capacity, i.e. the percentage by mass of encapsulated drug molecules per nanoparticle, increases the amount of drug delivered to the target site but also to other tissues around the body.

Designing nanoparticles to be more selective in their drug release, reduces the cytotoxicity to which healthy cells are exposed. This led to the investigation of drug delivery systems having enhanced targeting.

In active targeting, nanoparticles are designed in such a way as to directly interact with desired cells. Targeting moieties conjugated onto the surface (shown in Figure 1.2 as blue trapeziums), make the nanoparticles more specific to a target site. Two types of active targeting have been developed: (a) specific receptor targeting, involving direct ligand-receptor interactions, and (b) antibody mediated targeting, which involves antibody-antigen recognition. At a molecular level, tumour cells have overexpressed or unique receptors or antigens (shown in purple in Figure 1.2), differentiating them from healthy cells. The targeting moieties, ligands or antibodies, use molecular recognition to identify and interact only with cells having the corresponding receptors or antigens respectively. Once interaction occurs, the whole nanoparticle is engulfed via receptor-mediated endocytosis and the encapsulated drug is internalised by the cell. Binding to a target non-internalising receptor and releasing the drug extracellularly (Figure 1.2 (ii)), also makes the drug available to neighbouring cells lacking the target receptor. [19]

In ligand-receptor and antibody-antigen targeting, a high ligand or antibody density on the surface of nanoparticles is possible due to the high surface-area-to-volume ratio of nanoparticles. One example which has been quite promising, in both *in vitro and in vivo* experiments, is the interaction between the folate receptor, which is overexpressed in many tumour cells but absent in most human tissues, and the complementary folic acid ligand, covalently conjugated onto nanoparticles using surface carboxyl groups. The nanoparticle-ligand conjugates exhibited enhanced and selective targeting to folate receptor-positive cells *in vitro* [20] and significant tumour suppression *in vivo* [21]. This nanocarrier is currently in the clinical trial stage of development.

In active targeting, it is essential that the nanoparticle is highly-selective to molecules expressing distinguishing features (receptors/antigens). Detecting target cells rapidly and reducing non-specific binding to physiologically healthy cells, increases the effectiveness of the drug while decreasing toxicity. The toxic API is predominantly released at target sites or when a change in environmental conditions is encountered, without being released into other parts of the body. Consequently, the occurrence of serious side effects, such as organ damage, is significantly decreased and the patient's quality of life is greatly improved. The nanoparticles' high binding affinity to the cell

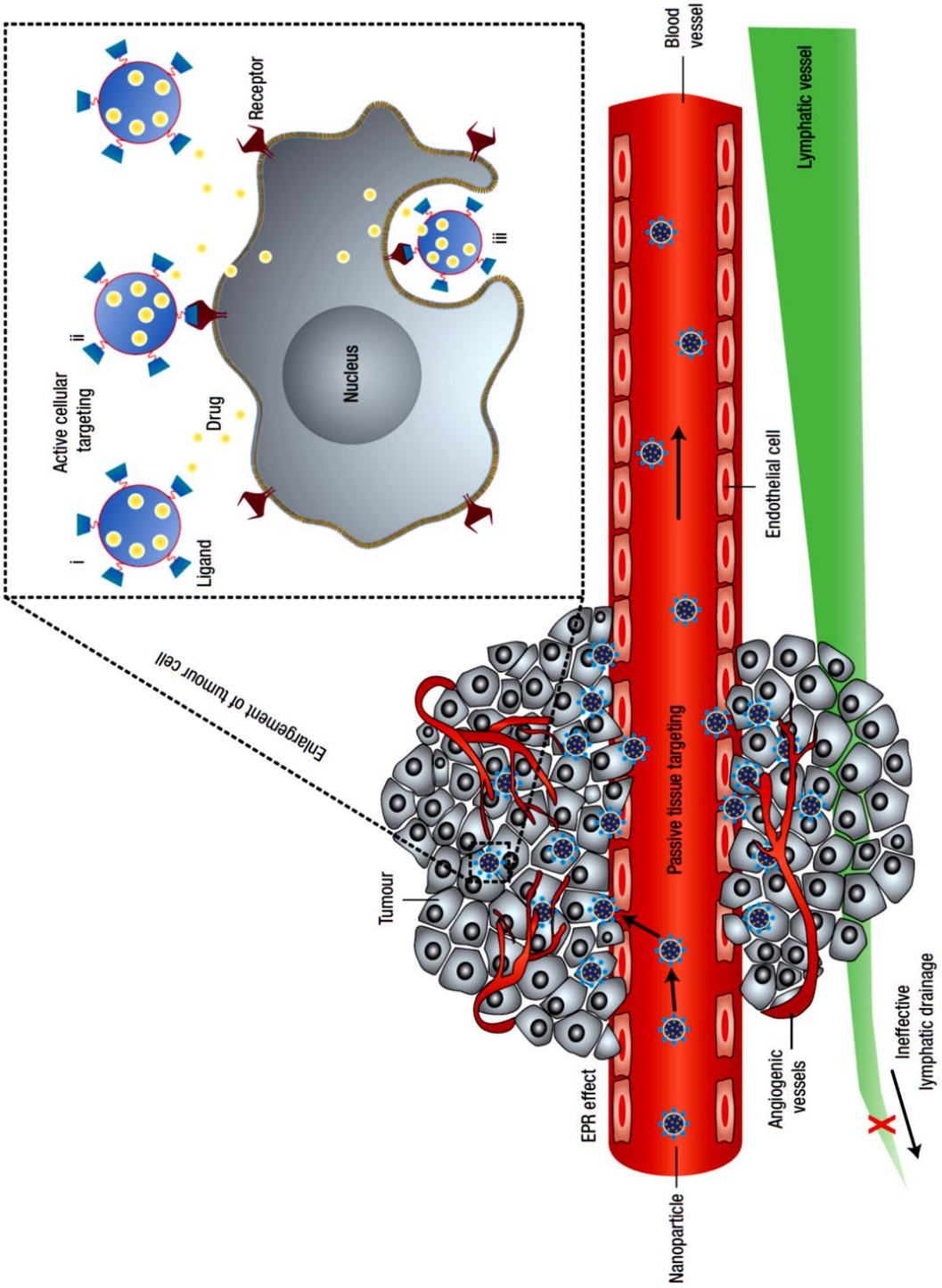

Figure 1.2. Schematic representation of passive tissue targeting (left) and active cellular targeting (inset). The nanoparticles may (i) release the drug in the environment closely-surrounding the cell; (ii) act as bound extracellular drug depositories for sustained release; or (iii) undergo receptor-mediated endocytosis. [22]

surface, also improves its distribution amongst the target cells. This can be achieved via receptor-mediated transcytosis in cases where receptors are expressed. [23]

Additional advantages over the use of traditional drug delivery systems, include protection of the drug against degradation by natural processes inside the body, and drug delivery to areas of the body inaccessible to systemic administration.

1.4. Nanobased Targeted Drug Delivery Systems

All nanobased targeted delivery systems have three main components: (a) the nanocarrier, a biologically inactive ingredient known also as the excipient, labelled as the core in Figure 1.3, (b) the API, the pharmaceutically active ingredient, shown in purple, and (c) the targeting moiety, conjugated onto the surface of the nanocarrier, shown in blue.

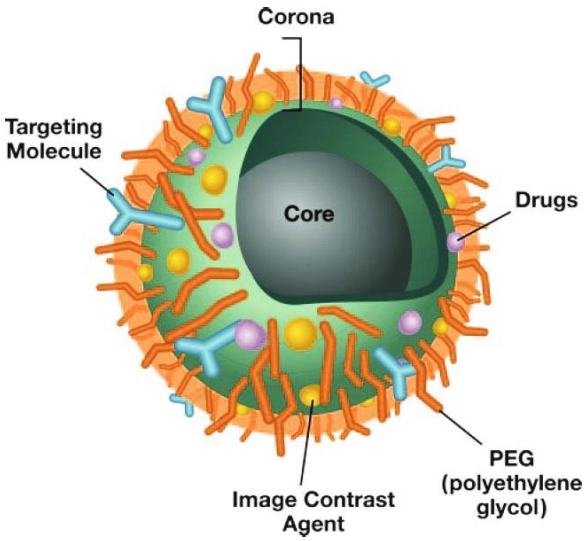

Figure 1.3. Schematic diagram of a multifunctional polymeric nanocarrier. [3]

1.4.1. The Nanocarrier

The nanocarrier family (Figure 1.4) currently includes lipid-based nanocarriers such as liposomes and micelles, dendrimers, carbon nanotubes (CNTs), inorganic nanocarriers such as quantum dots and gold nanoparticles e.g. nanoshells and nanocages,

and polymeric nanoparticles (PNPs). The latter are the most commonly explored materials for constructing nanobased drug delivery systems.

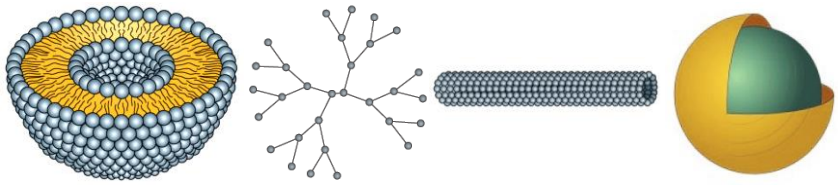

Figure 1.4. Different nanocarriers: Liposome, Dendrimer, Carbon nanotube, Gold nanoshell (from left to right). [3, 24]

Liposomes are colloidal carriers consisting of an aqueous core entrapped by one or more lipid bilayers. Lipid-based carriers are able to deliver both hydrophobic and hydrophilic drugs. However, liposomal systems often lack targeted release properties, depending solely on the EPR effect to achieve drug release at the target site. The commercially available liposomal doxorubicin, Doxil® (Figure 1.5), is one such system which is not capable of selective binding to target cells. Recent research on the post-modification of the surface of the approved form, presented evidence of the increased therapeutic efficacy when optimizing the current passive targeting form to a more selective active targeting form. [25]

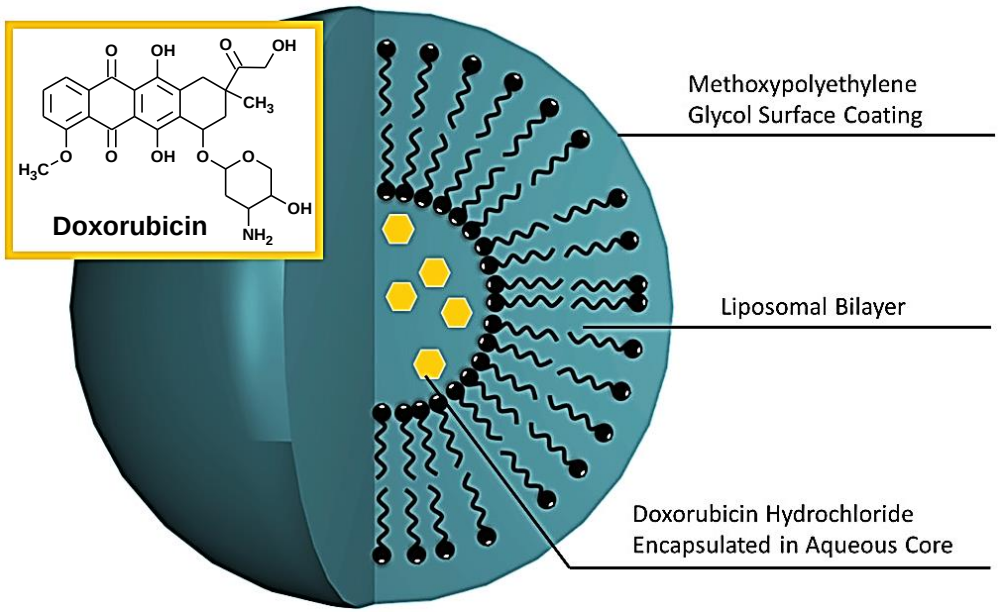

Figure 1.5. Liposomal doxorubicin (Doxil®) formulation. [26]

Dendrimers are highly-branched synthetic polymers originating from a nanosized core, to form highly selective cavities and cages throughout the macromolecule. Targeting moieties or imaging agents can be easily conjugated onto dendrimers to modify their surface functionality. Classified under organic nanoparticles, dendrimers have well-defined shapes, sizes and branching lengths. The promising polyamidoamine (PAMAM) dendrimers (Figure 1.6), measuring less than 5 nm, branch out from a central molecule of ethylene diamine, with the edgewise generation ending in primary amines. Cisplatin and methotrexate are two drugs that have been successfully loaded into PAMAM dendrimers. The resulting conjugates, tested *in vivo*, exhibited improved tumour reduction and lower cytotoxicity when compared with the free drugs. [26, 27]

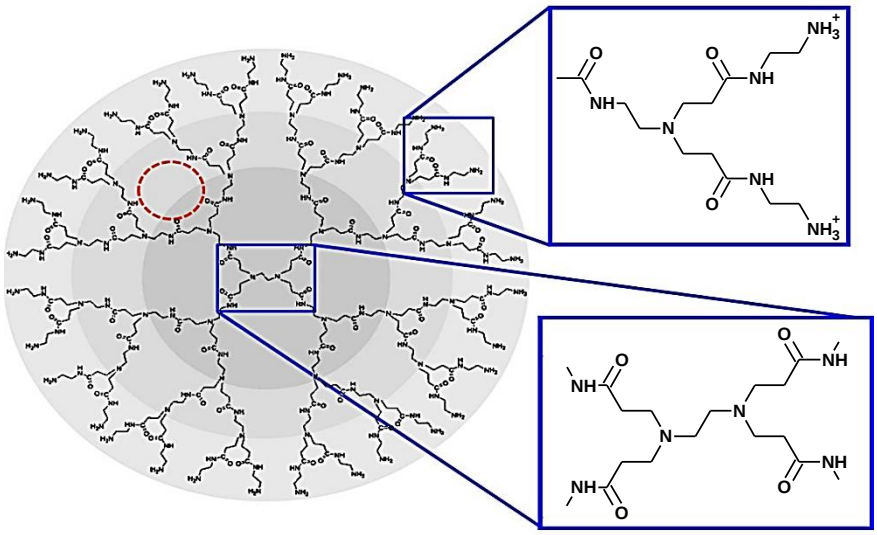

Figure 1.6. Polyamidoamine (PAMAM) dendrimers, branching out from a core ethylenediamine molecule. Drugs may be loaded into intramolecular cavities (red) or conjugated onto the surface. [27]

CNTs are simple layers of graphite rolled in a tubular shape, capable of exhibiting single- or multi-walled morphology. Functionalisation of the large surface area of the CNTs, through covalent or non-covalent attachment, improves their solubility in physiological environments. Multi-functionalisation of their surfaces allows for the attachment of different types of molecules having different functions. [28] Compared with free doxorubicin and with the Doxil® formulation, the same drug conjugated onto CNTs exhibited a higher loading efficiency, an enhanced therapeutic efficacy, and an even lower cytotoxicity. Dissociation of this drug-nanoparticle conjugate (Figure 1.7) in

acidic environments allows for the selective accumulation and targeted release of doxorubicin in tumour cells, which have a slightly acidic extracellular pH. [29]

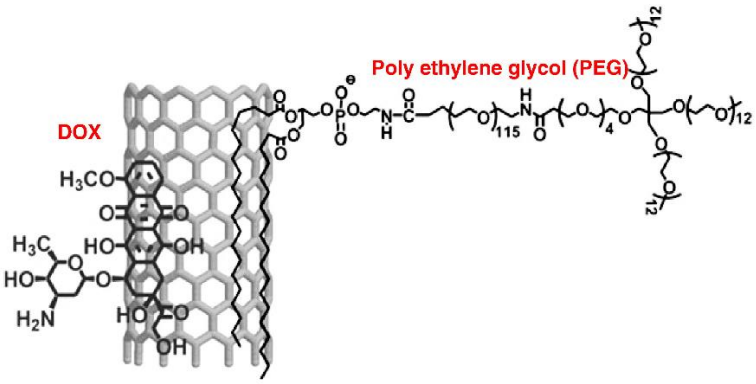

Figure 1.7. Single-walled carbon nanotube (CNT) doxorubicin conjugate. [30]

Nanoshells are composed of a dielectric silica core, covered by a thin metallic shell, usually gold. They can absorb or scatter electromagnetic radiation in the near infra-red region, the transmission of which is optimal in tissues, to heat up tumour cells causing irreversible thermal damage or to provide contrast for imaging purposes respectively. [31] Due to their fluorescent nature, quantum dots are similarly ideal for imaging and detection purposes. [32]

The application of gold nanoshells for drug delivery has also been reported. Hollow gold nanoshell doxorubicin conjugates underwent intracellular release of the drug only upon near infra-red laser irradiation. The resulting amplified cell-killing effect, from both photothermal heat and the cytotoxic effect of the drug, was combined with a greater loading capacity of the nanoshells, as high as 63 % by mass. [33, 34] Although extensively researched for their characteristic features, inorganic nanoparticles present the problem of unwanted long-term toxicity since they are not easily cleared from the body.

The top most studied nanocarrier, PNPs, can be described as stable matrix-type solid-colloidal particles. The dense matrix can be constructed out of natural polymers, e.g. collagen, or from synthetic polymers, e.g. polylactic acid. [35, 36] Several formulations are currently in pre-clinical development and clinical trials, while others are already marketed, e.g. Abraxane®, an albumin-bound paclitaxel nanoparticle (Figure 1.8).

Figure 1.8. Albumin-bound paclitaxel 130 nm nanoparticle (Abraxane®) formulation. [37]

The route of administration of drug formulations, using these different nanocarriers for passive or active targeting, may be invasive (intravenous, intramuscular, subcutaneous) or non-invasive (topical, oral, nasal, mucosal), and in conjunction with the location of the target site, greatly influences the characteristics of the chosen carrier.

1.4.2. The Active Pharmaceutical Ingredient (API)

The API is the component that provides a therapeutic effect. Nanobased drug delivery systems have been approved for the treatment of tumours, neurodegenerative diseases and infectious diseases, amongst others. The API can be encapsulated, entrapped within the particle impregnating the structure in a uniform or spatially-localised way, or conjugated onto the surface of the nanoparticle. For the latter, the drug may be physically adsorbed or chemically linked to the surface. Weak intermolecular forces (van der Waals) or stronger intramolecular forces (covalent and ionic bonds) render the drug molecules coating the surface, immobile while also allowing for dissociation and release of the drug in specific environmental conditions. It is vital that nanocarriers transport the drug without any chemical modification, i.e. the API itself remains unaltered, so that upon release at the target site, the expected and desired therapeutic effect is obtained.

1.4.3. The Targeting Moiety

The targeting moiety is a crucial component in active targeted drug delivery systems, as discussed in section 1.3. It enhances selective penetration via molecular recognition, i.e. it produces a chemical signal, acting as a compass and driving the

nanoparticle, to which it is attached, to a particular target area. It also provides an alternative route by which drugs enter tumour cells, possibly addressing the challenges presented by multidrug resistance. Targeting moieties include small molecules, peptides, proteins, fatty acids, sugars, aptamers and antibodies. Molecular biology techniques can be used to engineer and design targeting agents, tailor-made to bind to specific conformations on the cell surface.

The chosen targeting molecule must be conjugated onto the surface, so that it is able to detect its complementary cell surface receptor molecule. Once in its vicinity, it must bind and interact with it extracellularly, triggering an intracellular signalling response – endocytosis of the nanocarrier. The interaction between the targeting moiety and its complementary receptor, governs the binding affinity of the nanoparticle to the cell surface, consequently affecting the amount of non-specific binding, in effect determining the efficacy of the drug. [38]

1.5. Smart Nanobased Drug Delivery Systems

The last decade of the second generation of controlled-release drug delivery systems (2000-2010) was centred on nanobased targeted systems, which allow for distribution control of the drug. The incorporation of smart polymers, developed earlier on as part of the second generation, into nanoparticle systems, allows for controlled-release of the drug. [39] Achieving controlled-release is an important aspect of drug delivery systems. The drug concentration at the target site needs to be within the therapeutic window of the drug, i.e. a dose that will effectively produce the desired therapeutic effect but still remains in the range of acceptable toxicity. Most of the carrier systems discussed so far, depend on nanoparticle degradation and/or drug diffusion through the matrix, in order to release the drug. Conversely, smart or intelligent systems depend on the accurate and highly sensitive detection of endogenous or exogenous stimuli for better control over drug release, making on-demand and pulsatile release patterns possible.

Referred to as controlled-release technology (CRT), the drug is released in response to time or physical or chemical stimuli, i.e. changes in its surrounding environment, e.g. pH, enzymes, light, temperature, magnetic fields and ionic strength. Large changes in

shape, volume, mechanical properties or permeation rates, are amongst responses exhibited, depending on the type of stimulus.

Stimuli-responsive polymers can be found conjugated onto the surface of the core or acting as linkers, binding drugs to the core. Otherwise, stimuli-responsive vehicles may be constructed from nanocarriers that cannot change their structures in response to a stimulus, such as polymeric micelles, using temperature, pH, magnetic field or UV sensitive polymers. [40] The environmental conditions at the target site and the stability of these polymers with respect to different stimuli, thus determine the release pattern of the drug. By limiting the rate of release of medications throughout the body, CRT may revive the use of drugs that were previously unsafe for disease treatment.

Drug delivery systems can be tailored to chemically recognise biomolecules, such as enzymes, sugars and oligonucleotides. Due to their high specificity for functional groups or particular types of chemical bonds, enzymes provide a large range of ideal triggers. Differences in the type of hydrolytic enzymes intracellularly and extracellularly, and between healthy and cancerous cells, allow the design of nanocarrier systems which can selectively release the drug inside tumour cells. This is made possible by the introduction of an enzyme-cleavable molecule as an integral part of the nanocarrier or as a linker between the drug and the nanocarrier. The drug delivery system remains stable while in circulation in blood plasma, but upon internalisation by cells, the enzyme-sensitive polymer is irreversibly cleaved, such that the drug is released. [41] For example, the β-glucuronide linker is hydrolysed by the intracellular enzyme β-glucuronidase. Following linker cleavage at the glycosidic bond, the free drug is released via 1,6-elimination, together with the loss of carbon dioxide (Figure 1.9). [42, 43] Such self-immolative polymers undergo an intramolecular electronic cascade which allows for signal amplification, when one linker cleavage triggers the release of more than one drug molecule. [44, 45]

Similarly, hydrolysis of pH-sensitive linkers results in the release of the bound drug molecules in areas having a lowered pH, such as inflammation zones, the extracellular environment of tumour cells, and endosomes. Stable at neutral pH and in blood plasma, which has a pH of 7.4, these linkers are cleaved in environments having a slightly acidic pH between 4 and 6. Figure 1.10 shows the low pH-mediated degradation of hydrazones, which leads to the simple and rapid release of the drug. This environment-responsive cleavage is part of an antibody-drug conjugate, milatuzumab-doxorubicin, currently in clinical trials. [46]

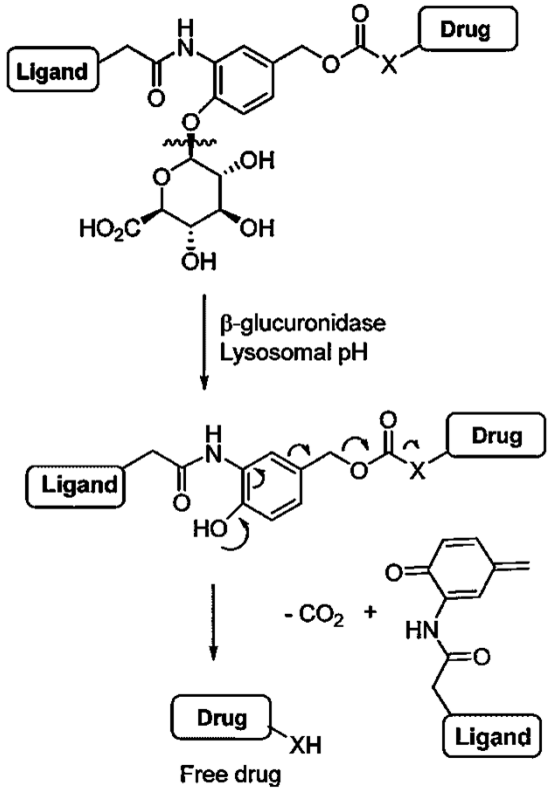

Figure 1.9. *β*-glucuronide hydrolysis by the enzyme *β*-glucuronidase, followed by 1,6-elimination to liberate the drug. X refers to O or NH. [47]

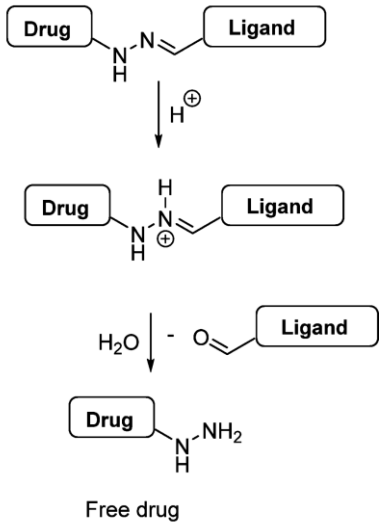

Figure 1.10. Acid-mediated cleavage of hydrazone linkers. [47]

Alternatively, instead of a degradation response, a lower pH may elicit a change in the conformation or solubility of a polymer and ultimately the nanoparticle. This is achieved through ionisation of polymers from a neutral to a charged state, e.g. the protonation of amine groups in poly(N,N-dimethylaminoethyl) (DMAEMA) leading to conformational rearrangements, [48] or from a hydrophilic to a hydrophobic state, e.g. the ionisation of poly(N-isopropylacrylamide) (PNIPAm) based hydrogels leading to swelling and phase separation. The ionisation generates electrostatic repulsion between the polymers which results in a reversible structural or solubility change, in effect triggering the escape of drug molecules. [49]

Temperature-sensitive drug delivery systems can be triggered to elicit a response via external local cooling or heating within a specific time period. Pure PNIPAm is one of the most studied thermo-responsive polymers. [50, 51] Hydrophilic at temperatures below the lower critical solution temperature (LCST), it undergoes a reversible phase transition, at 32 °C, to form hydrophobic globules in aqueous solution, allowing the release of drug molecules. Copolymerisation of PNIPAm with DMAEMA results in hydrogels that are both temperature and pH-responsive without reduction in their sensitivity to the stimuli. The LCST is affected by the type and extent of chemical modification on PNIPAm, allowing for control over the temperature at which the drug is released. An LCST of around 40 to 42 °C is desirable, so that the drug is retained as part of the nanocarrier at the average normal body temperature of 37 °C, but rapidly delivered upon slight deviations from the physiological temperature. [49, 52]

However, due to the associated limitations of using temperature as an external stimulus, temperature-responsive polymers are often substituted by or used in combination with other stimuli-responsive materials, such as light-responsive molecules or magnetic nanoparticles. Photo-sensitive polymers are chemically stable in the absence of light, but are easily degraded when exposed to specific wavelengths. The photo-sensitive Si–C axial bond on silicon phthalocyanines, is homolytically cleaved when exposed to visible-near infra-red wavelengths, to release the conjugated photodynamic therapy (PDT) drug in its active form (Figure 1.11). [53]

Recent advances in the development of photo-responsive materials have produced systems exhibiting reversible structural changes in response to on and off cycles of light stimuli or irradiation at different wavelengths, i.e. the stimuli-responsive polymer acts as a gate or shutter opening and closing on-demand. [54] The reversible photoisomerisation of azobenzene and its derivatives is one example which enables the pulsatile release of

drug molecules, in contrast to the quick release achieved via traditional systems exhibiting irreversible structural changes. [55]

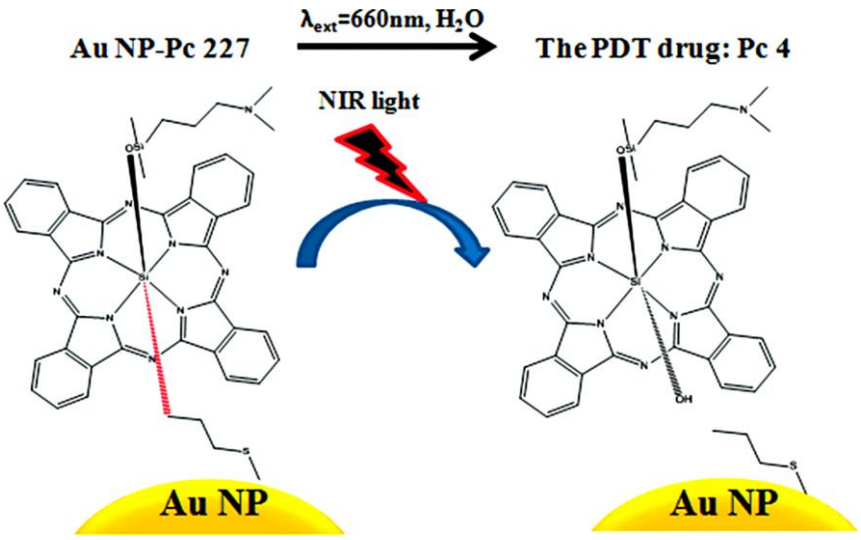

Figure 1.11. Photo-triggered release of the photodynamic therapy (PDT) drug, Pc 4, from a drug precursor, Pc 227, covalently bonded onto gold nanoparticles via a thiol group. [53]

Photo-sensitivity can also be used to elevate the local temperature at the target site. The application of therapeutic drugs in combination with photothermal heat, as discussed in section 1.4.1, demonstrates a synergistic effect which improves efficacy, through near infra-red irradiated gold nanoshells. A therapeutic effect can alternatively be combined with a diagnostic effect, through magnetic nanoparticles such as magnetite, which act as contrasting agents for imaging purposes, such as magnetic resonance imaging (MRI). This not only allows for visualisation of the nanovehicles, but also for their controlled guidance under the influence of permanent magnetic fields. Upon accumulation of the nanocarrier at the target site, where chemotherapy is achieved through burst release, external stimulation of the magnetic nanoparticles using oscillating magnetic fields generates heat, a process termed hyperthermia, thereby destroying diseased cells. Thermal ablation only affects the desired cells in which the nanocarriers accumulate. Normal healthy cells are left unaffected by the applied magnetic field. Unlike the near infra-red irradiation-triggered inorganic nanoparticles, magnetic nanocarriers present a diluted potential of long-term toxicity, because they degrade to iron ions in acidic environments. [56] Quantum dots may similarly act as multifunctional theragnostic nanosystems, combining therapeutics with diagnostics. Composed of semi-conducting

materials, quantum dots act as fluorescent probes by emitting light in the range of blue to infra-red wavelengths, for imaging purposes. When conjugated with APIs, they provide an additional therapeutic effect without compromising fluorescence intensity. Nonetheless, the problem of long-term cytotoxicity still remains. [57]

Controlled-release in drug delivery systems can be further improved by increasing sensitivity to more than one stimulus. Combining magnetic nanoparticles with temperature-sensitive polymers allows for an on-demand pulsatile drug release. The application of an alternating magnetic field onto the magnetic nanoparticles results in the generation of heat, an increase in temperature, which in turn triggers a structural or solubility response from the temperature-responsive polymers. A more controlled, pulsatile release pattern is achieved through on and off cycles of the magnetic field stimulus. [58, 59] The conjugation of photo-sensitive and temperature-responsive polymers, follows a similar mechanism. [60] Despite their appeal, the translation of drug delivery systems, combining two or more stimuli-responsive materials, into pharmaceutical developments is very complex, and most systems have yet to prove their viability *in vitro* and *in vivo*.

1.6. Essential Parameters for the Development of Nanocarrier Systems

In nanomedicine, the remarkable development of active targeting and controlled-release must be accompanied by the development of materials tailored for their specific application in the human body. It is essential to ensure the safety of the drug delivery system, i.e. safe transport and release of the drug, and minimal cytotoxicity combined with the biocompatibility of the material. Proof of efficacy, drug loading, release kinetics and biodegradability of the system are also key to determining the nanocarriers' interaction with the body. [61]

At less than 100 nm, nanocarriers can enter all cells by endocytosis, unlike larger particles which can only be taken up by macrophages. Although this allows for a less limited distribution *in vivo*, which in part can be controlled by tuning the nanosystem's size, it also presents an increased toxicological risk. Particle size also affects the degree of drug loading and the release profile of the conjugated drug. The smaller the nanocarrier, the larger its surface-area-to-volume ratio, such that drug molecules are more likely to be positioned on the outermost surface, as compared with their possible

encapsulation within larger nanocarriers. Furthermore, entrapped drugs are released at a slower rate than conjugated drugs. [62] When post-synthetic adsorption or absorption methods are used, the drug loading capacity is dependent on the solubility of the drug in the nanomaterial. Hence, composition, molecular weight and chemical interactions between nanoparticles and drug molecules, are all factors that should be considered. Nonetheless, a high API density, much higher than in other drug carrier systems, is possible due to the high surface-area-to-volume ratio of the nanocarriers. [63]

The type and strength of the interaction between the nanomaterial and drug molecules also affect the rate of drug release. This interaction needs to be stable enough to deliver the drug to the desired area but also reversible so that desorption is achieved at the target site. Additionally, nanoparticle degradation and drug diffusion through the carrier, aid in the release of the drug. Release rates can also be adjusted through the use of stimuli-responsive linkers binding drugs to the core, as discussed in section 1.5, or through surface or pore surface functionalisation of porous nanocarriers. Inorganic mesoporous solids, such as mesoporous silica nanoparticles (MSNs), have high order and discrete pores, into which drug molecules can be entrapped. Their tuneable nanoparticle size combined with a narrow pore size distribution and a high surface-area-to-pore-volume ratio, allow high loading capacities of differently-sized drug molecules. Selective surface functionalisation allows MSNs to achieve specific interactions with drugs, controlling the rates at which drug molecules are released. One of the most common MSNs, SBA-15, was found to effectively control the rate of release of ibuprofen, when functionalised with amine groups. [64] Stable to pH, mechanical stress, heat and hydrolytic degradation, the drug release properties of functionalised MSNs make them suitable for controlled drug delivery. [65]

The biocompatibility of a material refers to its ability to elicit an appropriate host response in a specific situation. When the body is exposed to foreign materials, an immunologic response is triggered to immediately remove them, creating a biologic barrier to nanocarrier systems. [66] When biocompatible surfaces come in contact with bodily fluids, the severity of this adverse response is reduced. The biocompatibility parameter is therefore highly dependent on the tolerability of anatomic environments to interactions between a specific nanocarrier and tissues, on the duration of exposure and on the route of administration. If a nanomaterial induces an adverse effect in a particular tissue type, it will not necessarily provoke the same or similar response in a different tissue or application.

Surface charge of nanocarriers is one important factor that has been found to affect the immune response, with a negatively charged surface evoking a lesser response than a postively charged one. Additionally, surface modification of nanocarriers by hydrophilic polymers can also decrease the strength of tissue reaction. One of the most commonly used hydrophilic polymers is polyethylene glycol (PEG), covalently bonded to nanocarriers as functionalised PEG derivatives. Conjugated onto the surface of drug delivery systems as part of the corona (Figure 1.3), PEG repels certain plasma proteins, by forming condensed high energy conformations, and effectively reduces interaction and uptake by phagocytic cells involved in the elicited immune response, via a steric shielding effect (Figure 1.12). This improves the systems' biocompatibility, and in turn prolongs the nanocarriers' circulation lifetime in the bloodstream, increasing the drug's bioavailability and subsequently reducing dosing frequency. [67, 68]

PEGylation, however, also has its weaknesses, including the possibility of antibodies that clear PEGylated nanocarrier systems from the body, limiting its duration and effectiveness inside the body. Other commonly used polymers include dextran, zwitterionic polymers, and polyglycerols. [69, 70, 71] In conjunction with biocompatibility, particle size can also be used to further improve the systems' circulation lifetime, as it affects the rate of clearance of nanocarriers from the bloodstream, with nanocarriers ranging from 50 to 300 nm removed slower than larger nanoparticles. [72, 73]

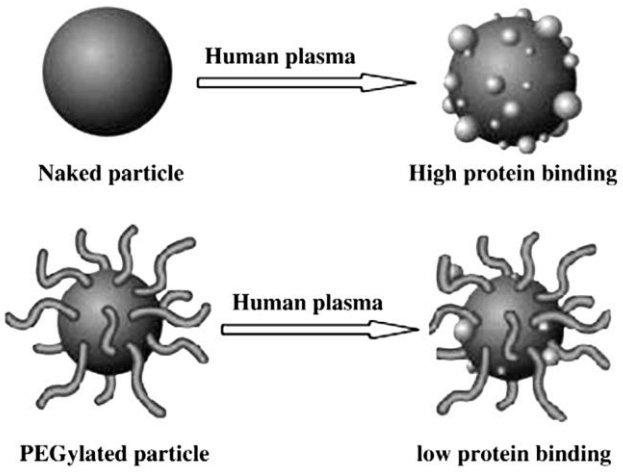

Figure 1.12. Comparison of the triggered protein adsorption immunological response for naked and PEGylated nanoparticles. [74]

Testing for a nanocarrier's biocompatibility during preclinical stages, involves a combination of *in vitro* and *in vivo* studies since findings from the former do not predict the latter's outcomes. A more in-depth understanding of the complex interactions and mechanisms involved in biocompatibility is required and would prove invaluable in designing better drug nanovehicles. [61]

After surviving immediate clearance and providing the desired therapeutic effect, degradation or at best, removal of the empty nanoparticles from the target site in a timely manner, is imperative. This prevents the build-up of a physical barrier against the delivery of fresh nanoparticles at the desired site. The biodegradable parameter of nanocarriers is thus important to avoid irreversible accumulation and hence limit the toxicity risk. PNPs are often constructed using biodegradable, naturally occurring polymers, such as gelatin and chitosan, or synthetic polymers, including polylactic acid (PLA) and poly(lactic-*co*-glycolic) acid (PLGA). Biodegradable materials undergo degradation *in vivo* to form toxicologically safe and biocompatible by-products, such as alcohol, acids and low molecular weight products. Elimination of these by-products is then easily carried out via normal metabolic pathways. PLA is hydrolysed to lactic acid while PLGA is hydrolysed to its co-polymer substituents, lactic acid and glycolic acid, both naturally produced in the human body during metabolism. [75, 74, 76]

In spite of all efforts, the total amount of administered nanoparticles accumulated at the target site is often only increased by a small percentage, compared with non-specific targeting. All administered nanoparticles depend on blood circulation to reach target sites, resulting in a majority of nanoparticles ending up in non-target sites. Additionally, the drug may leak out of the nanoparticle during circulation. The EPR effect limits diffusion of target site-accumulated nanoparticles back into the bloodstream, such that there is an overall increase of nanoparticles at the target sites. However, active targeting does not increase the chances of nanoparticles reaching the target sites. Rather, it makes their interaction specific to desired cells, once at the target sites.

These technologies do not yet represent a 'magic bullet', as postulated by Paul Ehrlich's revolutionary concept, which goes straight to the target site and only interacts with desired cells. Although their evolution started around seventy years ago, the current reality is that these systems are distributed throughout the body, significantly interacting with the target receptor, but still interacting with non-target sites albeit to a lesser extent, limiting side effects. Nonetheless, his vision of 'aiming precisely' has been of valuable

inspiration for the significant achievements made in the field of disease management, bridging the divide between chemistry, biology and medicine. [77]

1.7. An Introduction to Covalent Organic Frameworks (COFs)

From the discussed nanobased drug delivery systems, PNPs are possibly the most effective carriers, as they consist of a biodegradable matrix having a higher loading capacity and circulation time than the other nanocarrier systems. Additionally, they are found to be more stable *in vivo*, with a more homogenous size distribution and can deliver multiple synergistic drugs simultaneously. Similar to MSNs and porous materials, these nanoparticles can provide controlled-release profiles, via diffusion of drug molecules through the matrix and/or degradation of the matrix itself. In spite of the low number of approved nanoparticle formulations, PNPs have been widely studied in regards to cancer therapeutics, and are regarded as huge potential nano-platforms in this field.

Covalent organic frameworks (COFs) are a recently developed class of crystalline porous polymers that allows the atomically precise integration of organic units, to create predesigned skeletons and nanopores. They are entirely composed of light-weight elements (Hydrogen, Carbon, Nitrogen, and Oxygen) through covalent bonding, integrated into extended porous networks in 2 or 3 dimensions. Highly ordered and characterised by discrete pores, COFs can thus be classified under PNPs.

The first 2D members, COF-1 (Figure 1.13) and COF-5 (Figure 1.14), were successfully synthesised in 2005 through a one-step condensation reaction of discrete molecules, under solvothermal reaction conditions that are efficient and high-yielding. [78] Exhibiting a boroxine and a boronate-ester linkage respectively, these boron-based frameworks are however easily susceptible to hydrolytic degradation by water molecules in air.

This first 3D members, COF-102 and COF-103, were then synthesised in 2007 also through a one-step condensation reaction, using tetrahedral monomers with a higher Brunauer-Emmett-Teller (BET) surface area. [79] This led to an increased pore volume and lower density of the constructed structures. Boron-based, these frameworks were however also susceptible to attack by water vapour. Thus, new types of linkages were developed (Figure 1.15), including (i) covalent triazine-based frameworks (CTFs) synthesised through the cyclo-trimerisation of nitrile building units via harsh ionothermal

conditions of molten zinc chloride at 400 °C [80, 81]; (ii) hydrazone linkages synthesised through the dehydration of hydrazide and aldehyde monomers [82]; and (iii) Schiff-base type, imine linkages synthesised through the co-condensation of aldehyde and amine monomers [83].

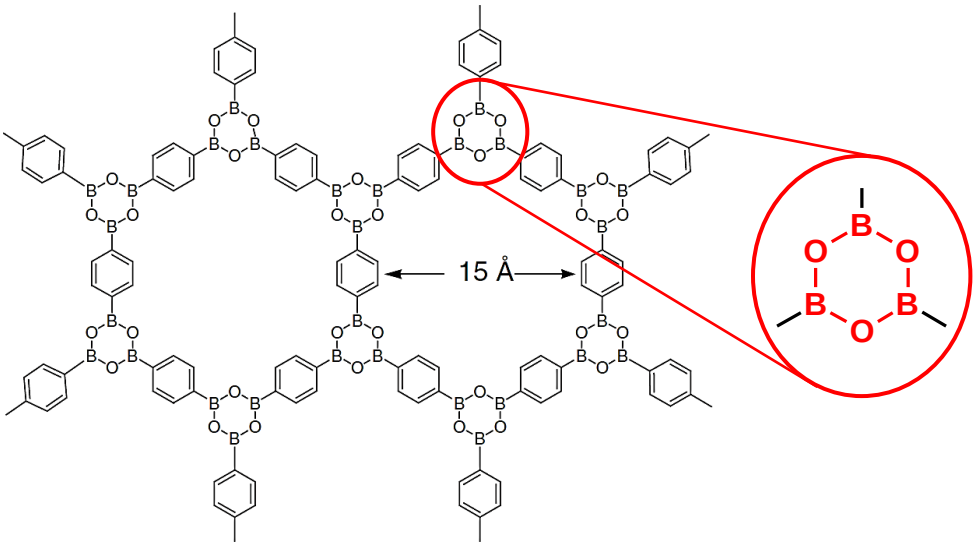

Figure 1.13. COF-1 with a six-membered boroxine linkage (inset). [78]

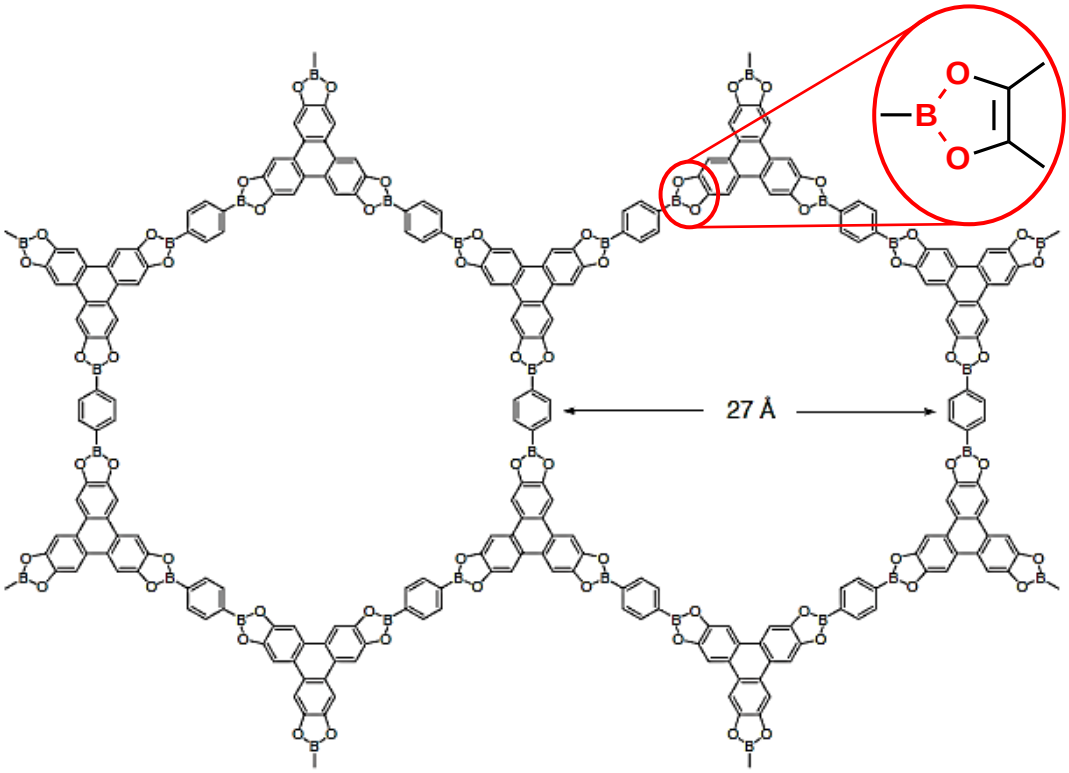

Figure 1.14. COF-5 with a five-membered boronate-ester linkage (inset). [78]

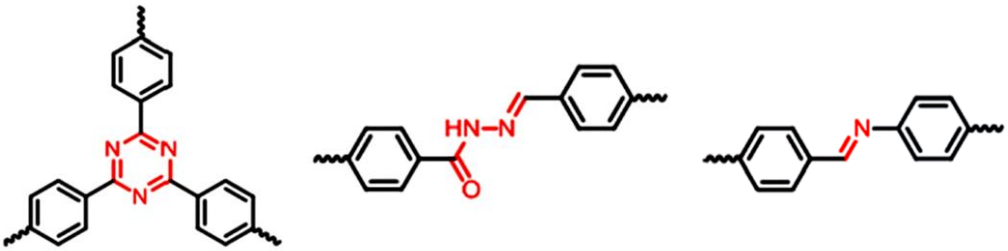

Figure 1.15. Covalent triazine-based linkage (left), hydrazone linkage (middle), and imine linkage (right). [84]

Crystalline in nature, these materials allow the formation of a monodisperse size distribution of stable well-defined pores, through their atomically precise skeletons and structural homogeneity. Microscopic reversibility is thus an essential requirement for the synthesis of crystalline COFs. This was achieved through thermodynamically controlled dynamic covalent chemistry (DCC) which allows the formation, breakage and reformation of covalent bonds, leading to stable structures where the polymer skeleton forms alongside the crystallisation process, resulting in an ordered structure having discrete pores. The reversibility involved in DCC also allows for error-checking, thereby reducing the incidence of structural defects. Additionally, to ensure that the rigidity and structural integrity of the monomers are not modified during framework formation, reticular chemistry is employed to assemble previously designed rigid secondary building units into predetermined networks held together by strong bonding.

Reaction conditions, including temperature, pressure, solubility, and chemical kinetics, also have an effect on the reversibility required for the formation of COFs. Therefore, synthetic routes must be carefully chosen. Various synthetic techniques have been used to construct COFs. The first frameworks were synthesised via the solvothermal method, by which monomers and solvents are placed in a sealed tube and heated under pressure, to a predetermined temperature between 85 and 120 °C, for the designated time. [78] Although this route allows for slow dehydration and reversible conditions, the resulting material is collected as a solid powder, which may limit its application as an interface in electrodes and devices. Oriented thin-film synthesis on single-layer graphene was hence developed in solvothermal systems, to create planar insoluble monolayer COFs for use in optoelectronic devices. [85, 86] Another synthetic technique, microwave-assisted synthesis, often replaces the solvothermal method, as it does not require a sealed vessel. Accelerating chemical reactions, microwave irradiation promotes better porosity

and provides the possibility for large-scale synthesis. Through a microwave extraction and purification step, residues and impurities trapped in the pores of the framework are removed more efficiently, freeing up occupied pores and hence promoting better porosity. [87, 88]

Sonochemical synthesis makes use of acoustic cavitation, i.e. the formation and collapse of bubbles in solution, to produce exceedingly high local temperatures and pressures, which result in fast heating and cooling rates, and accelerate the crystallisation rate. Creating smaller crystals than solvothermal synthesis, this technique is very economical with low power consumption. [89] An alternative simple, solvent-free construction of COFs, is through mechanochemical solid-state synthesis. Large amounts of monomers are brought close together by a catalytic amount of solvent, increasing the reaction rate upon grinding. Referred to as liquid-assisted grinding (LAG) synthesis, this technique increases the product to solvent ratio and improves crystallinity of the resulting material when compared to neat grinding. [90, 91]

Due to the diversity of available building units and the different linkages formed, COFs can be designed and programmed to have unique chemical and physical properties. Additionally, the structure of the building monomers, i.e. their molecular length and size, the relative orientation of functional groups, i.e. their symmetry, and the chemical and physical environments of crystallisation, such as temperature and pH, can be adjusted to govern the size and structure, surface area and available unoccupied volume of the channel/pore of the framework. This allows a tunability parameter to be added to the COFs' pore size uniformity. COF porosity can be tuned through (i) a bottom-up approach, using increasingly long building monomers [92], alkyl functionalised building units [93], functionalised open docking sites [94], and monomer truncation [95]; (ii) post-synthetic engineering of the skeletons [96]; (iii) the incorporation of smart molecules, stimuli-responsive in nature [97]; and (iv) extension of the reaction time [98].

This permanent yet tuneable porosity of COFs, is combined with large surface areas, high thermal stabilities, and the lowest mass densities of any organic material. This unique combination of characteristics has led to immense interest in these materials over the last ten years, with the design of COFs specifically tailored for their application in optoelectronics [99, 100], adsorption and storage of hydrogen, methane, carbon dioxide and ammonia gases [101, 102], and heterogeneous catalysis [103], amongst others.

The COFs ability to accommodate guest molecules in their pores, demonstrated through their application for gas adsorption and storage, can be further extended to the

incorporation of APIs as guests, to create COF drug carriers. Owing to their high and tuneable porosity, COFs are intrinsically designed to potentially overcome the encapsulation efficiency, loading capacity, and controlled- and sustained-release limitations of certain nanoparticles, providing an alternative route to enhance the drug loading capacity of nanoparticles and additional control on the release of the entrapped drug molecules.

1.8. Metal Organic Frameworks (MOFs) as drug carriers

Metal Organic Frameworks (MOFs) are a closely related class of crystalline porous polymers. Prior to the synthesis of COFs, the concepts of reticular chemistry and DCC were initially used to create MOFs. First reported in 1999 by Yaghi, MOFs make use of a functional variety of organic polytopic linkers to integrate inorganic metal ions or polyatomic metal-containing clusters into predesigned networks. [104]

MOFs were also the first of both to be used as nanocarriers in the field of therapeutics. Providing a rigid and stable closed network having permanent well-defined pores, with a narrow pore size distribution and tuneable parameters, similar to COFs, MOFs are able to accommodate a high loading capacity of drug molecules. However, their microporous nature restricts the size of guest molecules, significantly limiting their efficient use for controlled-release drug delivery. This problem was bypassed in 2004 through the development of mesoporous metal (Cr) carboxylates, having pore diameters over 2 nm and complemented by unparalleled surface areas, without compromising the materials' crystallinity. [105]

In 2006, these materials, named as MIL-100 and MIL-101, having cage sizes of 2.5 – 2.9 nm and 2.9 – 3.4 nm respectively, were then studied with regards to the adsorption and delivery of ibuprofen, an anti-inflammatory drug. A number of characterisation techniques determined that the structural framework of both materials was retained after their dehydrated forms were loaded from a hexane solution of the drug. Nitrogen adsorption data showed remarkable adsorption of the drug molecules, with no remaining porosity left accessible for nitrogen. At 33 and 58 % respectively, the exceptionally high loading capacity of MIL-100 and MIL-101, is much higher than that of PNPs at around 6 % and that of liposomes at 0.4 %. [106] This means that only very

small amounts of the drug-MOF conjugate would be required to deliver high drug doses, assuming complete release as demonstrated *in vitro*.

Tuning of the pore size controls the extent of drug adsorption. The 0.48 x 0.58 nm pentagonal apertures of the MIL-100 smaller cages, close to the size of the ibuprofen molecule (~ 1.0 x ~ 0.5 nm), limited drug loading to a selective occupation of the larger cages, accessible through 0.86 nm hexagonal apertures. Conversely, the large 1.2 nm and 1.47 – 1.6 nm pentagonal and hexagonal apertures of MIL-101, allowed ibuprofen introduction into both the smaller and larger cages, which easily accommodated between 56 and 92 drug molecules respectively. MOFs can thus act as molecular sieves, with one guest selectively occupying the largest pores while the smaller empty cages host another differently-sized guest. [107] Controlled-release of the drug molecules took place over 3 and 6 days respectively for MIL-100 and MIL-101. At pore walls, interactions between the framework and the drug molecules take place via π-π interactions between the organic linkers and the aromatic rings of the ibuprofen molecules, and through van der Waal forces. Inside the pore volume, interactions between drug molecules are weaker and the first to be broken. [107] Sustained release is exhibited via breakage of these interactions, i.e. desorption of the drug molecules, exchange of the guest molecules with ones from the aqueous physiological medium, and subsequent diffusion of the drug from the pores.

Utilising the same concept, the rest of the Materials of Institut Lavoisier (MIL) family, all characterised by very large pores and surface areas, could be similarly applied for the delivery of challenging antiviral or anticancer drugs. Different trivalent metal cations, including aluminium(III), chromium(III), iron(III), and vanadium(III), have been used to synthesize MIL-n type compounds. A change in the identity of the metal centre results in an altered toxicity of the carrier, and has been used to construct less-toxic analogues, such as MIL-101(Fe) instead of MIL-101(Cr) and MIL-53(Fe) instead of MIL-53(Cr). [108, 109] *In vivo* studies of pure porous iron(III) carboxylate frameworks, resulted in the absence of an immune response, indicating that these materials were biocompatible and presented very low toxicity. [106]

Structurally-flexible frameworks adapt their pore size to the dimensions of the drug molecules, upon adsorption, optimising the interactions involved between the two. The type and extent of this pore size flexibility depend on the nature of the guest molecules, the identity of the metal centre, and the temperature. In MIL-53, a metal hydroxoterephthalate, this reversible breathing effect occurs through the formation of strong hydrogen bonding with water molecules, and their breakage upon dehydration.

Without altering the chemical bonds of the framework, similar interactions with different guest molecules, such as ibuprofen, have shown an extended release time of the drug over three weeks. [109] Thus, the stronger the interactions between the drug and the framework, the stronger the confinement effect and the energy barrier, leading to a longer release time achieved by the carrier. Furthermore, functionalisation of the pore surface, apart from providing a regular site for the post-synthetic docking of drug molecules, can also be used to impart a positive or negative charge to the pore, for better entrapment of hydrophilic drugs having opposite charges. [110] The introduction of basic ($-NH_2$) or acidic ($-OH$ or $-COOH$), polar ($-Cl$ or $-Br$) or apolar ($-CH_3$) groups in MIL-53(Fe), successfully carried out through direct synthesis using differently functionalised organic linkers, demonstrates that intraframework interactions between functionalised linkers also affect pore volume variations. Nonetheless, these intraframework interactions may be counterbalanced by interactions between the functionalised framework and guest molecules. [111]

In spite of these advantageous characteristics for drug delivery, the systemic circulation *in vivo* of MOFs is limited by their large particle size, often > 200 nm. Scaling-down MOFs to the nanoscale range, allows for their improved implementation as drug delivery nanovehicles. Modification and control of the reaction conditions, e.g. temperature, time, and volume, of synthetic methods, including solvothermal, sonochemical and microwave techniques, have been employed to generate nanoscale MOFs (NMOFs). The synthesis of NMOFs was first reported in 2009 for nanoMIL-101(Fe), onto which a fluorophore and an anticancer agent were separately, post-synthetically loaded (Figure 1.16). The biodegradable nanoparticles were then coated with a thin silica layer in order to enhance their stability *in vitro* and slow down framework decomposition and guest molecule release. Functionalisation of the silica layer with a cyclic peptide complementary to specific overexpressed tumour receptors, further increased the efficacy of the drug. [112] Conjugation of both the fluorophore and the anticancer agent onto the same NMOF, would create a multifunctional theragnostic nanosystem, combining therapeutics with real-time monitoring, enabling personalised patient treatment.

The loading of guest molecules into porous frameworks was initially achieved by soaking the material in a saturated solution of the molecules. This introduced an additional parameter – choice of solvent – that influences the loading process. Moreover, as observed for the release time, the kinetics of entrapment depend on the strength of the

interaction between the drug and the framework, such that the stronger these interactions, the slower the diffusion of guest molecules into the pores. [113] In 2010, the biologically active molecule, nicotinic acid, was incorporated into an iron-based MOF through the bottom-up approach, replacing the organic linker between metal ions. The resulting therapeutically-active MOF, Bio-MIL-1, exhibited an even higher 'loading capacity', than MIL-101, at 71.5 %, allowing even smaller amounts of the formulation to administer high API doses. Framework degradation takes place over 1 hour, quickly releasing nicotinic acid molecules, in a phosphate buffer solution (PBS) at 37 °C and a pH of 7.4, simulating physiological conditions. In spite of the rapid degradation and associated release, the integration of a drug molecule as part of the network, provides an alternative to the need for large-sized pores to accommodate the molecules. Furthermore, it switches the toxic effect due to the organic linkers with a desired therapeutic effect from the drug molecules, resulting in an overall reduced cytotoxicity of the MOF. [114]

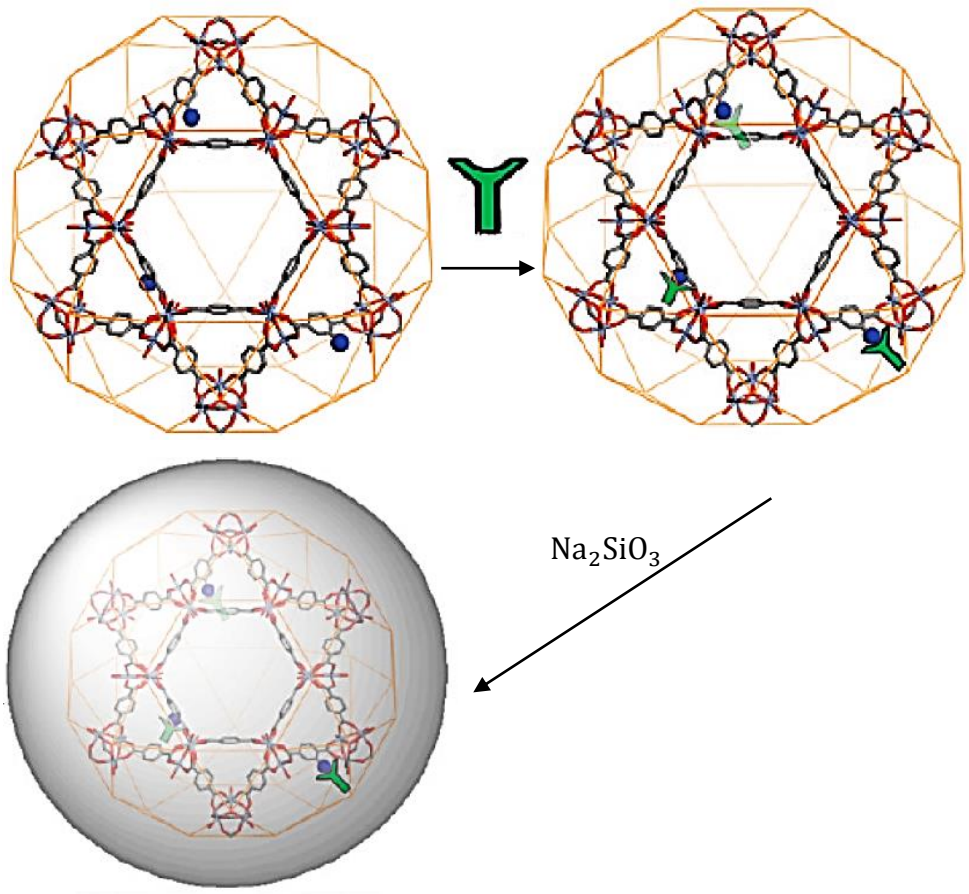

Figure 1.16. Post-synthetic loading of the fluorophore 1,3,5,7-tetramethyl-4,4-difluoro-8-bromomethyl-4-bora-3*a*,4*a*-diaza-*s*-indacene (Br-BODIPY) or the anticancer agent cisplatin prodrug, shown in green, onto amino groups in NMOF-101(Fe), and subsequent coating of the nanoparticles with silica. [112]

Incorporation of stimuli-responsive molecules into NMOFs has recently generated smart NMOF drug delivery systems. The design of these materials was based on the previous functionalisation of MSN-drug systems with stimuli-responsive nucleic acids. Supramolecular nucleic acids can act as 'DNA switches' when exposed to appropriate triggers and counter-triggers, such as pH [115], heat [116], enzymes [117] and light [118]. Drug-loaded NMOFs capped with stimuli-responsive nucleic acids via click chemistry [119, 120], or coated with an acrylamide hydrogel crosslinked with nucleic acid duplexes [121], exhibit selectivity and improved control on the release of the entrapped drug molecules. Similar to the responsive systems discussed in section 1.5, reversible structural reconfiguration, i.e. unlocking, of the nucleic acids is respectively triggered by acidic pH, characteristic of tumour extracellular microenvironments, or the adenosine triphosphate (ATP) biomarker, overexpressed in many tumour cells. Incorporation of nucleic acid-based hydrogels improves on the loading capacities and background leakage resulting from drug-filled pores incompletely-capped by nucleic acid gates.

Bifunctional caps have been developed to add an active targeting aspect to the stimuli-responsive property of nucleic acids. This was achieved through the conjugation of a targeting aptamer, of which the complementary receptor is expressed on diseased cells, and a biomarker-sensitive aptamer, having an overexpressed corresponding protein, as part of the nucleic acid duplex. The former aptamer facilitates identification of the diseased cells, while the latter enables reversible unlocking of the nucleic acid gates to release the entrapped molecules. This further improves the efficacy of the bifunctional capped NMOFs, combining active targeting with controlled-release. [122]

Zeolitic imidazolate frameworks (ZIFs), a subclass of MOFs, have also been used to construct controlled-release drug delivery carriers, due to their decomposition in acidic pHs and their stability at physiological pH. [123, 124] This led to the development of a new hybrid nanocarrier system having a core of nanoparticles made from bovine serum albumin protein and doxorubicin drug molecules, coated with a thin pH-sensitive ZIF-8 shell (Figure 1.17). The ZIF-8 framework imparts its pH-responsiveness to the hybrid material, safely storing doxorubicin under physiological conditions. This was demonstrated through the release, at pH 7.4, of less than 8 % of the drug molecules from hybrid nanocarriers over 24 hours, compared with the release of more than 60 % of doxorubicin, over 4 hours, in the absence of the ZIF shell. Conversely, in an acidic pH of 5, the ZIF shell first undergoes dissolution during which no doxorubicin is released. After complete dissolution of the ZIF layer over 3 hours, most drug molecules are released

within a 24-hour period. These hybrid materials are characterised by an enhanced efficacy over free doxorubicin and ZIF systems, owing to the combined biocompatibility of the protein and pH-responsiveness of the ZIF. Loading capacity, at an obtained maximum of 19 %, is however limited by changes in the morphology of the hybrid system. [125]

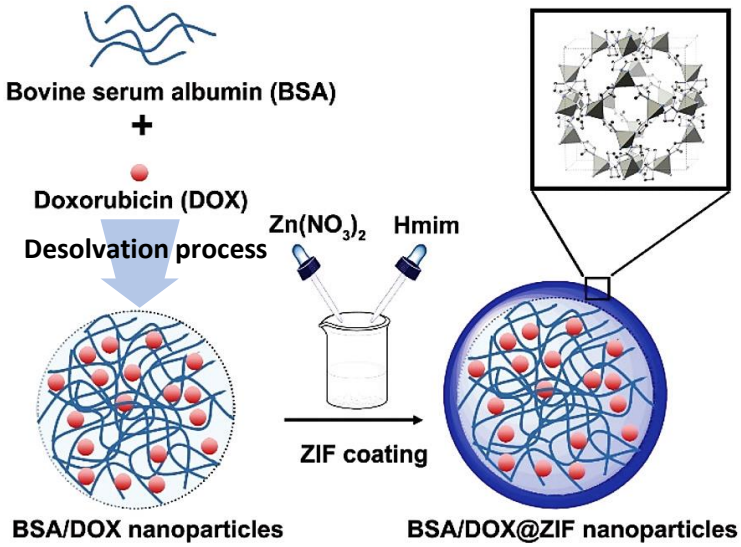

Figure 1.17. Synthesis of the core nanoparticles and their coating with a ZIF-8 shell, to create the hybrid nanocarrier formulation. [125]

Presented as hybrid inorganic-organic solids, the design possibilities of similar MOFs are massive, allowing the construction of new compositions and topologies tailored for specific drug molecular structures and dosing requirements. Their biodegradability further corroborates the use of NMOFs as nanocarriers. The metal to ligand bonds forming the network are relatively labile, allowing the frameworks' breakdown into simpler by-products and preventing their irreversible accumulation inside the body. Major framework degradation, in PBS, for specific MIL frameworks e.g. MIL-100, starts after 7 days, creating a window for sustained release of the drug. Conversely, for other MIL networks e.g. MIL-101(Fe), degradation is rapid, leading to burst release kinetics of the drug. For other systems, such as the smart hybrid protein-ZIF nanocarriers, drug release is stimuli-dependent. Although their application as drug carriers is remarkable, NMOFs present the problem of unwanted cytotoxicity, much like the previously discussed inorganic nanocarriers, due to the presence of metal-containing inorganic linkers alongside organic building units. Some metals are found in notable

amounts inside the body, such as iron and zinc. However, there is yet limited data on the interactions involved between NMOFs and biological systems.

1.9. Covalent Organic Frameworks (COFs) as drug carriers

The absence of metal ions in COFs, in itself lowers the degree of unwanted cytotoxicity. [126, 127, 128] This is a key feature essential for the COFs' more extensive use as drug carriers. Their application as nanocarriers in the field of therapeutics was first reported in 2011, around six years after MOFs were first studied with regards to drug delivery. The drug of choice was once again ibuprofen, loaded from a hexane solution, into a triazine-piperazine-based porous aromatic framework (PAF) synthesised from cyanuric chloride, a trigonal planar linker, and piperazine, a linear linker, via a one-step nucleophilic substitution and polymerisation reaction over four hours, under mild conditions (Figure 1.18). The PAF-6 2D framework, insoluble in organic solvents, is characterised by an ordered plate-shaped morphology made of wavy covalent sheets and a uniform micropore size of 1.18 nm. *In vitro* testing in PBS pH 7.4 demonstrated an almost complete release of ibuprofen molecules over 46 hours, with an initial burst release over the first 10 hours (Figure 1.19). Although this is comparable to the release patterns of some of the MOFs discussed in section 1.8, it nonetheless provides a promising alternative for drug delivery. [129]

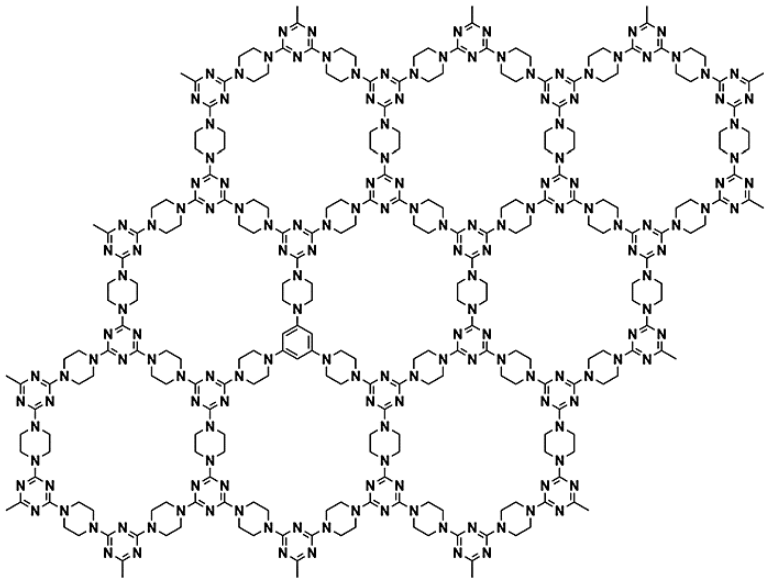

Figure 1.18. PAF-6, a 2D triazine-piperazine-based framework. [129]

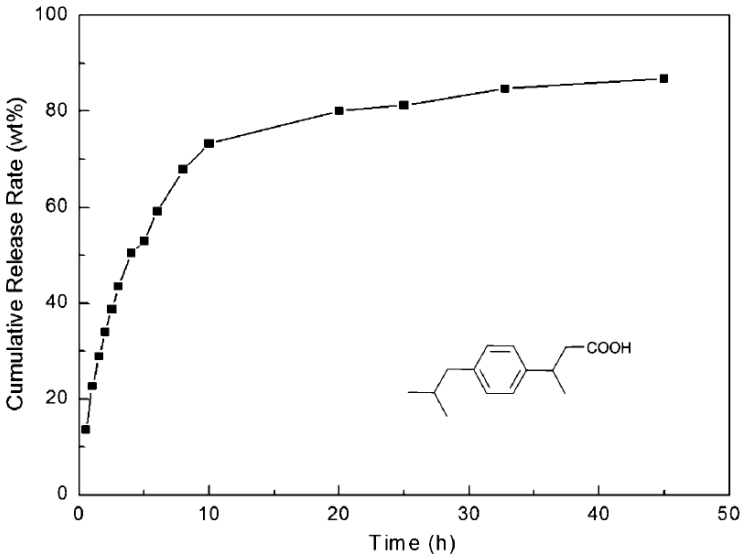

Figure 1.19. The release pattern of ibuprofen from PAF-6 in PBS pH 7.4. [129]

The high electron density of a triazine-based framework, due to the free lone pair of electrons present on the large number of nitrogens, allows for the binding interaction with drug molecules upon loading. Similar to the application of PAF-6, this led to the development of a nanoscale covalent purely-triazine-based framework (NCTF) better suited for drug delivery, due to the nanometre size of the framework particles. Conversely to the traditional harsh conditions of ionothermal CTF synthesis, the framework was synthesised from cyanuric chloride, the same trigonal planar linker used for PAF-6, and biphenyl, a linear linker, via a Friedel-Crafts reaction over 16 hours, under mild conditions [130]. The resulting 2D CTF was scaled-down to the nanosize range, forming NCTFs, via sonication for 30 minutes. Characterised with 1.21 nm micropores, the 2D NCTF accommodated doxorubicin molecules through hydrophobic and π-π interactions, upon drug loading from PBS over 24 hours. Drug release was rapid during the first 24 hours, with a pH of 4.8 accelerating the release in PBS at 37 °C, when compared with a pH of 7.4 (Figure 1.20). [131] This resulted through the protonation of doxorubicin at acidic pH, minimising the hydrophobic interactions with the framework. [132] This pH-sensitivity allows the selective release of doxorubicin in acidic extracellular environments of tumours. Additionally, the efficacy of doxorubicin was considerably increased when compared with free doxorubicin molecules, due to a greater amount of drug molecules being delivered through the framework. Furthermore, *in vitro* studies on the NCTF

indicated that the pure framework was non-toxic, thus eliminating any cytotoxicity arising from the nanoparticle itself. [131]

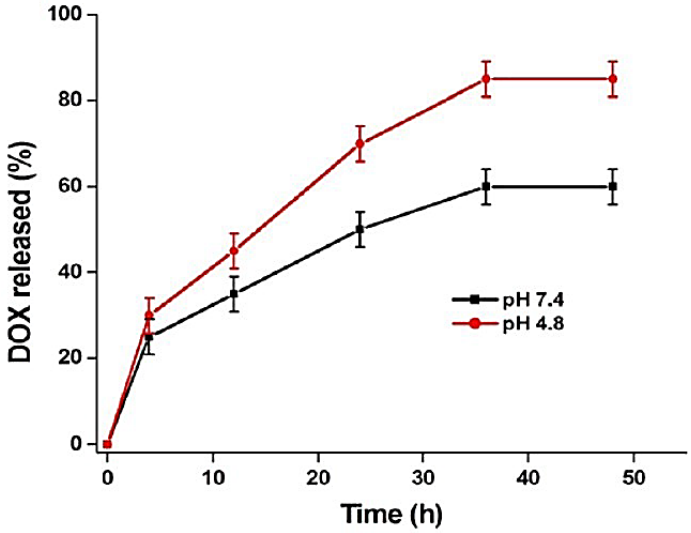

Figure 1.20. The release pattern of doxorubicin from NCTF in PBS pH 4.8 and 7.4. [131]

Utilising the same synthetic concept, biphenyl building units were substituted by tetraphenylporphyrin monomers, to construct a predominantly mesoporous 2D porphyrin-based CTF, which was then loaded with ibuprofen molecules from a hexane solution over 12 hours. At a loading capacity of 19 %, the amorphous porphyrin-based CTF rapidly released 70 % of the loaded drug molecules during the first six hours, at 37 °C in PBS pH 7.4, slowly reaching 90 % over 48 hours. Although this structure presents a higher loading capacity, it exhibits reduced control over the release of the guest molecules, when compared with the previously discussed NCTF. [133]

Evolving from a triazine-piperazine-based PAF to a purely triazine-based COF, a triazine-imine-based COF was next studied as a drug carrier. By eliminating the possibility of keto-enol tautomerization, the lone pair of electrons on imine nitrogens was free to reversibly interact with and anchor guest molecules through hydrogen bonding, upon diffusion into the framework. The 2D triazine triphenyl imine (TTI) COF (Figure 1.21), synthesised from an equimolar mixture of two trigonal planar linkers triazine triphenyl aldehyde and triazine triphenyl amine, exhibited a very high BET surface area for the 2.4 nm mesopores, which have a narrow size distribution. Polyphenolic molecules of quercetin, an anticancer drug, were loaded into the framework from a THF solution

over 16 hours, interacting with the nitrogen atoms in the TTI-COF through hydrogen bonding, without affecting the structural morphology of the framework. The high loading capacity achieved, as indicated through a substantial reduction in the BET surface area, was made possible through the formation of strong drug to framework interactions, stabilising the molecules. Through *in vitro* experiments, the pure framework was found to be non-toxic and biocompatible, while the drug loaded framework exhibited a faster and enhanced efficacy of quercetin, compared to the free drug molecules. [134]

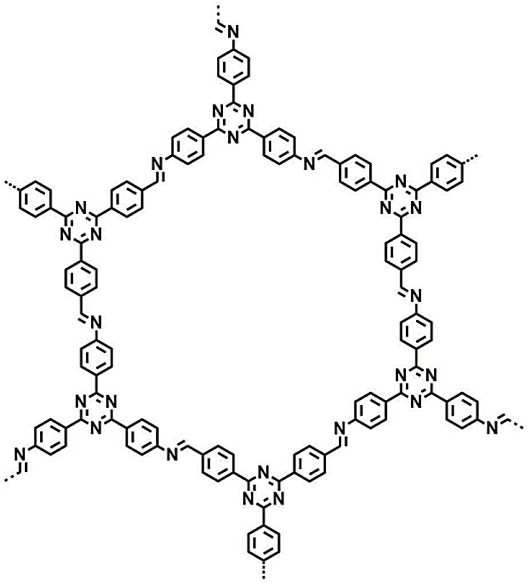

Figure 1.21. TTI-COF, a 2D triazine-imine-based framework. [134]

Research on another triazine-imine-based framework and a purely imine-based framework, was reported in the same year, for the delivery of three different drugs. The two nanoscale COFs (NCOFs), named PI-3-COF and PI-2-COF (Figure 1.22), were synthesised via a condensation reaction between 1,3,5-triformylbenzene, a trigonal planar linker, and triazine triphenyl amine, another trigonal planar linker, or 4,4'-biphenyldiamine, a linear linker, respectively, under solvothermal conditions. [135] The resulting 50 nm polyimine networks were characterised as having uniform 1.1 and 1.4 nm micropores respectively, and relatively high surface areas, making them good potential drug carriers.

Drug molecules having a molecular size comparable to the pore diameter of the frameworks, were chosen and loaded from hexane solutions over six hours. A 30 % loading capacity was reached for the anticancer drug 5-fluorouracil in PI-2-COF, and

slightly lower in PI-3-COF due to its smaller pore size. Loading did not affect the morphology of the framework, except for a minor expansion in pore diameter. [136] The latter observation, accompanied by a reduced surface area, confirms the successful loading of drug molecules into the pores of the framework, stabilised via strong hydrogen bonding with framework nitrogens and π-π interactions between aromatic rings of drug molecules and the framework. [137] *In vitro* testing revealed the low cytotoxicity and good biocompatibility of the pure frameworks, release profiles extending over 3 days for the loaded frameworks, and an increased efficacy of the drug-PI-2-COF system over the drug loaded PI-3-COF, owing to the higher loading capacity of the former. In spite of this, the larger pore size of PI-2-COF is thought to result in an easier release of the drug molecules than PI-3-COF does, thus giving similar release rates (Figure 1.23).

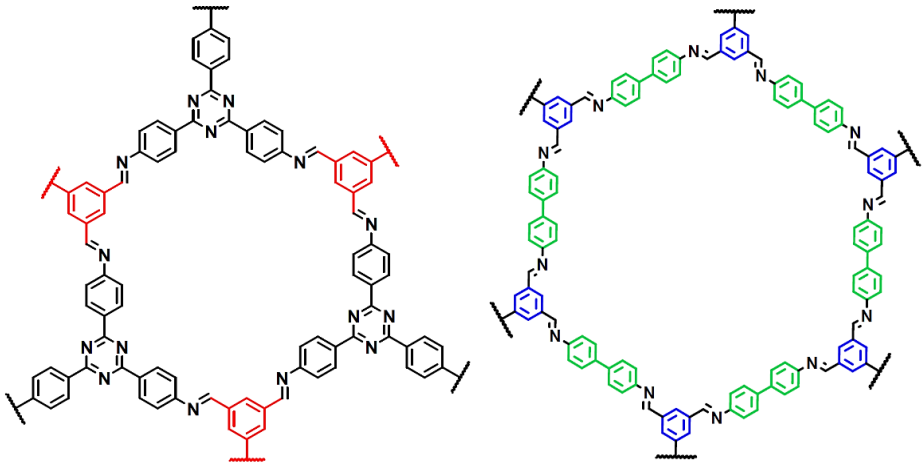

Figure 1.22. 2D PI-3-COF (left) and PI-2-COF (right). [136]

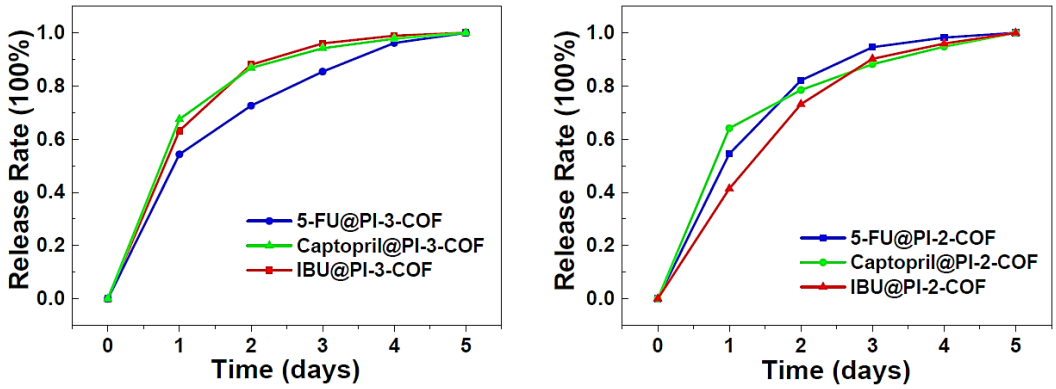

Figure 1.23. The release patterns of 5-fluorouracil, captopril and ibuprofen from PI-3-COF and PI-2-COF in PBS pH 7.4. [136]

Loading and release of the two other drug molecules tested, captopril, administered for the treatment of hypertension and heart failure, and ibuprofen, exhibited the same tendencies as 5-fluorouracil. [136]

An enhanced pH-sensitive control on the storage and release of guest molecules was reported for a new imine-linked DT-COF (Figure 1.24), synthesised from 3,3'-dimethoxybenzidine (DMB), a linear linker, and 1,3,5-triformylbenzen (TFB), a trigonal planar linker, via a Schiff-base condensation reaction under solvothermal conditions for three days. Carboplatin (cis-diammine(cyclobutene-1,1-dicarboxylate)-platinum(II)), an anticancer drug, was loaded from an aqueous solution over 24 hours under dark conditions. Insoluble in organic solvents, DT-COF is characterised by a high thermal stability and a mesopore size of 3.0 nm. At a high loading capacity of 26.8 %, drug release was initially rapid followed by sustained-release, over 120 hours, with a pH of 5.0 greatly accelerating the release in PBS at 37 °C, when compared with a pH of 7.4 (Figure 1.25). The pH-sensitivity of DT-COF is far more pronounced than that of NCTF, allowing for better control on the storage at physiological pH and release at acidic pH, of the loaded drug molecules. [138]

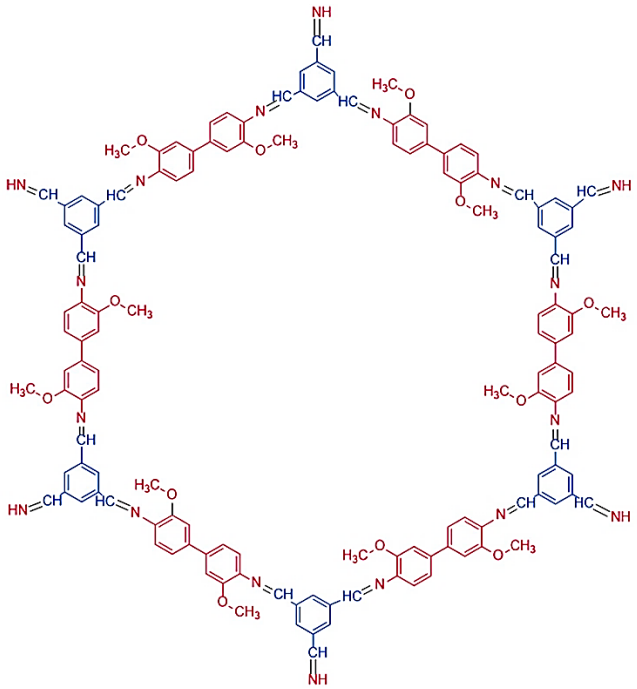

Figure 1.24. DT-COF, a 2D imine-based framework. [138]

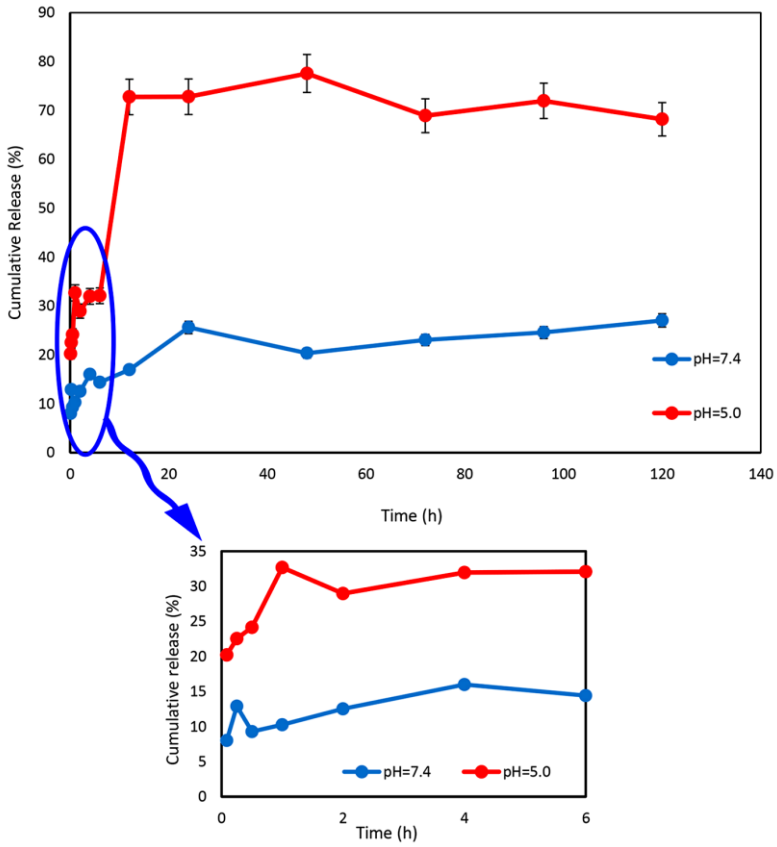

Figure 1.25. The release pattern of carboplatin from DT-COF in PBS pH 5.0 and 7.4. [138]

Improvement on the loading capacity and control on guest release, was also reported for a new type of linkage, polyimide linkage, synthesised via a dehydration-imidization reaction between linear pyromellitic dianhydride monomers and tetrahedral building blocks, tetraaminoadamantane and tetra(4-aminophenyl)methane, under solvothermal conditions. Named PI-COF-4 and PI-COF-5 (Figure 1.26), these polyimide extended networks, with a diamond topology, were characterised by a narrow size distribution for the 1.3 and 1.0 nm pores respectively.

The first 3D COFs to be studied for drug delivery, PI-COF-4 and PI-COF-5 were loaded with ibuprofen molecules from a hexane solution for 2 hours. Retention of their structural integrity was confirmed via powder X-ray diffraction (PXRD), with loading capacities of 24 and 20 % respectively. Controlled-release was confirmed through release profiles (Figure 1.27), which once again demonstrated a direct relation to the size and geometry of the pores, with PI-COF-4 exhibiting a faster initial burst release than PI-COF-5 after 12 hours. Around 95 % of the loaded ibuprofen molecules, was released after

six days. Similar loading and release patterns were observed for captopril and caffeine molecules. [139]

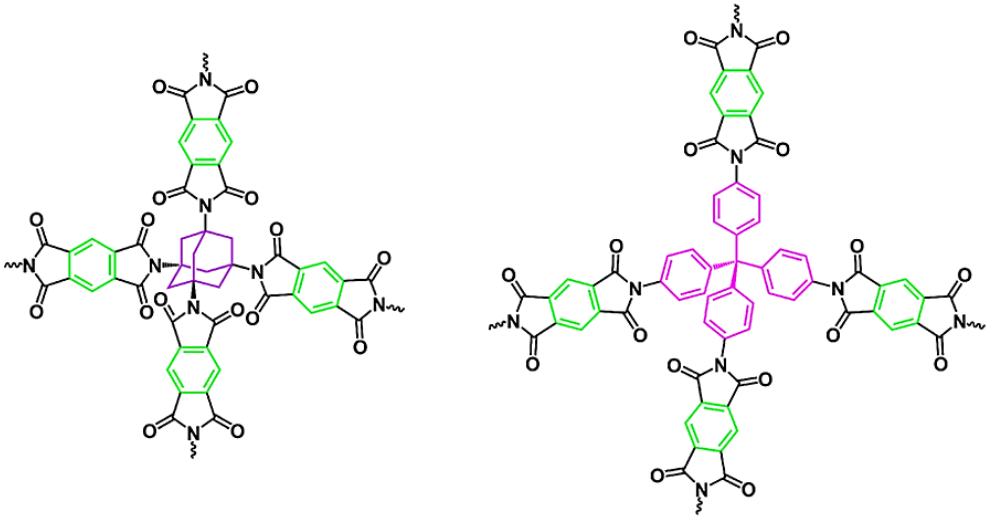

Figure 1.26. 3D PI-COF-4 (left) and PI-COF-5 (right). [139]

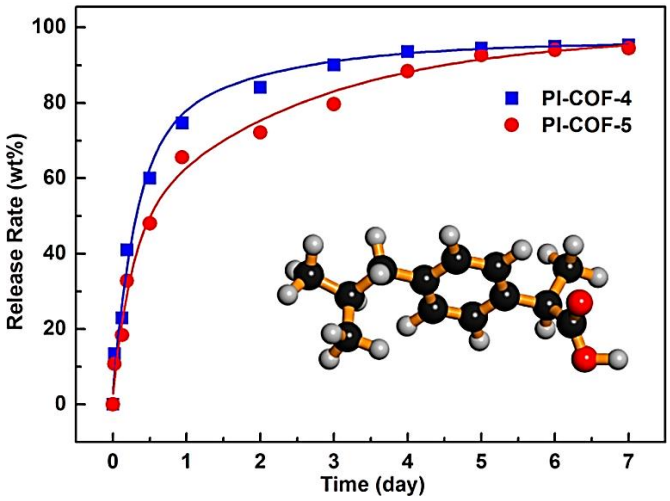

Figure 1.27. The release pattern of ibuprofen from PI-COF-4 and PI-COF-5 in PBS pH 7.4. [139]

A 2D triazine-polyimide-based framework (PI-CTF) was later reported for the delivery of sorafenib, another anticancer drug. Synthesised from cyanuric chloride, a trigonal planar linker, and *p*-hydroxybenzaldehyde, a linear bifunctional linker, via a nucleophilic substitution reaction followed by a facile solution-suspension for three days at room temperature, sorafenib molecules were loaded into the 0.63 nm micropores of PI-CTF, from a DMF solution over six hours. At a drug loading capacity of 83 %, the highest

reported for COFs thus far, PI-CTF exhibited a certain degree of pH-responsiveness with drug release profiles showing an initial burst release followed by a slower release of the loaded drug molecules, resulting in a preferential 66 % sustained release at pH 5.3, after 48 hours, compared with 48 % release at pH 7.4 (Figure 1.28). Dissolution and diffusion of drug molecules adsorbed onto the surface of the framework produced the initial burst release, while the slower release was caused by dissolution and diffusion of drug molecules from the pores of the framework. *In vitro* studies further revealed the low cytotoxicity and good biocompatibility of the pure framework. [140]

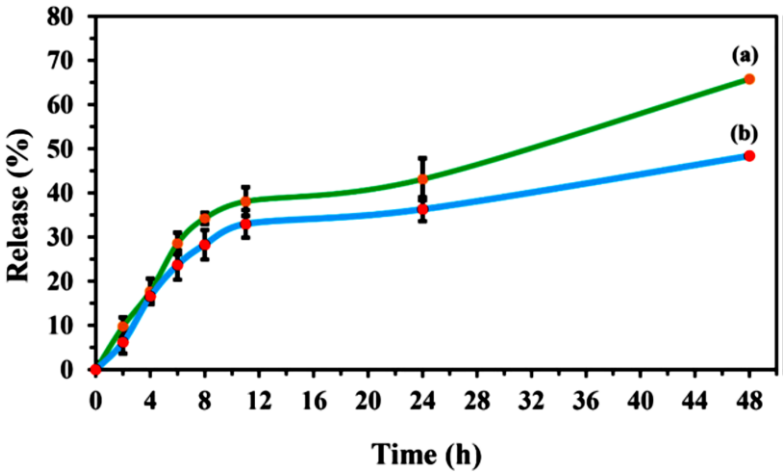

Figure 1.28. The release pattern of sorafenib from PI-CTF in PBS pH 5.3 (a) and 7.4 (b). [140]

In 2021, a cage-based COF was presented as a drug carrier, for the first time, following the unprecedented synthesis of the first two cage-based COFs in 2019 [141], blurring the borderline between 2D and 3D frameworks and incorporating porous organic cages into extended networks. Cage-COF-TT was synthesised from bis(tetraoxacalix[2]arene[2]triazine), a prism-like organic molecular cage acting as a trigonal planar linker, and terephthaldicarboxaldehyde, a linear linker, via a Schiff-base condensation reaction under solvothermal conditions for three days, to form a 2D network characterised by 1.0 nm hexagonal pores. Loading capacities of 17.7, 21.4 and 22.3 % were reached for ibuprofen, 5-fluorouracil and captopril drug molecules respectively, upon stirring in a hexane solution of ibuprofen or aqueous solutions of 5-fluorouracil and captopril, over six hours. Cage-COF-TT released 78 % ibuprofen and 87 % captopril in PBS at pH 7.4 after 12 hours (Figure 1.29), a faster release profile, when compared with

49 % ibuprofen and 52 % captopril release from PI-COF-5, a previously discussed 3D COF with comparable pore size, under the same conditions. [142]

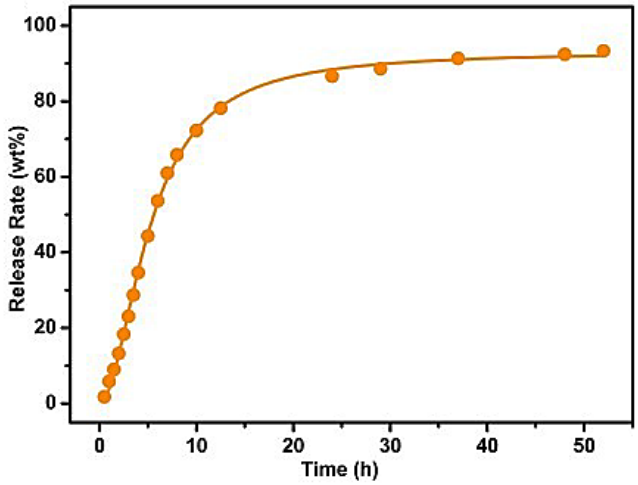

Figure 1.29. The release pattern of ibuprofen from Cage-COF-TT in PBS pH 7.4. [142]

To specifically enhance the π-conjugation effects of COFs and consequently their fluorescence ability, a p-π conjugated trigonal planar monomer, tri(4-formyl-phenyl)amine, was reacted with benzidine, a linear monomer, under solvothermal conditions, to construct an intensely conjugated network. This allowed a bright blue solvent-dependent photoluminescence to be observed when the COF was excited under different wavelengths. 35 % loading of doxorubicin from a PBS solution over 24 hours, was achieved through π-π and hydrogen bond interactions with the framework. The fluorescent property of both the COF and doxorubicin, resulted in an effective fluorescence resonance energy transfer (FRET) system, through which a fluorescence signal was imparted when different amounts of drug molecules were loaded. As more doxorubicin molecules are absorbed by the COF, the photoluminescence intensity of doxorubicin gradually decreases until quenching is achieved when all doxorubicin molecules are loaded into the COF. This unique property enables drug loading, and release, to be monitored not only by UV-Vis spectrophotometry, but also with the naked eye, through a gradual colour change to red and orange-red respectively under natural and UV light (Figure 1.30). *In vitro* experiments revealed the good biocompatibility and low cytotoxicity of the pure COF, an enhanced efficacy of the doxorubicin loaded COF over free doxorubicin molecules, and enhanced release under acidic conditions. [143]

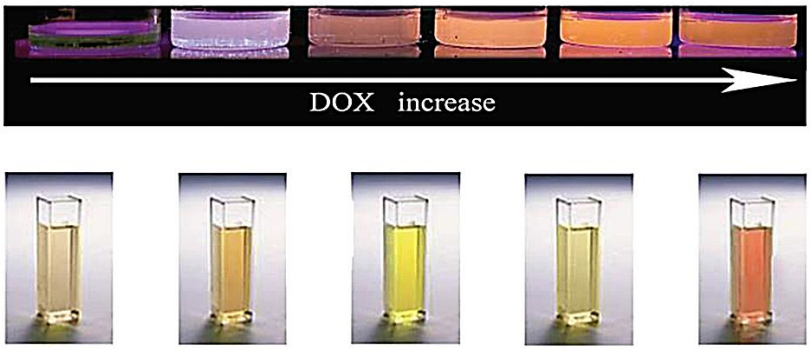

Figure 1.30. Gradual solution colour change observed under UV (top) and natural light (bottom), upon increasing doxorubicin loading. [143]

Hollow spherical particles are a special type of colloidal materials, having a large hollow inner cavity with a large surface area, surrounded by an intact porous shell. Crystallites of the shell material first assemble, with or without a template, into coiled dense spheres. Further deposition of crystallites onto the outer surface of the spheres is combined with dissolution of the core and shell recrystallization, without influencing the internal ordering of the shell crystallites, to form the hollow spheres. The hollow cavity forms a much larger pore, on the macroporous scale, than the mesopores of the shell. Unlike the initial application of MOFs in the field of therapeutics, hollow spherical particles constructed from COF shells were first to be studied with respect to drug molecule loading, to overcome the micropore size limitations of accommodating larger molecules as guests. Hollow spherical particles constructed from MOF shells were then later reported as promising drug-delivery systems. [144, 145]

COF-DhaTab, a hollow spherical Schiff-based COF, was solvothermally synthesized from 2,5-dihydroxyterephthalaldehyde, a linear linker, and 1,3,5-tris(4-aminophenyl)benzene, a trigonal planar linker, and studied with respect to the adsorption of the enzyme trypsin as the guest molecule. [146] COF-DhaTab is more chemically stable, due to strong intramolecular hydrogen bonding, than the previously synthesised mesoporous boron-based COFs which, although now with improved stability, exhibit a degree of hydrolytic degradation, hindering their use as drug carriers. [147, 148] Its spherical morphology, arising from inside-out Ostwald ripening, also remains intact when in aqueous and PBS pH 7.4 environments, confirming its potential application in biomedicine. The shell, characterised by meso-sized 3.7 nm pores, surrounds a macroporous hollow cavity with a diameter of between 0.5 and 2 micrometres.

The globular protein trypsin, with an average size of 3.8 nm, was found to preferentially occupy the COF 3.7 nm pores, over the macroporous inner cavity (Figure 1.31). There is a considerably large difference in the size of the guest molecule and the macropore, such that interaction between the two is infeasible. The enzyme is able to adjust its conformation through partial unfolding in order to enter and fit into the mesopores, after which it then goes back to a globular structure. Although immobilized, the enzyme does not lose its activity. Additionally, doxorubicin loading and release in the hollow sphere was achieved in PBS at pH 5, (Figure 1.32), pointing towards the reversible binding of drug molecules within the macroporous void. [146]

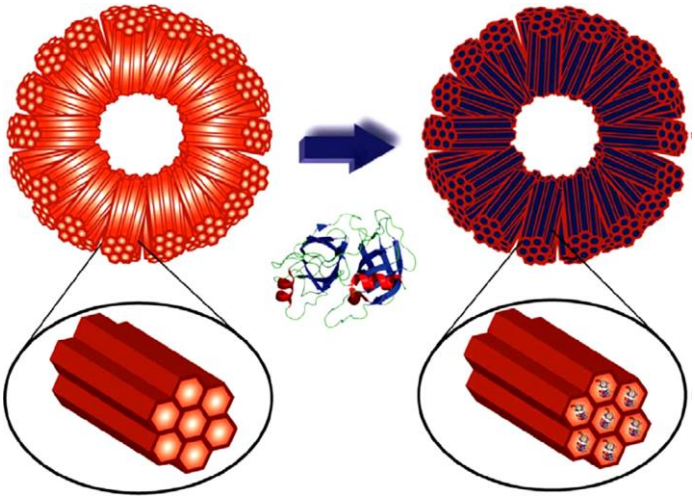

Figure 1.31. Preferential adsorption of the enzyme trypsin into the meso-sized pores of COF-DhaTab. [146]

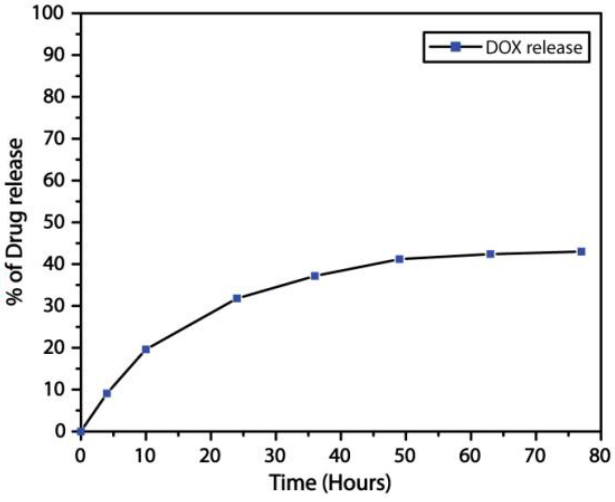

Figure 1.32. The release pattern of doxorubicin from the hollow spheres of COF-DhaTab in PBS pH 5. [146]

Even with the development of NCOF, research to further reduce the size of the networks was reported in 2017, through the exfoliation of 2D COF layers to form covalent organic nanosheets (CONs). Reducing a bulky COF structure to just a thin layer, improves its dispersibility in aqueous media. CONs were thus studied for the potential replacement of COFs in therapeutics. TpASH, a 2D COF, was synthesised from 1,3,5-triformylphloroglucinol, a trigonal planar linker, and 4-aminosalicylhydrazide, a linear linker, via a Schiff-base condensation reaction under salt-mediated conditions. The phenolic hydroxyl group on the diamine monomers in the framework, was used as an anchoring site for functionalisation with amine groups, required for the anchoring of targeting moieties. This was achieved through several post-synthetic modifications, which weaken the π-π stacking interactions between the COF 2D layers, resulting in their chemical delamination. The rendered CONs are conjugated with folic acid, the targeting moiety, for active ligand-receptor targeted delivery of the loaded drug, in this study 5-fluorouracil, to the tumour site and subsequent receptor-mediated endocytosis of the drug loaded CON. [149]

At a drug loading capacity of just 12 %, CONs are not characterised by a high loading efficiency, compared with those of 2D polyimine COFs and 3D polyimide COFs. This is however, the first reported case of active targeting in COFs, demonstrating the potential synthesis of COF targeted drug delivery systems. Apart from exhibiting distribution control and minimising adverse side effects on non-targeted sites, the drug loaded CONs were readily endocytosed by targeted cells but were non-toxic to non-targeted cells. Furthermore, a certain degree of pH-responsiveness was demonstrated through drug release profiles, which show a preferential 74 % sustained release at pH 5, after 72 hours, compared with 50 % release at pH 7.4 (Figure 1.33). This further enhances the controlled-release of 5-fluorouracil molecules. [149]

Pore surface functionalisation allows COFs to achieve specific interactions with guest molecules effectively controlling their release. COF-HQ, a bottom-up functionalised COF, was thus studied to improve the loading capacity and potentially the pH-sensitivity of COFs. The 8-hydroxyquinoline group, incorporated as part of one of the original COF linkers during solvothermal synthesis (Figure 1.34), played a significant role in improving the 5-fluorouracil loading capacity of COF-HQ over the non-functionalised imine-based COF, from aqueous solution over three hours. The partial protonation of a large number of conjugated nitrogen atoms in the functionalised

framework, led to an increased number of non-covalent interactions with the 5-fluorouracil drug molecules, resulting in enhanced drug loading.

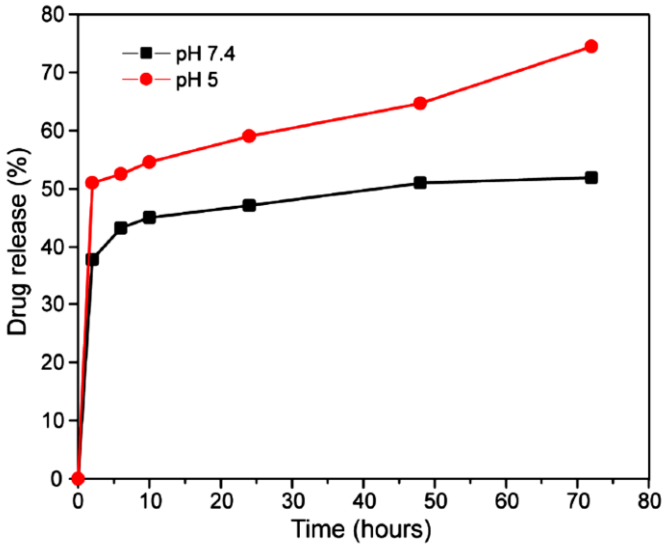

Figure 1.33. The release pattern of 5-fluorouracil from TpASH CONs in PBS pH 5.0 and 7.4. [149]

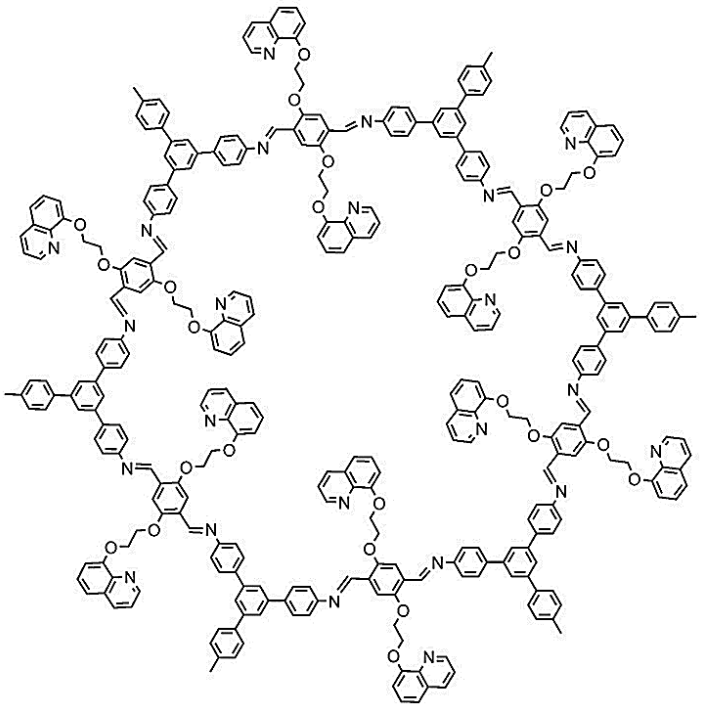

Figure 1.34. COF-HQ, an 8-hydroxyquinoline functionalised framework. [150]

Drug release was similarly affected by the additional interactions arising from the pore surface functionalisation, with a 13.9 % increase in the release of drug molecules at pH 5.0 recorded over release at pH 7.4 (Figure 1.35). At acidic pH, full protonation of the nitrogen atoms in the framework destroyed the hydrophobic interactions with the drug molecules, making the 5-fluorouracil loaded system less stable and accelerating drug release. Although this study proves that functionalisation is an effective factor in improving the loading capacity of the original COF, the authors fail to address the difference in drug release between the functionalised and non-functionalised COF at either pH. [150]

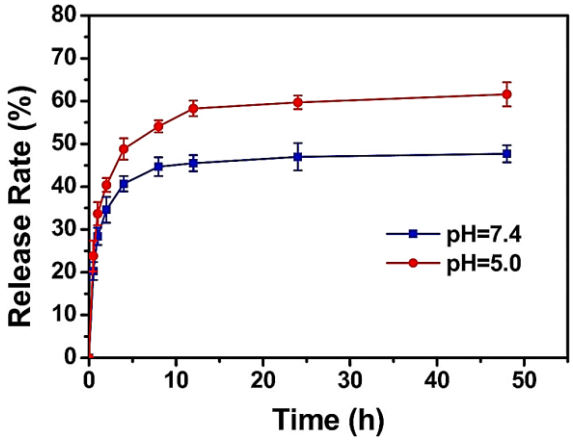

Figure 1.35. The release pattern of 5-fluorouracil from COF-HQ in PBS pH 5.0 and 7.4. [150]

A similar approach was reported for CF-25, another pore-surface functionalised COF, to incorporate primary amino groups onto a boronate-ester framework, through bottom-up solvothermal synthesis. In this study, the anticancer drug of choice, camptothecin, was loaded as a ligand via covalent links to the incorporated functionality, without exerting significant structural or topologic influence, the first reported drug loading via covalent bonds. The acute hydrophobic effect imparted by the loaded camptothecin ligand, limits the amount of water adsorbed to the loaded framework, in effect stabilising and slowing down the hydrolytic degradation of the boronate-ester framework. In PBS pH 7.4, the loaded CF-25 was stable for up to six hours with minimal drug release, after which structural collapse led to 15 % of the loaded drug molecules to be released over 24 hours. Sustained release was successfully achieved at this pH, when

compared to the rapid structure degradation recorded at pH 5.8, consistent with boronate-ester hydrolysis. [151]

For all of these discussed COF materials, drug loading was achieved post-synthetically through entrapment of the molecules within the pores via covalent bonds or non-covalent interactions to the pore walls. In 2017, the anticancer agent phloroglucinol was used as a building block, incorporating it as part of the framework skeleton. Synthesised from trigonal planar 2,4,6-triformylphloroglucinol and linear 4,4'-ethylenedianiline linkers, via a Schiff-base condensation reaction, the resulting 2D COF was named EDTFP-1 and characterised with a pore size of 1.5 nm. Release profiles, obtained in PBS at 37 °C, indicate the rapid release of 70 % of drug molecules over 5 hours. Similar for both pH 5.5 and 7.4, the release patterns suggest a lack of pH-sensitivity. No explanation about the release process is given by the authors. Furthermore, the presented PXRD data which was obtained after treatment at pH of 5.5, 7.0 and 7.4, and proves the good chemical stability of the framework across all three pHs, appears to contradict the release of skeleton-incorporated drug molecules via framework degradation. In line with this, the authors report the potential anticancer activity of the EDTFP-1 material, through enhanced cytotoxicity against four cancer cell lines, suggesting its application as a novel chemotherapeutic agent. [152]

In 2019, another alternative to post-synthetic drug loading was presented for the first time, where guest molecule loading took place in situ, alongside the polymerisation and crystallisation process, via a one-pot synthesis. At a drug loading capacity of 32.1 %, one of the highest recorded for COFs thus far, the resulting 2D framework was synthesised via a Schiff-base condensation reaction by first mixing doxorubicin with 2,5-dimethoxyterephthaldehyde (DMTP) monomers for one hour and then adding 1,3,5-tris(4-aminophenyl)benzene (TAPB) building units. [153, 154] The crystallinity of the drug loaded COF was slightly reduced, when compared with that of the pure COF, owing to Schiff-base interactions between the amino groups on doxorubicin and the carbonyl groups on the aldehyde monomers. The BET surface area for the 3.3 nm mesopores was also significantly reduced for the one-pot synthesis framework, demonstrating the successful adsorption of doxorubicin molecules within the pores. Over two hours, 40 % of initially loaded drug molecules was burst released at pH 7.4, while at pH 6.5 and 5.0, 80 % and higher was even more rapidly released. This pH-sensitivity arises from the increasing chemical instability and linkage degradation of the drug loaded COF with decreasing pH. *In vitro* and *in vivo* testing revealed the good biocompatibility and low

cytotoxicity of the pure COF, and an enhanced efficacy of the doxorubicin loaded COF over free doxorubicin molecules. The latter can be attributed to the COF carrier's EPR effect and its ability to improve the dispersibility and permeability of the drug, while reducing its side effects. [153]

One of the key features essential for the COFs' use as drug carriers is the low degree of unwanted cytotoxicity. For all of the COF materials discussed in this section, with the exception of EDTFP-1, *in vitro* testing revealed the non-toxic or low cytotoxicity and good biocompatibility of the pure frameworks. In 2018, the Schiff-base solvothermal condensation of trigonal planar 1,3,5-tri(4-formylbiphenyl)benzene and trigonal planar 2,4,6-tris(4-aminophenyl)-1,3,5-triazine, was used to construct a triazine-based COF, TrzCOF, characterised with a pore size of 3.5 nm and studied for its cytotoxic potential on cancer cell lines. *In vitro* studies indicate the outstanding anticancer activity of TrzCOF on the human colorectal carcinoma HCT-116 cell line. 40-50 μg mL^{-1} concentration of the linkers did not elicit a cytotoxic effect, whereas a low concentration of 8.31 ± 1.67 μg mL^{-1} TrzCOF inhibited 50 % of cell viability. This concentration of TrzCOF is slightly lower than the concentration of EDTFP-1, 9.89 ± 1.16 μg mL^{-1} [152], to reduce cell viability of HCT-116 by 50 %, suggesting its application as a novel chemotherapeutic agent. [155]

As discussed in section 1.6, in order to further improve the biocompatibility of nanocarrier systems and decrease the strength of an immune response *in vivo*, surface modification via hydrophilic polymers is often adopted by nanoparticles. The first conjugation of PEG onto COF drug carriers was reported in 2018. Integrated as a means to adjust the stability and dispersibility of COFs, the resulting polymer-COF nanocomposite, denoted as PEG-CCM@APTES-COF-1, was self-assembled via the surface PEGylation of 3-aminopropyl triethoxysilane (APTES) functionalised COF-1 [156], through PEG-modified monofunctional curcumin (CCM) derivatives. The so formed hybrids resemble a micelle, with the APTES-COF-1 on the inside (the core) and PEG-CCM on the outside (the corona), as shown in Figure 1.36.

PEGylation did not affect the crystallinity of the functionalised framework, however did improve its stability and dispersion in aqueous conditions, while negatively impacting its thermal stability. The imparted hydrophilicity of PEG to the nanocomposite, led to a higher loading efficiency of doxorubicin molecules. Furthermore, the strong fluorescence ability of the CCM-derived PEG, and hence of the nanocomposite, allowed real-time tracking of the hybrid upon uptake. This revealed its efficient accumulation at

tumour sites, combined with the EPR effect and a prolonged blood circulation lifetime, and enhanced efficacy of doxorubicin loaded nanocomposites compared with the free drug molecules, through both *in vitro* and *in vivo* testing. [157]

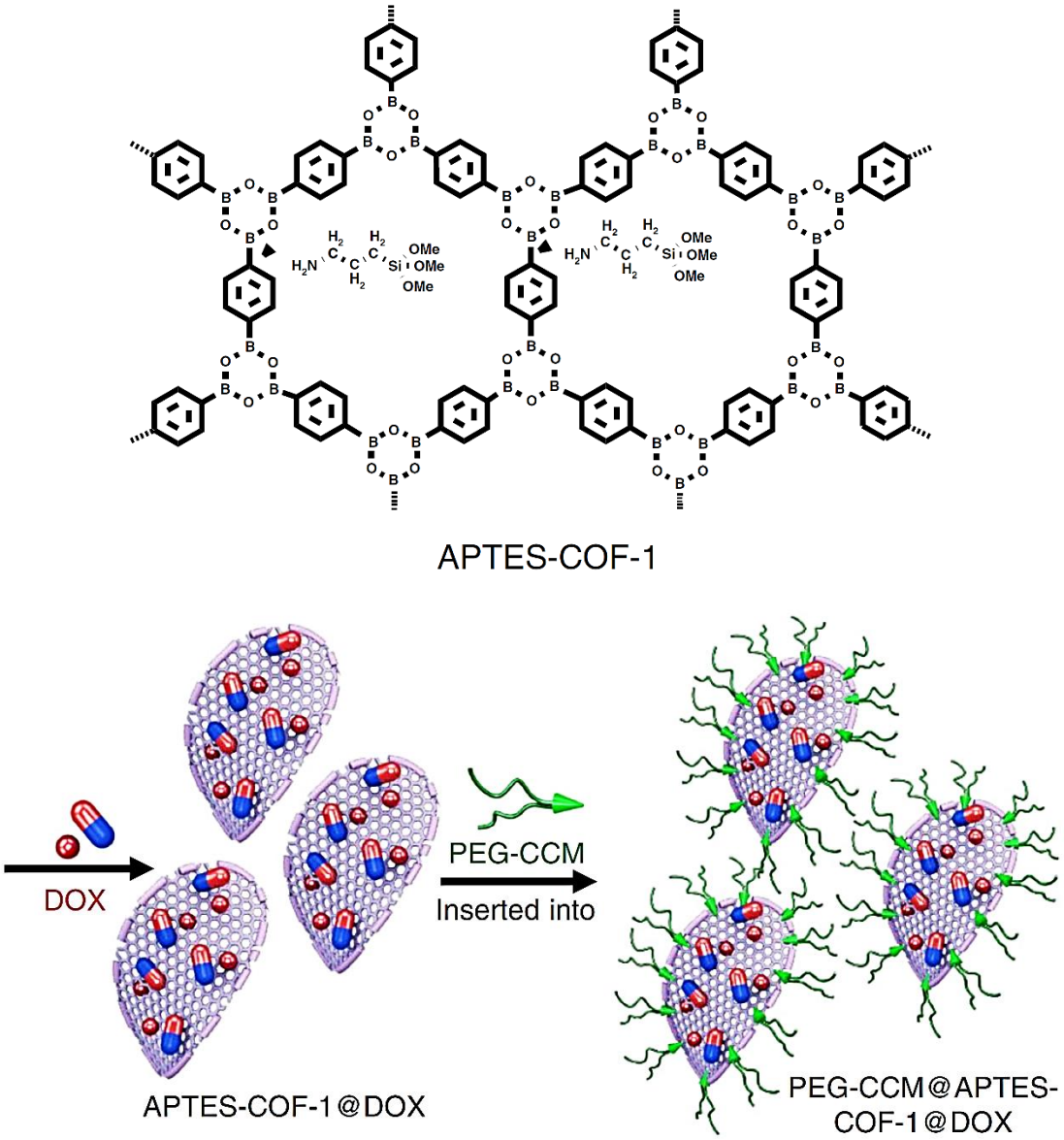

Figure 1.36. Schematic representation of doxorubicin (labelled as DOX) loading into APTES functionalised COF-1, and the self-assembly of PEG-CCM@APTES-COF-1 nanocomposite. [157]

PEG-CCM@APTES-COF-1, assembled as 150 nm thin platelets, was also loaded with pazopanib in 2020, and was able to exhibit brain tumour accumulation in mice, the first nanocarrier system to successfully cross the blood-brain barrier, a semi-permeable border of endothelial cells which is highly selective and severely hinders drug delivery to

the central nervous system. *In vitro* and *in vivo* testing revealed an enhanced efficacy of pazopanib loaded nanocomposites compared with the free drug molecules and the non-toxic nature of the framework. [158]

The incorporation of smart, stimuli-responsive polymers as building monomers or via post-synthetic conjugation, is another controlled-release aspect to be considered during the design and synthesis of potential drug nanocarrier COFs. The 2D NCTF discussed earlier already exhibits preferential drug release in acidic pH, due to a higher solubility of doxorubicin molecules upon protonation, leading to the loss of hydrophobic interactions with the framework, and faster and easier release of the drug molecules. [131] Similarly, pH-responsiveness is also exhibited by CONs, DT-COF, PI-CTF, COF-HQ, CF-25 and TAPB-BMTP-COF, either due to a corresponding mechanism or due to chemical instability and degradation of the framework linkages. Nevertheless, the sensitivity of these two materials to pH is not achieved directly through the incorporation of smart building units or polymers.

The intracellular environment of tumour cells has a higher concentration of glutathione, differentiating it from the surrounding extracellular environment and healthy cells. Reduced glutathione (GSH) acts as a reducing agent, cleaving disulfide bonds, whilst oxidised glutathione (GSSG) acts as an oxidizing agent, forming disulfide bonds. Redox-responsive COFs were reported in 2020, for the intracellular-triggered release of drug molecules. GSH-sensitive disulfide bonds were incorporated through the 4,4'-diaminodiphenyl disulfide linear monomer, into a 2D COF, F68@SS-COF, via a Schiff-base solvothermal reaction, followed by PEGylation of the SS-COF by Pluronic F68. Doxorubicin was effectively loaded at over 20 % capacity into the resulting nanocomposite through hydrophobic and π-π stacking interactions. PEGylation allowed for the steric stabilisation of the hydrolysis-prone imine links in acidic pH. Nonetheless, F68@SS-COF is able to undergo structural disintegration through cleavage of the disulfide bonds in the presence of intracellular high-GSH concentration, rapidly releasing a significantly higher amount of loaded doxorubicin molecules than in the absence of GSH (Figure 1.37). *In vitro* studies further revealed the high extracellular stability and good biocompatibility of F68@SS-COF imparted by PEGylation. [159]

This redox specific release was replicated in a pH and redox dual-sensitive COF, denoted as HY/SS-CON. Utilising the same synthetic concept, 4,4'-dihydrazidediphenyl disulfide linear monomers were substituted in place of the 4,4'-diaminodiphenyl disulfide building units, to construct the 2D hydrazone-linked, disulfide-containing COF, followed

by PEGylation using Poloxamer 188. Doxorubicin was loaded at 18 % capacity from a hexane solution over 24 hours under dark conditions into the 2.5 nm pores of the resulting nanocomposite.

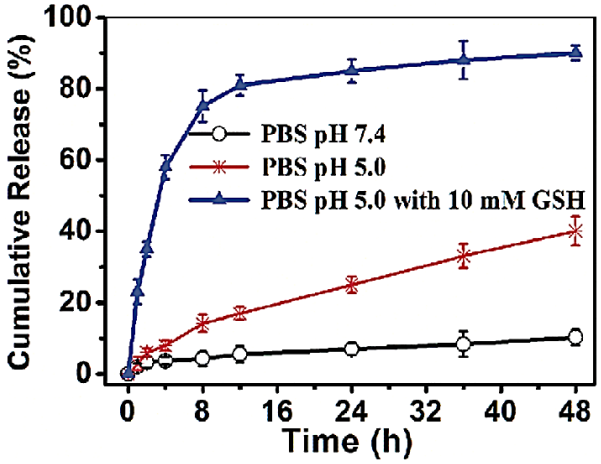

Figure 1.37. The release pattern of doxorubicin from F68@SS-COF in PBS pH 5.0 with GSH, pH 5.0 without GSH and pH 7.4 without GSH. [159]

Similar to F68@SS-COF, PEGylation allowed for the steric stabilisation of HY/SS-CON resulting in a high extracellular stability, as confirmed by the low 10 % drug release over 72 hours. Conversely, acid-induced structural disintegration of HY/SS-CON was observed at pH 5.0, resulting in a higher amount of drug released, than at pH 7.4. In the presence of GSH at pH 5.0, the acid and GSH-triggered disintegration of both the hydrazone linkages and the disulfide bonds, led to an even faster and greater 50 % drug release over four hours (Figure 1.38). [160]

A thioether-functionalised triazole-based COF, TCOF-PEG, was also constructed for a pH and redox dual-sensitive drug release response. Synthesised via click chemistry between 1,3,5-triethynylbenzene and 2,5-bis(ethylsulfonyl)-1,4-diaminobenzene, TCOF (Figure 1.39) was PEGylated using amino PEG via hydrogen bonding and electrostatic interactions with the thioether group and triazole ring of the framework, to yield TCOF-PEG. Following the same release patterns as HY/SS-CON, protonation of the nitrogen atoms in the triazole ring at acidic pH, releases the loaded doxorubicin at a higher rate than at physiological pH. The presence of GSH at pH 5.0, further triggers the release of loaded drug molecules, via GSH attack on the carbon atom of the tautomerised triazole ring in acidic pH, which leads to conformational changes resulting in 70 – 80 % drug release over 72 hours (Figure 1.40). [161]

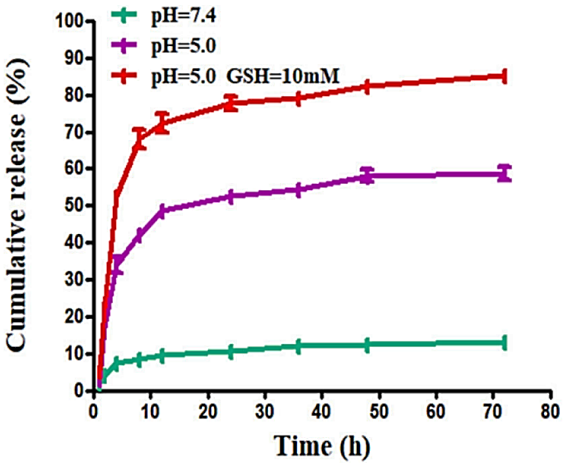

Figure 1.38. The release pattern of doxorubicin from HY/SS-CON in PBS pH 5.0 with GSH, pH 5.0 without GSH and pH 7.4 without GSH. [160]

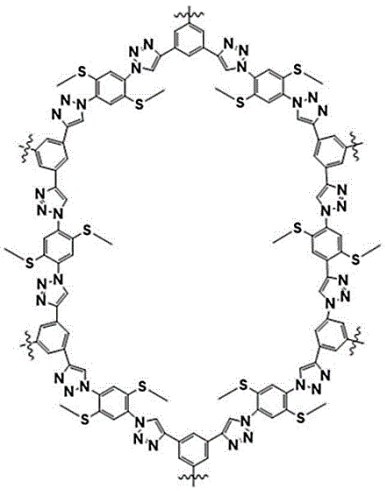

Figure 1.39. TCOF, a 2D thioether-functionalised triazole-based framework. [161]

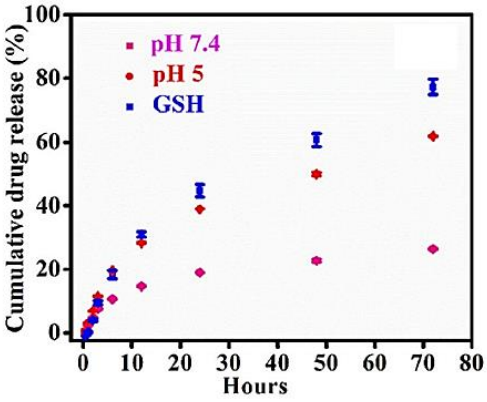

Figure 1.40. The release pattern of doxorubicin from TCOF-PEG in PBS pH 5.0 with GSH, pH 5.0 without GSH and pH 7.4 without GSH. [161]

Owing to the incorporation of the GSH-sensitive disulfide bonds or thioether functionalisation, F68@SS-COF, Hy/SS-CON and TCOF-PEG can all be categorised as smart electro-sensitive COF nanocarriers. The remarkable design of these smart COF nanocarriers could facilitate the development of multifunctional COF nano-constructs, which bring together the active targeting, controlled-release and biocompatibility aspects of drug carriers.

Azobenzene, which is photo-responsive in nature, undergoes a reversible structural isomerisation upon UV irradiation. Its chemical incorporation into a 2D COF was reported in 2014, followed by incorporation into an atomic monolayer, surface COF, reported in 2016. Condensation of azobenzene-derived diboronic acid monomers and 2,3,6,7,10,11-hexahydroxytriphenylene, under solvothermal conditions, yielded the Azo-COF [162], while self-condensation of the same azobenzene-derived diboronic acid monomers resulted in the surface COF. Upon UV irradiation, the azobenzene groups undergo *trans* to *cis* isomerisation, slightly reducing the crystallinity of the Azo-COF, while breaking open the boroxine ring at one end and deconstructing the surface COF, to release the loaded guest molecules (Figure 1.41). [163] To date, this bottom-up approach to achieve smart UV-sensitive COFs has not been reported for COF application in drug delivery, which would allow for better and selective control on the loading and release of drug molecules.

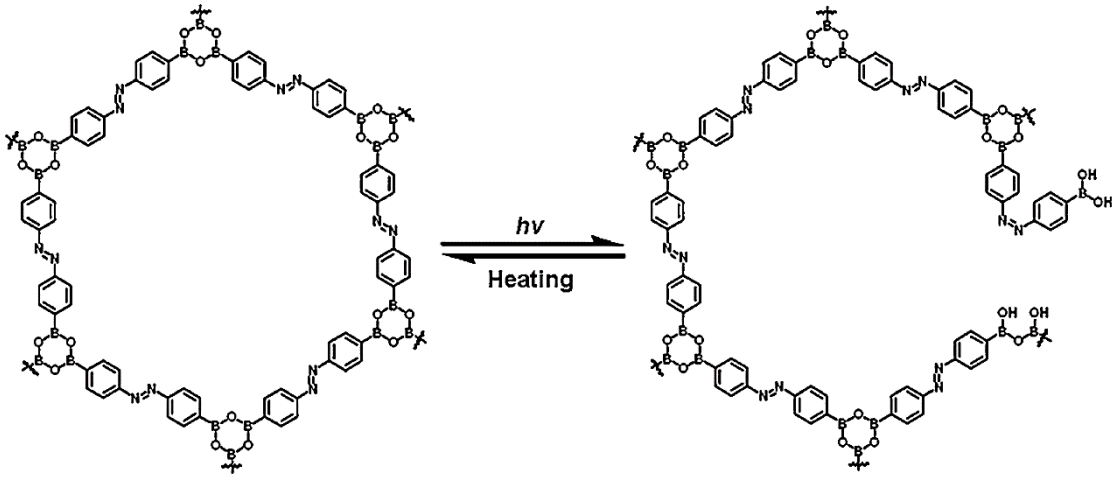

Figure 1.41. Boroxine ring breakage upon photo-triggered *trans* to *cis* isomerisation of the azobenzene groups. [163]

Since 2018, the application of COFs as drug nanocarriers was further combined with photodynamic [164, 165, 166] or photothermal therapy [167, 168]. This dual functionality provides a broader approach to the therapeutic application of COFs, synergistically inducing tumour cell death, which could potentially lead to a significant reduction in the amount of anticancer drug molecules required to achieve an equivalent chemotherapeutic response, in effect decreasing the occurrence of serious side effects. In 2020, the application of COFs as drug nanocarriers was expanded to include photothermal therapy, in combination with MRI imaging for the novel diagnostic application of COFs. [169, 170]

The synthesis and development of COFs as drug carriers is still very much in its infancy. Nonetheless, there is great potential for these framework materials in the field of therapeutics, due to their innate structural regularity, and tuneable high surface areas and large pore volumes. These structural characteristics allow an enhanced drug solubility and protection from degradation in biological environments. Although COFs are better than MOFs for this application, due to the absence of toxic metals which reduces COF cytotoxicity, COF interactions with biological systems, i.e. their safety, is still largely unknown and requires further investigation.

1.10. Identifying the Research Gap

The novel application of COFs as drug carriers is just a decade old, with only a relatively small number of research groups working on it worldwide. As thoroughly reviewed in section 1.9, interest in this application of COFs has snowballed during the last couple of years, yet, the published literature to date is quite limited. The majority of the frameworks reported for this use were synthesised from triazine-based and Schiff-based linkages. Nonetheless, the beginnings of a general trend can be recognised, from the initial application of frameworks heavily-based on nitrogen to ones with a higher carbon content and the incorporation of oxygen and boron atoms. Additionally, only two of the frameworks had a 3D skeleton, PI-COF-4 and PI-COF-3, while all the rest had a 2D network.

Ibuprofen and doxorubicin were the most frequently employed API molecules to study the loading and release mechanisms of the discussed COFs. Loaded drug molecules were mostly within the nanometre range, close in size to the pores of the frameworks.

Only a small number of mesoporous networks, which can accommodate molecules larger than 2 nm or large amounts of molecules, was studied. The largest pores studied in hollow spherical nanoparticles are able to accommodate larger guests such as enzymes, increasing the recyclability of the costly enzyme molecule and also improving the stability of enzymes under extreme conditions. Drug release is sustained for a longer period of time at slower release rates, the stronger the host-guest interactions are, since they stabilize the loading and alignment of drug molecules in the pores. The optimal strength of interactions needs to be achieved to prevent insufficient drug accumulation at the target site due to too strong host-guest interactions. The drug delivery capability of COFs is directly related to their pore size and geometry. Drug loading was consistently carried out via non-covalent interactions between the framework wall and API molecules, with only one COF loading the API via covalent bonds. Upon loading, COF nanocarriers generally remain intact, and exhibit a slight expansion of the pore diameter.

Cell viability investigations show that all of the COF nanocarriers, with the exception of EDTFP-1 and TrzCOF, when tested without payload, did not impart a cytotoxic effect as no significant loss in cell viability was observed, while when loaded, nanocarriers imparted a higher cytotoxicity than the free drug. This indicates that COF nanocarriers enable better drug penetration into cells and are especially beneficial for the transport of hydrophobic, poorly soluble or poorly dispersible drugs across such biological membranes.

There is a limited number of COF nanocarriers which go beyond passive targeting. Although lately successfully designed and synthesised, the incorporation of a targeting moiety or hydrophilic and/or stimuli-responsive polymers onto the outer surface of COFs, is still very much unexplored. Only a few controlled-release strategies have been tested, most of which involve the incorporation of smart pH or electro-sensitive polymers. Hybridization with hydrophilic polymers further opens up a new route for the design of multifunctional nanocomposites for more efficient and controllable drug delivery.

The lack of significant research in the application of COF networks to the field of therapeutics, more specifically in their selective active targeting and smart stimuli-responsive design and synthesis for this application, has left an extensive gap in literature. The ultimate goal is to achieve nanocarriers with high targeting specificity, controlled-release properties, outstanding drug loading capacity and good biocompatibility, but to date this remains a challenge. Further optimization *in vivo* is also required for the design of optimal drug delivery carriers, since findings from *in vitro* studies do not predict the

former's outcomes. A more in-depth understanding of the host-guest interactions involved in these COF crystalline frameworks for the loading, transport and specific release, as well as the complex interactions and mechanisms involved *in vivo* is thus invaluable in designing better and controllable drug nanovehicles.

2. Statement of Scope

The aim of this thesis was to structurally engineer new functionalised stimuli-responsive COF materials, loaded with pharmaceutical molecules, for use as drug nanocarrier systems, and to determine their sensitivity and release response to simulations of varying conditions encountered in the human body.

The objectives consisted of: (i) the synthesis and crystallisation of new COF networks, through the use of a series of monomers under different solvent conditions, via a variety of synthetic techniques, to form the core of the nanocarrier system; (ii) the loading of APIs into the pores and onto the surface of newly synthesised COF structures, through non-covalent intermolecular interactions; and (iii) the conjugation of smart pH, electro, and UV stimuli-responsive polymers onto the surface of the loaded drug-COF carriers, to form the corona of the nanocarrier system. Following the achievement of each of the objectives, characterisation of the resulting COF structures, COF-API conjugates and COF-API-Polymer complexes, was to be carried out using EU-funded advanced instrumentation at the new solid-state and crystal engineering laboratory set up at the Malta Life Sciences Park. The final nanocarrier complexes' sensitivity and responsiveness to stimuli, was then to be investigated *in vitro*, through the drug release response in simulated physiological conditions.

Continuation onto: (i) conjugation of functionalities and/or hydrophilic polymers onto the surface of the loaded drug-COF carriers; (ii) computational assessment of the suitability of the final nanocarrier complexes as drug delivery systems through docking programs, by simulating the molecular recognition process for an optimised conformation between the nanoconstruct and specific sites in the body; and (iii) fine tuning of the final complexes based on knowledge gained from the sensitivity testing, docking exercise, and release kinetics, would provide a more comprehensive contribution to the limited list of smart COF nanocarriers with stimuli-responsive controlled-release properties.

The development and production of a new type of drug delivery system, must follow a set protocol during which vigorous testing is carried out in various stages, to achieve approval from the relevant regulatory bodies thereby enabling its commercialisation. Chemical compatibility of the components, stability, biocompatibility, drug release, reproducibility, and *in vivo* toxicology are a few of the key features tested for, before human clinical trials are allowed to commence. [171] It is thus

very important to note that the aim of this research work was not to create a fully-functional system through the described protocol, as this goes beyond the scope of the study. This thesis was intended to test and explore the potential of COFs to form a smart stimuli-responsive, single entity with drug molecules, and control their release upon a certain stimulus *in vitro*.

3. Methodology and Instrumentation

3.1. COF Design and Synthesis

The structural design and engineering of new COF materials is based on the symmetry, rigidity and geometry of the building units. Combined with the reversible bond formation provided by DCC, these monomers' characteristics govern the expected topology and pore structure of the frameworks. The wide variety of monomer combinations leading to COF synthesis as reported in literature through several synthetic techniques, has inspired the following research work.

3.1.1. Monomer Selection

A series of monomers having C_2, C_3 or T_d symmetry (Table 3.1) were chosen, the majority of which, for the first time, to build new COF materials. Depending on the symmetry of the reactive end groups, 2D or 3D COFs were formed. The selected monomers have amine, aldehyde, boronic acid, hydrazide, hydroxy, or carboxylic acid reactive end groups, to yield different types of linkages, namely imine, boronate anhydride, hydrazone, boronate ester, and ester links. Most of the linkers have rigid π bonds as part of an aromatic ring, to preserve their structural integrity during framework formation, ensuring that the predetermined networks were synthesised. Various molecular lengths and sizes of building linkers were also chosen, to tune the size and structure, surface area and available unoccupied volume of the pores of the frameworks.

Monomer selection allowed for the synthesis of differently-linked COFs which would then be tested for their sensitivity in simulated physiological conditions. It should be noted that since the construction of a fully-functional drug delivery system is not the purpose of this research work, the selected monomers have not been screened by the generally recognised as safe and effective (GRASE) [172, 173] standard required for approval by regulatory bodies.

Table 3.1. Details for the chemicals used as linkers in COF synthesis.

Code	Chemical (IUPAC name)	Brand	Purity	Formula	Structure
C1	4-(3,4-diamino phenyl)benzene-1,2-diamine	Molekula	GPR	$C_{12}H_{14}N_4$	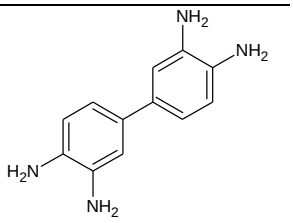
C2	(3,5-diformyl phenyl)boronic acid	abcr	96 %	$C_8H_7BO_4$	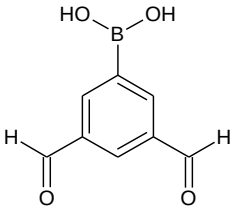
C3	Ethanedihydrazide	TCI	≥96.0 %	$C_2H_6N_4O_2$	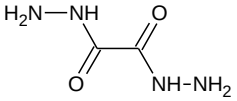
C4	N',N'-bis(3-aminopropyl) propane-1,3-diamine	TCI	>95.0 %	$C_9H_{24}N_4$	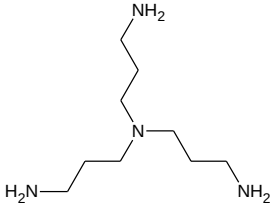
C5	Triphenylene-2,3,6,7,10,11-hexol hydrate	TCI	>95.0 %	$C_{18}H_{12}O_6.xH_2O$	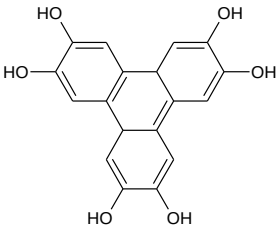
C6	2-amino-2-(hydroxymethyl) propane-1,3-diol	Molekula	99.0 %	$C_4H_{11}NO_3$	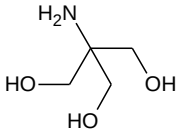
C7	Terephthal aldehyde	Acros Organics	98 %	$C_8H_6O_2$	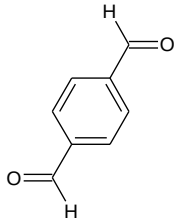
C8	Pyridine-2,5-dicarboxylic acid	Molekula	>99 %	$C_7H_5NO_4$	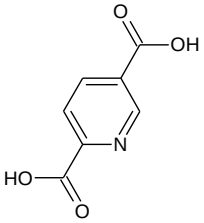

Code	Chemical (IUPAC name)	Brand	Purity	Formula	Structure
C9	Pyridine-2,6-dicarbaldehyde	abcr	95 %	$C_7H_5NO_2$	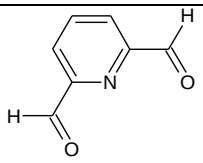
C10	1,1'-ferrocenedicarboxaldehyde	Molekula	>98 %	$C_{12}H_{10}FeO_2$	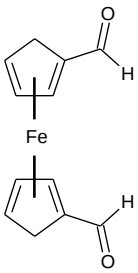
C11	4-[(4-aminophenyl) diazenyl]aniline	Molekula	≥98.0 %	$C_{12}H_{12}N_4$	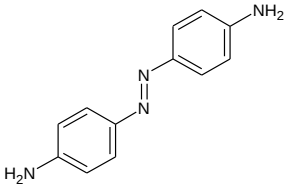
C12	N',N'-bis(2-aminoethyl)ethane-1,2-diamine	Acros Organics	96 %	$C_6H_{18}N_4$	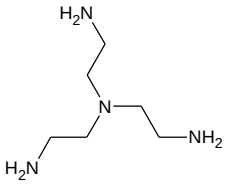
C13	2,5-dimethylbenzene-1,4-diamine	Carbo synth	98 %	$C_8H_{12}N_2$	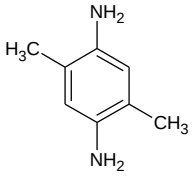

All chemicals were used without further processing.

3.1.2. Synthetic Techniques

Traditional nanoparticle drug delivery systems are synthesised using techniques including sol-gel synthesis [174], microemulsion processing [175] and spray-drying [176]. These affect physical and chemical properties, such as particle size, size distribution and area of application.

COF materials are conversely synthesised using techniques which allow reversible bond formation. Thus, reaction conditions need to be carefully selected in order to achieve

a thermodynamically stable, crystalline porous network exhibiting a minimal number of defects.

3.1.2.1. Reflux Synthesis

In 2006, the classic solvothermal synthetic technique was modified into a catalyst-free dehydration technique using reflux at ambient pressure to successfully construct COFs [177], overcoming the former's sealed vessel protocol. As inspired by this facile synthetic technique, the monomer combinations for MCS1, MCS2, MCS3, MCS4, MCS5, MCS6, MCS11, MCS12 (Table 3.2) were first sonicated for 10 – 20 minutes to enhance the dissolution of each linker, and then reacted in 40 mL of solvent, under reflux at atmospheric pressure, in a 100 mL round-bottomed flask, for 72 hours. Upon cooling to room temperature, the product was collected, washed and subsequently dried under vacuum for 24 hours.

Similarly, based on the reported synthesis of ferrocene-based organometallic compounds in 2014 [178], the monomer combination for MCS10 was reacted in 100 mL of solvent, under reflux at atmospheric pressure, in a 250 mL round-bottomed flask, for five hours, after sonication. Upon cooling to room temperature, the reaction mixture was allowed to stand in the dark for 48 hours, and was concentrated via rotary evaporation, after which the product was precipitated and collected, washed and dried under vacuum.

3.1.2.2. Liquid-Assisted Grinding (LAG) Synthesis

The first LAG synthesis of COFs, published in 2013 [90, 91], marked a major achievement in the successful green solid-state synthesis of framework materials, as an alternative to wet synthesis and the harsh conditions employed by other synthetic techniques. As inspired by this work and optimised during the author's B.Sc. [179] and M.Sc. dissertations [180], the monomer combinations for MCS7, MCS8, MCS9, MCS10, MCS13 and MCS14 (Table 3.2) were reacted in the presence of a catalytic amount of solvent, in 25 mL Teflon grinding jars using a Retsch MM400 ball mill, at a frequency of 25 s^{-1} for a maximum of 12 minutes, and allowed to undergo evaporative crystallisation from 1.5 mL of solvent.

3.1.2.3. Microwave-Assisted Synthesis

Another facile synthetic technique, microwave irradiation is recently being widely employed for organic synthesis. Microwave-assisted synthesis of COFs was first reported in 2009 [87, 88]. It allowed the rapid, large-scale synthesis of the framework in an open vessel, overcoming the sealed vessel requirement of solvothermal synthesis. Based on this work, the monomer combination for MCS13 (Table 3.2) was irradiated in the presence of 20 mL of solvent, under atmospheric conditions, in an open 100 mL borosilicate beaker using a 150 W standard microwave oven, for a total of 15 minutes, after which it was collected and allowed to crystallise. [181]

Table 3.2. Monomer combinations for reflux, LAG and MW synthetic reactions.

Reaction code	Monomer combination	Synthetic technique
MCS1	**C1**+**C2**	Reflux
MCS2	**C2**+**C3**	Reflux
MCS3	**C2**+**C4**	Reflux
MCS4	**C2**+**C5**+**C1**	Reflux
MCS5	**C2**+**C5**+**C3**	Reflux
MCS6	**C2**+**C6**	Reflux
MCS7	**C6**+**C7**+**C8**	LAG
MCS8	**C6**+**C9**+**C8**	LAG
MCS9	**C4**+**C9**	LAG
MCS10	**C4**+**C10**	Reflux; LAG
MCS11	**C2**+**C11**	Reflux
MCS12	**C2**+**C5**+**C11**	Reflux
MCS13	**C7**+**C12**+**C4**	LAG; MW
MCS14	**C7**+**C13**	LAG

3.1.3. Controlling the Rate of Crystallisation

As demonstrated by the research work carried out for the author's B.Sc. [179] and M.Sc. dissertations [180], crystallisation environment may affect the formation of framework materials. When testing a series of different solvents, ranging from non-polar,

to polar aprotic and polar protic solvents, during the synthesis and crystallisation of potential COFs, a change in the crystal system and space group was observed for the same monomer combination having the same type of bond. [182] As inspired by these findings, a wider range of solvents (Table 3.3) was employed in this research work, in order to determine the best crystallisation conditions for the optimal rate of crystal formation. Crystallisation was carried out in 4 mL Fisher soda lime glass vials, at room temperature.

Table 3.3. Details for the solvents used in COF synthesis.

Chemical (IUPAC name)	**Brand**	**Purity**	**Formula**	**Structure**
Ethanol	Carlo Erba	99.9 %	C_2H_6O	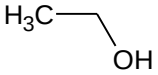
Oxolane	Riedel-de Haën	≥99.9 %	C_4H_8O	
Benzene	Biochem Chemo pharma	99.5 %	C_6H_6	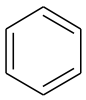
Methanol	Carlo Erba	99.9 %	CH_4O	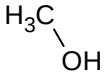
Ethoxyethane	Aldrich Chemical	U.S.P.	$C_4H_{10}O$	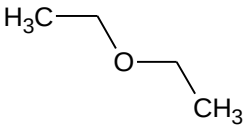
Dichloromethane	Fisher Chemical	99.9 %	CH_2Cl_2	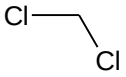
N,N-dimethylacetamide	Carlo Erba	99.95 %	C_4H_9NO	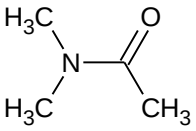
1,4-dioxane	Carlo Erba	99.8 %	$C_4H_8O_2$	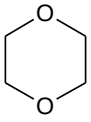
1,3,5-trimethylbenzene	Alfa Aesar	>98 %	C_9H_{12}	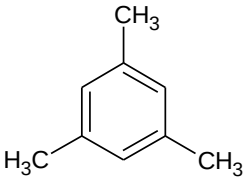

Chemical (IUPAC name)	Brand	Purity	Formula	Structure
Acetic acid	BDH	GPR	$C_2H_4O_2$	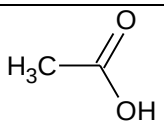
N,N-dimethylformamide	Aldrich Chemical	ACS	C_3H_7NO	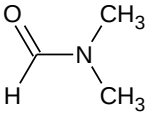

All solvents were used without further processing.

3.2. API Loading

API molecules can either diffuse into the pores, becoming entrapped within the COF network via interactions with the channel walls and neighbouring API molecules, or conjugate onto the surface of the COF nanoparticle via interactions with the framework edges. The strength of these host-guest interactions is a major factor affecting the release profile of the loaded API molecules. Strong covalent bonds or various weak intermolecular interactions, including hydrophobic, π-π and hydrogen bond interactions, may be exploited to, respectively, chemically link or physically adsorb the API molecules to the pores and surface of the framework, depending on the functionalities involved.

The chosen API molecule has a small molecular size and multiple functional groups, ensuring a high potential for the molecule to effectively diffuse into the channels of the framework and intermolecularly interact with its pore walls and surface, without itself undergoing any chemical modification.

Based on the consistently-reported drug loading process discussed in section 1.9, and upon successful synthesis and characterisation of the new COF materials, the formation of the COF-API conjugates was carried out via post-synthetic loading of the selected API molecule (Table 3.4) from an oversaturated 32 mL hexane solution, in which the framework material was chemically stable as investigated through control tests, by stirring for six hours, under atmospheric conditions.

Table 3.4. Details for the API and solvent used in API loading.

Code	Chemical (IUPAC name)	Brand	Purity	Formula	Structure
C14	5-fluoro-1H-pyrimidine-2,4-dione	Molekula	≥95 %	$C_4H_3FN_2O_2$	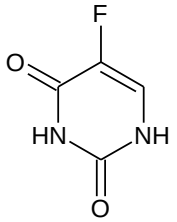
	Hexane	Carlo Erba	HPLC	C_6H_{14}	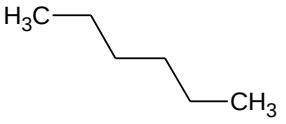

3.3. Conjugation of Smart Stimuli-Responsive Polymers

All of the designed COFs in section 3.1 include imine or hydrazone links in combination with other linkages, making them sensitive to pH due to their susceptibility to acid catalysed hydrolysis back to the starting monomers, resulting in framework degradation. As reviewed in section 1.9, this affords a certain degree of pH sensitivity to the COF. The direct incorporation of smart stimuli-responsive polymers, allows for the potentially more accurate detection of specific physical or chemical stimuli, through a structural or solubility response, achieving better control on the release of guest molecules. The smart polymers **C9**, **C10**, **C11**, were thus chosen for their respective pH, electro, and UV sensitivity.

In acidic pH, the nitrogen atom of pyridine-2,6-dicarbaldehyde, **C9**, is protonated to form the conjugate acid, transforming the polymer from a neutral to a charged state, generating electrostatic repulsion between the polymers, potentially resulting in a conformational rearrangement or solubility change. This leads to the destabilisation of the COF, triggering the escape of the loaded API molecules. [183] A similar neutral to charged transformation is exhibited by 1,1'-ferrocenedicarboxaldehyde, **C10**, upon exposure to oxidising conditions, reversibly forming the hydrophilic ferrocenium cation, increasing the nanocarrier complex's wettability by a significant contact angle drop for water. This leads the previously blocked channel-doors of the framework to 'open', resulting in the release of the loaded API molecules. [184] Upon UV irradiation with wavelengths between 320 – 380 nm, reversible *trans* to *cis* structural isomerisation is

demonstrated by 4-[(4-aminophenyl)diazenyl]aniline, **C11**, via an inversion mechanism of the N–C bond or a rotation mechanism of the N=N bond, once again resulting in a conformational rearrangement, allowing the release of the loaded API molecules. [185]

The recently published pH and redox responsive COF nanocarrier systems [159, 160, 161], incorporate smart polymers as one of the building units of the framework. Based on this work, the chosen smart polymers were used as linkers for MCS8, MCS9, MCS10, MCS11, MCS12, incorporating them as part of the pre-drug-loaded framework through a bottom-up approach. This also inspired their post-synthetic conjugation onto the surface of the COF-API nanoparticle conjugates via intermolecular interactions with framework edges. Upon successful synthesis and characterisation of the COF-API conjugates, the selected smart polymers were conjugated from an oversaturated 5 mL hexane solution, in which the drug-loaded framework was chemically stable, by stirring for six hours, under atmospheric conditions. The latter COF-API-Polymer complexes were thus self-assembled [157], whilst ensuring that the unnecessary release of loaded drug molecules was not triggered by high or low temperatures.

3.4. Characterisation

COFs are generally found as crystalline powders, insoluble in many organic solvents, thus requiring the use of techniques for solid-state characterisation, including microscopy, X-ray diffraction (XRD), FTIR spectroscopy, thermogravimetric analysis (TGA), and solid-state NMR spectroscopy.

3.4.1. X-Ray Diffraction (XRD)

An initial screen of the sample under a light microscope, in polarised and unpolarised light, can be used to quickly determine the presence of a crystalline material. A Leica Z16 APO microscope equipped with a QImaging QICAM Fast 1394 digital CCD camera was used to screen the samples. Crystallinity is an essential requirement for COFs. However, since they are obtained as crystalline powders, determining their crystallinity is somewhat limited by the microscope's magnification.

XRD is a much more powerful tool in characterising crystalline materials. A lot of information on the structure and morphology, regularity, atomic connectivity and

porosity, can be obtained from the XRD analysis of crystalline materials. For powder samples, PXRD is used, while in the event of a single crystal, single crystal XRD (SCXRD) is employed. Each crystal structure has a unique PXRD pattern and extracting information from these patterns can sometimes be quite challenging. The unit cell parameters, *a*, *b*, *c*, α, β and γ, are found via indexing of the peak positions. Fitting these parameters to the experimental pattern via Pawley/Le Bail fitting, which refines the dimensions, follows the determination of the space group symmetry adopted by the crystal system. Crystal structure solution and Rietveld refinement then make use of the peak intensities to obtain and refine the atomic coordinates, and hence the atomic connectivity, within the crystal structure.

The lowest energy conformation of the asymmetric unit, stoichiometrically representing the expected links formed between building monomers, is used as a rigid body model to carry out crystal structure solution. Parameters are automatically randomised based on the approximate errors in the parameters. When the refinement of bond lengths, bond angles and torsion angles in the rigid body fails to produce an occupancy of 1 for each atom, appropriately weighted restraints are applied to fix the target bond length or bond angle value, with a tolerance of 1 and 0.001 respectively, and control the refinement of the parameters. Upon achievement of a correct solution, temperature factors are applied and refined, to produce the best agreement between the observed and calculated PXRD patterns. The Crystallographic Information File (CIF) for the crystal structure is then checked for consistency and integrity of its contents and the reported structure (unit cell geometry, space group symmetry, atomic positions, displacement parameters), and against typical ranges of values and expected behaviour, to flag potential errors and unusual findings for closer examination, possible correction and improvement.

Laboratory PXRD data were collected in Kiel, Germany, and at the new solid-state laboratory set up at the Malta Life Sciences Park, on a STOE Stadi P and Stadi MP or Stadi P diffractometer, respectively, using a curved germanium (111) monochromator, at Cu $K_{\alpha1}$ radiation with a wavelength of 1.54060 Å and Mo $K_{\alpha1}$ radiation with a wavelength of 0.70930 Å, using a Mythen detector. All laboratory measurements were carried out at a temperature of 293 K, using Hilgenberg capillaries of 0.01 mm wall thickness and 0.50 – 1.0 mm diameter, or rotating flat transmission sample holders with 3 or 6 mm openings. Flat plate samples were prepared by fixing a small amount of the solid between two pieces of commercially available sticky tape. Synchrotron measurements were collected at

beamline BM01 at the European Synchrotron Radiation Facility (ESRF) in Grenoble, France, on a PILATUS2M detector using a double crystal monochromator, at a wavelength of 0.64066 Å. [186] All synchrotron measurements were carried out using Hilgenberg capillaries of 0.01 mm wall thickness and 0.50 mm diameter, at a temperature of 120 K. Variable temperature PXRD measurements were collected according to the following temperature profile: (i) heating ramp from 120 to 500 K at 360 K/h; (ii) cooling ramp from 500 to 120 K at 360 K/h. Data integration was carried out using Bubble and SNBL Toolbox computer programs. [186]

Powder data were processed using TOPAS-Academic [187], while single crystal data were processed using CrysAlis PRO v.40 [188], ShelXT [189], ShelXL [190], and OLEX2 [191]. Full geometry optimisation for a lower energy conformation of uncharged molecules was carried out from a .mol format, using Turbomole V7.3 and TMoleX V4.4.1 as interface [192], at BP86-RI/def-TZVP level of theory, with COSMO-RS [193] activated and all default settings for convergence criteria retained.

3.4.2. FTIR Spectroscopy

Infra-red spectroscopy can be used as a quick indicator of new bond formation. Due to the characteristic adsorption at specific frequencies by different bonds or functional groups, a particular IR band can provide evidence of the formation of the desired bond. Furthermore, an IR spectrum can also indicate the presence of unreacted building monomers. FTIR spectra were collected using a Shimadzu Fourier Transform Infrared Spectrophotometer Model IRAffinity-1, from KBr-Sample discs, and processed by IR Solution FTIR control software.

3.4.3. Hot Stage Microscopy

Prior to and in combination with variable temperature XRD, hot stage microscopy can be used to determine the thermostability of the materials and any phase changes exhibited when the sample is exposed to a wide range of temperatures. A THMS 600 temperature-controlled stage system, equipped with Linksys32 System control software, was used to visually examine the samples throughout a pre-set temperature ramp

programme. Fine tuning the temperature profile according to the resulting data, can then be extended to a Simultaneous Thermal Analysis (STA) investigation of the sample.

3.5. Drug Release Profile

The release pattern of the loaded drug is dependent on several factors, including the strength of the interactions between the API molecules and the framework, the chemical stability of the COF, the strength of the stimulus, and the stability and structural or solubility response to the stimulus exhibited by the conjugated smart stimuli-responsive polymer. As the strength of the host-guest interactions increases, API molecule release is sustained for a longer period of time at a slower rate. However, this may be counteracted by the chemical instability of the framework linkages in simulated physiological conditions, as mentioned in section 3.3, which speeds up the release of the loaded molecules. Similarly, as the strength of the encountered stimulus increases, the drug release is also expected to increase. The release is further enhanced, as the stability of the smart polymer, with respect to a stimulus, decreases. Moreover, the greater the extent of conformational rearrangement and/or solubility change, the faster the unloading of the API molecules.

The final nanocarrier complexes' sensitivity and response to stimuli was investigated *in vitro* in simulated physiological conditions, using 1X phosphate buffered saline (PBS), obtained as tablets from Fisher BioReagents. Cumulative release of the loaded API molecule from the nanocarrier complexes was studied at pH 4.9 and pH 7.4 for the pH-sensitive complex, at oxidising and control conditions pH 7.4 for the electro-sensitive complex, and in UV irradiation and control conditions pH 7.4 for the UV-sensitive complex. The release of the COF-API conjugate was also studied for comparative purposes. 0.005 g of complex was dispersed in 5 mL of PBS, sealed in pre-treated regenerated cellulose dialysis membrane of molecular weight cut-off (MWCO) 10 kDa, obtained from Spectro/Por®7, and suspended in 100 mL of external PBS in a 250 mL borosilicate beaker, at 37 °C for 24 hours, while stirring. 4 mL aliquots withdrawn from the external PBS at time 0, 20 min, 40 min, 1, 2, 4, 6, 8, 12 and 24 hours, and replaced with fresh PBS to maintain the same volume, were analysed using UV-Vis spectrophotometry to determine the drug concentration. UV-Vis spectra were collected using a JASCO V-650 UV-Vis spectrophotometer, from 10x10 mm Quartz SUPRASIL

cuvettes, and processed by Spectra Manager II software. All aliquots were then left to evaporate to analyse the remaining powder using a combination of the characterisation techniques (section 3.4).

4. COF Synthesis

4.1. MCS1

4.1.1. Design and Synthesis

The reaction between 4-(3,4-diaminophenyl)benzene-1,2-diamine, **C1**, and (3,5-diformylphenyl)boronic acid, **C2**, involved the Schiff-base condensation of amine and aldehyde functional groups alongside the self-condensation of boronic acid. The combination of the C_2 monomer with the bifunctional C_3 monomer was expected to yield a 2D hexagonal extended network with imine and boronate anhydride links (Figure 4.1, Scheme 4.1).

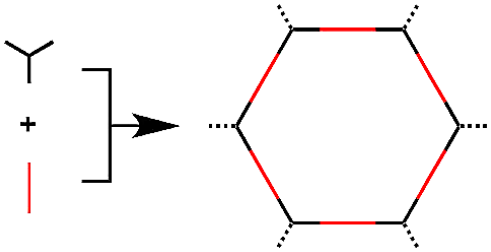

Figure 4.1. Hexagonal COF resulting from the combination of C_3 and C_2 monomers. [194]

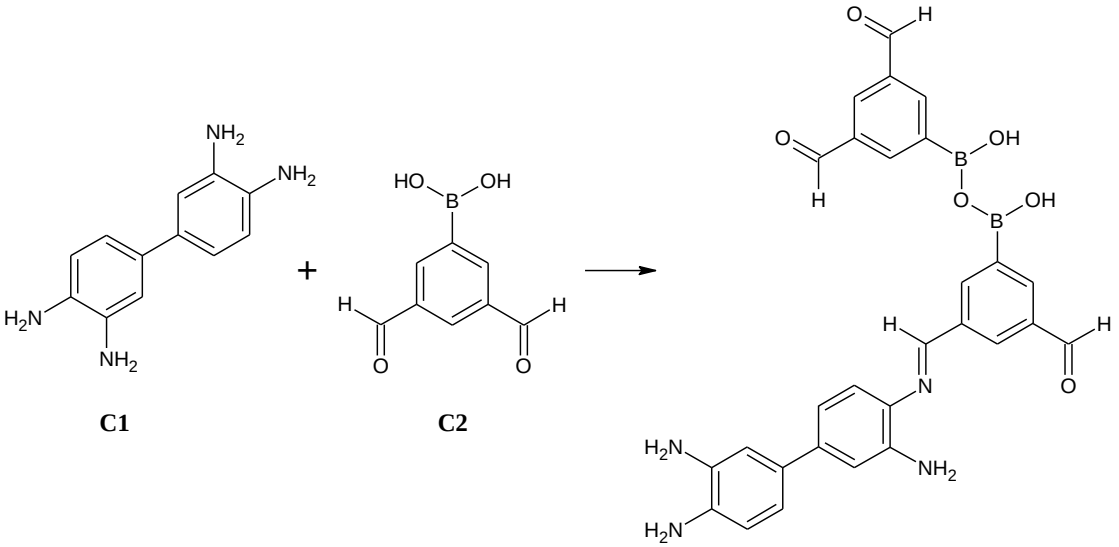

Scheme 4.1. The expected imine and boronate anhydride links formed between monomers **C1** and **C2**.

These building units were reacted together in a 1 + 1 condensation via reflux (section 3.1.2.1). A change in colouration was observed from the light brown and white colouration of the monomers respectively, to a mustard yellow crystalline powder obtained from reaction in 1:1 1,4-dioxane:1,3,5-trimethylbenzene (MCS1_001). Upon washing with oxolane (MCS1_002) and subsequent drying under vacuum (MCS1_003), the sample retained its colouration.

4.1.2. Characterisation and Analysis

The crystallinity of the samples was determined under the microscope, upon reflection of plane polarised light (Figure 4.2).

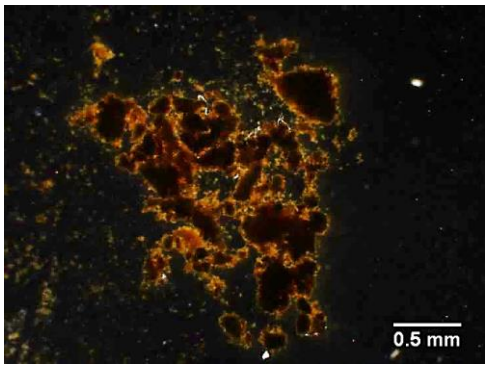

Figure 4.2. Photomicrograph of MCS1_001 from reflux with 1:1 1,4-dioxane:1,3,5-trimethylbenzene.

The X-ray powder patterns obtained for the three samples are very similar, showing a high background and reflections of low intensity. MCS1_001 has the best crystallinity, suggesting that the washing and drying protocol had an effect on the crystal structure. There were not enough peaks to carry out reliable indexing and thus no attempt was made to determine the crystal structure. Comparison of the laboratory data for MCS1_001, having the best diffraction pattern, with the patterns for the two monomers, reveals the formation of a mixture, a quasi-amorphous product with excess starting monomers (Figure 4.3). Variable temperature PXRD measurements will be carried out at high temperatures, to attempt improving the crystallinity and check whether a new compound was formed.

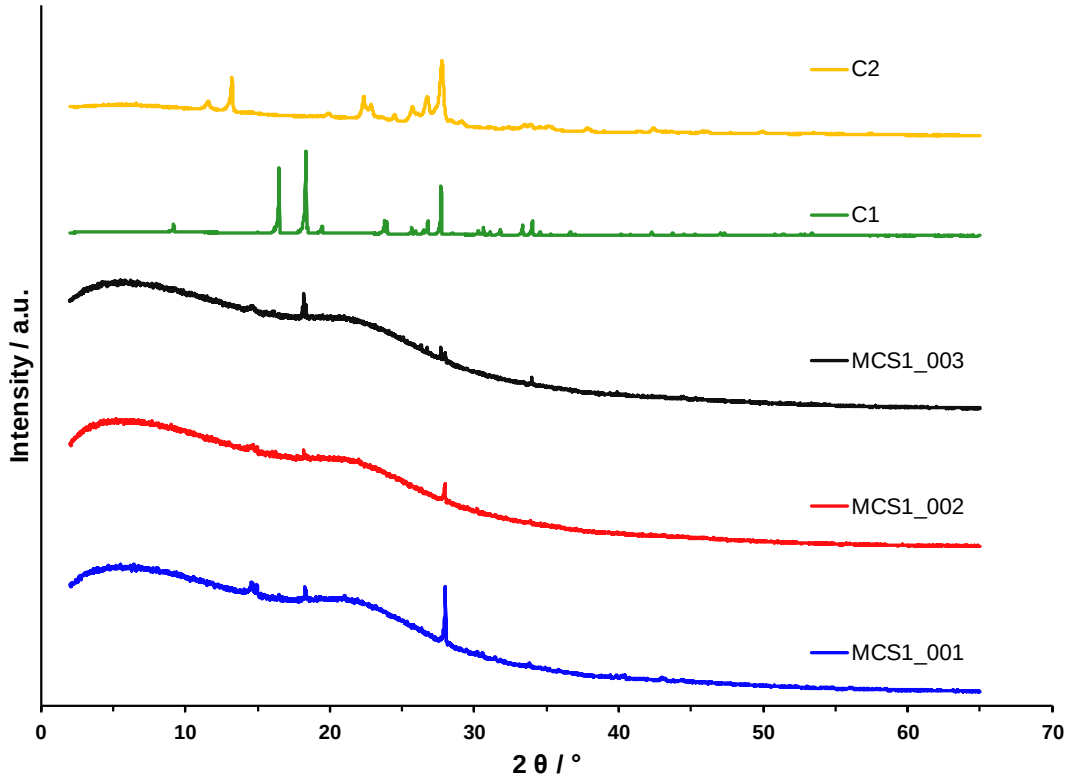

Figure 4.3. Laboratory PXRD patterns for MCS1_001 (blue), MCS1_002 (red) and MCS1_003 (black), obtained from a 1 + 1 condensation of the monomers via reflux in 1:1 1,4-dioxane:1,3,5-trimethylbenzene, upon washing with oxolane, and subsequent drying under vacuum, respectively, and for the **C1** (green) and **C2** (yellow) monomers, at 293 K.

The formation of new imine and boronate anhydride links between the two monomers was confirmed by FTIR spectroscopy. The spectrum for MCS1_001 shows bands at 1680-1640 cm^{-1}, characteristic of C=N stretching, indicating the successful formation of imine bonds. The C=O stretching band of the free aldehyde (1740-1720 cm^{-1}) and the N–H stretching and N–H bending bands of the free amine (3385 and 1500 cm^{-1}) are all absent, confirming that all of the amine and aldehyde end groups reacted during reflux. Similarly, the asymmetric B–O stretching band (1340 cm^{-1}), the symmetric B–C stretching band (1317 cm^{-1}), the in-place O–H bending band (972 cm^{-1}) and the out-of-plane vibration band (648 cm^{-1}), characteristic of boronic acid, are all absent, with the O–H stretching band at 3435 cm^{-1} significantly attenuated in MCS1_011. This confirms that all of the boronic acid end groups reacted during reflux, to form boronate anhydride links, exhibiting their characteristic in-plane C–H bending mode at 1006 cm^{-1} and out-of-plane vibration band at 702-669 cm^{-1}. The FTIR spectrum for MCS1_001 is noticeably different from the spectra of the pure starting monomers (Figure

4.4), providing evidence that a new imine and boronate anhydride linked structure was formed.

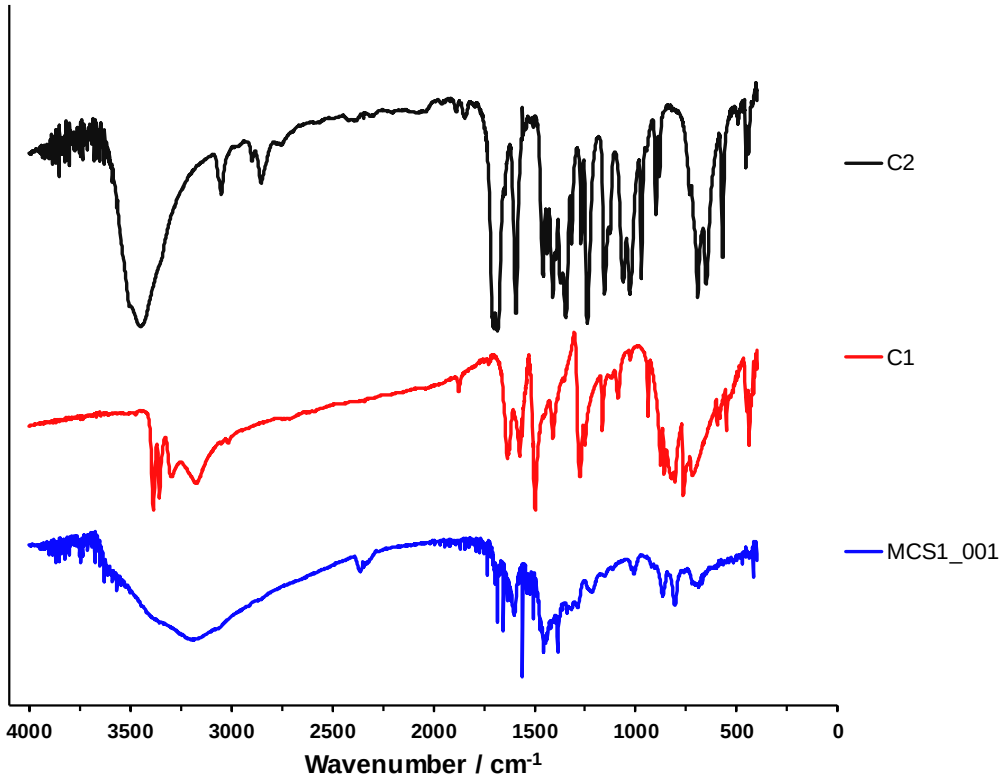

Figure 4.4. FTIR spectra for MCS1_001 (blue), obtained from a 1 + 1 condensation of the monomers via reflux in 1:1 1,4-dioxane:1,3,5-trimethylbenzene, and for the **C1** (red) and **C2** (black) monomers.

As demonstrated by hot stage microscopy, the new structure has a high thermal stability. A morphological change was only observed at a temperature of 475.8 °C, upon which the sample started to shrink (Table 4.1). This can be attributed to the new strong covalent imine and boronate anhydride bonds, which require a considerable amount of energy before being broken and exhibiting decomposition behaviour. No melting phase was observed at 175-177 °C or 259-261 °C, the much lower melting ranges of the starting molecules respectively, confirming the presence of strong intramolecular bonds, as opposed to the weak intermolecular bonds of the pure monomers, and the absence of unreacted linkers. STA will be carried out for a more in-depth and quantifiable investigation on the thermal stability and decomposition behaviour of the new structure.

Table 4.1. Temperature programme followed during hot stage microscopy of MCS1_001, corresponding observations and photomicrographs of the morphological changes.

Ramp	Rate (°C/min)	Limit (°C)	Observation	Photomicrograph of observed changes
1. Heating	15	350	No observed change	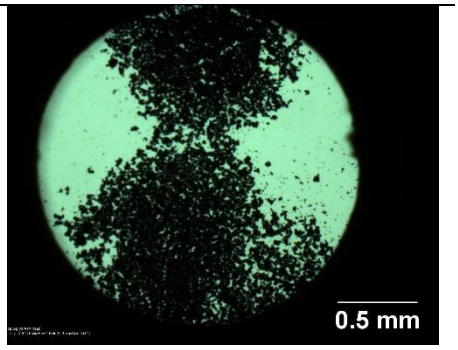
2. Heating	5	600	Slow shrinking at 475.8 – 510.0 °C	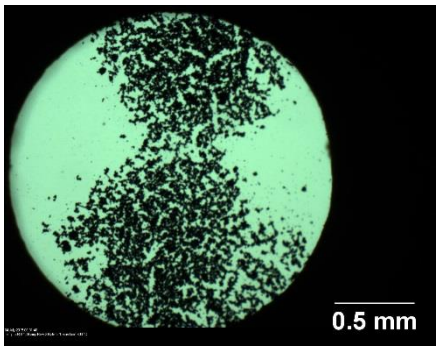
			Faster shrinking at 512.2 – 577.3 °C	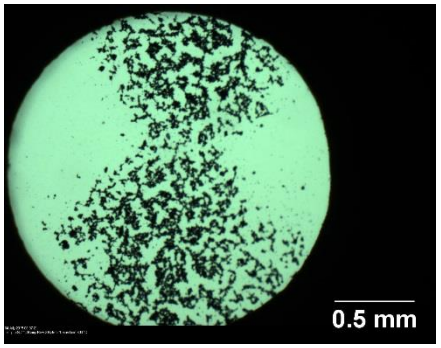 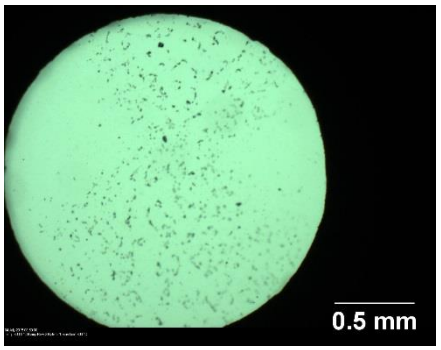
3. Cooling	20	65	No observed change	

4.1.3. Crystal Structure of (3,5-diformylphenyl)boronic acid, C2

The **C2** monomer was not found in the Cambridge Structural Database (CSD). Table 4.2 shows the unit cell parameters, after Pawley fitting, for a triclinic centrosymmetric $P\bar{1}$ (2) space group (Figure 4.5). Structure solution is currently underway at the time of writing.

Table 4.2. Unit cell parameters for **C2**.

Crystal System	Triclinic
Space Group	$P\bar{1}$ (2)
***a* (Å)**	4.223(9)
***b* (Å)**	15.022(9)
***c* (Å)**	37.330(1)
***α* (°)**	138.07(6)
***β* (°)**	75.24(1)
***γ* (°)**	101.98(6)
***V* (Å³)**	1529.88(8)
***R*-wp (%)**	1.41

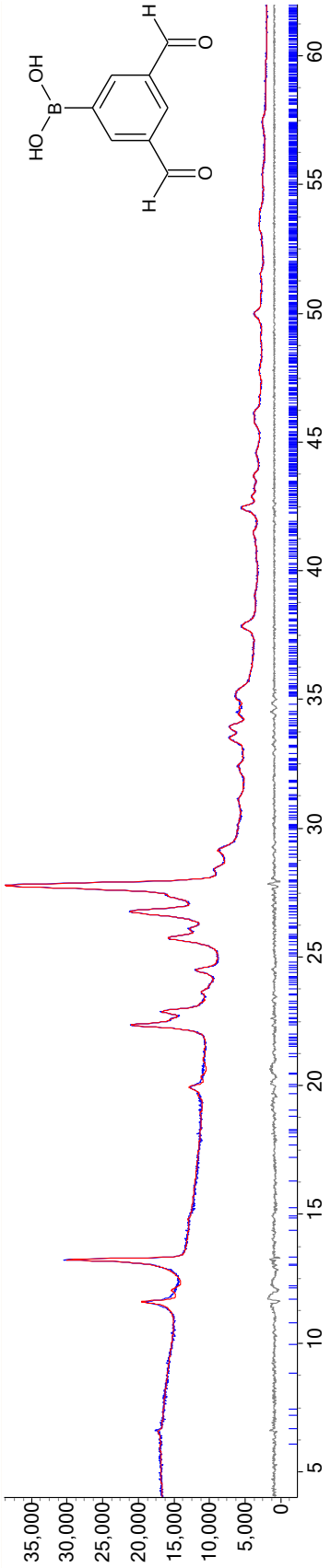

Figure 4.5. Pawley fit for **C2**, showing the observed powder pattern (blue), the calculated powder pattern (red), the difference plot (grey) and the peak positions. [187]

4.2. MCS4

4.2.1. Design and Synthesis

The reaction of the bifunctional C_3 monomer (3,5-diformylphenyl)boronic acid, **C2**, with the monofunctional C_3 monomer triphenylene-2,3,6,7,10,11-hexol hydrate, **C5**, and the monofunctional C_2 monomer 4-(3,4-diaminophenyl)benzene-1,2-diamine, **C1**, was expected to result in the co-condensation of boronic acid with dialcohol end groups and of aldehyde with amine end groups, to form a 2D boronate ester and imine linked COF, exhibiting hexagonal symmetry (Figure 4.6, Scheme 4.2).

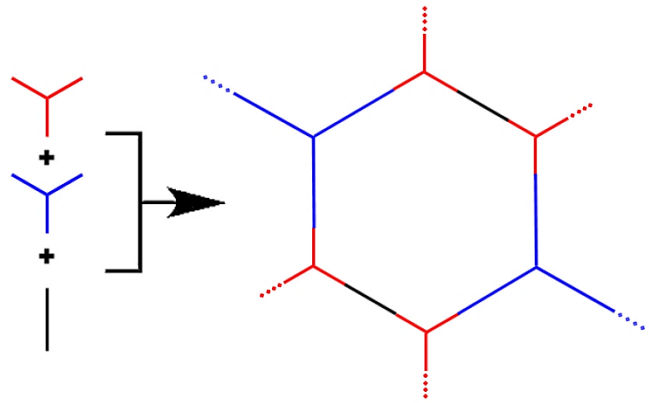

Figure 4.6. Hexagonal COF resulting from the combination of two C_3 monomers and one C_2 monomer.

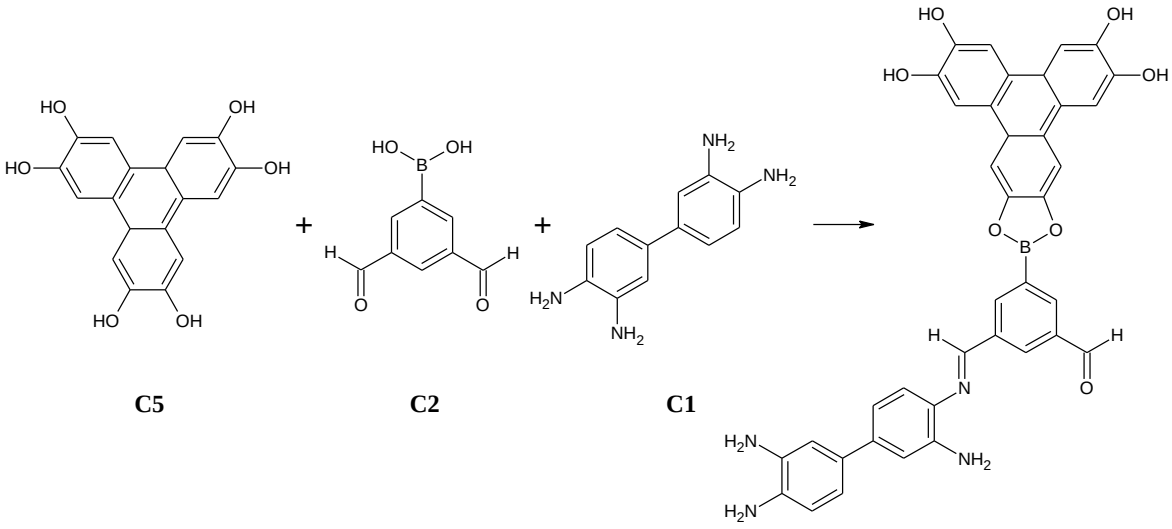

C5 **C2** **C1**

Scheme 4.2. The expected boronate ester and imine links formed between monomers **C5**, **C2** and **C1**.

These building blocks were reacted together in a 1 + 3 + 3 condensation via reflux (section 3.1.2.1). A change in colouration was observed from the black, white and light brown colouration of the monomers respectively, to a golden crystalline powder obtained from the acetic acid-catalysed reaction in 1:1 1,4-dioxane:1,3,5-trimethylbenzene (MCS4_001). Upon washing with oxolane (MCS4_002) and subsequent drying under vacuum (MCS4_003), the sample retained its colouration.

4.2.2. Characterisation and Analysis

The crystalline nature of the samples was determined under the microscope, upon reflection of plane polarised light (Figure 4.7).

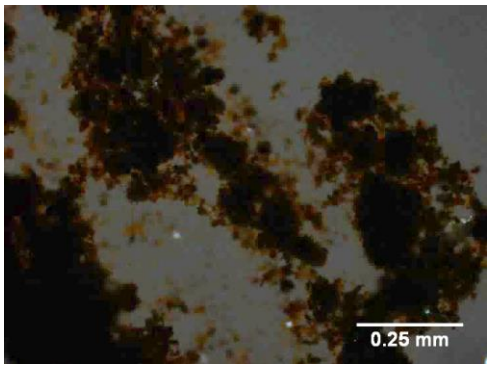

Figure 4.7. Photomicrograph of MCS4_001 from reflux with 1:1 1,4-dioxane:1,3,5-trimethylbenzene and acetic acid drops.

The X-ray powder patterns for the three samples are the same, showing a high background and few peaks of low intensity. MCS4_001 has the best crystallinity, suggesting that the washing and drying protocol had an effect on the crystal structure. Once again, there were too few peaks to carry out reliable indexing, or to effectively compare the laboratory data for MCS4_001, with the patterns for the three monomers (Figure 4.8). Variable temperature PXRD measurements will thus be carried out at high temperatures, to try to improve the crystallinity of the sample and check for the formation of a new crystal structure.

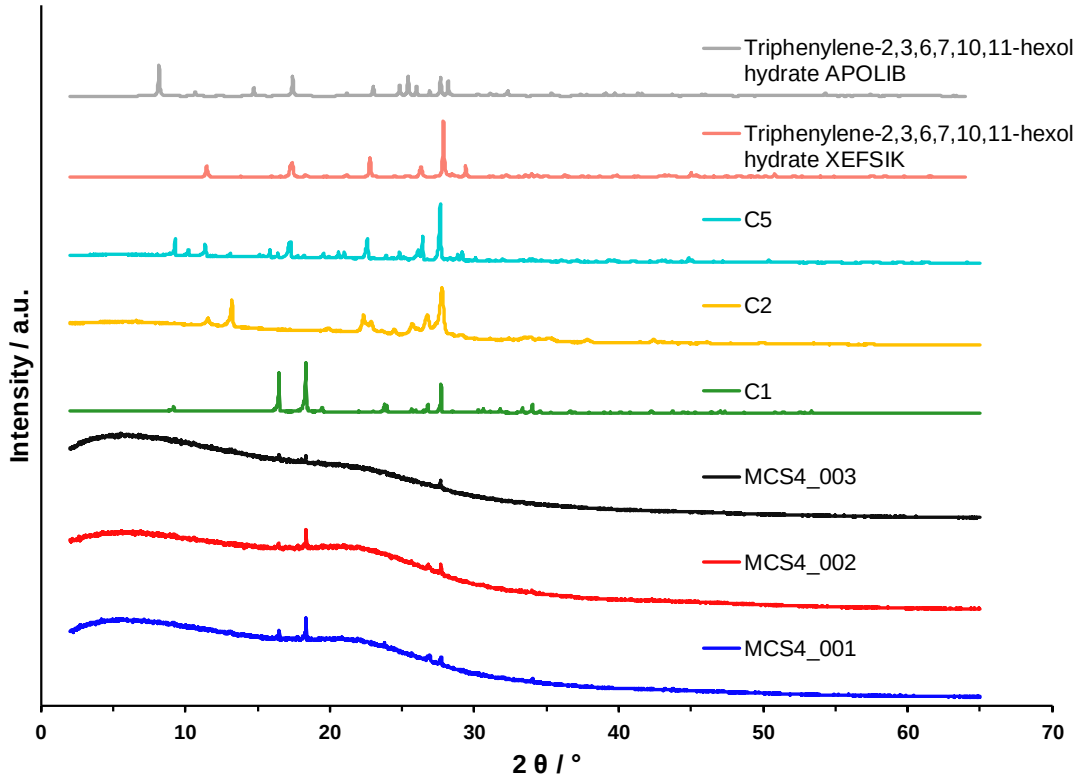

Figure 4.8. Laboratory PXRD patterns for MCS4_001 (blue), MCS4_002 (red) and MCS4_003 (black), obtained from an acetic acid-catalysed 3 + 3 + 1 condensation of the monomers via reflux in 1:1 1,4-dioxane:1,3,5-trimethylbenzene, upon washing with oxolane, and subsequent drying under vacuum, respectively, and for the **C1** (green), **C2** (yellow) and **C5** (turquoise) monomers at 293 K, and the simulated patterns of the **C5** monomer from the CSD (XEFSIK – salmon and APOLIB – grey).

The formation of new imine and boronate ester links between the three monomers was confirmed by FTIR spectroscopy. The spectrum for MCS4_001 shows weak bands at 1680-1640 cm^{-1}, characteristic of C=N stretching and indicative of the formation of imine bonds. The C=O stretching band of the free aldehyde (1740-1720 cm^{-1}) and the N–H stretching and N–H bending bands of the free amine (3385 and 1500 cm^{-1}) are all absent or significantly attenuated, confirming that all of the amine and aldehyde end groups reacted during reflux. Similarly, the O–H stretching band (3435 cm^{-1}), the asymmetric B–O stretching band (1340 cm^{-1}), the symmetric B–C stretching band (1317 cm^{-1}), the in-place O–H bending band (972 cm^{-1}) and the out-of-plane vibration band (648 cm^{-1}), characteristic of boronic acid, and the O–H stretching band (3450-3200 cm^{-1}), the O–H bending band (1436 cm^{-1}) and the C–O stretching band (997 cm^{-1}), characteristic of the free alcohol, are all absent in MCS4_001. This confirms that all of the boronic acid and dialcohol end groups reacted during reflux, to form boronate ester links, exhibiting their characteristic symmetric C–O and B–O stretching bands at 1240

and 1050 cm^{-1} respectively. The FTIR spectrum for MCS4_001 is noticeably different from the spectra of the pure starting monomers (Figure 4.9), providing evidence that a new imine and boronate ester linked structure was formed.

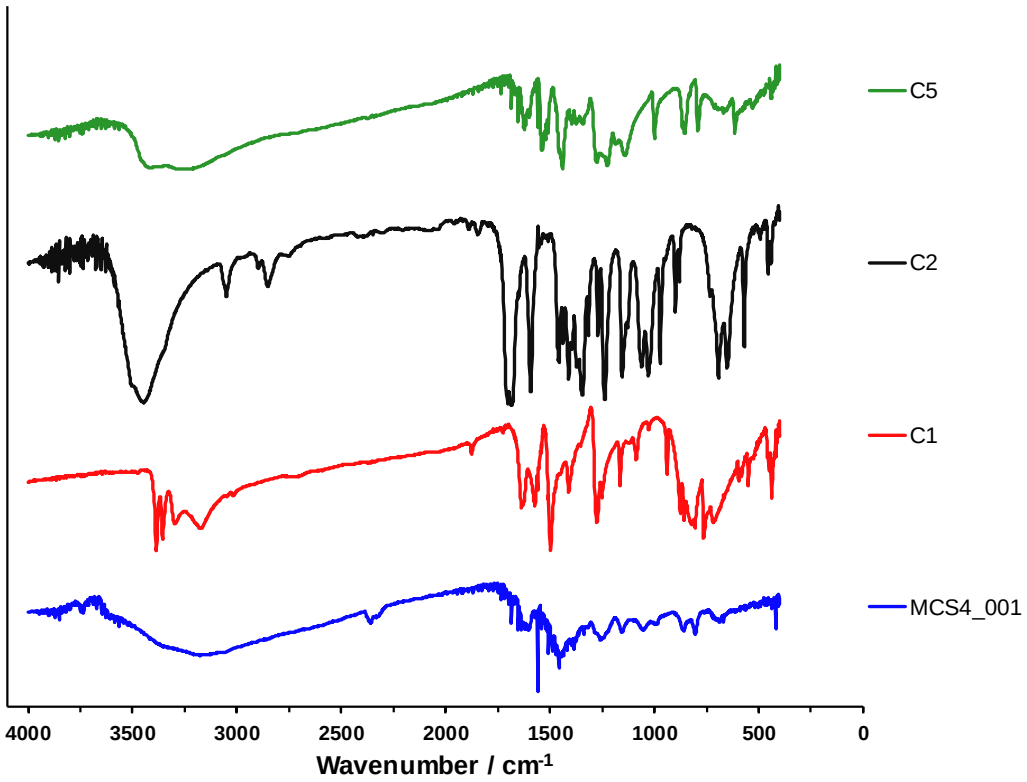

Figure 4.9. FTIR spectra for MCS4_001 (blue), obtained from an acetic acid-catalysed 3 + 3 + 1 condensation of the monomers via reflux in 1:1 1,4-dioxane:1,3,5-trimethylbenzene, and for the **C1** (red), **C2** (black) and **C5** (green) monomers.

Hot stage analysis revealed that the new structure has a high thermal stability. A morphological change was only observed at a temperature of 477.9 °C, upon which the sample started to shrink (Table 4.3). This can be attributed to the new strong covalent imine and boronate ester bonds, which require a substantial amount of energy before being broken and exhibiting decomposition behaviour. No melting phase was observed at 175-177 °C, 259-261 °C or 293-300 °C, the much lower melting ranges of the starting molecules respectively. This confirms the presence of strong intramolecular bonds, as opposed to the weak intermolecular bonds of the pure monomers, and the absence of unreacted linkers. STA will be carried out for a more in-depth and quantifiable investigation on the thermal stability and decomposition behaviour of the new structure.

Table 4.3. Temperature programme followed during hot stage microscopy of MCS4_001, corresponding observations and photomicrographs of the morphological changes.

Ramp	Rate (°C/min)	Limit (°C)	Observation	Photomicrograph of observed changes
1. Heating	15	350	No observed change	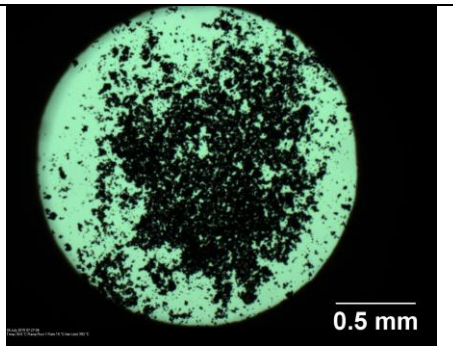
2. Heating	5	600	Slow shrinking at 477.9 °C	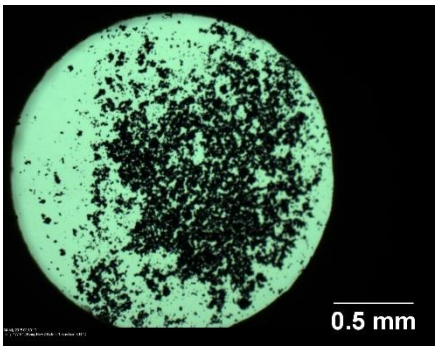
			Faster shrinking at 529.6 – 597.7 °C	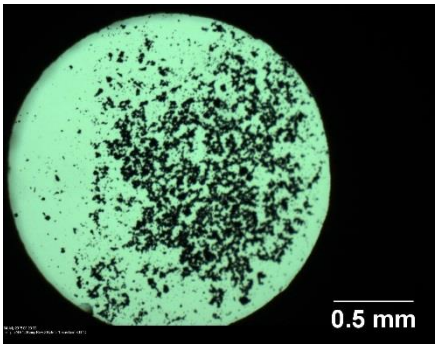 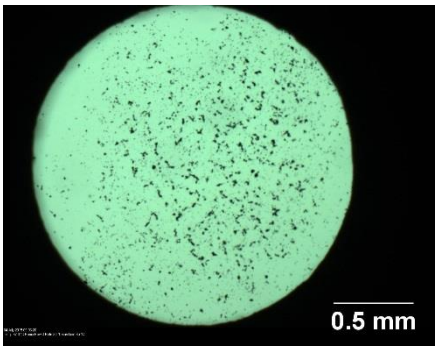
3. Cooling	20	65	No observed change	

4.2.3. New Polymorph for triphenylene-2,3,6,7,10,11-hexol hydrate, C5

Comparison of the laboratory data for the **C5** monomer with the simulated patterns for the reported structure, XEFSIK and APOLIB, as obtained from the CSD, confirms the discovery of a new polymorph for the dialcohol. Table 4.4 shows the unit cell parameters, after Pawley fitting, for a triclinic centrosymmetric $P\bar{1}$ (2) space group (Figure 4.10). Structure solution is currently underway at the time of writing.

Table 4.4. Unit cell parameters for **C5**.

Crystal System	Triclinic
Space Group	$P\bar{1}$ (2)
***a* (Å)**	10.305(1)
***b* (Å)**	18.458(5)
***c* (Å)**	36.086(4)
***α* (°)**	117.72(2)
***β* (°)**	104.38(0)
***γ* (°)**	104.86(2)
***V* (Å^3)**	5303.10(8)
***R*-wp (%)**	4.72

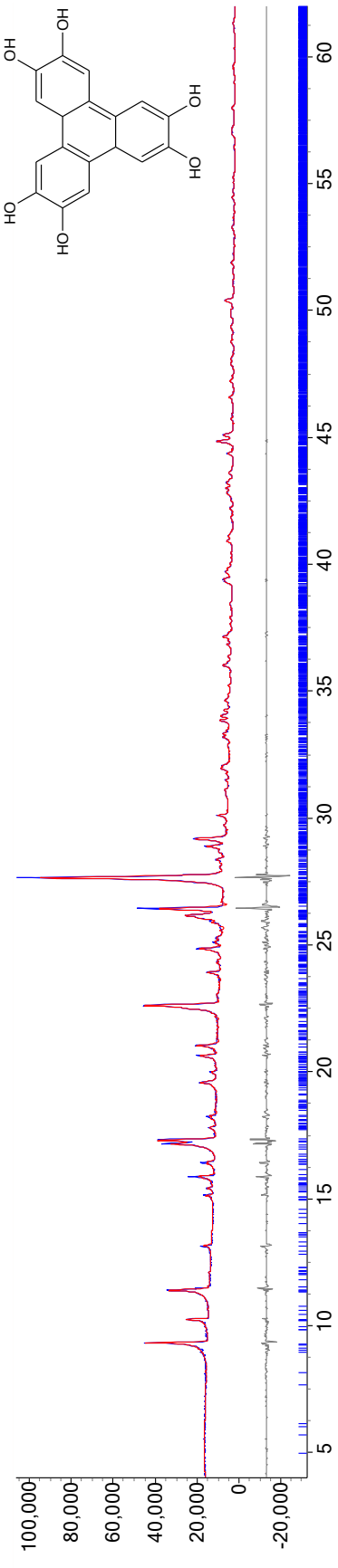

Figure 4.10. Pawley fit for **C5**, showing the observed powder pattern (blue), the calculated powder pattern (red), the difference plot (grey) and the peak positions. [187]

4.3. MCS6

4.3.1. Design and Synthesis

The reaction between (3,5-diformylphenyl)boronic acid, **C2**, and 2-amino-2-(hydroxymethyl)propane-1,3-diol, **C6**, is another monomer combination involving the Schiff-base condensation of amine and aldehyde functional groups alongside the co-condensation of boronic acid with dialcohol. The bifunctional **C6** linker has an innate T_d symmetry. However, this reaction is designed so that only the amine and two of its alcohol groups react, with the third alcohol group functionalising the pore wall through a bottom-up approach. It was expected that new imine and 1,3,2-dioxaborinane links form, into a 3D COF (Scheme 4.3). Computational analysis would be required to determine the structural topology of the framework.

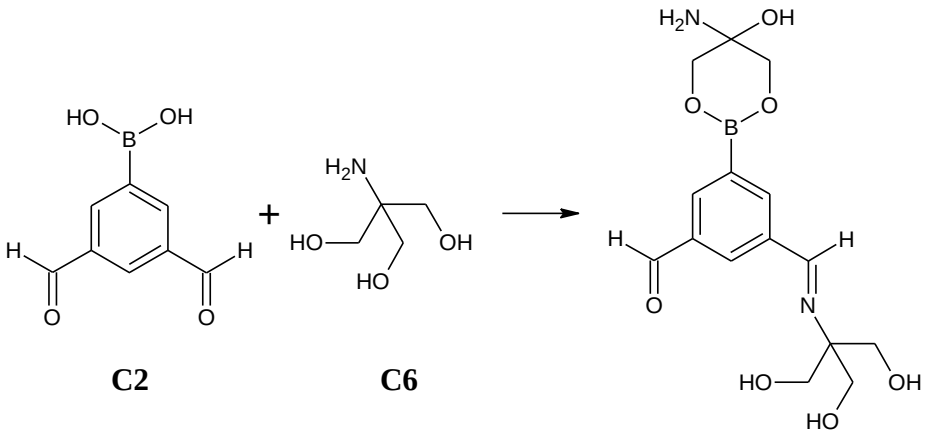

Scheme 4.3. The expected imine and 1,3,2-dioxaborinane links formed between monomers **C2** and **C6**.

These building blocks were reacted together in a 1 + 2 condensation via reflux (section 3.1.2.1). From the acetic acid-catalysed reaction of the two white coloured monomers in 1:1 1,4-dioxane:1,3,5-trimethylbenzene, a yellow-orange crystalline powder was obtained. Upon washing with oxolane (MCS6_001) and subsequent drying under vacuum (MCS6_002), the sample retained its colouration.

4.3.2. Characterisation and Analysis

The crystalline nature of the samples was determined under the microscope, upon reflection of plane polarised light (Figure 4.11).

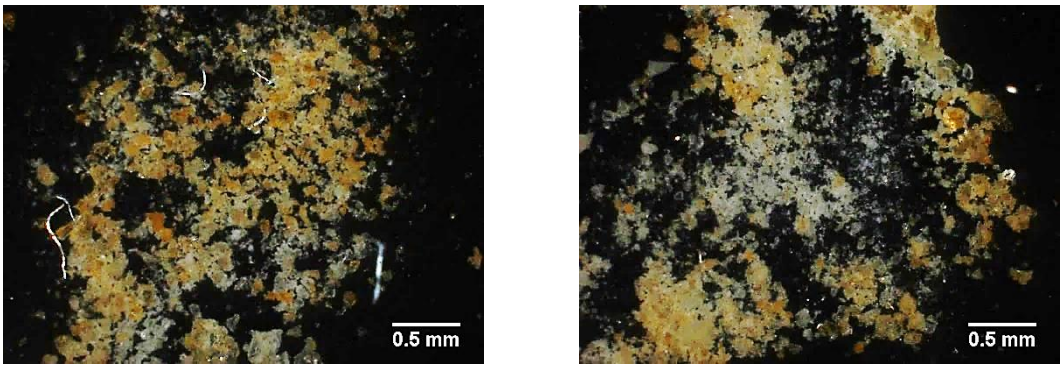

Figure 4.11. Photomicrographs of MCS6_001 (left) and MCS6_002 (right) from reflux with 1:1 1,4-dioxane:1,3,5-trimethylbenzene and acetic acid drops, after washing and drying respectively.

The X-ray powder patterns for the two samples both show a high background. However, the low intensity peaks are different in MCS6_001 and MCS6_002, indicating that the washing and drying protocol had an effect on the crystal structure. Furthermore, comparison of the laboratory data for the two samples with the patterns for the two monomers, confirms that the patterns are completely different and thus originate from different crystal structures (Figure 4.12). Reliable indexing could not be successfully carried out due to the overlapping of some of the reflections. Variable temperature PXRD measurements will thus be carried out at low and high temperatures, to check for peak resolution and better crystallinity respectively. Assuming the material exhibits a positive thermal expansion, the d spacing between the crystal lattice planes decreases upon cooling, resulting in peak resolution due to a shift to higher 2θ, as stated by Bragg's Law ($n\lambda = 2d\sin\theta$).

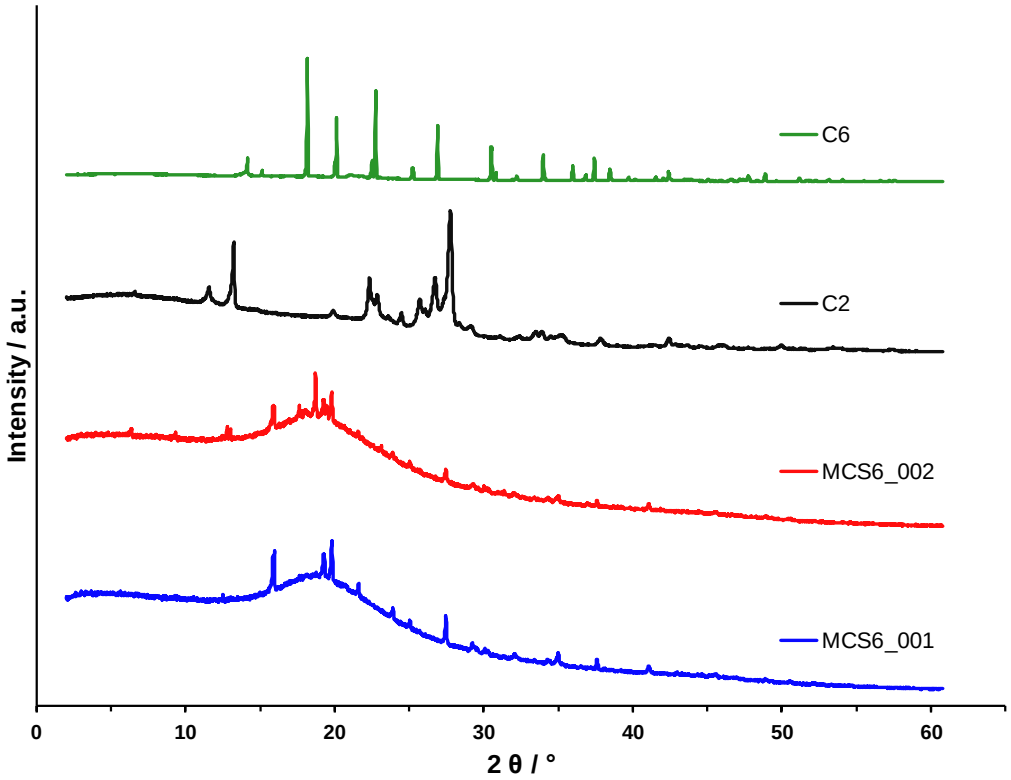

Figure 4.12. Laboratory PXRD patterns for MCS6_001 (blue) and MCS6_002 (red), obtained from an acetic acid-catalysed 1 + 2 condensation of the monomers via reflux in 1:1 1,4-dioxane:1,3,5-trimethylbenzene and upon washing with oxolane, and subsequent drying under vacuum, respectively, and for the **C2** (black) and **C6** (green) monomers, at 293 K.

The formation of new imine and 1,3,2-dioxaborinane links between the two monomers was confirmed by FTIR spectroscopy. The spectra for MCS6_001 and MCS6_002 are identical, showing weak bands at 1680-1640 cm^{-1}, characteristic of C=N stretching and indicative of the formation of imine bonds. The C=O stretching band of the free aldehyde (1740-1720 cm^{-1}) and the N–H bending band of the free amine (1598 cm^{-1}) are both absent, confirming that all of the amine and aldehyde end groups reacted during reflux. Similarly, the O–H stretching band (3435 cm^{-1}), the asymmetric B–O stretching band (1340 cm^{-1}), the symmetric B–C stretching band (1317 cm^{-1}), the in-place O–H bending band (972 cm^{-1}) and the out-of-plane vibration band (648 cm^{-1}), characteristic of boronic acid, and the O–H bending band (1398-1338 cm^{-1}) and the C–O stretching band (1072-977 cm^{-1}), characteristic of the free alcohol, are all absent or significantly attenuated in MCS6_001 and MCS6_002. This confirms that all of the boronic acid and dialcohol end groups reacted during reflux, to form 1,3,2-dioxaborinane links, exhibiting their characteristic symmetric C–O and B–O stretching bands at 1240 and 1095-1035 cm^{-1} respectively, and the out-of-plane vibration band at 688 cm^{-1}. The

FTIR spectra for MCS6_001 and MCS6_002 are noticeably different from the spectra of the pure starting monomers (Figure 4.13), providing evidence that a new imine and 1,3,2-dioxaborinane linked structure was formed.

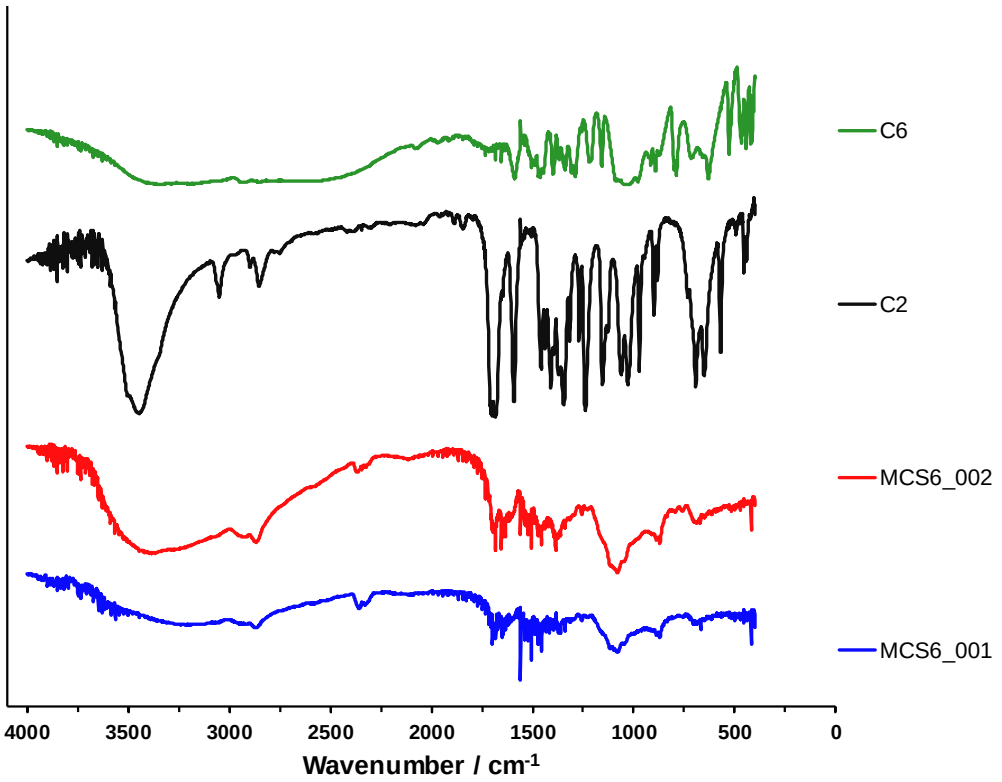

Figure 4.13. FTIR spectra for MCS6_001 (blue) and MCS6_002 (red), obtained from an acetic acid-catalysed 1 + 2 condensation of the monomers via reflux in 1:1 1,4-dioxane:1,3,5-trimethylbenzene and upon washing with oxolane, and subsequent drying under vacuum, respectively, and for the **C2** (black) and **C6** (green) monomers.

Hot stage analysis revealed that the new structures have a rather low thermal stability. A morphological change was observed at a temperature of 145.0 °C, upon which MCS6_001 started to melt, darken and shrink (Table 4.5). MCS6_002 followed the same pattern at a slightly higher temperature, skipping the melting phase. No melting phase was observed at 259-261 °C and 168-170 °C, the melting ranges of the starting molecules respectively. This confirms the absence of unreacted linkers and the formation of new covalent imine and 1,3,2-dioxaborinane bonds. Both samples exhibit possible decomposition behaviour at high temperatures. A better understanding of the structural changes taking place is required. Thus, a more in-depth and quantifiable investigation on the thermal stability and decomposition behaviour of the new structures, will be carried out using STA, in combination with variable temperature PXRD data.

Table 4.5. Temperature programme followed during hot stage microscopy of MCS6_001 and MCS6_002, corresponding observations and photomicrographs of the morphological changes.

MCS6_001					MCS6_002				
Ramp	**Rate (°C/min)**	**Limit (°C)**	**Observation**	**Photomicrograph of observed changes**	**Ramp**	**Rate (°C/min)**	**Limit (°C)**	**Observation**	**Photomicrograph of observed changes**
1. Heating	30	145	No observed change		1. Heating	30	145	No observed change	
2. Heating	2	255	Bubble formation at 145.0 – 215.5 °C		2. Heating	2	270	Bubble formation at 145.0 – 241.9 °C	
			Melting at 218.3 – 230.4 °C						

MCS6_001					MCS6_002				
Ramp	**Rate (°C/min)**	**Limit (°C)**	**Observation**	**Photomicrograph of observed changes**	**Ramp**	**Rate (°C/min)**	**Limit (°C)**	**Observation**	**Photomicrograph of observed changes**
3. Heating	5	600	Darkening till 435.6 °C	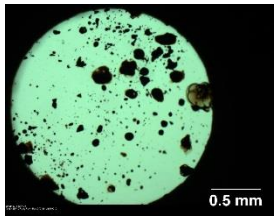	3. Heating	5	600	Darkening till 549.0 °C	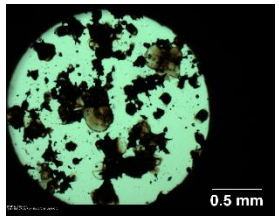
			Slow shrinking at 510.0 – 600.0 °C	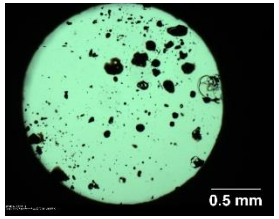				Slow shrinking at 497.8 – 600.0 °C	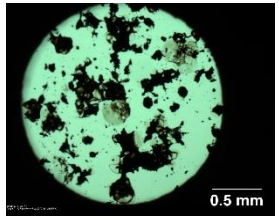
4. Cooling	20	65	No observed change		4. Cooling	20	65	No observed change	

4.4. MCS7

4.4.1. Design and Synthesis

The first LAG (section 3.1.2.2) reaction was carried out via a two-step procedure, through the Schiff-base condensation of the T_d linker 2-amino-2-(hydroxymethyl)propane-1,3-diol, **C6**, with the C_2 linker terephthalaldehyde, **C7**, followed by condensation of the remaining alcohol groups with the C_2 linker pyridine-2,5-dicarboxylic acid, **C8**. Unlike in MCS6, all of the functional groups of **C6** were expected to participate in bonding, to form a 3D imine and ester linked COF (Scheme 4.4). Computational analysis would be required to predict the structural topology of the framework.

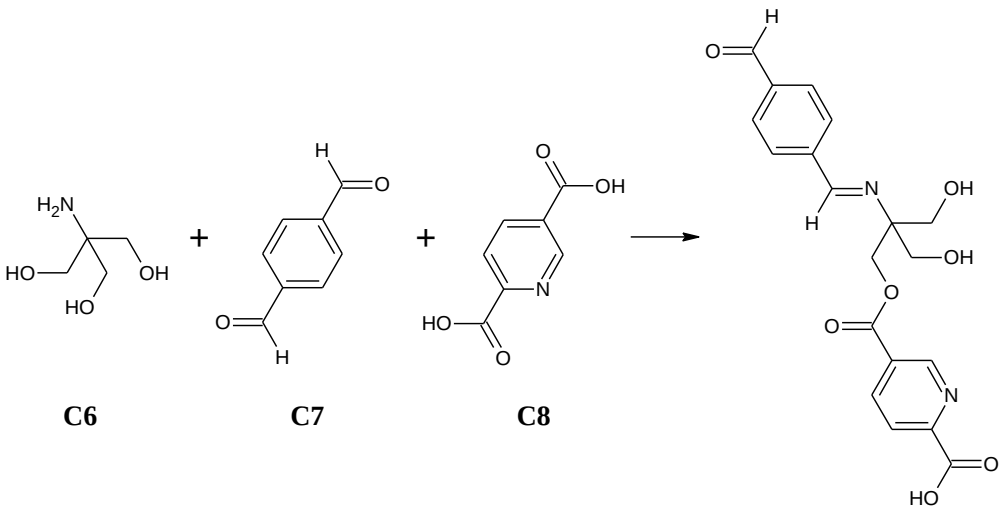

C6 **C7** **C8**

Scheme 4.4. The expected imine and ester links formed between monomers **C6**, **C7** and **C8**.

These building blocks were reacted together in a 2 + 1 + 3 and a 4 + 2 + 9 linker ratio, using a series of catalytic solvents (Table 4.6). No change in colouration was observed for any of the samples.

Table 4.6. Catalytic solvents used in LAG synthesis of MCS7 samples.

Sample Code		
2 + 1 + 3 condensation	**4 + 2 + 9 condensation**	**Catalytic solvent**
MCS7_001	MCS7_011	Water
MCS7_002	MCS7_012	Ethanol
MCS7_003	MCS7_013	Oxolane
MCS7_004	MCS7_014	Benzene
MCS7_005	MCS7_015	5:1 methanol:ethoxyethane
MCS7_006	MCS7_016	1:1 dichloromethane:N,N-dimethylacetamide
MCS7_007	MCS7_017	1:1 1,4-dioxane:1,3,5-trimethylbenzene
MCS7_008	MCS7_018	1:1 oxolane:methanol
MCS7_009	MCS7_019	1:1:0.05 1,4-dioxane:1,3,5-trimethylbenzene:acetic acid (3M)
MCS7_010	MCS7_020	1:3:0.2 1,4-dioxane:1,3,5-trimethylbenzene:acetic acid (3M)

4.4.2. Characterisation and Analysis

The crystalline nature of the samples was determined under the microscope, upon reflection of plane polarised light (Figure 4.14). Comparison of the laboratory PXRD data for the samples with the powder patterns for the three monomers and with their simulated patterns, JULZAR, JULZAR01 and KIDVOJ, from the CSD (Figure 4.15), confirms that six patterns (MCS7_009, MCS7_010, MCS7_016, MCS7_017, MCS7_019 and MCS7_020) are completely different and thus originate from different crystal structures. The patterns for MCS7_009 and MCS7_010 are the same as that for MCS7_016, while those for MCS7_016, MCS7_017 and MCS7_019 are similar but not identical. The pattern for MCS7_020 is not similar to any of the new patterns. This indicates that the

change in solvent affected the formation of the new structures. Two other patterns, MCS7_002 and MCS7_014, are also different from the patterns of the monomers, with some peaks in common with the reagents, indicating the presence of unreacted linkers.

The powder patterns obtained for MCS7_003, MCS7_004 and MCS7_007 (Figure 10.1), reveal the formation of a mixture, something new with excess starting monomers. Once the decomposition temperature of the excess linker is confirmed, STA and variable temperature PXRD will be carried out on these three samples, to obtain the pure new structures.

The powder patterns obtained for MCS7_005, MCS7_012, MCS7_013, MCS7_015 and MCS7_018 are identical and the same as the patterns for the **C7** and **C8** linkers, upon comparison, indicating that the reaction was not successful (Figure 10.2). Similarly, the pattern for MCS7_008 is the same as the simulated pattern of the aldehyde, JULZAR, as obtained from the CSD. No further analysis was thus carried out on any of these samples. Laboratory PXRD data collection for the remaining MCS7_006 and MCS7_011 is currently underway at the time of writing.

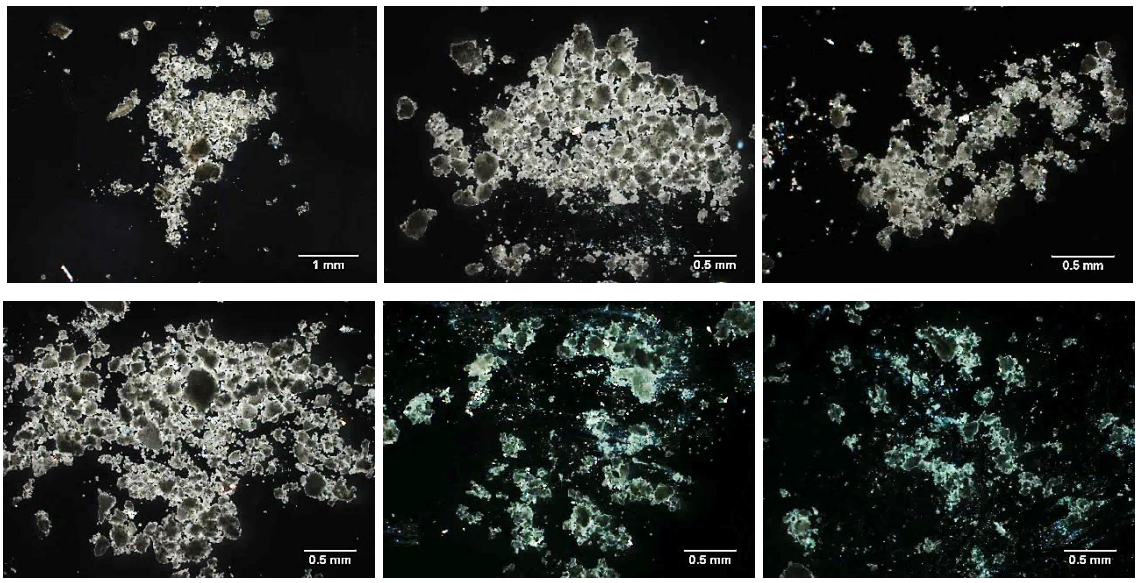

Figure 4.14. Photomicrographs of MCS7_002 from the 2 + 1 + 3 condensation (top left), and MCS7_014 (top centre), MCS7_016 (top right), MCS7_017 (bottom left), MCS7_019 (bottom centre) and MCS7_020 (bottom right) from the 4 + 2 + 9 condensation.

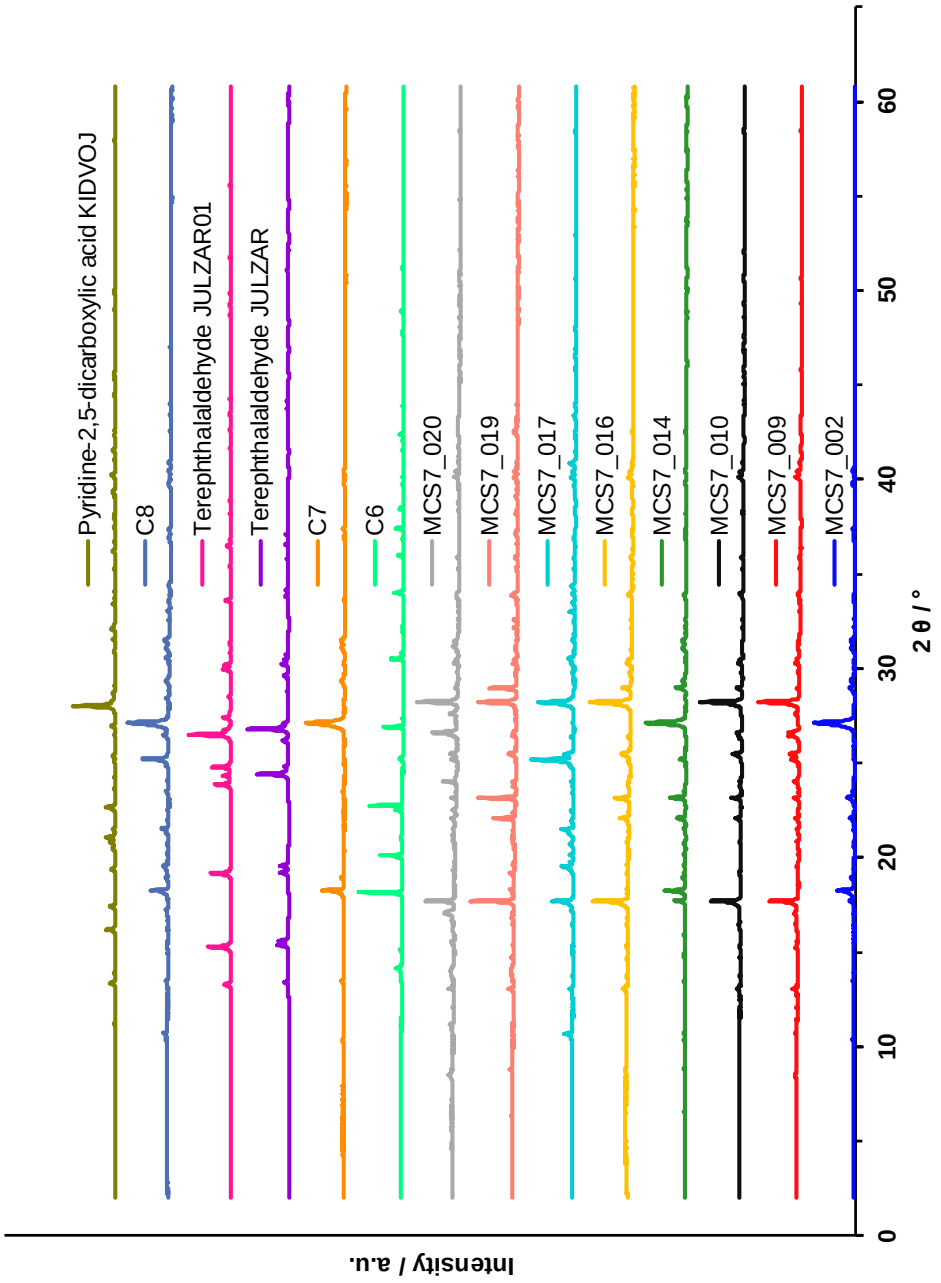

Figure 4.15. Laboratory PXRD patterns for MCS7_002 (blue), MCS7_009 (red), MCS7_010 (black), obtained from a 2 + 1 + 3 condensation of the monomers via LAG in a catalytic amount of ethanol, 1:1:0.05 1,4-dioxane:1,3,5-trimethylbenzene:acetic acid (3M), and 1:3:0.2 1,4-dioxane:1,3,5-trimethylbenzene:acetic acid (3M), respectively, MCS7_014 (green), MCS7_016 (yellow), MCS7_017 (turquoise), MCS7_019 (salmon) and MCS7_020 (grey), obtained from a 4 + 2 + 9 condensation of the monomers via LAG in a catalytic amount of benzene, 1:1 dichloromethane:N,N-dimethylacetamide, 1:1 1,4-dioxane:1,3,5-trimethylbenzene, 1:1:0.05 1,4-dioxane:1,3,5-trimethylbenzene:acetic acid (3M), and 1:3:0.2 1,4-dioxane:1,3,5-trimethylbenzene:acetic acid (3M), respectively, and for the **C6** (spring green), **C7** (orange) and **C8** (blue grey) monomers at 293 K, and the simulated patterns of the **C7** (JULZAR – violet and JULZAR01 – pink) and **C8** (KIDVOJ – olive) monomers from the CSD.

During synthesis of MCS7_001, there was not enough product collected from the first step of LAG, to continue the second LAG step. Laboratory PXRD data for this sample (Figure 4.16) confirms the formation of another new crystal structure, from the reaction between **C6** and **C7**.

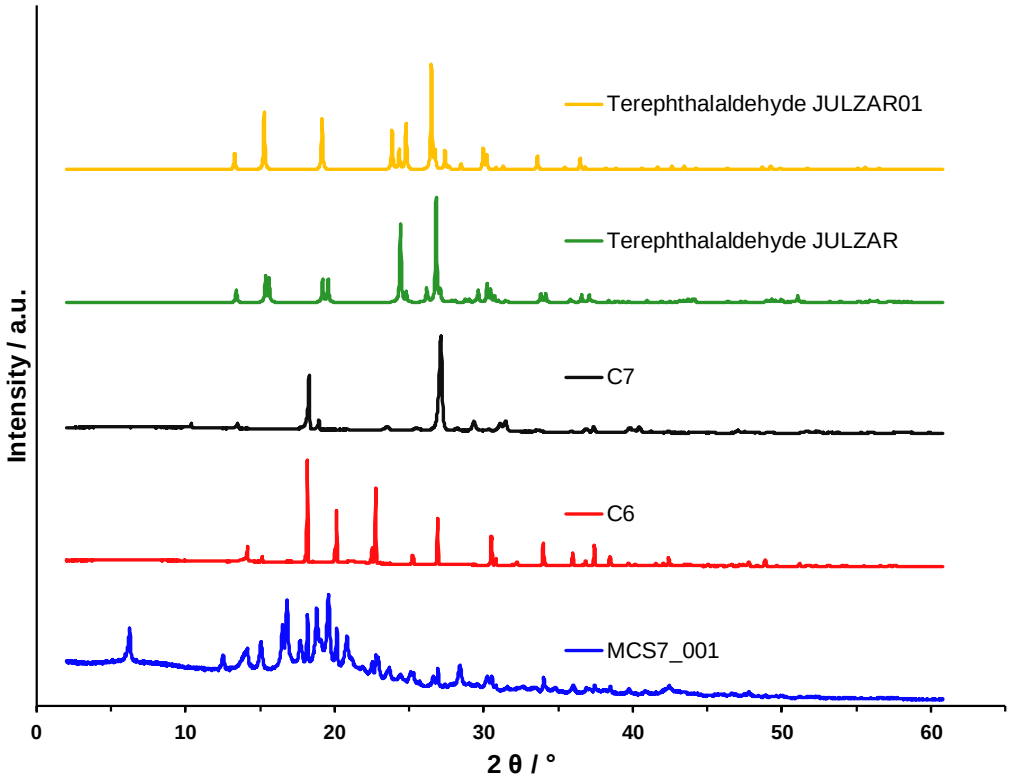

Figure 4.16. Laboratory PXRD patterns for MCS7_001 (blue), obtained from a 2 + 1 condensation of the monomers via LAG in a catalytic amount of water, and for the **C6** (red) and **C7** (black) monomers at 293 K, and the simulated patterns of the **C7** monomer from the CSD (JULZAR – green and JULZAR01 – yellow).

4.4.2.1. The new crystal structures

Pawley fitting on the unit cell parameters from indexing of MCS7_017, to fit the experimental powder pattern, confirmed that the new crystal structure belongs to the triclinic centrosymmetric $P\bar{1}$ (2) space group. Structure solution using rigid body analysis and subsequent Rietveld refinement, produced an *R*-wp of 11.799 % and an *R*_Bragg value of 3.919 (Table 4.7), for the simulated structure, indicating that this derived model structure is in good agreement with the observed experimental pattern (Figure 4.17).

The structure features the synthesised imine and ester links as expected in Scheme 4.4, with all four functional groups of **C6** participating in bonding with **C7** and **C8**, to form a four-armed building block (Figure 4.18). This building unit interacts with one other, using two of its pyridinedicarboxylate arms and its para-phenyldiimine arm, to form a cage, as shown in Figure 4.19 and Figure 4.20. Cages are then linked together via the third and remaining pyridinedicarboxylate arm of the building unit, to form linear chains. An axis connecting both C30 atoms of the same cage, alternates direction in successively linked cages, creating a herringbone motif. The elongated cages have dimensions of 8.962, 8.753 and 4.271 Å, and are found at a 25.555 Å distance along linked chains. The chains run parallel to each other, at an 18.867 Å distance along the *b* axis and a 51° angle to the *c* axis, and are linked via intermolecular hydrogen bonds.

Table 4.7. Chemical, crystallographic and refinement parameters of MCS7_017, obtained by laboratory PXRD using Cu $K_{\alpha 1}$ radiation. [195]

Empirical formula	$C_{95}H_{73}N_{13}O_{38}$
Formula weight (g mol^{-1})	2004.66
Temperature (K)	293
Crystal System	Triclinic
Space Group	$P\bar{1}$ (2)
***a* (Å)**	12.774(0)
***b* (Å)**	18.867(0)
***c* (Å)**	21.214(7)
***α* (°)**	80.15(9)
***β* (°)**	100.57(7)
***γ* (°)**	140.64(1)
***V* (Å^3)**	3183.94(7)
Z	2
ρ_{calc} **(g cm^{-3})**	2.091
Wavelength (Å)	1.5406
***F*(000)**	2076
***R*-wp (%)**	11.799
***R*_Bragg**	3.919
Starting angle (°, 2θ)	4.0
Final angle (°, 2θ)	60.0
Step width (°, 2θ)	0.015

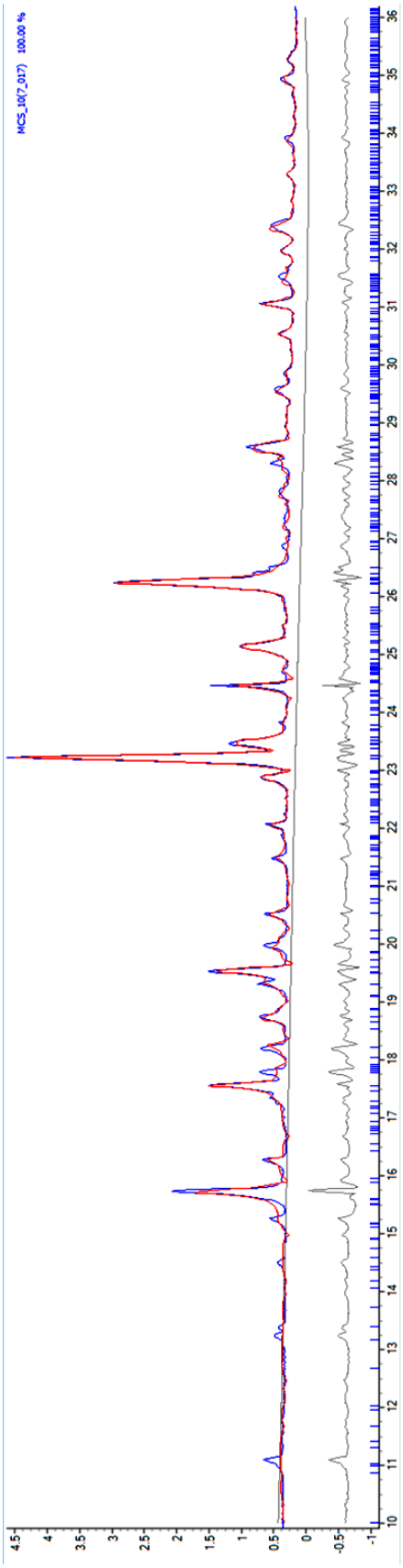

Figure 4.17. Rietveld plot for MCS7_017, obtained from a 4 + 2 + 9 condensation of **C6**, **C7** and **C8**, via LAG in a catalytic amount of 1:1 1,4-dioxane:1,3,5-trimethylbenzene, showing the observed powder pattern (blue), the calculated powder pattern (red), the difference plot (grey) and the peak positions. [187]

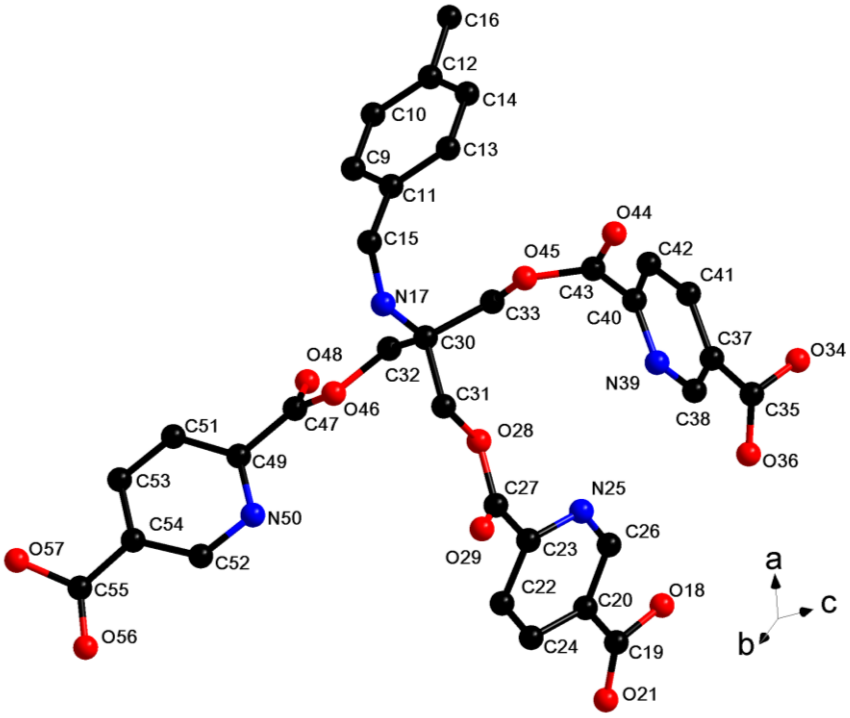

Figure 4.18. The building block of the new imine and ester linked structure (MCS7_017), showing the labelling scheme. Hydrogen atoms are omitted for clarity. [196]

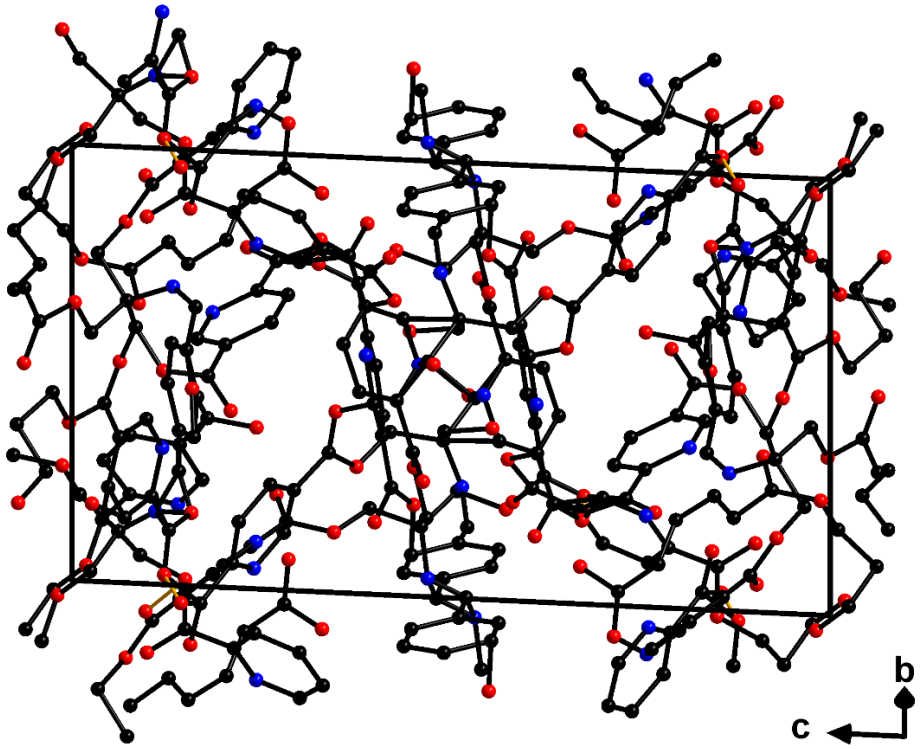

Figure 4.19. The crystal structure of the imine and ester linked chains, viewed along the *a* axis. Hydrogen atoms are omitted for clarity. [196]

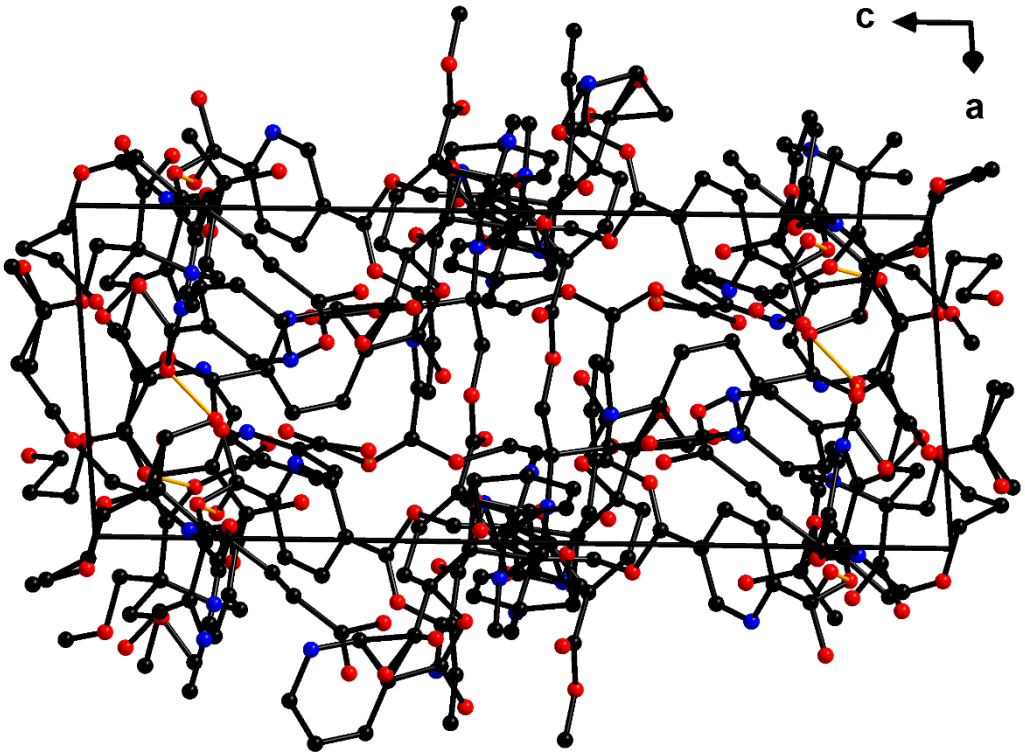

Figure 4.20. The crystal structure of the imine and ester linked chains, viewed along the *b* axis. Hydrogen atoms are omitted for clarity. [196]

Structure solution using rigid body analysis was also carried out on MCS7_016, following Pawley fitting on the unit cell parameters from indexing. The same rigid body (Scheme 4.5) used to solve MCS7_017, was also used for this structure, since the only difference in the synthetic method was a change in solvent. The lowest energy conformation of the rigid body was successful in solving this new crystal structure in the triclinic centrosymmetric $P\bar{1}$ (2) space group. Rietveld refinement is currently underway at the time of writing. Table 4.8 shows the unit cell parameters, after Pawley fitting (Figure 4.21). Although both MCS7_017 and MCS7_016 belong to the same crystal system and space group, the difference in unit cell parameters, and consequently in atomic coordinates, is a direct effect of the change in solvent from 1:1 1,4-dioxane:1,3,5-trimethylbenzene to 1:1 dichloromethane:N,N-dimethylacetamide respectively.

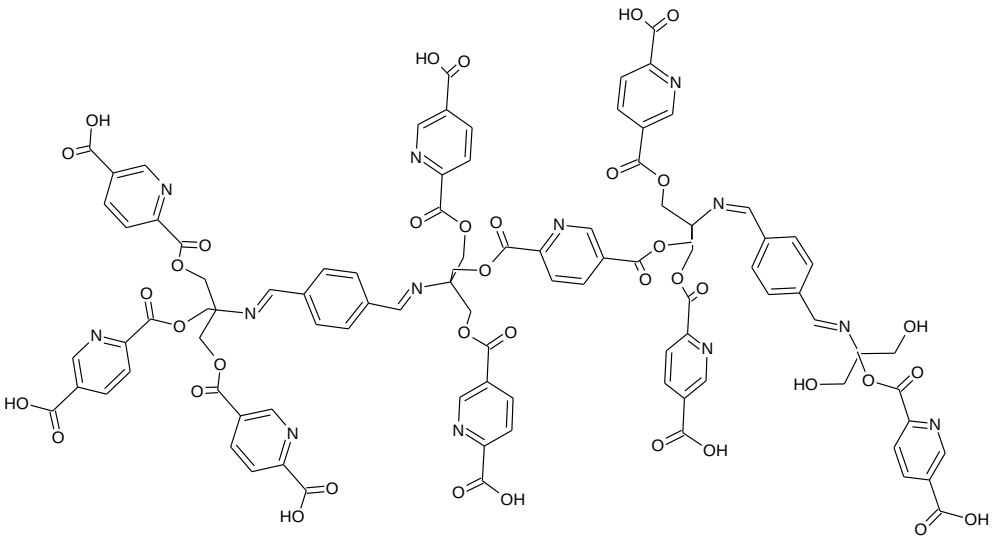

Scheme 4.5. The asymmetric unit used for the structure solution of MCS7_017 and MCS7_016, using rigid body analysis.

Table 4.8. Unit cell parameters for MCS7_016.

Crystal System	Triclinic
Space Group	$P\bar{1}$ (2)
***a* (Å)**	13.724(7)
***b* (Å)**	17.542(8)
***c* (Å)**	17.590(6)
***α* (°)**	73.30(8)
***β* (°)**	80.51(7)
***γ* (°)**	70.96(6)
***V* (Å^3)**	3823.25(4)
***R*-wp (%)**	3.22

The Pawley fitted unit cells for MCS7_002 and MCS7_014, also both belong to the triclinic centrosymmetric $P\bar{1}$ (2) space group. Structure solution using rigid body analysis for these two new structures, is also currently underway at the time of writing. Table 4.9 shows the unit cell parameters, after Pawley fitting (Figure 4.22). The unit cell parameters are once again affected by a change in solvent to non-polar benzene for MCS7_014, and to polar protic ethanol for MCS7_002. This change is accompanied by a change in linker condensation to a smaller ratio for the latter sample.

The powder patterns for MCS7_019 and MCS7_020 are yet to be indexed and Pawley fitted, followed by crystal structure determination. Only then, will a complete

comparison between all the new crystal structures synthesised as part of reaction MCS7, be possible. In the same manner, structure solution will also be carried out for MCS7_001 from the first LAG step.

Table 4.9. Unit cell parameters for MCS7_002 and MCS7_014.

	MCS7_002	MCS7_014
Crystal System	Triclinic	Triclinic
Space Group	$P\bar{1}$ (2)	$P\bar{1}$ (2)
***a* (Å)**	5.658(3)	16.959(6)
***b* (Å)**	19.130(2)	19.819(3)
***c* (Å)**	31.303(7)	23.694(1)
***α* (°)**	139.84(8)	76.36(2)
***β* (°)**	78.83(7)	56.58(9)
***γ* (°)**	77.14(2)	62.10(7)
***V* (Å^3)**	1737.48(2)	5873.25(7)
***R*-wp (%)**	4.57	4.64

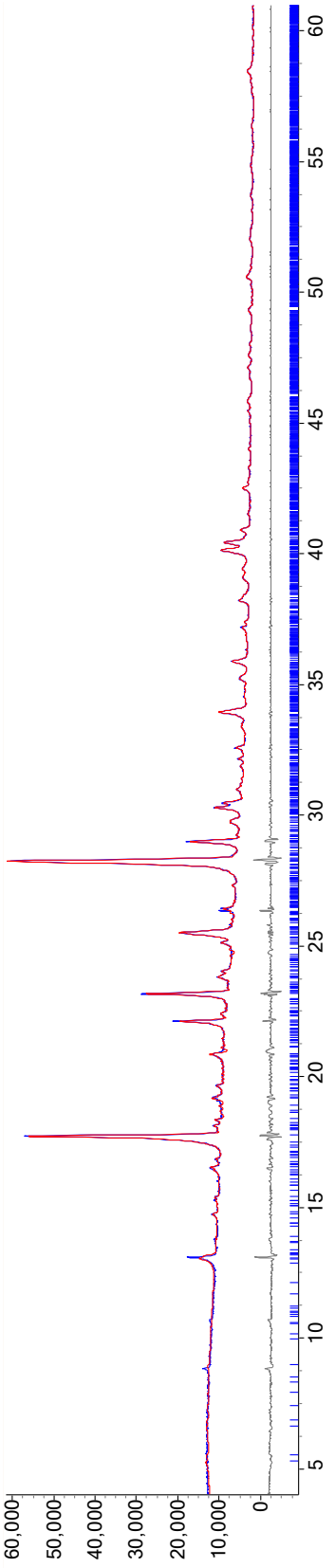

Figure 4.21. Pawley fit for MCS7_016, obtained from a 4 + 2 + 9 condensation of **C6**, **C7** and **C8**, via LAG in a catalytic amount of 1:1 dichloromethane:N,N-dimethylacetamide, showing the observed powder pattern (blue), the calculated powder pattern (red), the difference plot (grey) and the peak positions. [187]

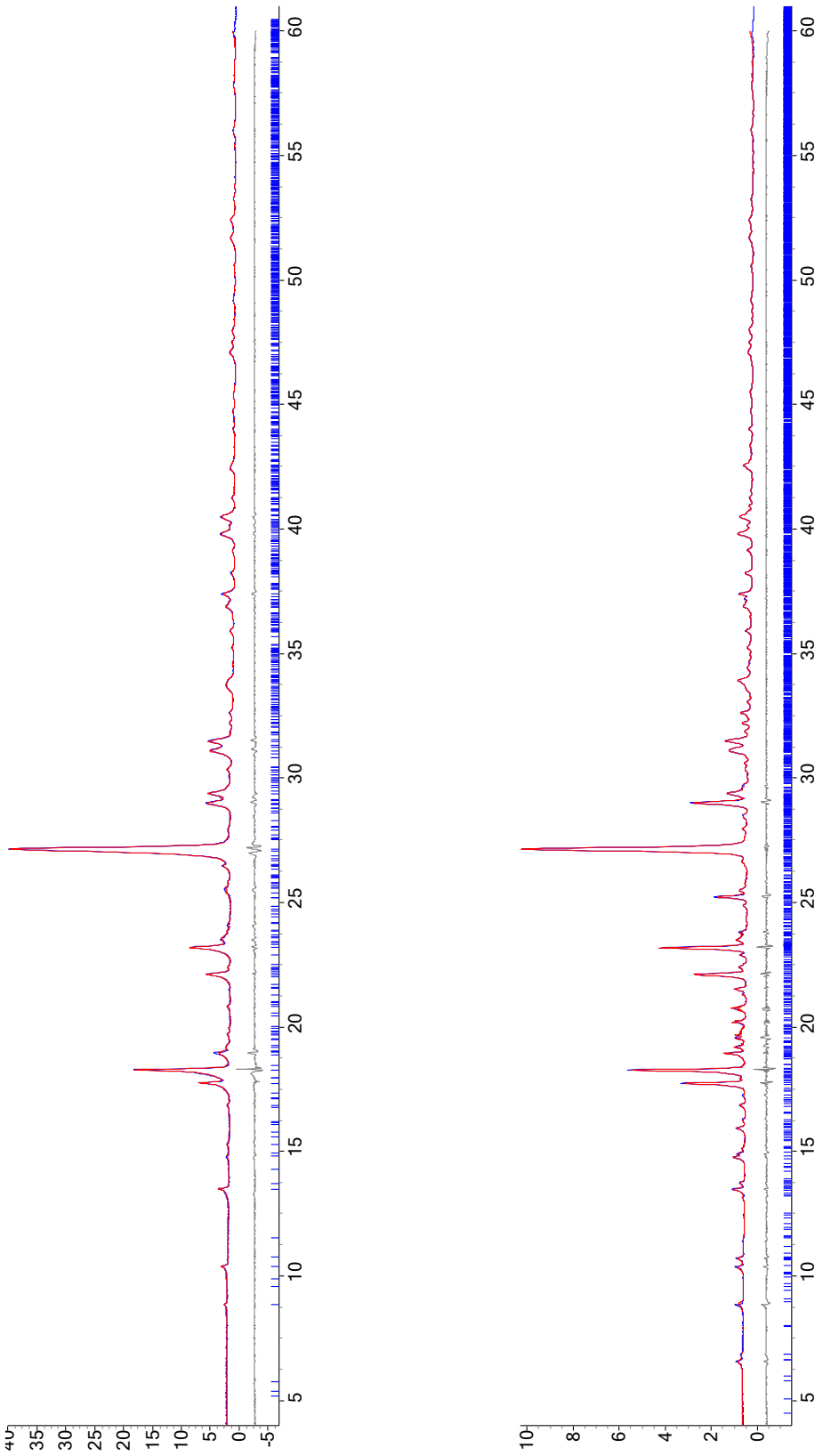

Figure 4.22. Pawley fits for MCS7_002 (top) and MCS7_014 (bottom), obtained from a 2 + 1 + 3 condensation of **C6**, **C7** and **C8**, via LAG in a catalytic amount of ethanol, and from a 4 + 2 + 9 condensation of the monomers, via LAG in a catalytic amount of benzene, respectively, showing the observed powder patterns (blue), the calculated powder patterns (red), the difference plots (grey) and the peak positions. [187]

4.4.2.2. Supportive Characterisation

The formation of new imine and ester links between the three monomers was supported by FTIR spectroscopy. The spectra for MCS7_002, MCS7_014, MCS7_016, and MCS7_017 are identical, showing weak bands at 1650 cm^{-1}, characteristic of C=N stretching and indicative of the formation of imine bonds. The C=O stretching band of the free aldehyde (1697 cm^{-1}) is replaced by the C=O stretching band of the aromatic ester bond (1720-1700 cm^{-1}), while the N–H bending band of the free amine (1589 cm^{-1}) is absent, confirming the formation of ester bonds and the absence of unreacted amine groups. The C–H stretching band of the free aldehyde (2850 cm^{-1}), is absent in all samples, confirming that all of the aldehyde groups reacted during LAG. Similarly, the O–H stretching band of the free carboxylic acid (3095 cm^{-1}) is absent in all samples, except in MCS7_002, supporting the presence of unreacted carboxylic acid linkers in the latter. The FTIR spectra for all four samples are noticeably different from the spectra of the pure starting monomers (Figure 4.23), providing evidence that new imine and ester links were consistently formed, despite the change in solvent and linker environments affecting the formation of the resulting crystal structures.

Hot stage microscopy revealed that the new structures are thermally stable up to 170 °C, upon which the samples start to shrink, melt and darken. MCS7_014 is the most thermally stable of the four tested samples, with the remaining MCS7_002, MCS7_016 and MCS7_017 following the same pattern of morphological changes at a maximum of 10 °C decrease in temperature (Table 4.10, Table 4.11). No melting phase was observed at 168-169 °C and 115-116 °C, the melting ranges of the **C6** and **C7** linkers respectively, confirming their complete reaction to form new, larger, covalently bonded units. All four samples had melted and started darkening, before the melting point of the **C8** linker (244 °C) was reached. The unit cell parameters and hence crystal packing, the atomic connectivity, and the solvent environment during synthesis, are all factors which may affect the thermal stability of a material. A more in-depth and quantifiable investigation will thus be carried out using STA and variable temperature PXRD, to better understand the behaviour of the new structures upon heating.

Characterisation of MCS7_001, MCS7_019 and MCS7_020 using techniques other than PXRD, including FTIR and hot stage microscopy, is currently underway at the time of writing.

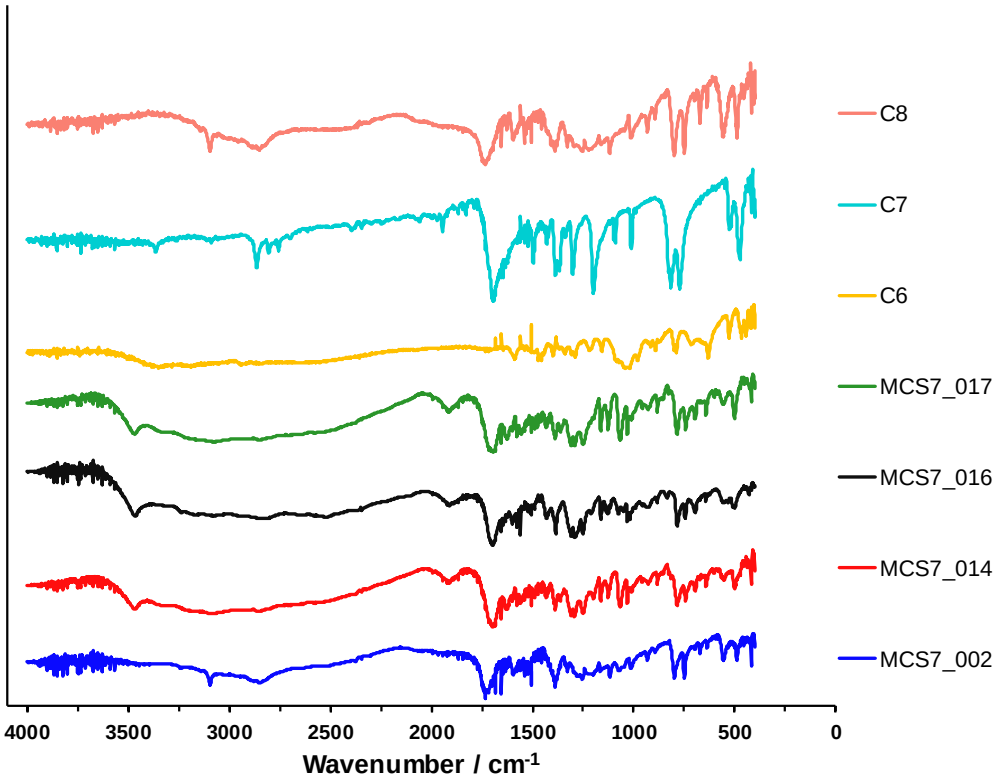

Figure 4.23. FTIR spectra for MCS7_002 (blue), obtained from a 2 + 1 + 3 condensation of the monomers via LAG in a catalytic amount of ethanol, MCS7_014 (red), MCS7_016 (black) and MCS7_017 (green), obtained from a 4 + 2 + 9 condensation of the monomers via LAG in a catalytic amount of benzene, 1:1 dichloromethane:N,N-dimethylacetamide, and 1:1 1,4-dioxane:1,3,5-trimethylbenzene, respectively, and for the **C6** (yellow), **C7** (turquoise) and **C8** (salmon) monomers.

Table 4.10. Temperature programme followed during hot stage microscopy of MCS7_002 and MCS7_014, corresponding observations and photomicrographs of the morphological changes.

MCS7_002					MCS7_014				
Ramp	**Rate (°C/min)**	**Limit (°C)**	**Observation**	**Photomicrograph of observed changes**	**Ramp**	**Rate (°C/min)**	**Limit (°C)**	**Observation**	**Photomicrograph of observed changes**
1. Heating	20	155	No observed change		1. Heating	20	175	No observed change	
2. Heating	2	350	Shrinking at 173.5 °C		2. Heating	2	350	Shrinking at 183.1 °C	
			Melting at 183.3 – 196.2 °C					Melting at 187.6 – 197.6 °C	

MCS7_002					MCS7_014				
Ramp	**Rate (°C/min)**	**Limit (°C)**	**Observation**	**Photomicrograph of observed changes**	**Ramp**	**Rate (°C/min)**	**Limit (°C)**	**Observation**	**Photomicrograph of observed changes**
2. Heating	2	350	Darkening till 350.0 °C	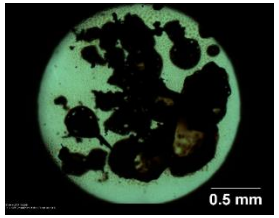	2. Heating	2	350	Darkening till 350.0 °C	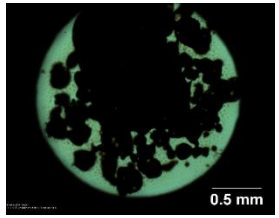
3. Cooling	20	65	No observed change		3. Cooling	20	65	No observed change	

Table 4.11. Temperature programme followed during hot stage microscopy of MCS7_016 and MCS7_017, corresponding observations and photomicrographs of the morphological changes.

MCS7_016					MCS7_017				
Ramp	**Rate (°C/min)**	**Limit (°C)**	**Observation**	**Photomicrograph of observed changes**	**Ramp**	**Rate (°C/min)**	**Limit (°C)**	**Observation**	**Photomicrograph of observed changes**
1. Heating	30	160	No observed change		1. Heating	20	170	No observed change	
2. Heating	2	245	Slow shrinking at 177.0 °C		2. Heating	2	350	Shrinking at 181.4 – 185.8 °C	
			Melting at 180.5 – 191.0 °C					Melting at 185.9 – 193.8 °C	

MCS7_016					MCS7_017				
Ramp	**Rate (°C/min)**	**Limit (°C)**	**Observation**	**Photomicrograph of observed changes**	**Ramp**	**Rate (°C/min)**	**Limit (°C)**	**Observation**	**Photomicrograph of observed changes**
2. Heating	2	245	Shrinking at 217.9 – 231.4 °C	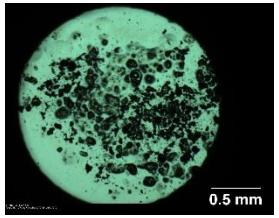	2. Heating	2	350	Darkening till 350.0 °C	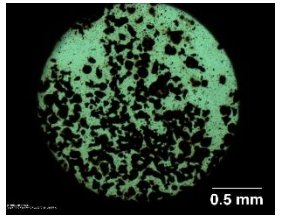
3. Heating	5	350	Darkening till 350.0 °C	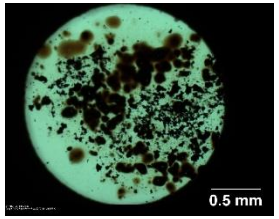					
4. Cooling	20	65	No observed change		3. Cooling	20	65	No observed change	

4.4.3. New Polymorph for terephthalaldehyde, C7

Comparison of the laboratory data for the **C7** monomer with the simulated patterns for the reported structure, JULZAR and JULZAR01, as obtained from the CSD, confirms the discovery of a new polymorph for the aldehyde. Table 4.12 shows the unit cell parameters, at Rietveld refinement stage, for a triclinic centrosymmetric $P\bar{1}$ (2) space group (Figure 4.24).

Table 4.12. Unit cell parameters for **C7**.

Crystal System	Triclinic
Space Group	$P\bar{1}$ (2)
***a* (Å)**	5.344(5)
***b* (Å)**	8.843(5)
***c* (Å)**	7.316(9)
***α* (°)**	79.47(9)
***β* (°)**	64.17(6)
***γ* (°)**	74.59(3)
***V* (Å^3)**	299.22(2)
***R*-wp (%)**	11.15
***R*_Bragg**	3.95

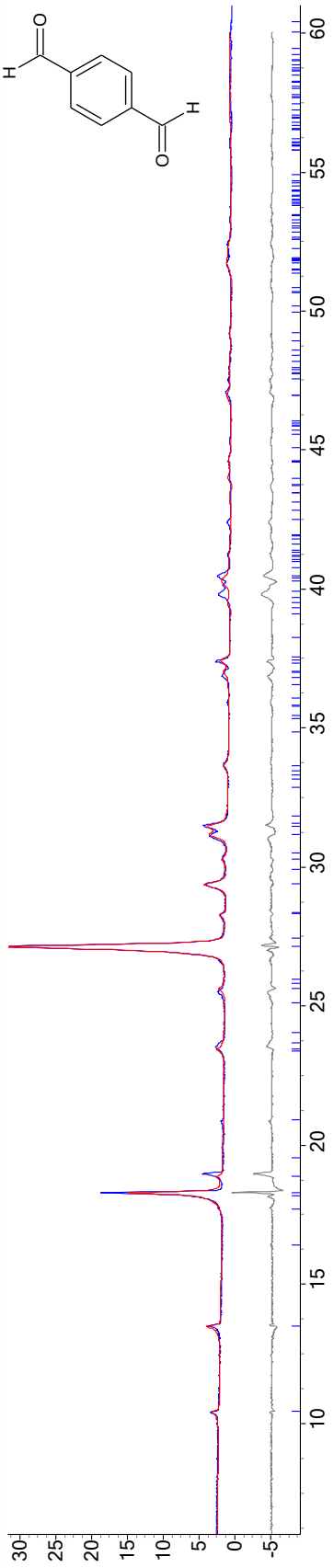

Figure 4.24. Rietveld plot for **C7**, showing the observed powder pattern (blue), the calculated powder pattern (red), the difference plot (grey) and the peak positions. [187]

4.4.4. New Polymorph for pyridine-2,5-dicarboxylic acid, C8

Comparison of the laboratory data for the **C8** monomer with the simulated pattern for the reported structure, KIDVOJ, as obtained from the CSD, confirms the discovery of a new polymorph for the carboxylic acid. Table 4.13 shows the unit cell parameters, at Rietveld refinement stage, for a triclinic centrosymmetric $P\bar{1}$ (2) space group (Figure 4.25).

Table 4.13. Unit cell parameters for **C8**.

Crystal System	Triclinic
Space Group	$P\bar{1}$ (2)
***a* (Å)**	11.547(5)
***b* (Å)**	14.529(6)
***c* (Å)**	22.705(2)
***α* (°)**	124.38(5)
***β* (°)**	120.42(2)
***γ* (°)**	67.09(0)
***V* (Å^3)**	2682.25(6)
***R*-wp (%)**	26.63
R_Bragg	5.49

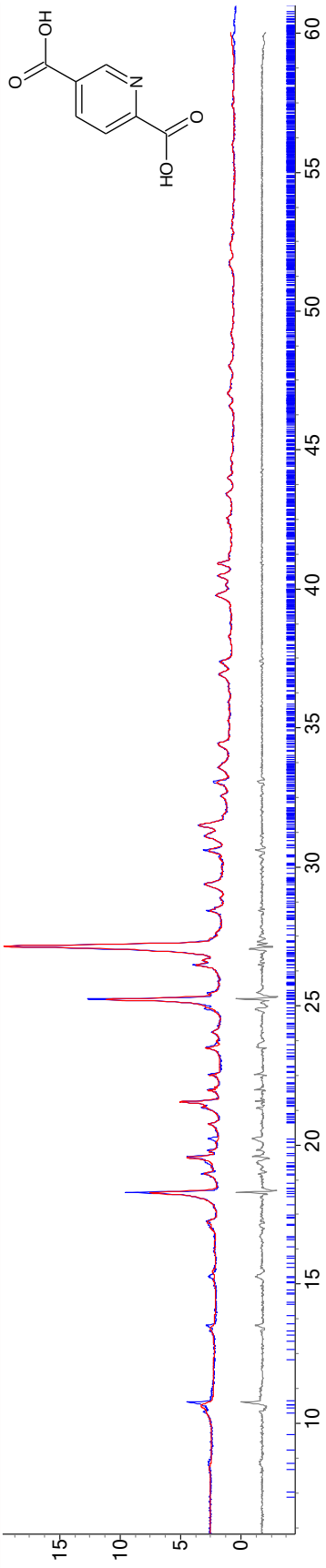

Figure 4.25. Pawley fit for **C8**, showing the observed powder pattern (blue), the calculated powder pattern (red), the difference plot (grey) and the peak positions. [187]

4.5. MCS8

4.5.1. Design and Synthesis

The first reaction incorporating pyridine-2,6-dicarbaldehyde, **C9**, the pH-sensitive smart polymer through a bottom-up approach, was carried out via another two-step LAG (section 3.1.2.2) protocol. The amine group of the same T_d monomer, **C6**, was reacted with the **C9** aldehyde, after which the remaining alcohol groups of **C6** were reacted with the same **C8** carboxylic acid, in a 2 + 1 + 3 and a 4 + 2 + 9 condensation ratio, using a series of catalytic solvents (Table 4.14). Similar to MCS7, all of the functional groups of **C6** were expected to participate in bonding, to form a 3D imine and ester linked COF (Scheme 4.6). Computational analysis would be required to predict the structural topology of the framework.

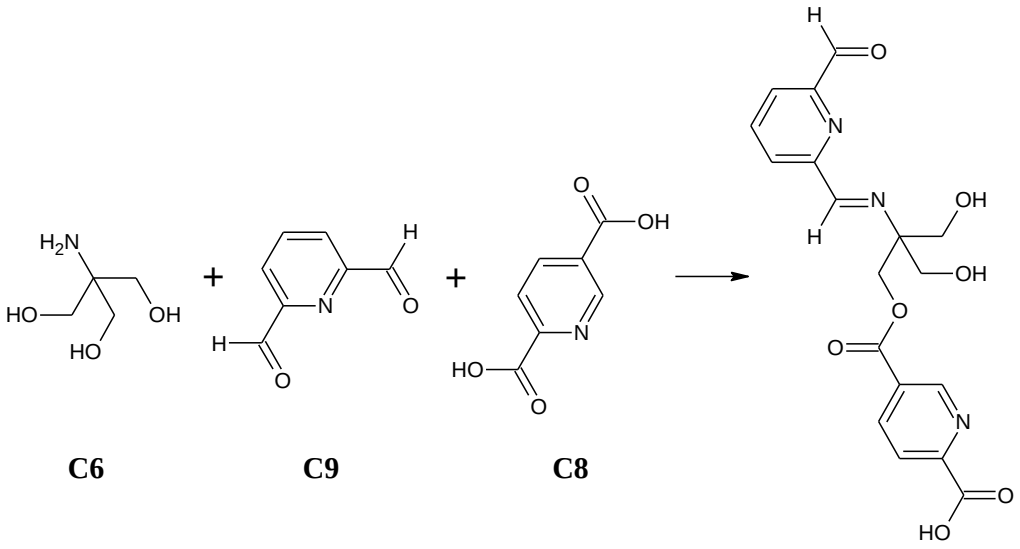

Scheme 4.6. The expected imine and ester links formed between monomers **C6**, **C9** and **C8**.

During the synthesis of MCS8_002, MCS8_003, MCS8_005, MCS8_006, MCS8_008 and MCS8_009, there was not enough product collected from the first step of LAG, to continue the second LAG step or carry out any characterisation. For all the other samples, a small change in colouration was observed from the white, brown and white coloured monomers respectively, to off-white crystalline powders.

Table 4.14. Catalytic solvents used in LAG synthesis of MCS8 samples.

Sample Code		
2 + 1 + 3 condensation	**4 + 2 + 9 condensation**	**Catalytic solvent**
MCS8_001	MCS8_011	Water
MCS8_002	MCS8_012	Ethanol
MCS8_003	MCS8_013	Oxolane
MCS8_004	MCS8_014	Benzene
MCS8_005	MCS8_015	5:1 methanol:ethoxyethane
MCS8_006	MCS8_016	1:1 dichloromethane:N,N-dimethylacetamide
MCS8_007	MCS8_017	1:1 1,4-dioxane:1,3,5-trimethylbenzene
MCS8_008	MCS8_018	1:1 oxolane:methanol
MCS8_009	MCS8_019	1:1:0.05 1,4-dioxane:1,3,5-trimethylbenzene:acetic acid (3M)
MCS8_010	MCS8_020	1:3:0.2 1,4-dioxane:1,3,5-trimethylbenzene:acetic acid (3M)

4.5.2. Characterisation and Analysis

The crystallinity of the samples was determined under the microscope, upon reflection of plane polarised light (Figure 4.26). Comparison of the laboratory PXRD data for the samples with the powder patterns for the three monomers and with the simulated pattern of the carboxylic acid, KIDVOJ, from the CSD (Figure 4.27), confirms that six patterns (MCS8_001, MCS8_004, MCS8_010, MCS8_011, MCS8_016 and MCS8_020) are completely different and thus originate from different crystal structures. All six patterns are relatively identical at first glance, with MCS8_016 having the best crystallinity. This indicates that the change in solvent did not seem to affect the formation of the new structures in this reaction. However, since the samples resulted from a different

condensation ratio and there are no peaks in common with the monomer with an increased ratio, **C8**, for the second half of the samples, there is a high possibility that the linker mole ratio together with the change in solvent affected the formation of the new structures.

The powder patterns obtained for MCS8_007, MCS8_012, MCS8_018 and MCS8_019 (Figure 10.3), reveal the formation of a mixture, something new with excess **C8** monomer. STA and variable temperature PXRD will be carried out on these four samples, to decompose the excess monomer and potentially obtain the pure new structures.

The powder patterns obtained for MCS8_013, MCS8_014, MCS8_015 and MCS8_017 are identical and the same as the pattern for the **C8** monomer, upon comparison, indicating that the reaction was not successful (Figure 10.4). No further analysis was thus carried out on any of these samples.

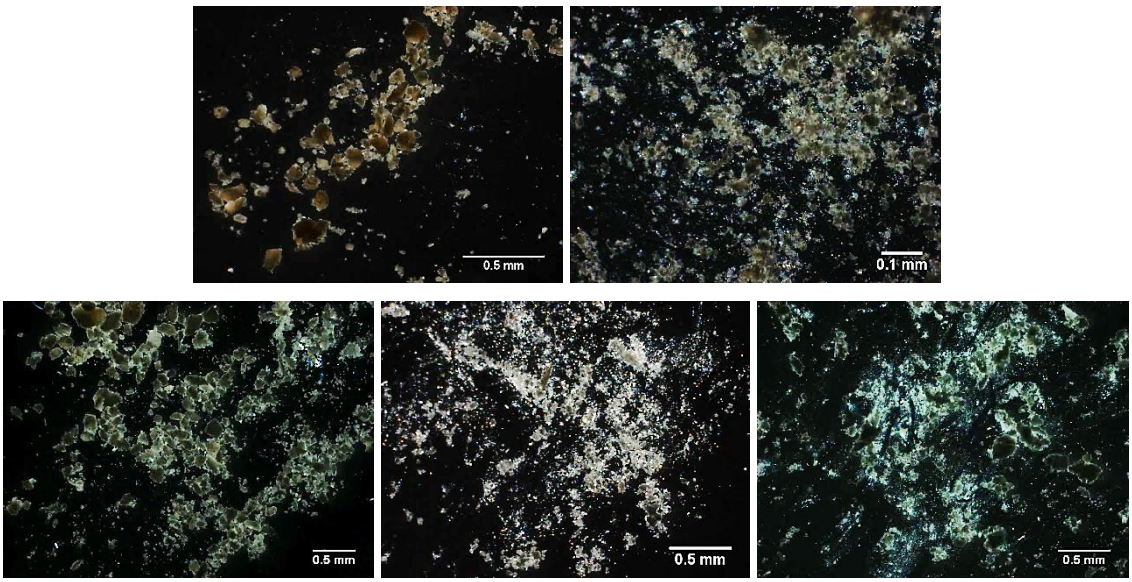

Figure 4.26. Photomicrographs of MCS8_001 (top left) and MCS8_010 (top right) from the 2 + 1 + 3 condensation, and MCS8_011 (bottom left), MCS8_016 (bottom centre) and MCS8_020 (bottom right) from the 4 + 2 + 9 condensation.

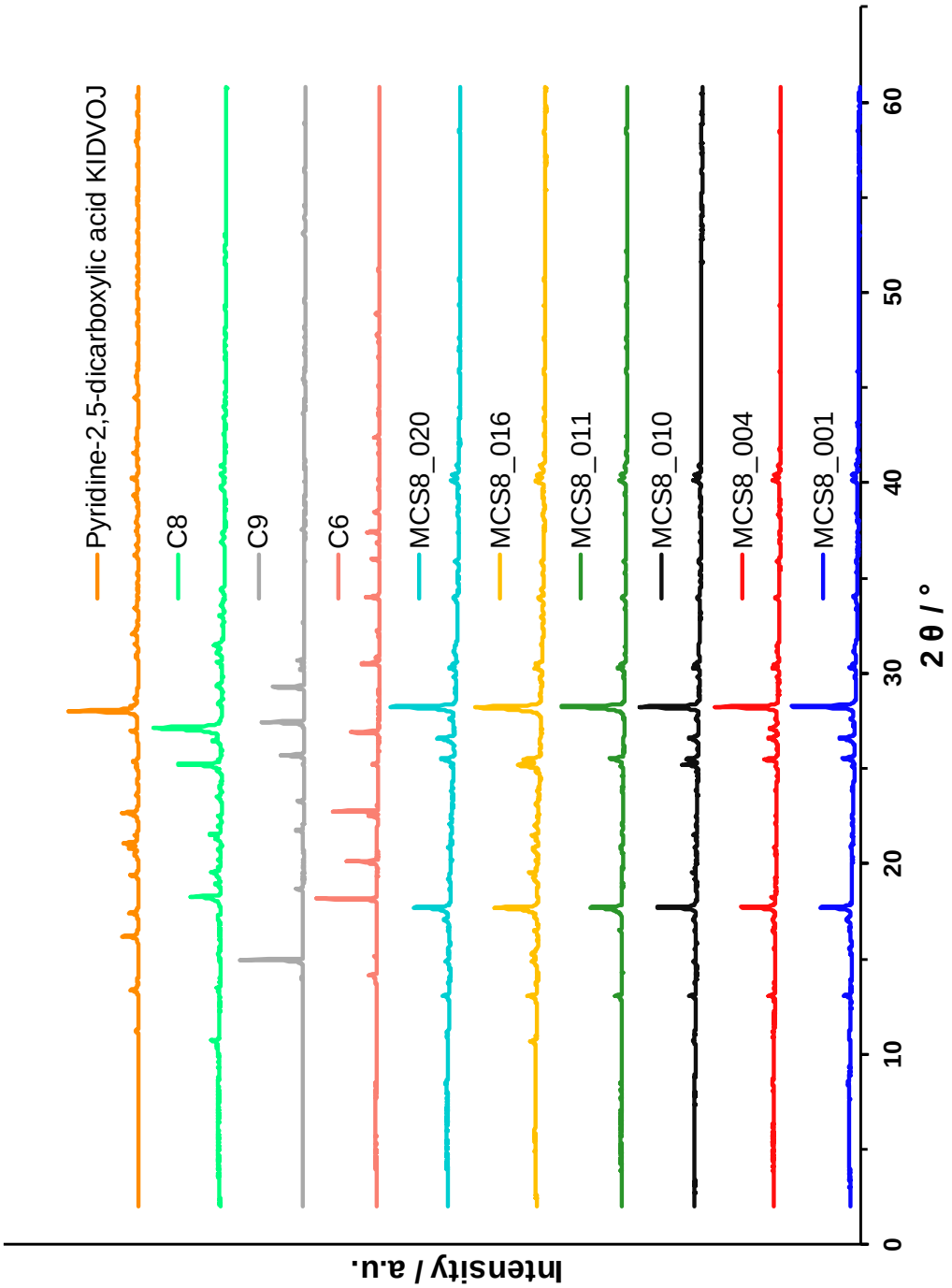

Figure 4.27. Laboratory PXRD patterns for MCS8_001 (blue), MCS8_004 (red), MCS8_010 (black), obtained from a 2 + 1 + 3 condensation of the monomers via LAG in a catalytic amount of water, benzene, and 1:3:0.2 1,4-dioxane:1,3,5-trimethylbenzene:acetic acid (3M), respectively, MCS8_011 (green), MCS8_016 (yellow) and MCS8_020 (turquoise), obtained from a 4 + 2 + 9 condensation of the monomers via LAG in a catalytic amount of water, 1:1 dichloromethane:N,N-dimethylacetamide, and 1:3:0.2 1,4-dioxane:1,3,5-trimethylbenzene:acetic acid (3M), respectively, and for the **C6** (salmon), **C9** (grey) and **C8** (spring green) monomers at 293 K, and the simulated patterns of the **C8** (KIDVOJ – orange) monomer from the CSD.

4.5.2.1. The new crystal structures

Pawley fitting on the unit cell parameters from indexing of MCS8_016, confirmed that the new crystal structure belongs to the triclinic centrosymmetric $P\bar{1}$ (2) space group. Structure solution was successfully carried out using the rigid body in Scheme 4.7. Rietveld refinement is currently underway at the time of writing. Table 4.15 shows the unit cell parameters, after Pawley fitting (Figure 4.28).

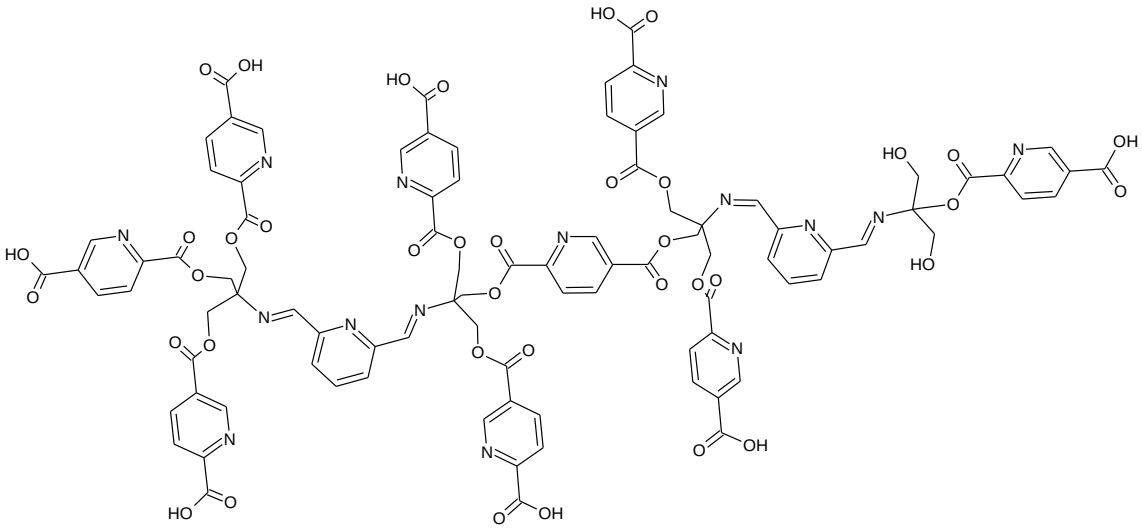

Scheme 4.7. The asymmetric unit used for the structure solution of MCS8_016, using rigid body analysis.

Table 4.15. Unit cell parameters for MCS8_016.

Crystal System	Triclinic
Space Group	$P\bar{1}$ (2)
***a* (Å)**	9.264(6)
***b* (Å)**	16.067(9)
***c* (Å)**	34.511(1)
***α* (°)**	133.44(1)
***β* (°)**	68.89(3)
***γ* (°)**	97.29(0)
***V* (Å³)**	3424.29(2)
***R*-wp (%)**	3.83

The Pawley fit for MCS8_010 (Figure 4.28) revealed that one crystallographic plane is shifted when compared to MCS8_016. The change in solvent from polar aprotic 1:1 dichloromethane:N,N-dimethylacetamide to predominantly non-polar 1:3:0.2 1,4-dioxane:1,3,5-trimethylbenzene:acetic acid (3M), could account for this shift in crystallographic planes. Both solvents in the former mixture are hydrogen bond acceptors, with the possibility of forming strong hydrogen bonds with the O–H hydrogen bond donor end groups. Conversely, in the latter solvent mixture, only dioxane is able to accept hydrogen bonds, in conjunction with the potential π-π intermolecular interactions between 1,3,5-trimethylbenzene and the aromatic rings of the new structure. The strength of intermolecular interactions is thus expected to be significantly stronger in MCS8_016 than in MCS8_010. The electron-withdrawing effects of the more polar 1:1 dichloromethane:N,N-dimethylacetamide solvent mixture, and the slightly larger size of the 1,3,5-trimethylbenzene molecule, could also play a role in the shifting of crystallographic planes, depending on the amount of solvent molecules present in the crystal structure. These potential solvent effects, may also be accompanied by the change to a smaller condensation ratio, with the same imine and ester links forming a different asymmetric unit in MCS8_010.

For similar potential linker ratio and solvent effects, the latter arising due to the small sized water solvent molecule, the powder pattern for MCS8_001 was also indexed and Pawley fitted. Table 4.16 shows the unit cell parameters, after Pawley fitting (Figure 4.28), belonging to the triclinic centrosymmetric $P\bar{1}$ (2) space group. Structure solution using rigid body analysis is currently underway at the time of writing.

Table 4.16. Unit cell parameters for MCS8_001.

Crystal System	Triclinic
Space Group	$P\bar{1}$ (2)
***a* (Å)**	14.878(7)
***b* (Å)**	17.840(5)
***c* (Å)**	17.191(3)
***α* (°)**	68.89(7)
***β* (°)**	99.16(8)
***γ* (°)**	98.61(7)
***V* (Å^3)**	4181.67(3)
***R*-wp (%)**	3.57

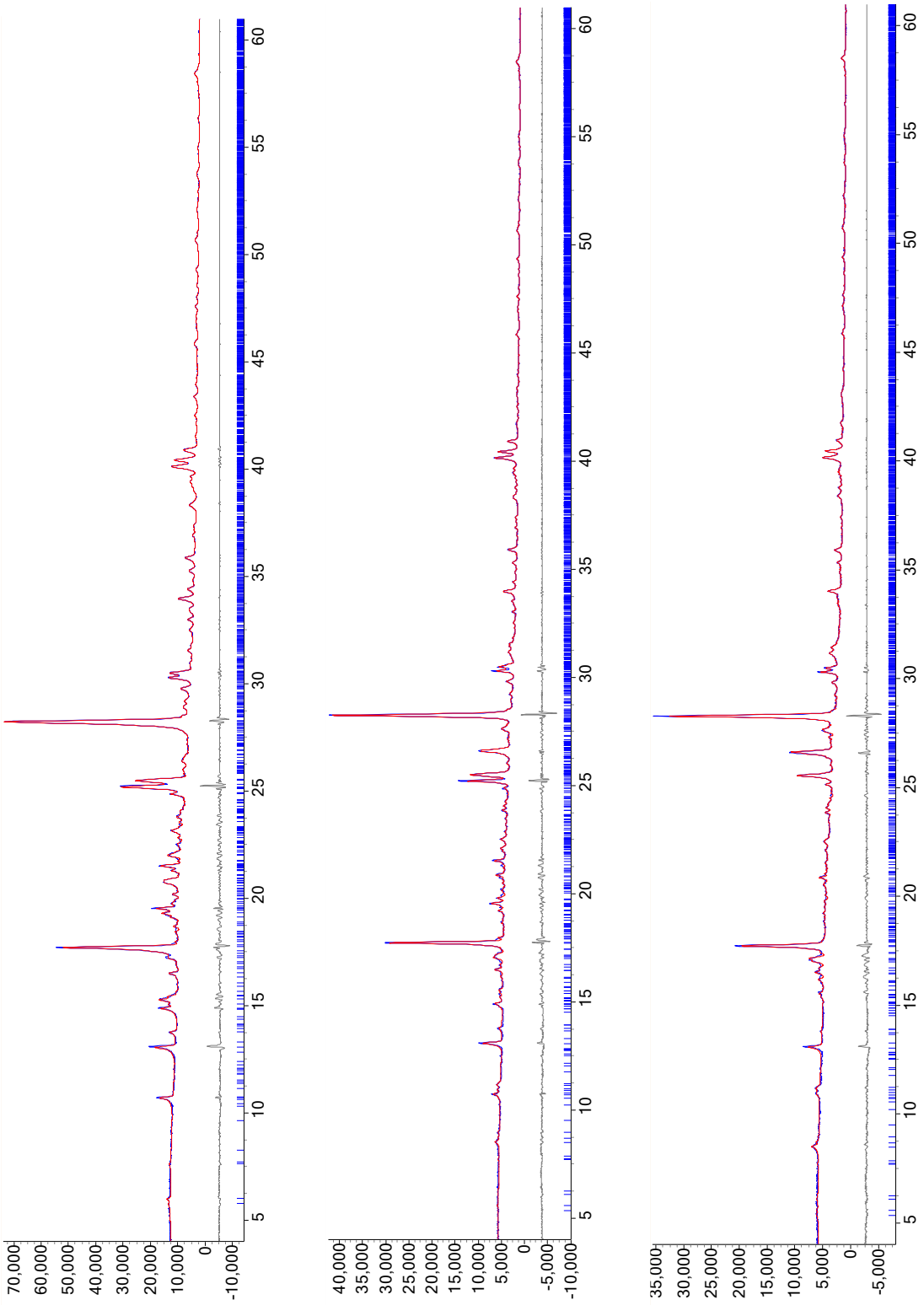

Figure 4.28. Pawley fits for MCS8_016 (top), obtained from a 4 + 2 + 9 condensation of **C6**, **C9** and **C8**, via LAG in a catalytic amount of 1:1 dichloromethane:N,N-dimethylacetamide, MCS8_010 (middle) and MCS8_001 (bottom), obtained from a 2 + 1 + 3 condensation of the monomers via LAG in a catalytic amount of 1:3:0.2 1,4-dioxane:1,3,5-trimethylbenzene:acetic acid (3M) and water, respectively, showing the observed powder patterns (blue), the calculated powder patterns (red), the difference plots (grey) and the peak positions. [187]

4.5.2.2. Supportive Characterisation

Once again, the formation of new imine and ester links between the three monomers was supported by FTIR spectroscopy. The spectra for MCS8_001 and MCS8_016 are identical, confirming the formation of the same new bonds in both samples, despite the change in solvent and linker environments. The FTIR spectra for these two samples are noticeably different from the spectra of the pure starting monomers (Figure 4.29), showing weak bands at 1650 cm^{-1}, characteristic of C=N stretching and indicative of the formation of imine bonds. The C=O stretching band of the free aldehyde (1740-1720 cm^{-1}) is shifted to 1720-1700 cm^{-1}, representative of the C=O stretching band of the aromatic ester bond, while the N–H bending band of the free amine (1589 cm^{-1}) is completely absent, confirming the formation of ester bonds and the absence of unreacted amine groups. The C–H stretching band of the free aldehyde (2850 cm^{-1}) and the O–H stretching band of the free carboxylic acid (3084 cm^{-1}), are absent in both samples, confirming the lack of unreacted aldehyde and carboxylic acid linkers respectively.

Hot stage microscopy revealed that the new structures, MCS8_001 and MCS8_016, are thermally stable up to 164 and 227 °C, respectively (Table 4.17). The slight melting phase observed for MCS8_001, at 184.9-194.0 °C, is missing for MCS8_016. No melting phase was observed at 168-169 °C and 119-122 °C, the melting ranges of the **C6** and **C9** linkers respectively, confirming their complete reaction to form new, larger, covalently bonded units. No change was observed at the melting point of the **C8** linker (244 °C) for MCS8_001, while MCS8_016 had already started exhibiting decomposition behaviour at that temperature. Similarly to the shift in crystallographic planes, this different thermal behaviour for the two samples, could potentially be due to a difference in the strength of the hydrogen bonding interactions involved in the crystal structures, when varying the catalytic solvent from water to 1:1 dichloromethane:N,N-dimethylacetamide. In order to validate and determine the extent of the solvent and condensation ratio effects, STA and variable temperature PXRD will be carried out on these new structures.

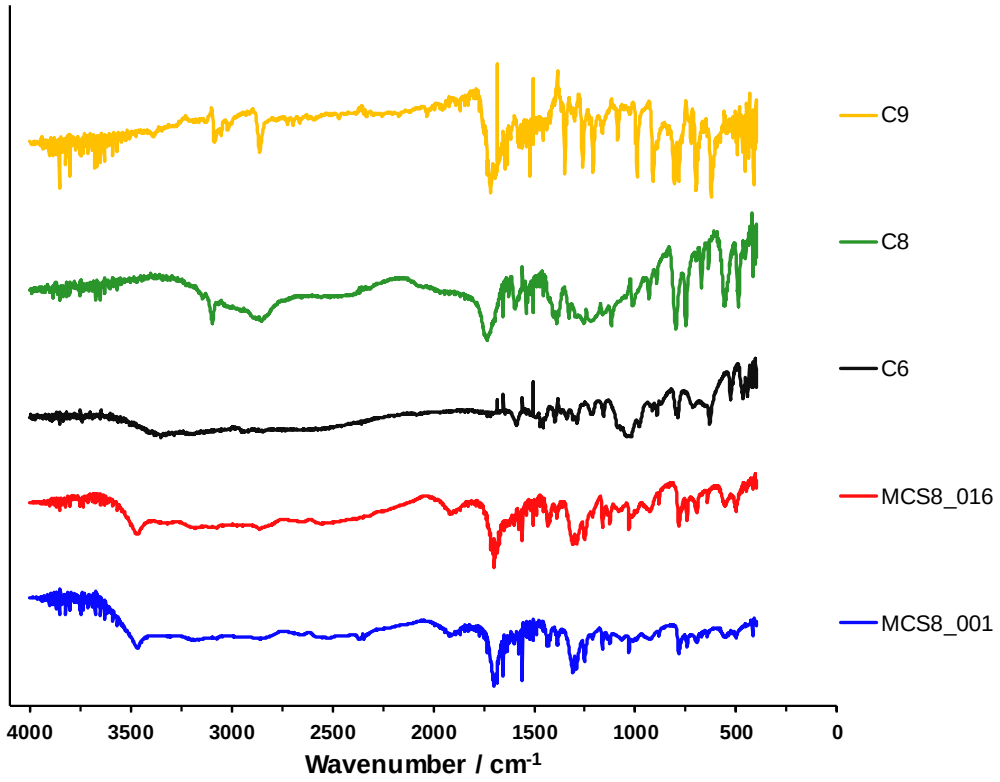

Figure 4.29. FTIR spectra for MCS8_001 (blue), obtained from a 2 + 3 + 1 condensation of the monomers via LAG in a catalytic amount of water, and MCS8_016 (red), obtained from a 4 + 9 + 2 condensation of the monomers via LAG in a catalytic amount of 1:1 dichloromethane:N,N-dimethylacetamide, and for the **C6** (black), **C8** (green) and **C9** (yellow) monomers.

Table 4.17. Temperature programme followed during hot stage microscopy of MCS8_001 and MCS8_016, corresponding observations and photomicrographs of the morphological changes.

MCS8_001					MCS8_016				
Ramp	**Rate (°C/min)**	**Limit (°C)**	**Observation**	**Photomicrograph of observed changes**	**Ramp**	**Rate (°C/min)**	**Limit (°C)**	**Observation**	**Photomicrograph of observed changes**
1. Heating	30	160	No observed change		1. Heating	30	160	No observed change	
2. Heating	2	265	Slow shrinking at 164.4 – 180.5 °C		2. Heating	2	275	Shrinking at 227.1 – 233.8 °C	
			Melting at 184.9 – 194.0 °C						

MCS8_001					MCS8_016				
Ramp	**Rate (°C/min)**	**Limit (°C)**	**Observation**	**Photomicrograph of observed changes**	**Ramp**	**Rate (°C/min)**	**Limit (°C)**	**Observation**	**Photomicrograph of observed changes**
3. Heating	5	450	Slow shrinking at 300.1 – 449.8 °C	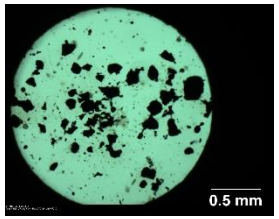	3. Heating	5	350	Darkening till 350.0 °C	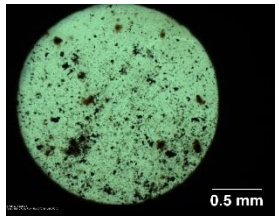
4. Cooling	20	65	No observed change		4. Cooling	20	65	No observed change	

4.5.3. Crystal Structure of pyridine-2,6-dicarbaldehyde, C9

The **C9** pH-sensitive smart molecule was not found in the CSD. Indexing and Pawley fitting is currently underway at the time of writing.

4.6. MCS13

4.6.1. Design and Synthesis

The combination of the C_2 monomer, terephthalaldehyde, **C7**, with the C_3 monomer, N',N'-bis(2-aminoethyl)ethane-1,2-diamine, **C12**, was expected to yield a 2D hexagonal extended network (Figure 4.1), which forms periodically aligned columns when its planar sheets are stacked. It was expected that the reaction between the aldehyde and amine functional groups, as shown in Scheme 4.8, would result in the formation of a 2D imine linked COF, exhibiting hexagonal symmetry.

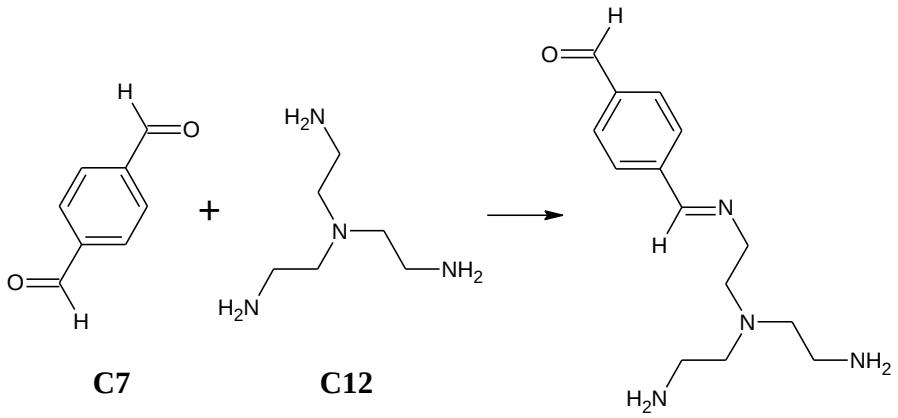

C7 **C12**

Scheme 4.8. The expected imine link formed between monomers **C7** and **C12**.

These building blocks were reacted together in a 1 + 1 condensation via two different synthetic techniques: LAG as listed in section 3.1.2.2 and microwave irradiation as listed in section 3.1.2.3. For LAG synthesis, a yellow crystalline powder was obtained from the water-catalysed reaction (MCS13_001), while a catalytic 1:1 dichloromethane:N,N-dimethylformamide solvent mixture yielded dark orange single crystals (MCS13_002). For microwave-assisted synthesis, a yellow crystalline powder, with a similar appearance to the former, was collected from a reaction in water solvent followed by washing in acetone (MCS13_004). A 2 + 1 condensation of the synthons via water-catalysed LAG synthesis also resulted in a yellow crystalline powder (MCS13_003). [181]

Further grinding of the MCS13_001 and MCS13_002 samples with the C_3 linker, N',N'-bis(3-aminopropyl)propane-1,3-diamine, **C4**, and additional **C7**, was carried out

to potentially increase the pore size of the framework. The same imine link was expected to form from a 1 + 2 + 4 condensation ratio using catalytic amounts of water (MCS13_005) or 1:1 dichloromethane:N,N-dimethylformamide (MCS13_006). This design goes a step further than the previously discussed reactions, by constructing a framework material from three different building monomers but using the same linkage throughout. Both samples formed hard yellow-orange materials. Laboratory PXRD data collection is currently underway at the time of writing.

4.6.2. Characterisation and Analysis

The crystallinity of the four samples was easily determined under the microscope, as shown in Figure 4.30 below.

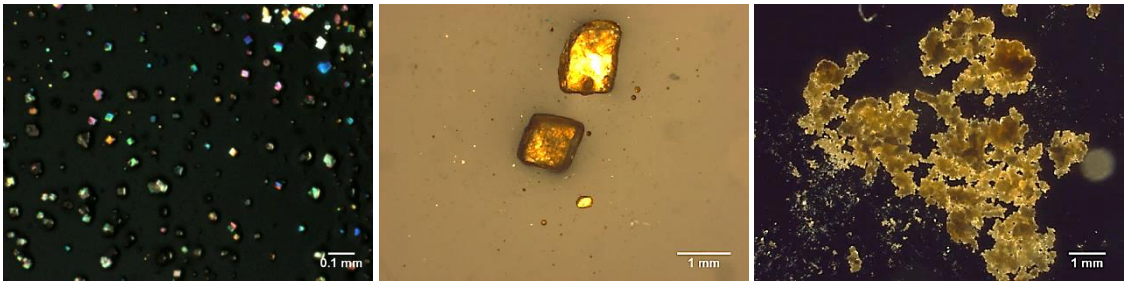

Figure 4.30. Crystalline powder of MCS13_001 (left), single crystals of MCS13_002 (centre) and crystalline powder of MCS13_004 (right).

Laboratory PXRD data for MCS13_001 and MCS13_003 and synchrotron measurements for MCS13_001, MCS13_002 and MCS13_004, were collected according to the specifications listed in section 3.4.1. Analysis of the synchrotron data determined that the obtained material was not the expected 2D imine linked COF with hexagonal symmetry. Instead, the dialdehyde and triamine monomers formed a clathrochelate cage (Figure 4.31), the isolation of which had been reported in 1992. [197] Synchrotron data comparison (Figure 4.32) of the obtained powder patterns for MCS13_001 and MCS13_002, and the calculated pattern from SCXRD data for MCS13_004, with the calculated pattern for the reported structure, KOMXAL, as obtained from the CSD, indicates that all four patterns are the same and thus arise from the same crystal structure.

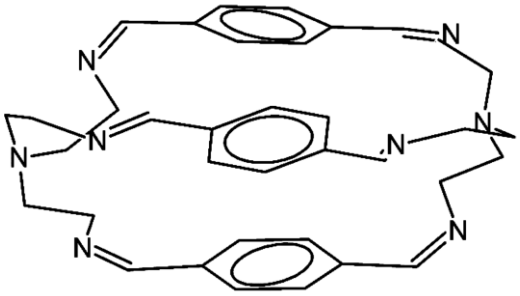

Figure 4.31. The obtained clathrochelate, hexaimine binucleating macrobicycle. [181]

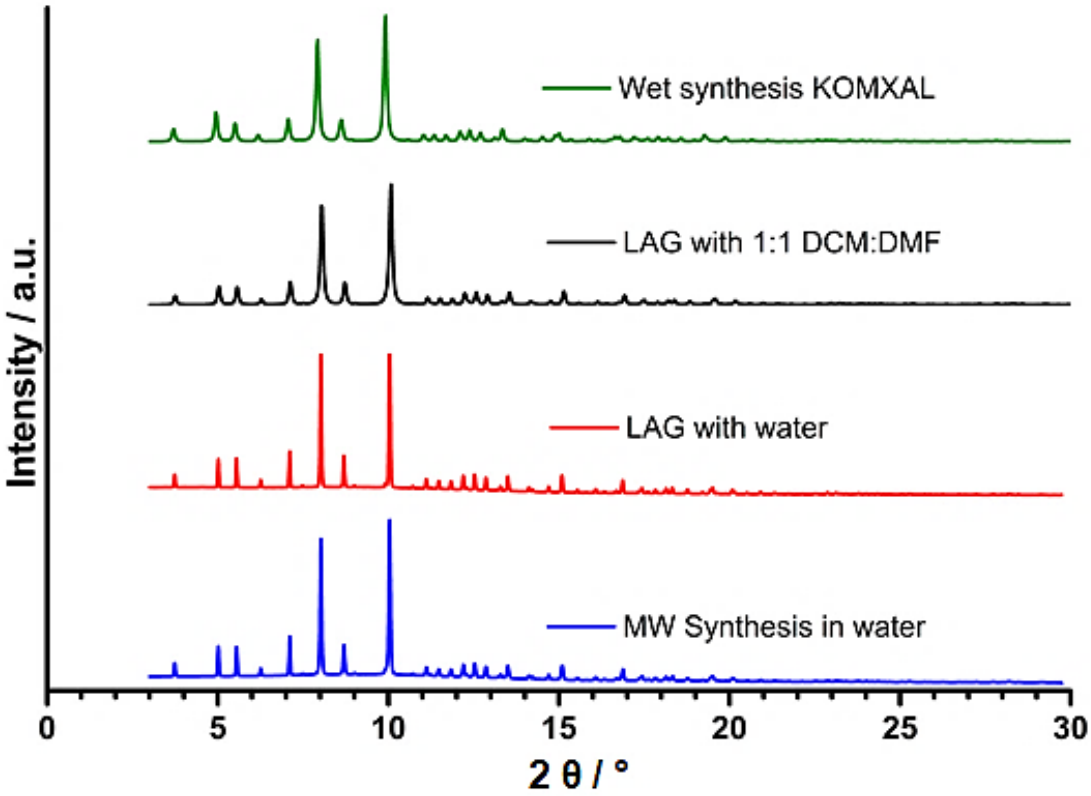

Figure 4.32. Synchrotron PXRD patterns of the clathrochelate cage obtained for MCS13_004 (blue), from a 1 + 1 condensation of **C7** and **C12** via microwave irradiation in water and subsequent washing in acetone, MCS13_001 (red), MCS13_002 (black – calculated from synchrotron SCXRD), from a 1 + 1 condensation of the monomers via LAG in a catalytic amount of water, and 1:1 dichloromethane:N,N-dimethylformamide, respectively, as compared with the reported structure, KOMXAL (green – calculated from single crystal data from the CSD). [181]

The free ligand (KOMXAL), isolated as the hexahydrate, had been formed via wet synthesis, from a template-free 3 + 2 Schiff-base condensation of the same **C7** and **C12** building blocks. The synthons were stirred for 3-4 hours in 100 mL of acetonitrile at ambient temperature, to generate the hexaimine binucleating macrobicycle which was recrystallised from methanol. [197] This cryptand is particularly exploited for its capacity

to form a homodinuclear cage complex, hosting two silver or two copper (II) ions. Due to their host-guest properties, clathrochelates are also used as phase transfer catalysts [198], ion-exchangers [199], and precursors for the formation of molecular Russian-doll superstructures [200].

The successful application of the LAG and microwave-assisted synthetic techniques in producing the same hexaimine clathrochelate as wet chemical synthesis, demonstrates their feasibility as green, rapid and facile alternative routes for traditional pathways. These techniques have recently been widely favoured over conventional wet synthetic techniques for the formation of organic systems in both academia and industry. The transfer of energy via mechanical force, i.e. grinding, and/or microwaves, reduces reaction time to minutes, providing a simple, highly efficient elevation of the internal temperature of a reaction mixture. In fact, for the macrobicyclic ligand synthesis, reaction time was reduced by more than 16 times, from 3-4 hours down to 12 to 15 minutes, as summarised in Table 4.18. By proof of concept, these powerful, economical, energy-efficient alternatives may potentially be employed for the synthesis of other cryptands, which is often very expensive and rather difficult, and for large-scale applications. [181]

Table 4.18. Comparison of different synthetic techniques for the formation of the hexaimine macrobicycle.

	Wet chemical synthesis	**LAG synthesis**		**MW synthesis**
	KOMXAL	**MCS13_002**	**MCS13_001**	**MCS13_004**
Ratio of synthons: C7 + C12	3 + 2	1 + 1	1 + 1	1 + 1
Reaction time	3-4 h	12 min at 25 s^{-1}	12 min at 25 s^{-1}	15 min at 150 W
Solvent	100 mL Acetonitrile	1:1 dichloromethane :N,N-dimethyl formamide (catalytic volume)	Water (catalytic volume)	20 mL Water

Additionally, a change in solvent mixture, from polar aprotic acetonitrile to 1:1 dichloromethane:N,N-dimethylformamide, two polar aprotic solvents, or to water, a polar protic solvent, did not affect the formation of the cryptand. Laboratory PXRD data for MCS13_001 and MCS13_003 (Figure 4.33), also presented the same powder patterns as the synchrotron measurements and the structure reported in literature. This indicates that a change in linker mole ratio from 3 + 2 to 1 + 1 or 2 + 1, also does not seem to affect the formation of the free clathrochelate ligand.

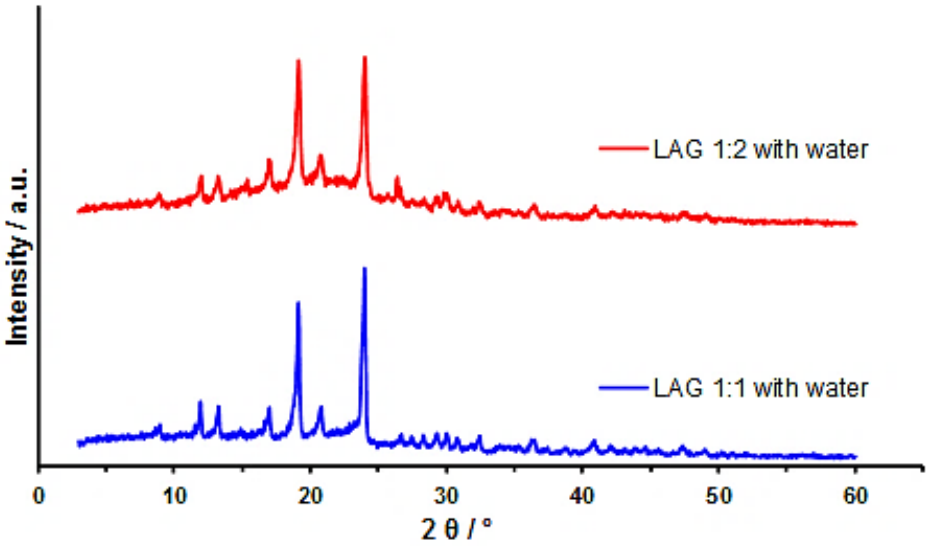

Figure 4.33. Laboratory PXRD patterns of the clathrochelate cage obtained for MCS13_001 (blue) and MCS13_003 (red), from a 1 + 1 and 2 + 1 condensation of **C7** and **C12**, respectively, via LAG in a catalytic amount of water.

The analysis of synchrotron variable temperature PXRD measurements (Figure 4.34) indicates that the Schiff-base capsule is not thermally stable over 360 K. Powder patterns at higher temperatures slowly start to lose the major peaks observed at low temperatures, until no diffraction peaks are observed. The crystalline cage transforms into an amorphous material upon heating over 360 K, possibly collapsing in an aperiodic way, i.e. it gets distorted, or disintegrates and is destroyed. Further analysis of the high temperature structures via electron microscopy is required to determine which of the two possibilities is taking place.

Micro-Raman mapping will also be carried out on the MCS13_001, MCS13_002 and MCS13_004 samples, synthesised using different techniques, in order to determine crystallite sizes and characterise the homogeneity of the samples.

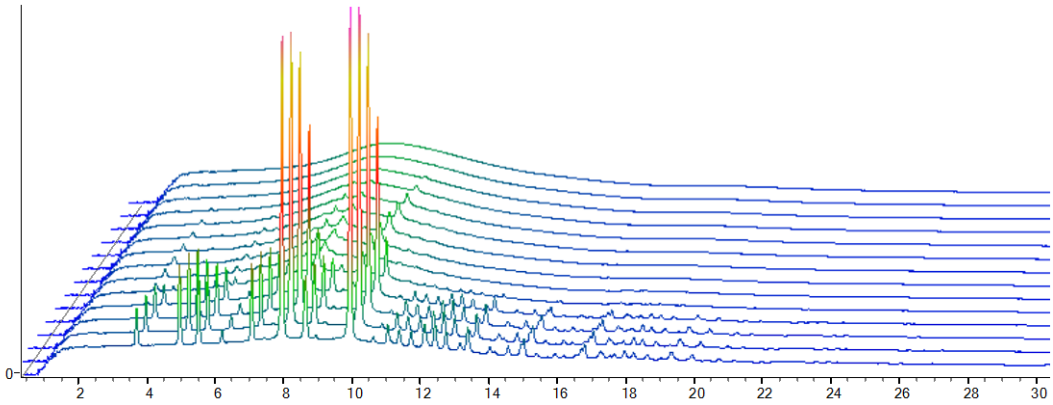

Figure 4.34. Synchrotron variable temperature PXRD data of MCS13_001, obtained from a 1 + 1 condensation of the monomers via LAG in a catalytic amount of water, upon heating from 336 to 414 K.

4.7. MCS14

4.7.1. Design and Synthesis

The reaction between terephthalaldehyde, **C7**, and 2,5-dimethylbenzene-1,4-diamine, **C13**, as building blocks, is another Schiff-base condensation. Using two C_2 monomers, it was expected that the reaction would result in the formation of a 2D linear imine linked polymeric chain (Figure 4.35, Scheme 4.9).

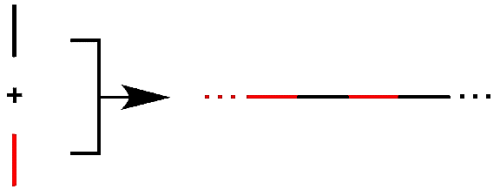

Figure 4.35. Linear polymeric chain resulting from the combination of two C_2 monomers.

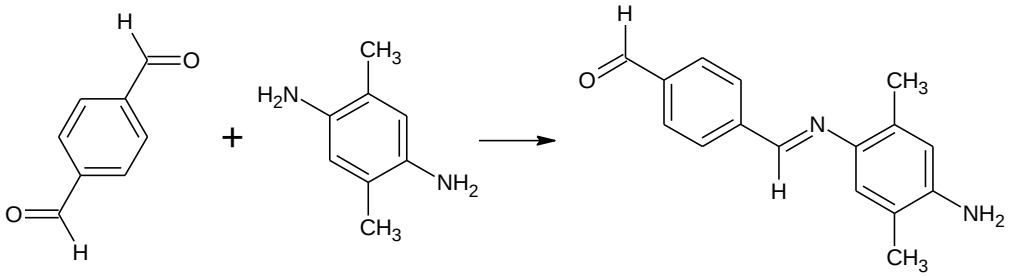

C7 **C13**

Scheme 4.9. The expected imine link formed between monomers **C7** and **C13**.

These building units were reacted together in a 1 + 2 condensation via LAG (section 3.1.2.2). A small change in colouration was observed from the light yellow and brown colouration of the monomers respectively, to an orange crystalline powder obtained from the oxolane-catalysed reaction (MCS14_001). [182] Although the two monomers are expected to react together in a 1 + 1 condensation according to the number of functional groups present, samples having this linker mole ratio did not produce crystalline materials, and therefore lack a key feature of COFs.

4.7.2. Characterisation and Analysis

The crystalline nature of the sample was determined under the microscope, upon reflection of plane polarised light (Figure 4.36). Comparison of the laboratory PXRD data for MCS14_001 with the patterns for the aldehyde and amine monomers, and the simulated patterns for the aldehyde, JULZAR and JULZAR01, from the CSD, confirms that the two patterns are completely different and thus originate from different crystal structures (Figure 4.37).

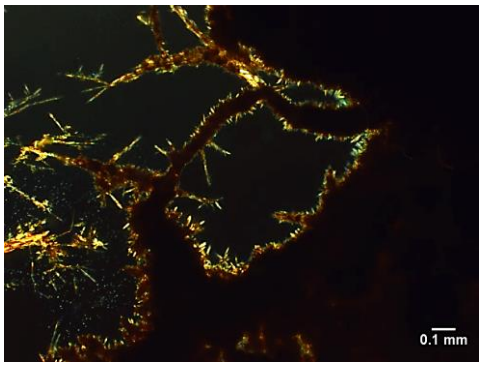

Figure 4.36. Crystalline powder of MCS14_001 from LAG with oxolane.

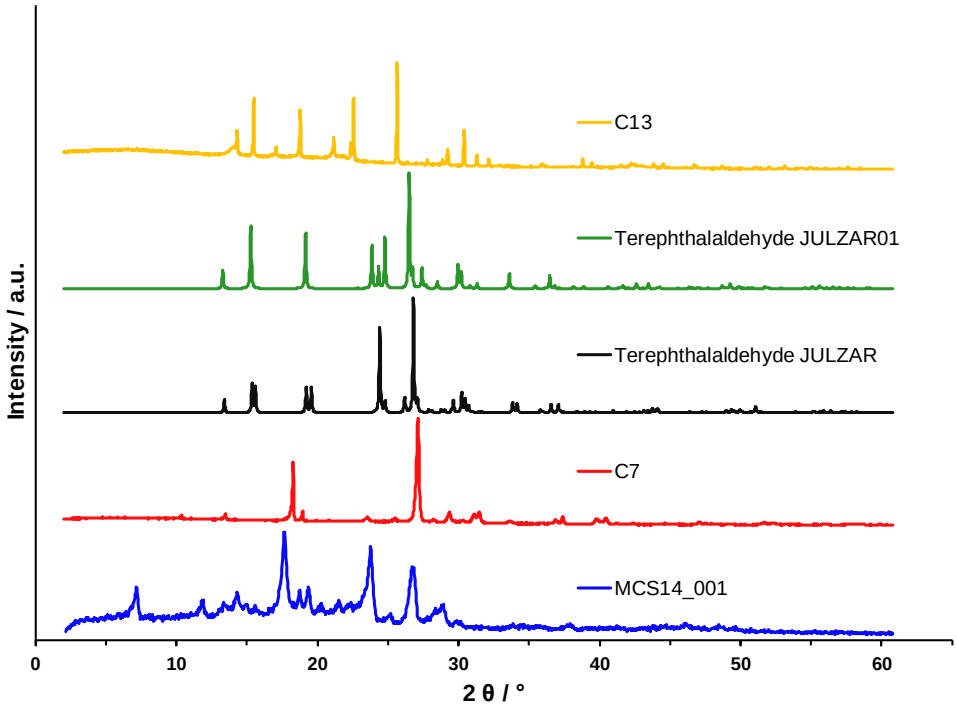

Figure 4.37. Laboratory PXRD patterns of MCS14_001, obtained from a 1 + 2 condensation of the monomers via LAG in a catalytic amount of oxolane, at 298 K (blue), for the **C7** (red) and **C13** (yellow) monomers at 293 K, and the simulated patterns of the **C7** (JULZAR – black and JULZAR01 – green) monomer from the CSD.

4.7.3. The New Crystal Structure

This crystalline material exhibited diffraction peaks corresponding to reflections from the (001), (010) and (100) planes, at ~ 7.18°, 12.06° and 15.18° respectively. Pawley refinement on the unit cell parameters confirmed these peak assignments for a triclinic centrosymmetric $P\bar{1}$ (2) space group (Table 4.19). Structure solution using rigid body analysis and subsequent Rietveld refinement, produced an *R*-wp of 11.687 % and an *R*_Bragg value of 4.280, for the simulated structure, indicating that this derived model structure is in good agreement with the observed experimental pattern (Figure 4.38).

The solved structure features the synthesised imine link (Figure 4.39) as expected in Scheme 4.9. Linear polymeric chains are however not constructed of successive imine links as would have been predicted. Rather, the nearest dimers along the *b* axis connect together via carbon to carbon bonds, 1.366 Å in length, between the C17 methyl group on the amine of one dimer and the C2 atom in the ring of the aldehyde of the second dimer. This results in linear chains along the *b* axis (Figure 4.40). These C17–C2 bonds are found at approximately 120° angles to the planes of the aromatic rings, creating a stair-like arrangement. The values for bond length and angle indicate that the C17 atom is possibly sp^2 hybridised. No such connection has been listed in the CSD thus far (CSD as accessed on 25th October 2018). [201]

Moving along the *c* axis, adjacent chains run parallel to each other, perpendicular to the axis. Conversely, when moving along the *a* axis, neighbouring chains alternate in their direction, such that they run antiparallel to each other and perpendicular to the axis. Each two antiparallel chains are linked via intermolecular hydrogen bonds between the free terminal amine group of one dimer, i.e. the hydrogen bond donor, and the nitrogen participating in the imine link of the other dimer on the antiparallel chain, i.e. the hydrogen bond acceptor (Figure 4.41). Additionally, these stacked antiparallel chains contain face-to-face aromatic rings, the centroids of which are within significant range for π-π interactions.

Table 4.19. Chemical, crystallographic and refinement parameters of phase A of MCS14_001, obtained by laboratory PXRD using Cu $K_{\alpha 1}$ radiation. [195]

Empirical formula	$C_{16}H_7N_2$
Formula weight (g mol^{-1})	455.48
Temperature (K)	298
Crystal System	Triclinic
Space Group	$P\bar{1}$ (2)
***a* (Å)**	6.054(2)
***b* (Å)**	7.316(4)
***c* (Å)**	12.915(7)
***α* (°)**	96.43(0)
***β* (°)**	106.32(3)
***γ* (°)**	90.49(5)
***V* (Å^3)**	545.11(3)
Z	1
ρ_{calc} (g cm^{-3})	1.376
Wavelength (Å)	1.5406
***F*(000)**	235
***R*-wp (%)**	11.687
***R*_Bragg**	4.280
Starting angle (°, 2θ)	4.0
Final angle (°, 2θ)	60.0
Step width (°, 2θ)	0.03

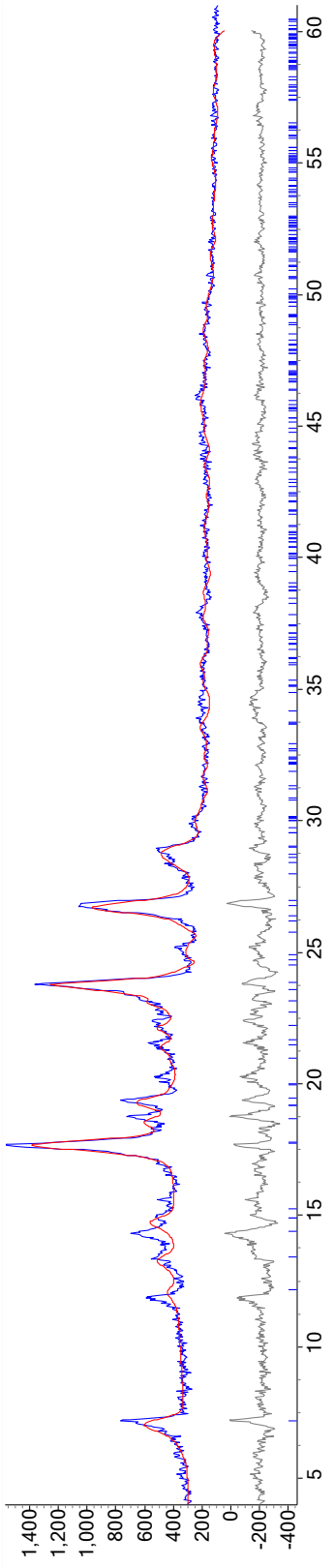

Figure 4.38. Rietveld plot for MCS14_001, obtained from a 1 + 2 condensation of **C7** and **C13** via LAG in a catalytic amount of oxolane, showing the observed powder pattern (blue), the calculated powder pattern (red), the difference plot (grey) and the peak positions. [187]

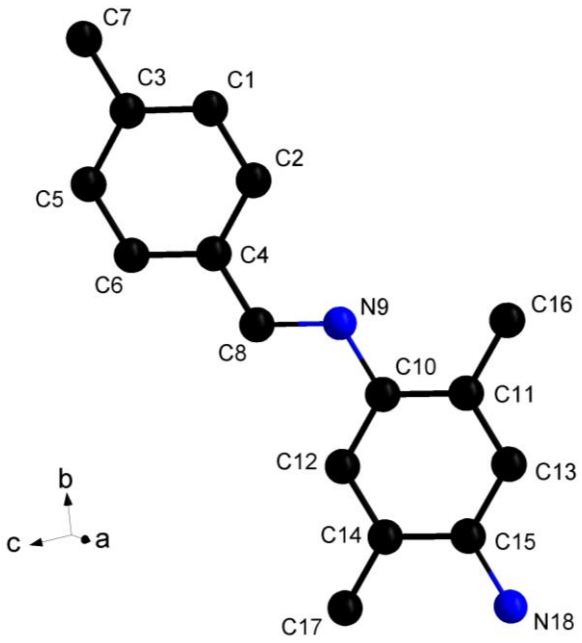

Figure 4.39. The asymmetric unit of the new crystalline imine linked structure (MCS14_001), showing the labelling scheme. [196]

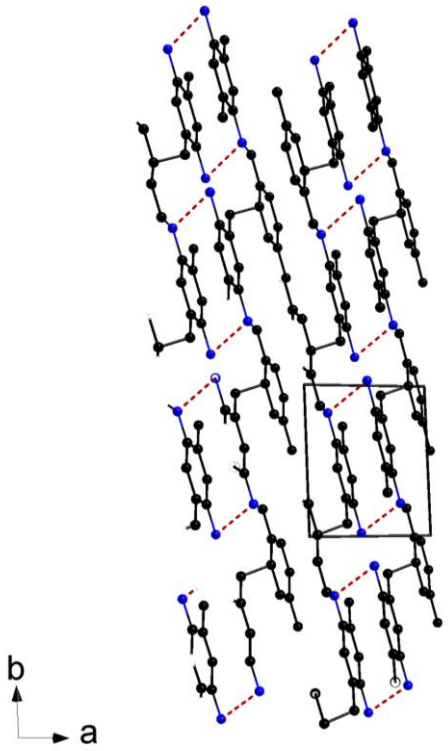

Figure 4.40. The crystal structure of the imine linked chains, viewed along the *c* axis. Hydrogen bonding interactions are shown as red dotted lines. [196]

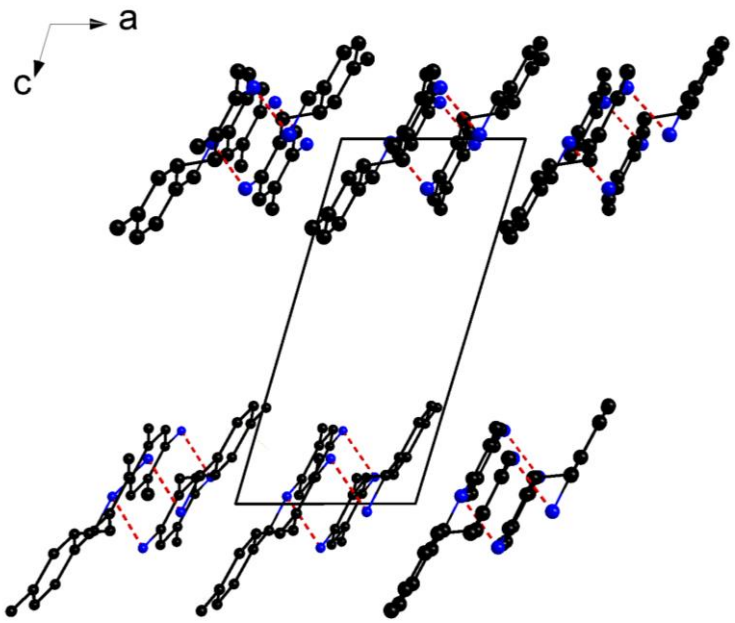

Figure 4.41. The crystal structure of the imine linked chains, viewed along the *b* axis. Hydrogen bonding interactions are shown as red dotted lines. [196]

4.7.4. Thermodynamic phase change

Comparison of the laboratory data collected at 298 K with synchrotron data collected at 120 K, indicates the presence of two different phases of this material, phase A and phase B respectively. Variable temperature PXRD measurements were thus carried out, in order to understand in real-time, the changes exhibited by the crystal structure, when subjected to heating and cooling.

Analysis of laboratory powder patterns, collected upon heating from 303 to 633 K (Figure 4.42), reveals a phase change taking place at 413 K, from phase A to this new phase C of the material. Going above 558 K, the major peaks start to disappear. The structure transforms into an amorphous material, indicating that this new crystalline Schiff-base structure is not thermally stable over 558 K. Furthermore, the analysis of synchrotron powder patterns, obtained by heating from 120 to 500 K and cooling back to 120 K (Figure 4.43), indicates that, upon heating, the structure undergoes a change from phase B to phase C at 438 K. No other phase change is observed upon cooling, suggesting that the material undergoes a temperature induced permanent phase change.

At this stage, it can be determined that phase B is the kinetic product while phase C is the thermodynamic product. Phase A could possibly be an isolated intermediate.

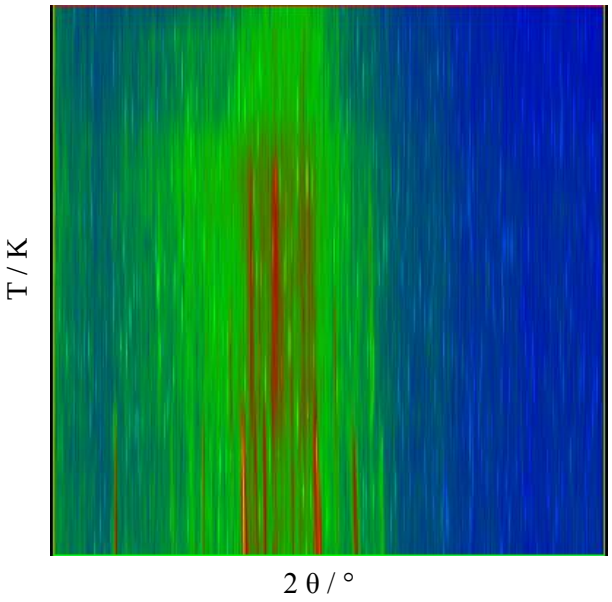

Figure 4.42. Laboratory variable temperature PXRD data of MCS14_001, obtained from a 1 + 2 condensation of the monomers via LAG in a catalytic amount of oxolane, upon heating from 333 to 573 K.

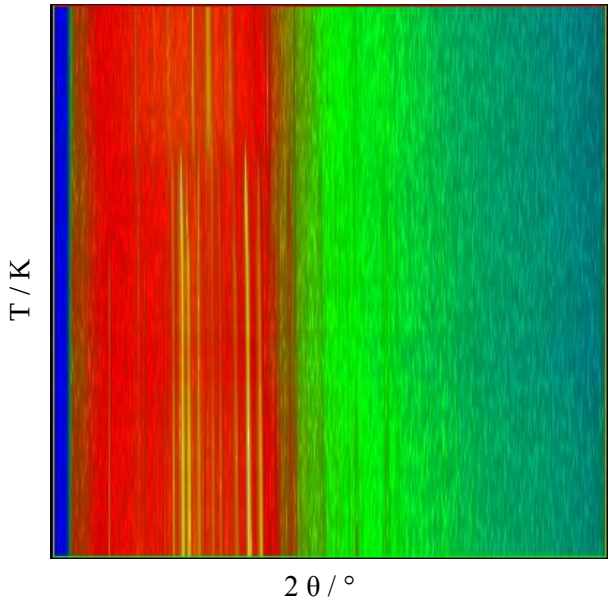

Figure 4.43. Synchrotron variable temperature PXRD data of MCS14_001, obtained from a 1 + 2 condensation of the monomers via LAG in a catalytic amount of oxolane, upon heating from 216 to 492 K.

Structure solution of the two discovered phases, phase B and phase C, was carried out using rigid body analysis, to identify any intermolecular and intramolecular changes in the crystal structure. The same rigid body used to solve phase A (Figure 4.39), was also used to solve the two other phases. Pawley fitting revealed a change in the crystal system and space group for phase B, to a monoclinic enantiomorphic polar *P*2 (3) space group,

while phase C retained the triclinic centrosymmetric $P\bar{1}$ (2) space group of phase A (Table 4.20, Figure 4.44). Significant differences are observed when comparing the unit cell parameters of phases A and C, indicating a positive thermal expansion along all three axes. The structure seems to lose its unique connectivity at low and high temperatures, with both phase B and phase C having the imine linked asymmetric unit as discrete molecules, alternating direction along the *c* axis, and arranged in planes which run perpendicular to the *b* axis. Rietveld refinement, for both phases, is currently underway at the time of writing.

Table 4.20. Unit cell parameters for phases B and C of MCS14_001.

	Phase B	Phase C
Crystal System	Monoclinic	Triclinic
Space Group	*P*2 (3)	$P\bar{1}$ (2)
***a* (Å)**	32.027(2)	10.928(5)
***b* (Å)**	4.689(5)	16.285(7)
***c* (Å)**	61.718(3)	27.905(4)
***α* (°)**	90	42.20(9)
***β* (°)**	77.70(1)	94.42(1)
***γ* (°)**	90	89.63(4)
***V* (Å^3)**	9056.92(1)	3311.88(4)
***R*-wp (%)**	1.35	1.61

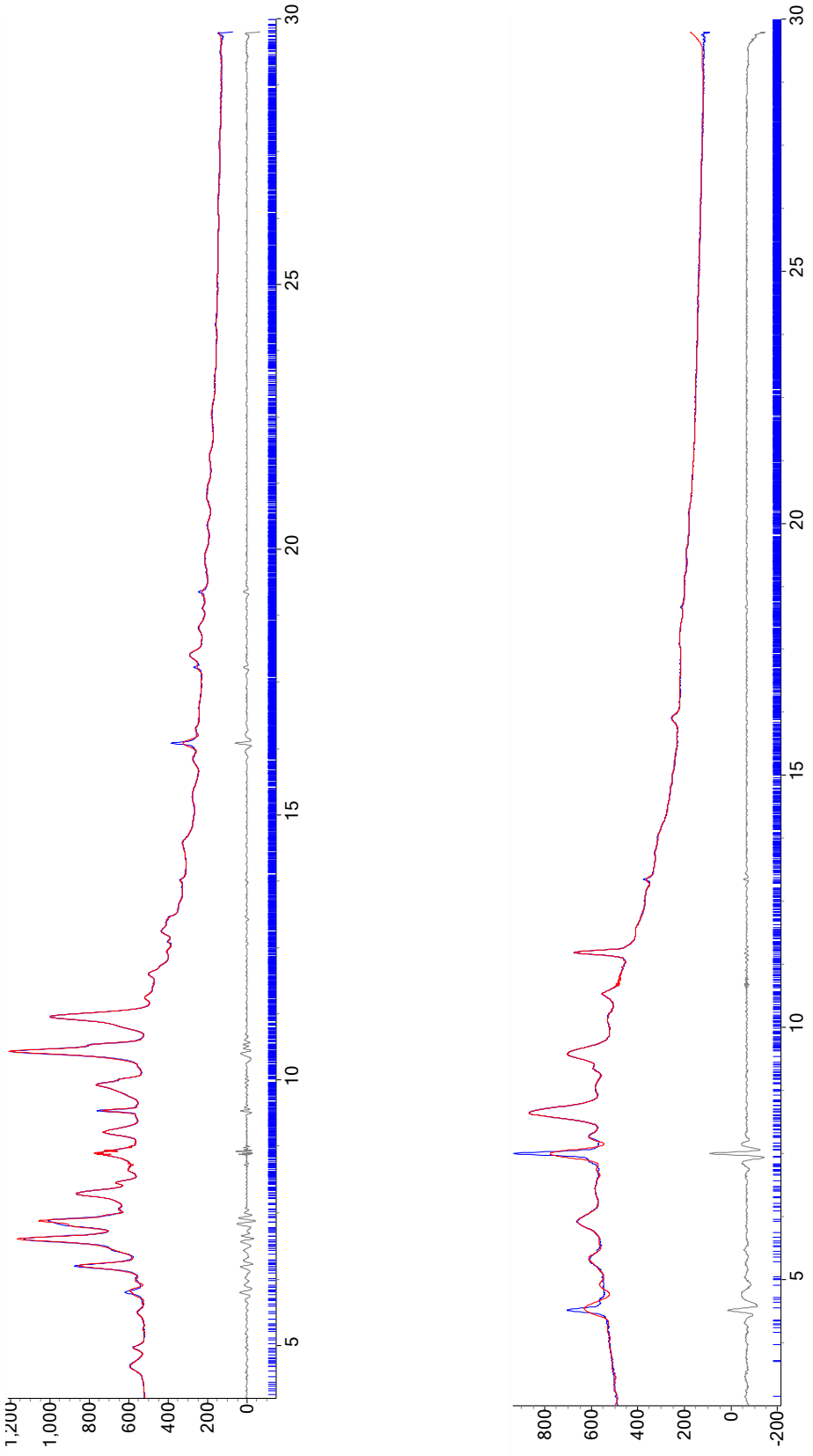

Figure 4.44. Pawley fits for phase B (top) and phase C (bottom) of MCS14_001, obtained from a 1 + 2 condensation of **C7** and **C13** via LAG in a catalytic amount of oxolane, showing the observed powder patterns (blue), the calculated powder patterns (red), the difference plots (grey) and the peak positions.

4.7.5. Supportive Characterisation

The formation of new imine links was supported by FTIR spectroscopy. The spectrum for MCS14_001, is visibly different from the spectra of the pure starting monomers (Figure 4.45), with a sharp band at 1680-1660 cm^{-1}, characteristic of C=N stretching, confirming the formation of new imine bonds. The C=O stretching band (1740-1720 cm^{-1}) and the C–H stretching band (2860 cm^{-1}) of the free aldehyde, and the N–H bending band (1635 cm^{-1}) and N–H stretching band (3400 cm^{-1}) of the free amine, are all absent or significantly attenuated, confirming the formation of a new structure with imine bonds and the absence of unreacted aldehyde and amine monomers.

STA will be carried out to supplement the thermal stability data obtained from variable temperature PXRD.

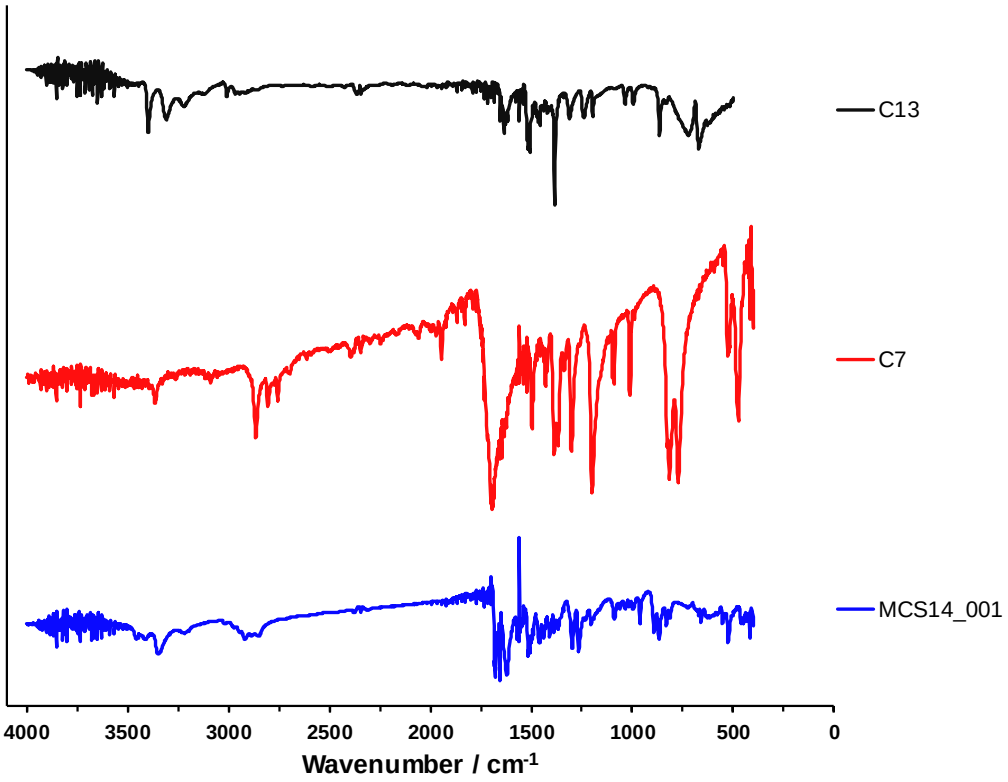

Figure 4.45. FTIR spectra for MCS14_001 (blue), obtained from a 1 + 2 condensation of the monomers via LAG in a catalytic amount of oxolane, and for the **C7** (red) and **C13** (black) monomers.

4.7.6. Crystal Structure of 2,5-dimethylbenzene-1,4-diamine, C13

The **C13** linker was not found in the CSD. Indexing and Pawley fitting is currently underway at the time of writing.

4.8. Unsuccessful Reactions

4.8.1. MCS2

The bifunctional C_3 linker (3,5-diformylphenyl)boronic acid, **C2**, was reacted in a 1 + 1 condensation via reflux (section 3.1.2.1), with the C_2 linker ethanedihydrazide, **C3**, in 1:1 1,4-dioxane:1,3,5-trimethylbenzene and acetic acid as catalyst. The condensation of aldehyde and hydrazide groups alongside the self-condensation of boronic acid groups, was expected to yield a 2D hydrazone and boronate anhydride linked COF, exhibiting hexagonal symmetry (Figure 4.1, Scheme 4.10). A cream crystalline powder was obtained (MCS2_001), washed with oxolane (MCS2_002) and subsequently dried under vacuum (MCS2_003).

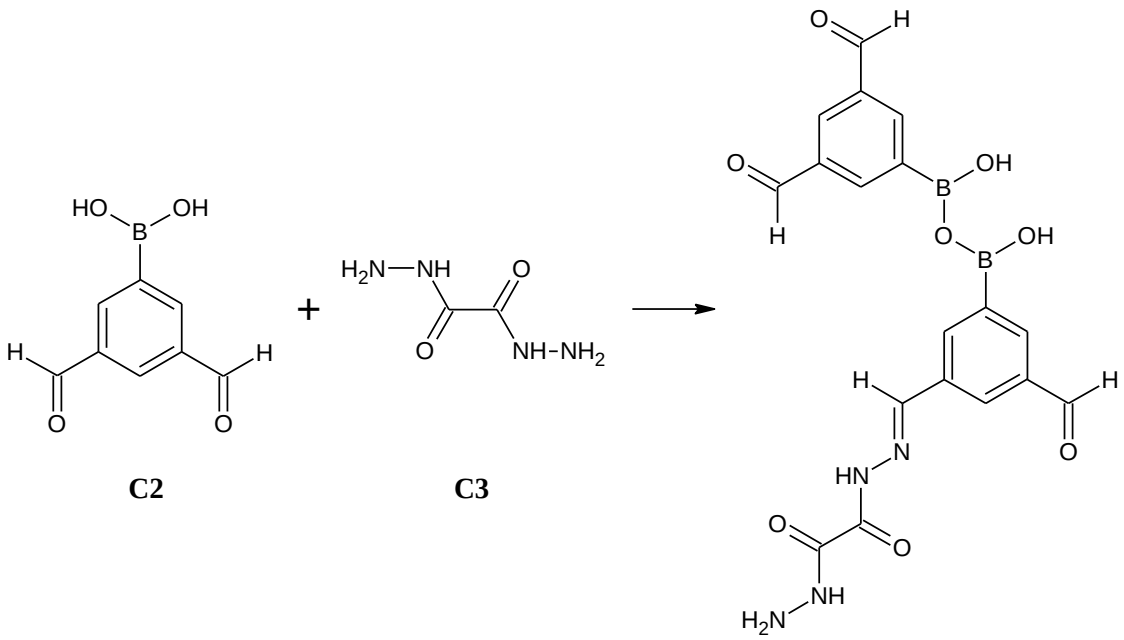

Scheme 4.10. The expected hydrazone and boronate anhydride links formed between monomers **C2** and **C3**.

The X-ray powder patterns obtained for the three samples are identical. The patterns are also the same as the pattern for the **C3** linker, upon comparison, indicating that the reaction was not successful (Figure 10.5). No further analysis was thus carried out.

4.8.2. MCS3

The same bifunctional C_3 linker (3,5-diformylphenyl)boronic acid, **C2**, was reacted in a 3 + 2 condensation via reflux (section 3.1.2.1), with the flexible C_3 linker N',N'-bis(3-aminopropyl)propane-1,3-diamine, **C4**, in 1:1 1,4-dioxane:1,3,5-trimethylbenzene. The Schiff-base condensation of aldehyde and amine groups alongside the self-condensation of boronic acid groups, was similarly expected to yield a 2D imine and boronate anhydride linked COF, exhibiting hexagonal symmetry (Figure 4.46, Scheme 4.11). A light-yellow powder was obtained (MCS3_001), washed with oxolane (MCS3_002) and subsequently dried under vacuum (MCS3_003).

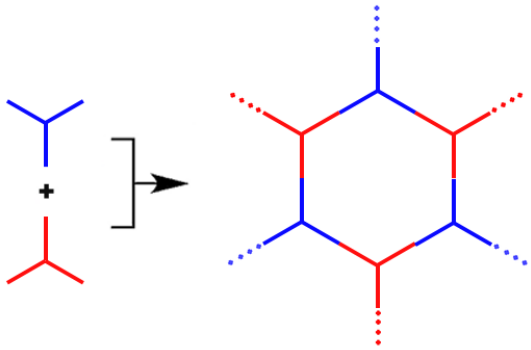

Figure 4.46. Hexagonal COF resulting from the combination of two C_3 monomers.

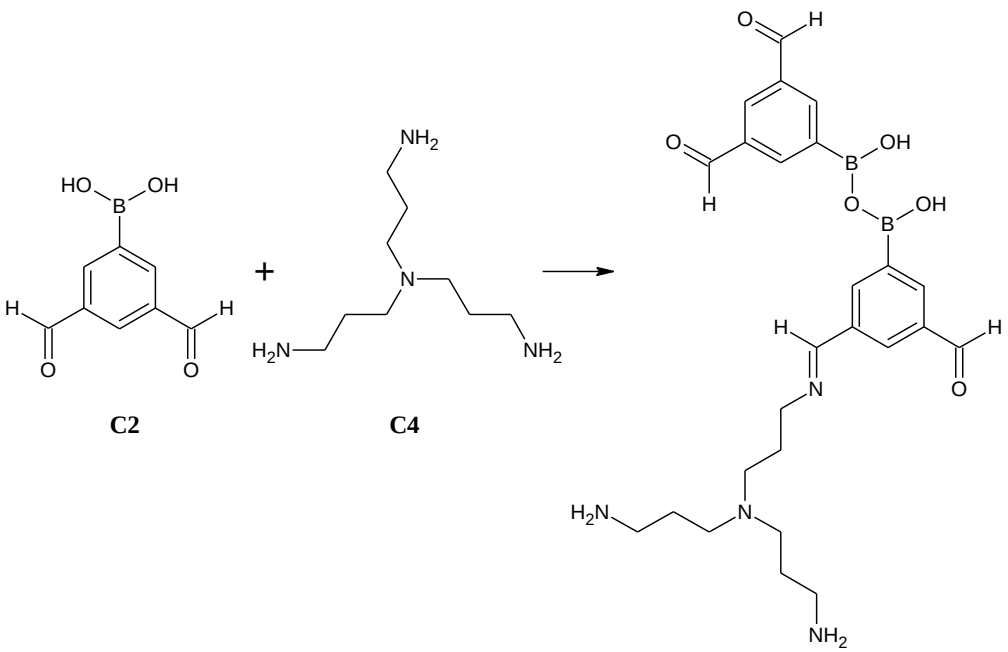

Scheme 4.11. The expected imine and boronate anhydride links formed between monomers **C2** and **C4**.

The X-ray powder patterns obtained for the three samples show broad peaks and a high background, indicative of amorphous materials (Figure 10.6). Since these samples lack crystallinity, a key characteristic of COFs, comparison with linker patterns was deemed unnecessary and no further analysis was carried out.

4.8.3. MCS5

Another synthetic reaction once again involved the bifunctional C_3 linker (3,5-diformylphenyl)boronic acid, **C2**, in reaction with the C_3 linker triphenylene-2,3,6,7,10,11-hexol hydrate, **C5**, and the C_2 linker ethanedihydrazide, **C3**, in a 3 + 1 + 3 acetic acid-catalysed condensation in 1:1 1,4-dioxane:1,3,5-trimethylbenzene, via reflux (section 3.1.2.1). The co-condensation of boronic acid with dialcohol end groups and of aldehyde with hydrazide end groups, was expected to result in the formation of a 2D boronate ester and hydrazone linked COF, exhibiting hexagonal symmetry (Figure 4.6, Scheme 4.12). A grey coloured powder was obtained (MCS5_001), washed with oxolane (MCS5_002) and subsequently dried under vacuum (MCS5_003).

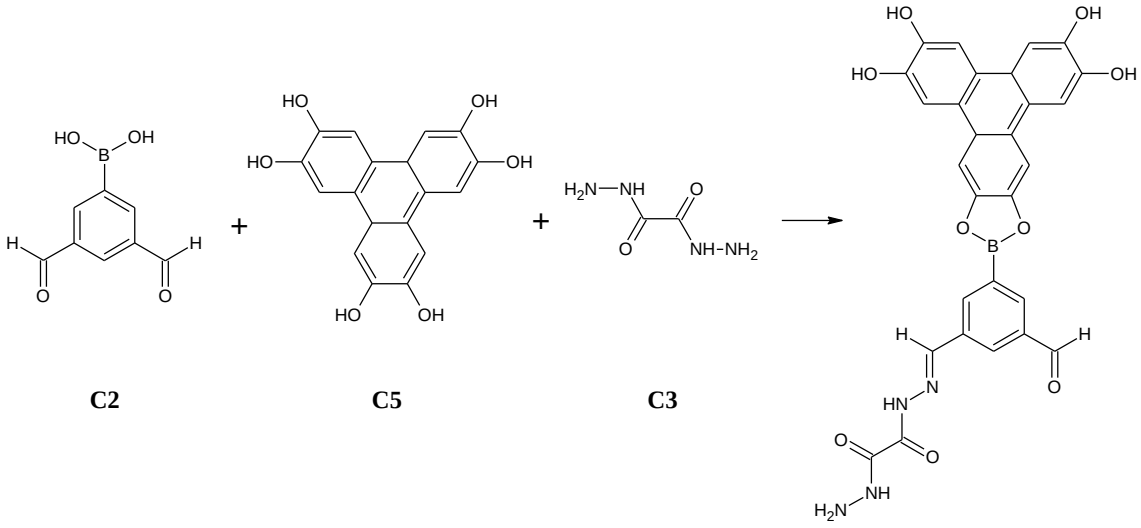

C2 **C5** **C3**

Scheme 4.12. The expected boronate ester and hydrazone links formed between monomers **C2**, **C5** and **C3**.

The X-ray powder patterns obtained for the three samples show just one broad peak and a high background, typical of amorphous materials (Figure 10.7). Since the crystallinity characteristic of COFs is missing, no further analysis was carried out.

4.8.4. MCS9

A second reaction incorporating the **C9** pH-sensitive smart polymer as part of the framework through a bottom-up approach, was carried out with the flexible C_3 linker N',N'-bis(3-aminopropyl)propane-1,3-diamine, **C4**, in a 2 + 1 condensation via LAG (section 3.1.2.2), using a series of catalytic solvents (Table 4.21). The condensation of aldehyde and amine groups was expected to result in a 2D imine linked COF (Scheme 4.13).

Table 4.21. Catalytic solvents used in LAG synthesis of MCS9 samples.

Sample Code	Catalytic solvent
MCS9_001	Water
MCS9_002	Ethanol
MCS9_003	Oxolane
MCS9_004	Benzene
MCS9_005	5:1 methanol:ethoxyethane
MCS9_006	1:1 dichloromethane:N,N-dimethylacetamide
MCS9_007	1:1 1,4-dioxane:1,3,5-trimethylbenzene
MCS9_008	1:1 oxolane:methanol
MCS9_009	1:1:0.05 1,4-dioxane:1,3,5-trimethylbenzene:acetic acid (3M)
MCS9_010	1:3:0.2 1,4-dioxane:1,3,5-trimethylbenzene:acetic acid (3M)

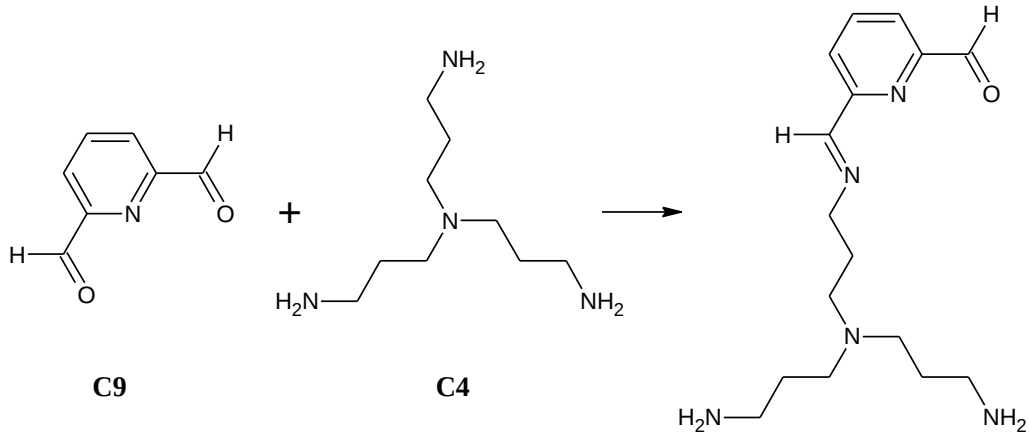

C9 **C4**

Scheme 4.13. The expected imine links formed between monomers **C9** and **C4**.

None of these tan-brown coloured samples resulted in crystalline powders. Instead, hard glass-like materials were formed, possibly due to the flexible liquid amine linker which does not provide rigidity to the structure. Laboratory PXRD data collection is currently underway at the time of writing.

4.8.5. MCS10

The only reaction incorporating 1,1'-ferrocenedicarboxaldehyde, **C10**, the electro-sensitive smart polymer through a bottom-up approach, was first carried out via reflux (section 3.1.2.1), in a 2 + 1 acetic acid-catalysed condensation with the flexible C_3 linker N',N'-bis(3-aminopropyl)propane-1,3-diamine, **C4**, in ethanol. A very low yield of the black solid was obtained (MCS10_001) and subsequently washed with oxolane and ethoxyethane (MCS10_002). Thus, the reaction mixture was concentrated to 0.1 times of the original volume, via rotary evaporation, after which, addition of ethoxyethane to oversaturation, precipitated the product which was washed with ethoxyethane and dried (MCS10_003). The same monomer combination was also carried out via LAG (section 3.1.2.2), using the same linker ratio as the reflux synthesis, and a series of catalytic solvents (Table 4.22). The condensation of aldehyde and amine groups was expected to result in a 2D imine linked COF (Scheme 4.14).

Table 4.22. Catalytic solvents used in LAG synthesis of MCS10 samples.

Sample Code	Catalytic solvent
MCS10_004	Ethanol + acetic acid drops
MCS10_005	Water + acetic acid drops
MCS10_006	5:1 methanol:ethoxyethane + acetic acid drops
MCS10_007	1:1 1,4-dioxane:1,3,5-trimethylbenzene + acetic acid drops
MCS10_008	Oxolane + acetic acid drops
MCS10_009	1:1 dichloromethane:N,N-dimethylacetamide + acetic acid drops

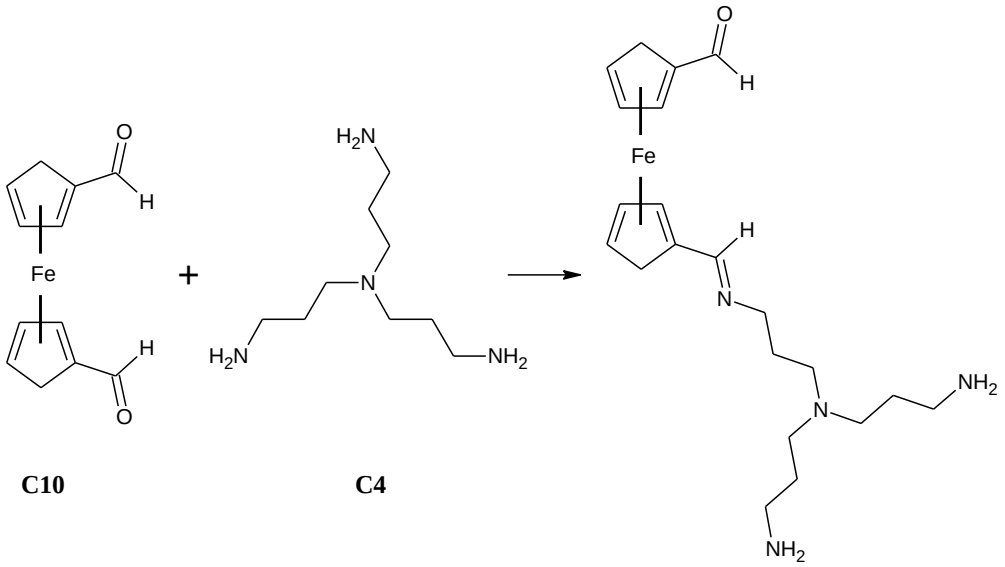

C10 **C4**

Scheme 4.14. The expected imine links formed between monomers **C11** and **C4**.

Similar to MCS9, all the dark brown LAG samples formed a hard glass-like material. The X-ray powder patterns obtained for the MCS10_003, MCS10_006 and MCS10_009 samples show one broad reflection and a high background, typical of amorphous materials (Figure 10.8). No further analysis was carried out for these samples. Laboratory PXRD data collection for the remaining reflux and LAG samples, is currently underway at the time of writing.

4.8.6. MCS11

The first reaction incorporating 4-[(4-aminophenyl)diazenyl]aniline, **C11**, the UV-sensitive smart polymer through a bottom-up approach, was carried out via reflux (section 3.1.2.1), in a 1 + 1 condensation with the bifunctional C_3 linker (3,5-diformylphenyl)boronic acid, **C2**, in 1:1 1,4-dioxane:1,3,5-trimethylbenzene. A 2D imine and boronate anhydride linked COF, exhibiting hexagonal symmetry, was expected to form through the Schiff-base condensation of aldehyde and amine groups, and the self-condensation of boronic acid groups (Figure 4.1, Scheme 4.15). A rust coloured powder was obtained (MCS11_001), washed with oxolane (MCS11_002) and subsequently dried under vacuum (MCS11_003).

The X-ray powder patterns obtained for the three samples show next to no reflections and a high background, representative of amorphous materials (Figure 10.9). No further analysis was carried out.

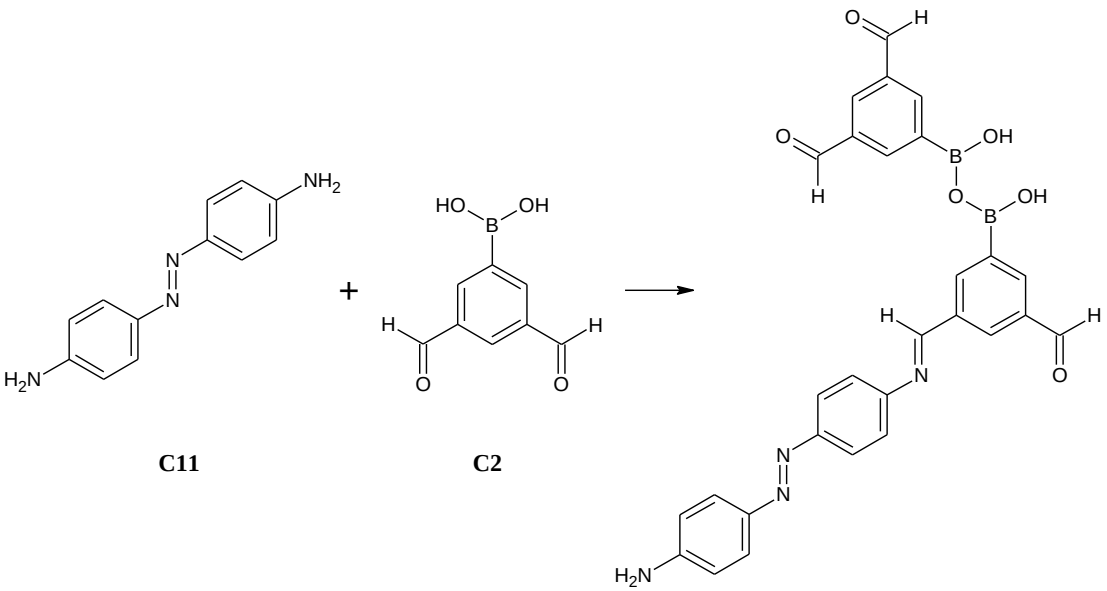

C11 **C2**

Scheme 4.15. The expected imine and boronate anhydride links formed between monomers **C11** and **C2**.

4.8.7. MCS12

The second reaction incorporating the **C11** UV-sensitive smart polymer as part of the framework, was carried out in a 3 + 3 + 1 acetic acid-catalysed condensation with the bifunctional C_3 linker (3,5-diformylphenyl)boronic acid, **C2**, and the C_3 linker triphenylene-2,3,6,7,10,11-hexol hydrate, **C5**, in 1:1 1,4-dioxane:1,3,5-trimethylbenzene, via reflux (section 3.1.2.1). The co-condensation of aldehyde with imine end groups and of boronic acid with dialcohol end groups, was expected to result in the formation of a 2D imine and boronate ester linked COF, exhibiting hexagonal symmetry (Figure 4.6, Scheme 4.16). A black coloured powder was obtained (MCS12_001), washed with oxolane (MCS12_002) and subsequently dried under vacuum (MCS12_003).

The X-ray powder patterns obtained for the three samples similarly show few broad peaks and a high background, indicative of amorphous materials (Figure 10.10). No further analysis was carried out.

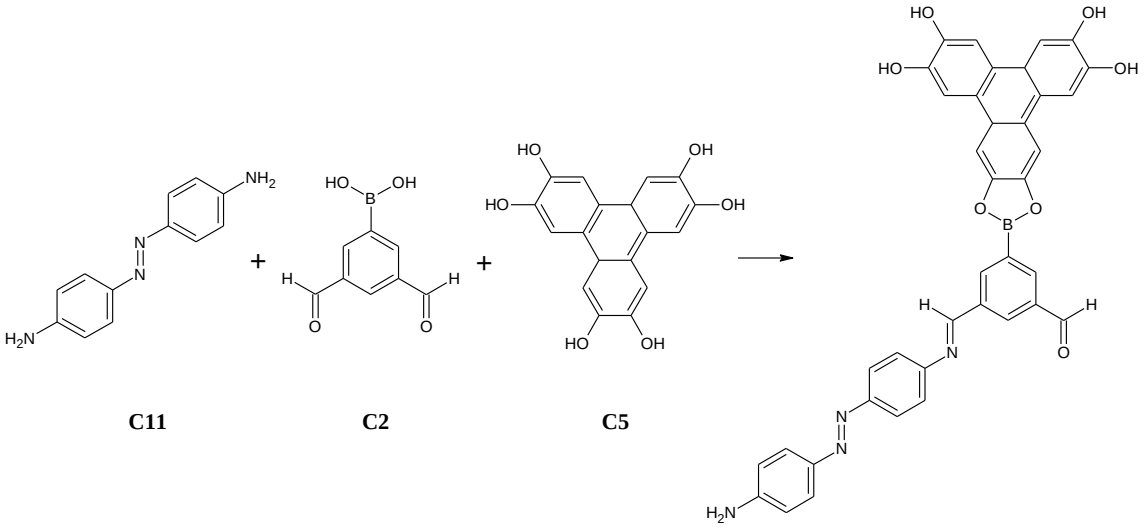

Scheme 4.16. The expected imine and boronate ester links formed between monomers **C11**, **C2** and **C5**.

4.9. Concluding Overview

A total of twelve compounds showing novel diffraction patterns with three different linkages, including the first ever reported potential COF with 1,3,2-dioxaborinane links, were successfully synthesised from four of the fourteen reactions carried out, using two different techniques and multiple solvent environments. A substantial amount of computational work using crystal structure determination software, has led to the characterisation of a new cage-based imine and ester linked extended network, the hexaimine macrobicyclic cryptand, and a new Schiff-base structure exhibiting three separate phases. A number of manuscripts with the above findings are currently being prepared.

The first objective of this thesis was reached, with the characterised cage-based MCS7_017 crystal structure providing an ideal network to be used as the core of the nanocarrier system.

Laboratory PXRD data were collected for the first time for three of the starting monomers, while data for three polymorphs of three other linkers were also collected. These will also be prepared for publication, once crystal structure determination is complete.

5. API Loading

5.1. Design and Loading Parameter Testing

The synthesis, characterisation and crystal structure determination of MCS7_017, identified this product as a cage-based crystalline extended network, with pore size dimensions of 8.962, 8.753 and 4.271 Å. This allowed the testing of its API loading potential for its application as a drug delivery system.

5-fluoro-1H-pyrimidine-2,4-dione, **C14**, is a planar heterocyclic aromatic drug molecule, commonly used to treat cancer. Its largest dimensions of 5.344 and 4.865 Å, are comparable in size to the framework pore dimensions, potentially favouring the molecule's easy diffusion deep into the core network. It has the ability to act as a hydrogen bond donor via its N(–H) atoms and as a hydrogen bond acceptor using its O and F atoms. The post-synthetic loading of **C14** into the cages and onto the surface of the new structure, was thus expected to mainly occur through the formation of strong intermolecular hydrogen bond interactions. This physical adsorption attaches the API molecules to the cage walls and the surface edges of the framework, without chemical modification, such that the desired therapeutic effect is immediate upon release.

The extent of drug loading can be affected by a number of methodology parameters, including solvent, loading time and ratio of framework:API concentration. Hence, several small-scale loading tests were carried out, in order to fine tune the parameters for maximum API loading onto MCS7_017. Loading from an oversaturated methylsulfinylmethane solution of **C14**, was initially designed, due to a high solubility of the API molecule in the solvent. However, the solubility of the framework in this polar aprotic solvent, significantly limited its use. For this reason, the crystallites of the structure were not used in the nanometre range, but as synthesised, in the millimetre range. The framework was found to be soluble in most common laboratory polar organic solvents, possibly due to its high content of nitrogen and oxygen atoms, but largely insoluble in hexane and hexane with oxolane drops. Loading from **C14** solutions in hexane and hexane with oxolane drops was thus tested, for a loading time of 2, 6 and 8 hours. 0.005 and 0.125 g amounts of framework were used per 5 mL volume of the oversaturated solutions. Control tests without **C14**, were carried out to investigate the structural integrity of the crystal structure, under each parameter combination. Upon

collection of the loaded and control framework from solution, laboratory PXRD data were collected to confirm successful **C14** loading into the crystal structure of MCS7_017 and determine the best combination of methodology parameters.

5.2. Characterisation and Analysis

API loading was carried out on the product of a rough scale-up synthesis of MCS7_017. Comparison of the laboratory PXRD data for the scale-up product, MCS7_017SU, with the original powder pattern of MCS7_017, confirms the formation of the same structure (Figure 10.11). The FTIR spectrum for the scale-up product was also the same as the spectrum for the original structure, supporting PXRD analysis that the same imine and ester linked structure was synthesised (Figure 10.12). Once this was confirmed, the above-mentioned loading tests were then carried out.

Comparison of the powder patterns from the control MCS7_017 tests, using hexane (Figure 10.13) and hexane with oxolane drops (Figure 10.14) as solvent, a stirring time of 2, 6 and 8 hours, and 0.005 and 0.125 g amounts of the framework, with the pattern for the original crystal structure, confirms the structural integrity of MCS7_017 under every parameter combination. Patterns for samples from hexane with oxolane drops, were however less crystalline, indicating that the oxolane drops affected the crystal structure. Subsequent comparison of the loaded MCS7_017 samples with the control samples under the same parameter combinations, revealed the presence of slight differences after loading, indicating the inclusion of **C14** molecules within the crystal structure. The most change overall was observed for a loading time of 6 hours, with the larger ratio of framework:API concentration masking any impurities arising during the loading process.

The optimal parameters for maximum drug loading were thus identified as hexane solvent, a loading time of 6 hours and 0.125 g amounts of framework per 5 mL volume of the oversaturated solution. FTIR spectroscopy further provides evidence of successful drug loading, with the 1400-1200 cm^{-1} bands corresponding to C–F stretching, significantly more pronounced in the spectra for the loaded samples (Figure 10.15, Figure 10.16).

Actual API loading (MCS7_077) was thus carried out using a 0.800 g amount of the original structure, from 32 mL of an oversaturated hexane solution of **C14**, for 6 hours.

Figure 5.1 shows the material obtained after actual drug loading, upon reflection of plane polarised light.

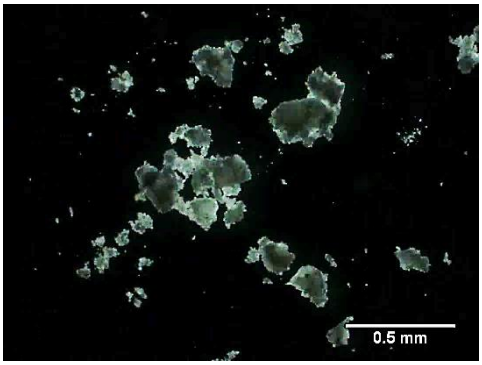

Figure 5.1. Photomicrograph of MCS7_077 from API loading.

Just like the powder patterns discussed above, for loading test samples, the pattern for MCS7_077 is the same as that of the original crystal structure, but with slight differences (Figure 5.2). New peaks are present at ~ 22.07°, 23.15°, 26.42° and 28.97°, while original reflections at 24.01°, 26.38° and 29.76° are missing. Moreover, the intensity of peaks at 17.70°, 18.65°, 19.51°, 21.67°, 23.46°, 24.63°, 27.10°, 28.19° and 31.51° is noticeably different. This demonstrates that the framework is structurally flexible, adapting its unit cell parameters and hence its atomic coordinates respectively, to accommodate the loaded API molecules into the structure, within the unit cell. This is similarly supported by FTIR C–F stretching bands at 1400-1200 cm^{-1}, for MCS7_077 (Figure 5.3).

A value for the loading capacity could not be calculated from the UV-Vis spectra of the supernatant solution before and after loading, since loading was carried out from an oversaturated solution of the API. A quantifiable investigation using STA, will be carried out to determine the loading capacity of the MCS7_017 structure. A BET pore surface analyser will be used to obtain nitrogen gas adsorption isotherms for the original and loaded structures, to assess the reduction in surface area and available unoccupied volume of the cages of the framework. X-ray microscopy (XRM) on the original and loaded fragments, will also be carried out to investigate differences between the surfaces of the two samples.

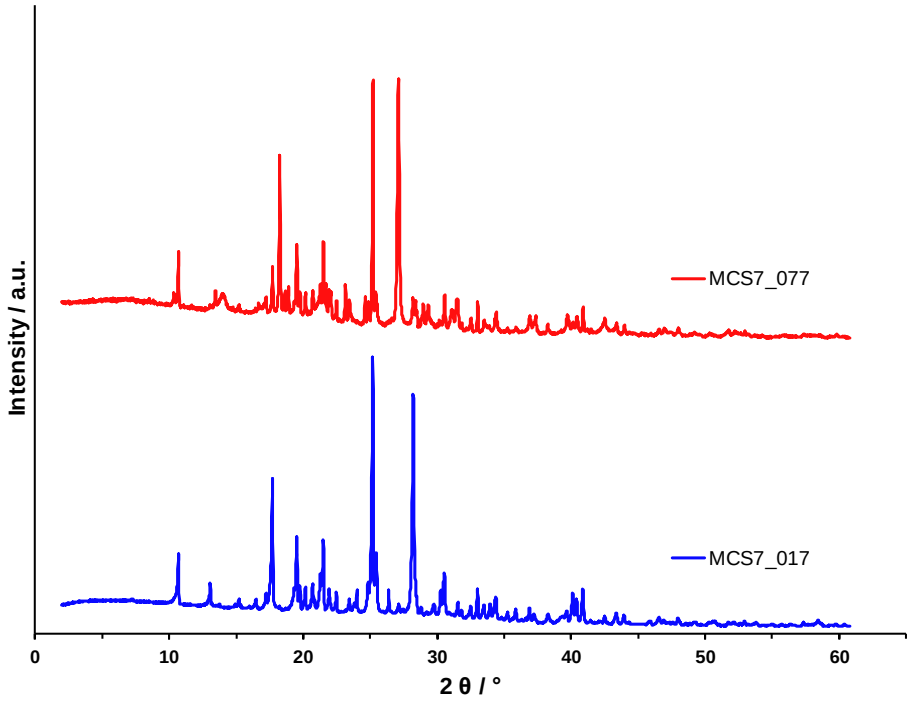

Figure 5.2. Laboratory PXRD patterns for the original MCS7_017 structure (blue) and the drug loaded MCS7_077 (red), obtained from a 4 + 2 + 9 condensation of **C6**, **C7** and **C8**, via LAG in a catalytic amount of 1:1 1,4-dioxane:1,3,5-trimethylbenzene, and upon loading of **C14** onto MCS7_017 from an oversaturated hexane solution via stirring for 6 hours, respectively, at 293 K.

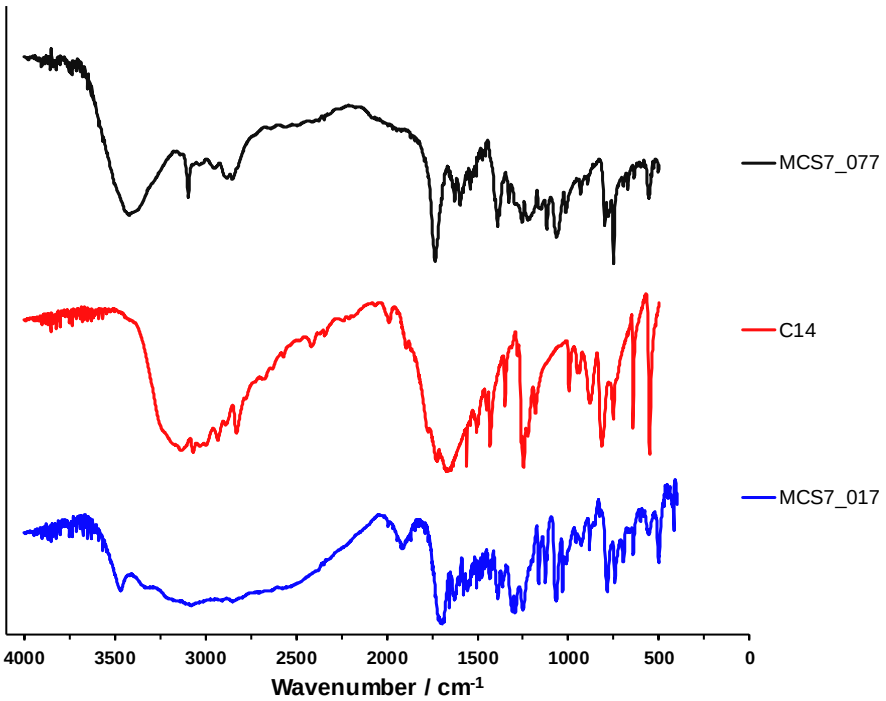

Figure 5.3. FTIR spectra for the original MCS7_017 structure (blue), obtained from a 4 + 2 + 9 condensation of **C6**, **C7** and **C8**, via LAG in a catalytic amount of 1:1 1,4-dioxane:1,3,5-trimethylbenzene, the pure API **C14** (red), and the drug loaded MCS7_077 (black), obtained upon loading of the API onto MCS7_017 from an oversaturated hexane solution via stirring for 6 hours.

5.3. Concluding Overview

Loading of **C14** into the new cage-based MCS7_017 crystal structure, was successfully achieved, after loading parameter optimisation. The API loading carried out on this structure, demonstrates the application of COFs as nanocarriers in drug delivery systems, for use in the field of therapeutics. These findings are currently being prepared as part of a manuscript.

The second objective of this thesis was reached, with the COF-API conjugate, MCS7_077, providing a suitable model to transform the passive targeting conjugate into the smart stimuli-responsive system.

6. Conjugation of Smart Stimuli-Responsive Polymers

6.1. Design and Conjugation

The synthesis of the COF-API conjugate, MCS7_077, allowed the testing of its smart polymer conjugation potential for its application as a controlled-release drug delivery system.

Pyridine-2,6-dicarbaldehyde, **C9**, is a small planar heterocyclic aromatic molecule (Table 6.1). It has two O atoms and one N atom through which it can accept hydrogen bonds. Similarly, the larger organometallic sandwich molecule, 1,1'-ferrocenedicarboxaldehyde, **C10**, has two O atoms which are able to act as hydrogen bond acceptors (Table 6.1). The planar aromatic molecule, 4-[(4-aminophenyl)diazenyl] aniline, **C11**, has the ability to act as a hydrogen bond donor via its N(–H) atoms and as a hydrogen bond acceptor using its azo N atoms (Table 6.1). These three smart molecules can additionally form π-π interactions, due to their aromaticity.

Table 6.1. Molecular structures of the smart stimuli-responsive molecules.

C9	Pyridine-2,6-dicarbaldehyde	pH sensitive	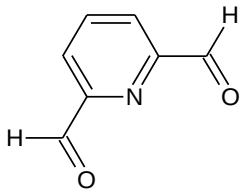
C10	1,1'-ferrocenedicarboxaldehyde	Electro sensitive	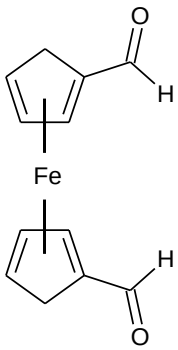
C11	4-[(4-aminophenyl) diazenyl]aniline	UV sensitive	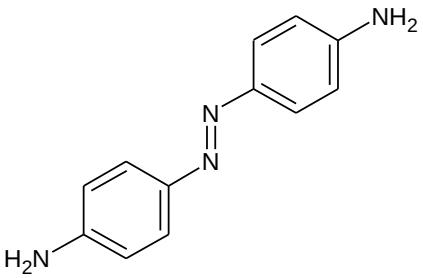

The post-synthetic conjugation of pH sensitive **C9**, electro sensitive **C10**, and UV sensitive **C11**, onto the surface of the new conjugate, to form the corona of the nanocarrier system, was thus expected to occur through the formation of intermolecular π-π and hydrogen bond interactions. This physical adsorption attaches the smart molecules to the surface edges of the COF-API conjugate, without affecting their ability to accurately detect and respond to stimuli. The corona is expected to block the cages and channel-doors of the structure, in such a way as to effectively trap the loaded API molecules inside the core of the COF-API-Polymer complex, until it is activated by a specific stimulus, triggering drug release.

The extent of smart molecule conjugation can be affected by the same parameters discussed in section 5.1. The optimal parameters identified for maximum drug loading, were thus employed for smart molecule conjugation (hexane solvent, a loading time of 6 hours and 0.125 g amounts of conjugate per 5 mL volume of oversaturated solution of **C9** (MCS7_080), **C10** (MCS7_082), and **C11** (MCS7_085)), since adsorption of the molecules is expected to take place via a similar mechanism. A control test without any of the smart molecules, was also carried out to investigate the structural integrity of the conjugate, under conjugation conditions. Upon collection of the conjugated and control conjugate from solution, laboratory PXRD data were collected according to the specifications listed in section 3.4.1, to confirm successful smart molecule conjugation onto the surface of conjugate particles.

6.2. Characterisation and Analysis

Figure 6.1 shows the material obtained after smart molecule conjugation, upon reflection of plane polarised light. Upon visual comparison of the resulting cream, pink and orange coloured samples respectively, with the white coloured original MCS7_017 and drug loaded MCS7_077 samples (Figure 6.2), it is evident that conjugation of the brown, dark red and orange coloured smart molecules, was successful.

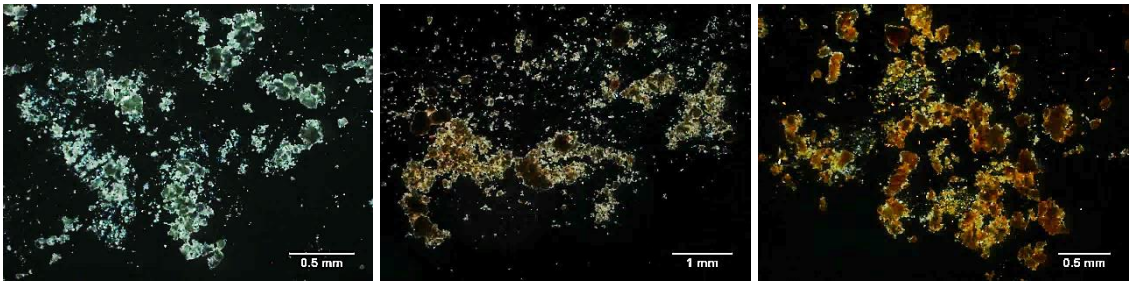

Figure 6.1. Photomicrographs of MCS7_080 (left), MCS7_082 (centre) and MCS7_085 (right) from conjugation of pH, electro, and UV responsive smart molecules respectively.

Figure 6.2. Change in colouration from the white coloured original MCS7_017 and drug loaded MCS7_077, and the cream coloured MCS7_080, pink coloured MCS7_082 and orange coloured MCS7_085, from conjugation of pH, electro, and UV responsive smart molecules respectively (left to right).

Comparison of the X-ray powder pattern for the control with the pattern for the drug loaded MCS7_077 structure, confirms that the COF-API conjugate is structurally integrous under conjugation conditions. This indicates that during conjugation, the previously-loaded drug molecules were not released. Patterns for MCS7_080 (Figure 6.3), MCS7_082 (Figure 6.4) and MCS7_085 (Figure 6.5), are the same as that of the conjugate, but with slight differences after conjugation. The powder pattern for MCS7_080 shows different peak intensities at 17.70°, 23.15°, 25.42° and 28.19°, and is missing reflections at 22.08° and 28.95°. These differences can be attributed to different unit cell parameters and atomic coordinates, indicating **C9** molecule inclusion within the crystal structure. However, these observed changes counter some of the differences recorded for drug loading at the same 2 θ angles, which might indicate potential partial API molecule release from MCS7_080 aided by the presence of the smart molecule, and a reversible breathing effect of the framework.

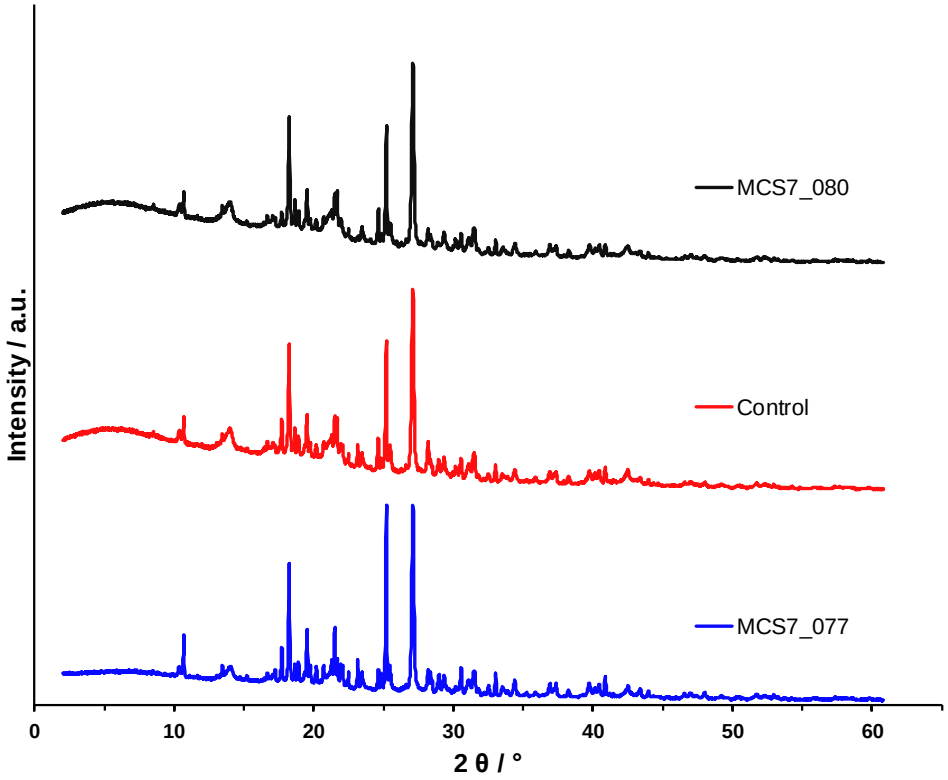

Figure 6.3. Laboratory PXRD patterns for the API loaded MCS7_077 structure (blue), the control (red) and the pH responsive smart molecule conjugated MCS7_080 (black), obtained via stirring of MCS7_017 in oversaturated hexane solution of **C14**, MCS7_077 in hexane solvent, and MCS7_077 in oversaturated hexane solution of **C9**, respectively, using a conjugation time of 6 hours, and 0.125 g amounts of the drug loaded structure, at 293 K.

The pattern for MCS7_082 shows new peaks at 22.23°, 23.42°, 23.56°, 32.38°, 32.80° and 33.33°, and different peak intensities at 17.71°, 21.68°, 28.19°, 29.98° and 42.50°. Reflections at 13.99°, 22.09°, 23.16° and 28.95° are missing. The presence of new peaks demonstrates that the unit cell parameters are modified for the second time, suggesting the inclusion of **C10** molecules within the crystal structure. Similar to MCS7_080, some of the differences counter those observed for MCS7_077, which might indicate the potential partial release of loaded drug molecules or the rearrangement of loaded molecules within the unit cell.

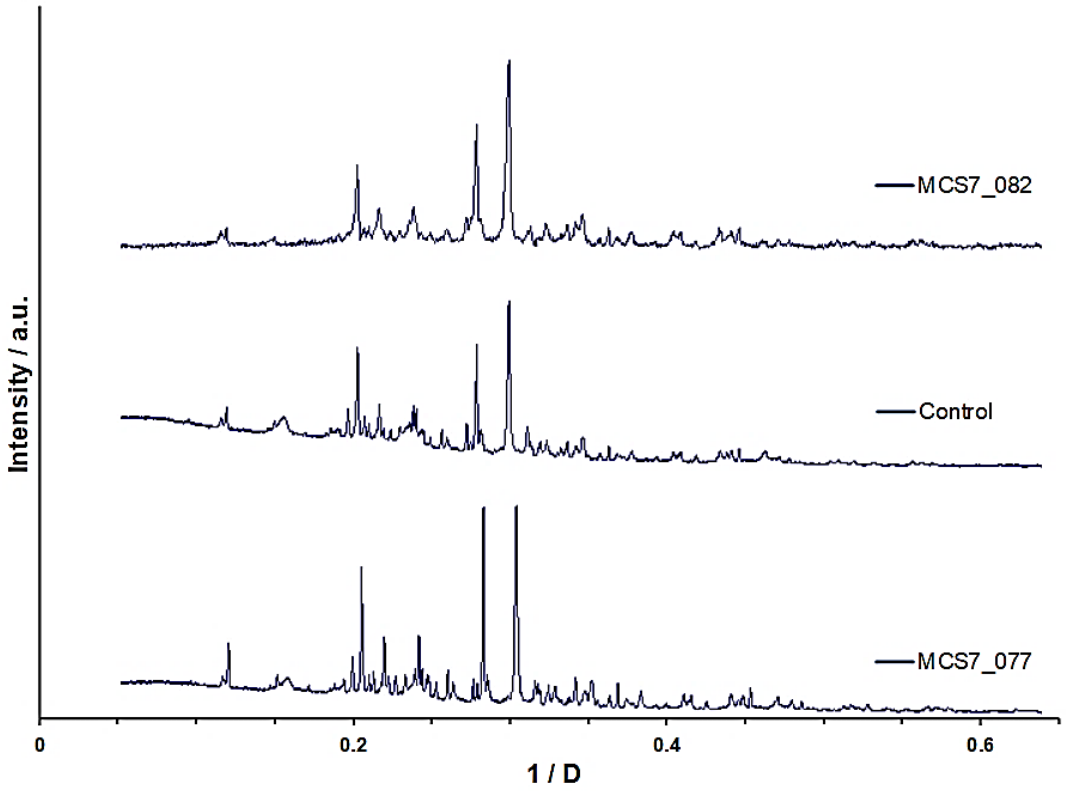

Figure 6.4. Laboratory PXRD patterns for the API loaded MCS7_077 structure (bottom), the control (middle) and the electro responsive smart molecule conjugated MCS7_082 (top), obtained via stirring of MCS7_017 in oversaturated hexane solution of **C14**, MCS7_077 in hexane solvent, and MCS7_077 in oversaturated hexane solution of **C10**, respectively, using a conjugation time of 6 hours, and 0.125 g amounts of the drug loaded structure, at 293 K. [202]

The pattern for MCS7_085 shows a new peak at 20.03° and different reflection intensities at 22.06°, 23.16° and 28.98°. This once again demonstrates an adjustment of the unit cell parameters and atomic coordinates, which could be attributed to the potential inclusion of **C11** molecules and partial release or rearrangement of API molecules within the unit cell.

The small size of the smart molecules, comparable to the cage dimensions of the original structure, could have potentially led to their diffusion into the pores of the framework, in addition to their successful conjugation onto the surface as part of the corona.

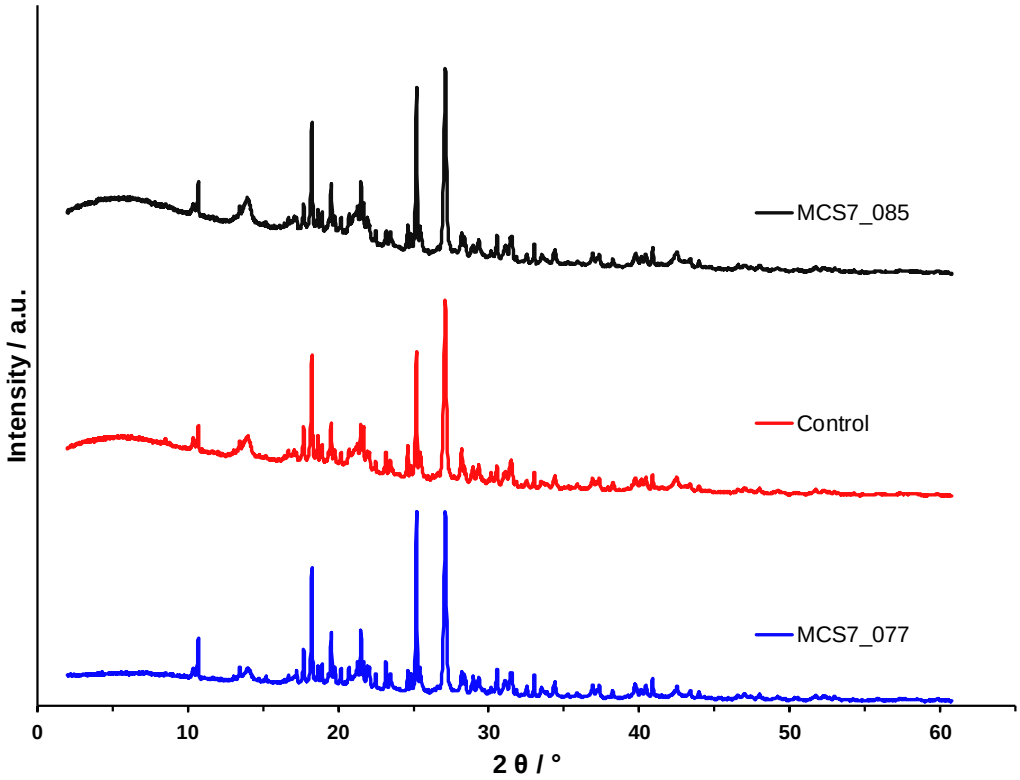

Figure 6.5. Laboratory PXRD patterns for the API loaded MCS7_077 structure (blue), the control (red) and the UV responsive smart molecule conjugated MCS7_085 (black), obtained via stirring of MCS7_017 in oversaturated hexane solution of **C14**, MCS7_077 in hexane solvent, and MCS7_077 in oversaturated hexane solution of **C11**, respectively, using a conjugation time of 6 hours, and 0.125 g amounts of the drug loaded structure, at 293 K.

The FTIR spectra for MCS7_080 (Figure 6.6) and MCS7_082 (Figure 6.7), were identical to the spectrum for MCS7_077. The characteristic C=O stretching band of the aldehyde end groups of **C9** and **C10** (1720-1680 cm^{-1}), coincides with the same stretching band (1720-1700 cm^{-1}) of the aromatic ester link of the framework. Furthermore, the M–C stretching band for **C10** at 475 cm^{-1}, falls outside the recorded wavenumber range. Similarly, the spectrum for MCS7_085 (Figure 6.8) was also identical to that of the conjugate, and could not provide evidence of successful smart molecule conjugation. The characteristic azo N=N stretching band of **C11** (1384 cm^{-1}), is found at the same wavenumber range as the C–F stretching band from the conjugate. Therefore, FTIR spectroscopy could not be used to support PXRD analysis.

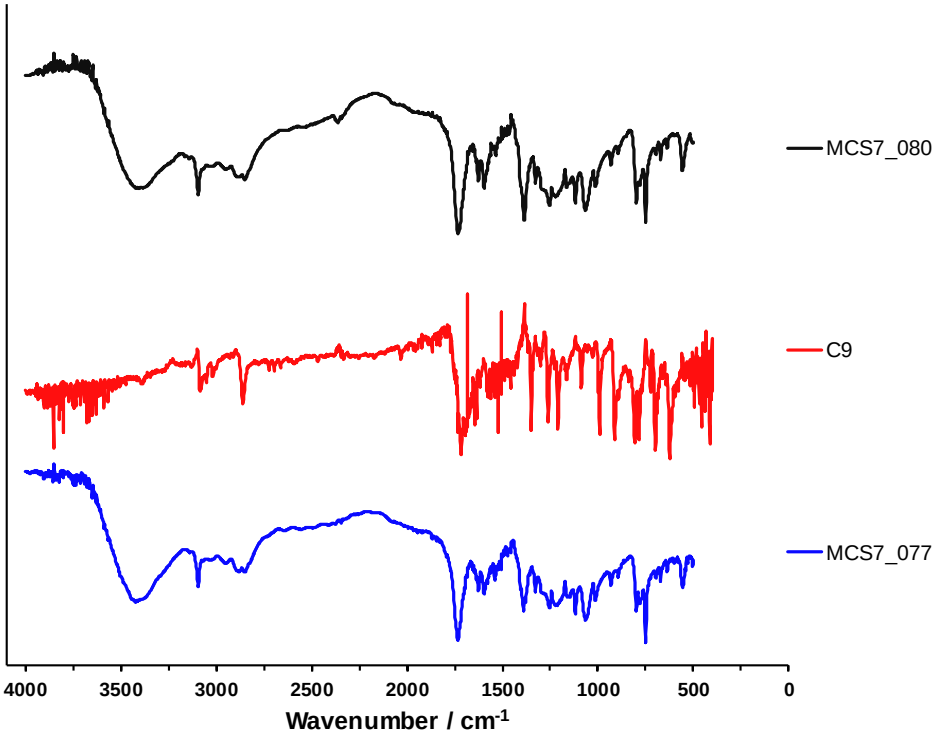

Figure 6.6. FTIR spectra for the API loaded MCS7_077 structure (blue), obtained via stirring of MCS7_017 in oversaturated hexane solution of **C14** for 6 hours, **C9** (red), and the pH responsive smart molecule conjugated MCS7_080 (black), obtained via stirring of MCS7_077 in oversaturated hexane solution of **C9** for 6 hours.

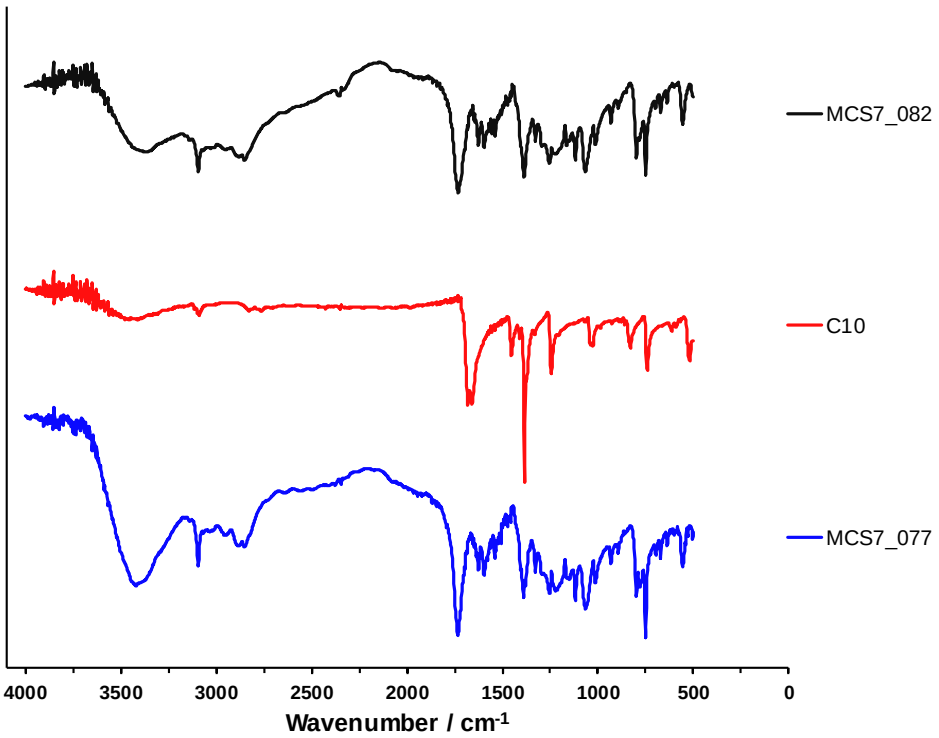

Figure 6.7. FTIR spectra for the API loaded MCS7_077 structure (blue), obtained via stirring of MCS7_017 in oversaturated hexane solution of **C14** for 6 hours, **C10** (red), and the electro responsive smart molecule conjugated MCS7_082 (black), obtained via stirring of MCS7_077 in oversaturated hexane solution of **C10** for 6 hours.

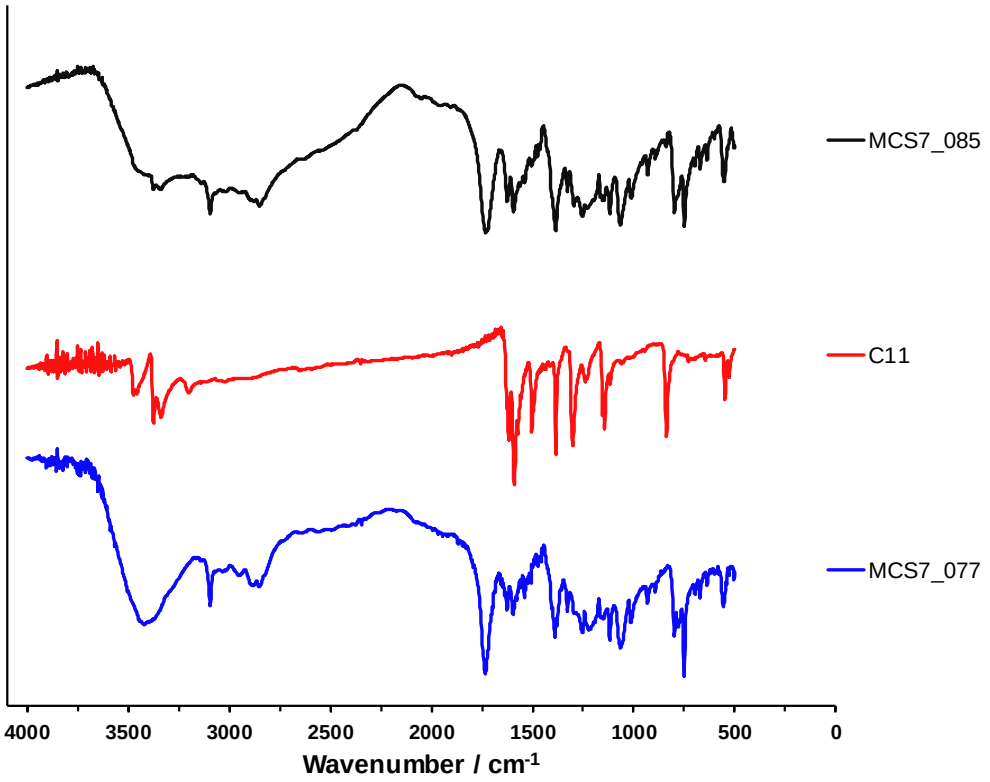

Figure 6.8. FTIR spectra for the API loaded MCS7_077 structure (blue), obtained via stirring of MCS7_017 in oversaturated hexane solution of **C14** for 6 hours, **C11** (red), and the UV responsive smart molecule conjugated MCS7_085 (black), obtained via stirring of MCS7_077 in oversaturated hexane solution of **C11** for 6 hours.

Investigations using STA and BET pore surface analyser will be carried out to determine the extent of smart molecule conjugation and possible partial unloading of the API molecules, to confirm whether the smart molecules diffused into the structure, and to check if the surface conjugated smart molecules effectively block the cages and channel-doors of the framework.

XRM data will be collected for these three COF-API-Polymer complexes and compared with data for the COF-API conjugate and for the original structure. All five samples will eventually be sent to our collaborators abroad, in Limerick, Ireland, for scanning electron microscopy (SEM), to further compare the differences between the surface and core of the samples, and to investigate whether the smart molecules are surface conjugated or pore loaded.

6.3. Concluding Overview

Post-synthetic conjugation of pH sensitive **C9**, electro sensitive **C10**, and UV sensitive **C11**, onto the surface of the COF-API carrier, was carried out. The final COF-API-Polymer complexes, MCS7_080, MCS7_082 and MCS7_085, feature the complete designed construct, as smart stimuli-responsive drug delivery systems, thus fulfilling the third objective of this thesis. This smart molecule conjugation, demonstrates that COFs can be employed to synthesise intelligent drug-nanocarrier systems, which go beyond the passive targeting nanocarrier applications reported in literature thus far. These findings are also currently being prepared as part of a manuscript for publication.

7. Drug Release Profile

7.1. Design

The sensitivity and responsiveness of the final COF-API-Polymer complexes, MCS7_080, MCS7_082 and MCS7_085, to the respective target stimulus, determines their potential application as drug delivery systems with controlled-release technology (CRT).

As discussed in section 3.5, the release pattern of the loaded drug is dependent on several factors. The acid-labile imine links in the core of the carrier, themselves impart a certain degree of pH responsiveness, accelerating drug release, due to framework degradation. Additionally, at neutral or acidic pH, the loaded API molecules are positively charged, by ionisation at the O atoms. Similarly, the N atoms in the framework may become protonated in acidic pH. Upon ionisation, the intermolecular hydrogen bond interactions between the cage walls and the drug molecules were expected to become weaker, resulting in an easier diffusion of drug molecules through the matrix and a quicker release profile in acidic pH.

Upon protonation of **C9** in acidic pH 4.9 and oxidation of **C10** by iron (III) sulfate, the smart molecules (Table 6.1) were expected to become hydrophilic, undergoing structural rearrangement and resulting in an increased solubility of the whole complex in simulated physiological conditions. Conversely, the *trans* to *cis* isomerisation of **C11** by UV irradiation, was expected to result in the conformational rearrangement of the surface conjugated smart molecules, without increasing the solubility of the complex. These changes would trigger an even faster escape of the loaded API molecules, such that drug release was expected to occur at an increased rate upon application of the target stimulus to each of the complexes. The smart final complexes were thus expected to exhibit better control on the release of guest molecules, than the COF-API conjugate, due to their potentially more accurate detection of acidic pH, oxidising conditions and UV irradiation.

The drug release properties of the three final complexes were tested under control conditions and under application of the target acidic pH, oxidising conditions and UV irradiation stimulus, for each of the samples respectively. The release profile of the COF-API conjugate was also tested under control conditions, for comparability purposes. The

potential degradation of the core under simulated physiological conditions, was assessed through another 'release' study on the pure crystal structure.

7.2. Release Profile for the COF-API Conjugate

Figure 7.1 shows a typical set of UV-Vis spectra obtained from the release studies (Figure 10.18 – Figure 10.23). The UV-Vis results for the drug loaded framework revealed that λ_{max} at 223 and 271 nm, did not match the absorbance maximum at 266 nm, for **C14**. [203] The release study on the pure crystal structure also presented the same maxima (Figure 10.17), indicating that instead of monitoring the release of the loaded drug molecules, framework dissolution or degradation was being recorded. After measuring a series of concentrations for the starting monomers, it was determined that the absorbance maxima from the release studies, were identical to those of **C8** (Figure 10.24), the carboxylic acid linker. The structural instability of the cage-based imine linked framework in simulated physiological conditions, was thus confirmed. This degradation can be advantageous with respect to its application as a drug carrier. It limits the carrier's impact on the body, where it would have been broken down and eliminated, as well as the impact on the environment, where many materials and nanoparticles can persist for a long time and lead to immunologic reactions and eco-toxicological risks, through bioaccumulation across food chains.

Due to framework degradation, UV-Vis spectroscopy could not be used to directly measure the concentration of drug released. Nonetheless, since drug molecules are released upon framework degradation, the UV-Vis results can still provide a valid assessment of the carriers' sensitivity and response to stimuli, assuming that both processes follow the same profile. The calibration curve for **C8** (Figure 10.25) was used in conjunction with the Beer-Lambert law ($A = \varepsilon cl$) (section A3.1), to calculate release profiles under control and stimuli conditions, based on UV-Vis absorbance values.

Comparison of the release profile for the pure crystal structure with the profile for the COF-API conjugate (Figure 7.2), revealed a faster initial release for the drug loaded carrier, indicating that the loaded API molecules could have sped up the rate of framework degradation. At 12 hours, a 22.8 % increase in release is observed for the COF-API conjugate. However, both started to level off at 4 hours.

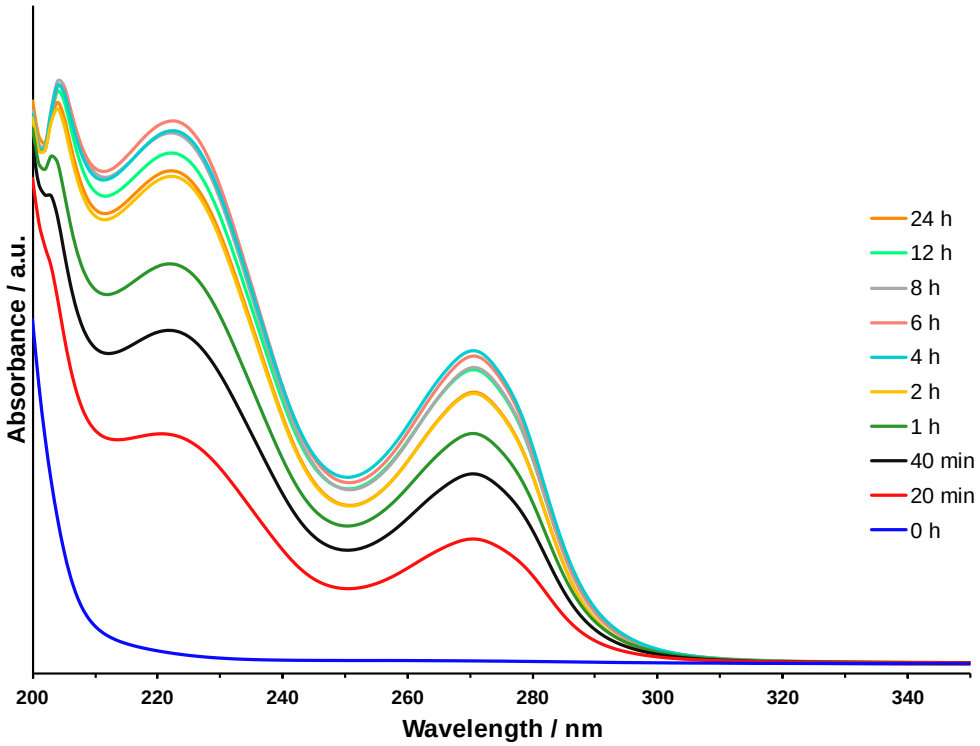

Figure 7.1. UV-Vis spectra for the release study on MCS7_077, obtained upon loading of **C14** onto MCS7_017, in PBS pH 7.4, at time 0, 20 min, 40 min, 1, 2, 4, 6, 8, 12 and 24 hours.

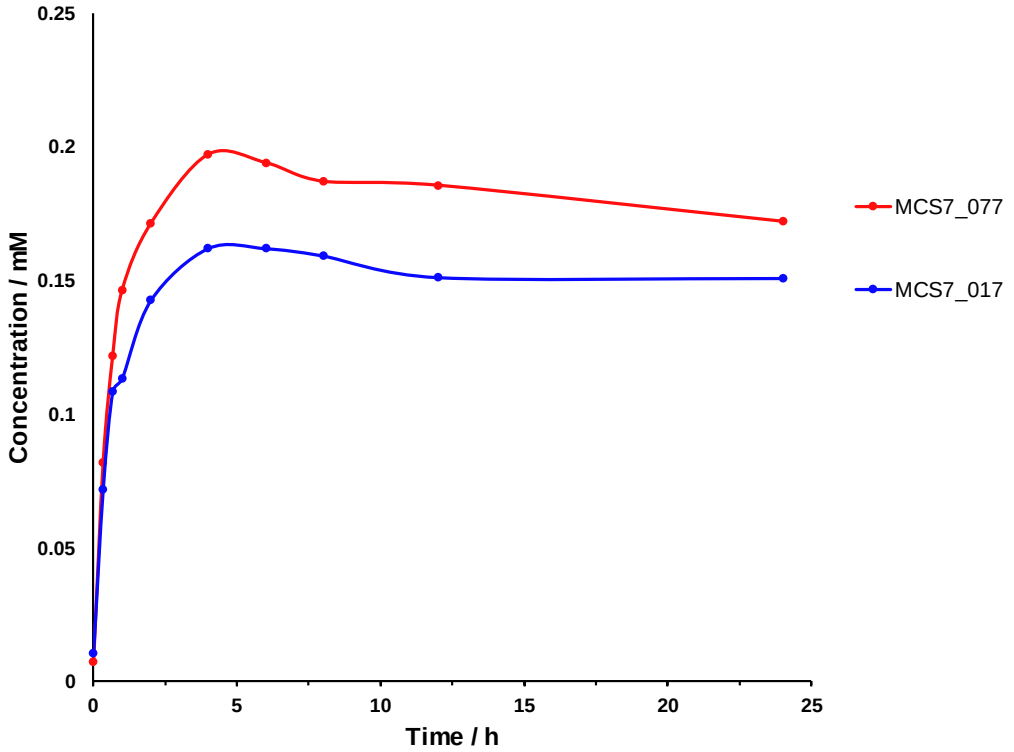

Figure 7.2. Release profiles for MCS7_017 (blue), obtained from a 4 + 2 + 9 condensation of **C6**, **C7** and **C8**, via LAG in a catalytic amount of 1:1 1,4-dioxane:1,3,5-trimethylbenzene, and MCS7_077 (red), obtained upon loading of **C14** onto MCS7_017, in PBS pH 7.4.

7.3. pH Responsive Release

Comparison of the release profiles for the pH sensitive complex under acidic pH 4.9 and control pH 7.4, with the profile for the COF-API conjugate at pH 7.4, indicated that release was 44.3 % lower for the **C9** conjugated complex at pH 7.4, while at pH 4.9 release was comparable to that for the COF-API carrier (Figure 7.3). This demonstrates that the surface conjugated smart molecule has a significant effect on the release profile. The final complex is expected to be larger in size than its precursor, due to its smart molecule corona. The surface conjugated smart molecules could be blocking the cages and channel-doors of the structure, and covering the core itself, in such a way as to effectively trap the loaded API molecules inside a protected core. This makes the complex less prone to attack by solvent, resulting in a slower release.

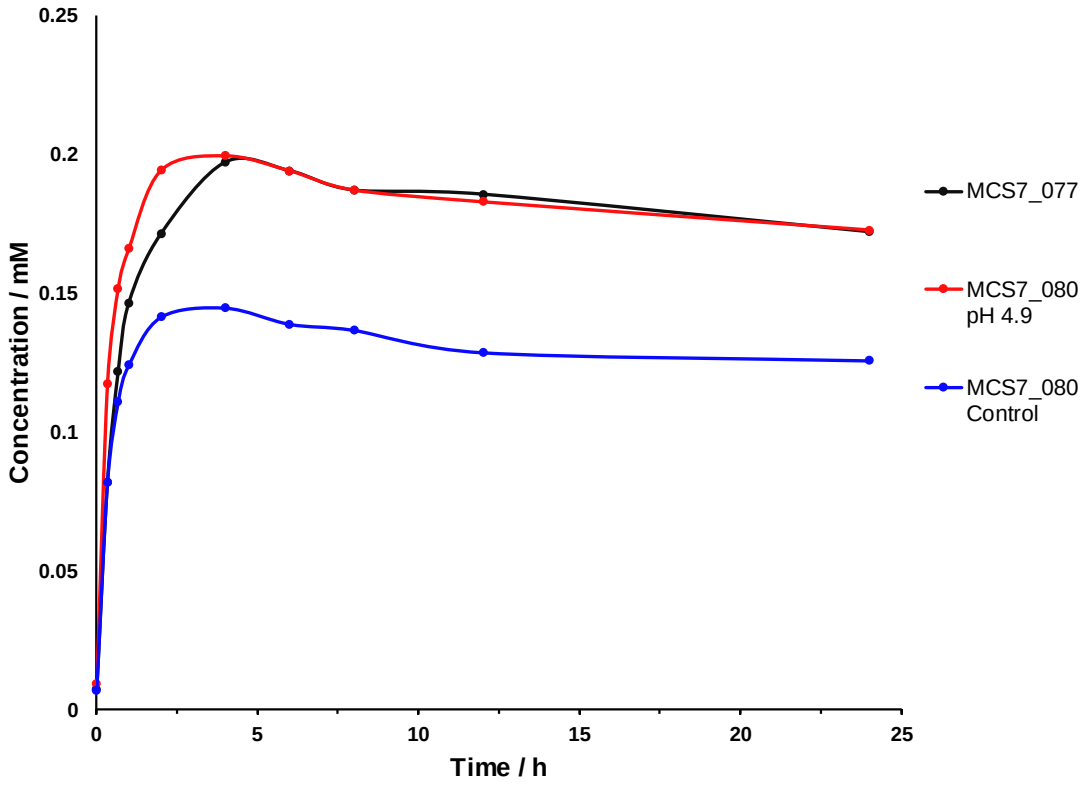

Figure 7.3. Release profiles for MCS7_080, obtained upon loading of **C9** onto MCS7_077, in PBS pH 7.4 (Control – blue) and pH 4.9 (red), compared with the release profile for MCS7_077 (black), obtained upon loading of **C14** onto MCS7_017, in PBS pH 7.4.

At pH 7.4, the pH sensitive molecule remains unprotonated and thus inactivated. However, at the target stimulus, pH 4.9, the smart molecule is activated by protonation,

to become positively charged. This increases the solubility of the whole complex and generates electrostatic repulsion between the surface conjugated molecules, making the carrier more susceptible to release. At 12 hours, a 42.2 % higher release is observed at pH 4.9 than at pH 7.4. Release starts to level off after just 2 hours, two hours earlier than for the COF-API conjugate.

7.4. Electro Responsive Release

A similar pattern for the release profiles of the electro sensitive complex under oxidising and control conditions, was obtained (Figure 7.4). Release for the inactivated smart complex was 18.4 % lower than for the COF-API conjugate, confirming once again the physical effect of the surface conjugated smart molecule on the release profile, as discussed in section 7.3.

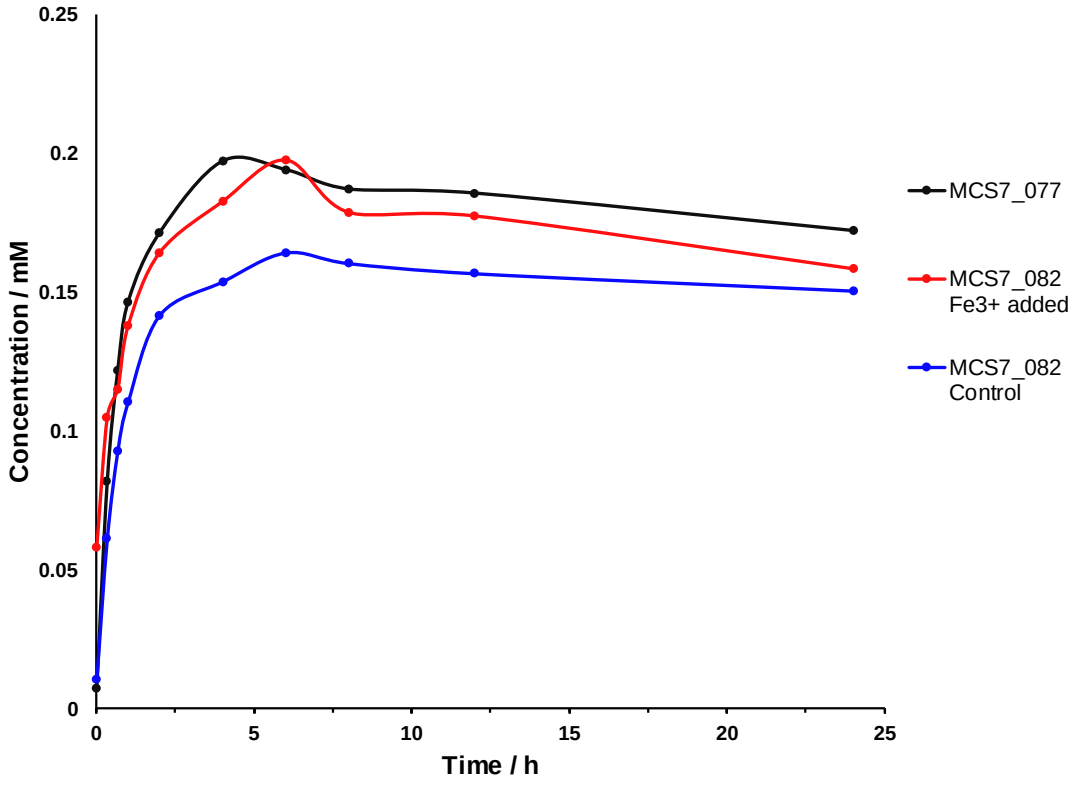

Figure 7.4. Release profiles for MCS7_082, obtained upon loading of **C10** onto MCS7_077, in PBS pH 7.4, without addition of Fe^{3+} (Control – blue) and with addition of Fe^{3+} (red), compared with the release profile for MCS7_077 (black), obtained upon loading of **C14** onto MCS7_017, in PBS pH 7.4.

Chemical oxidation of **C10** by 1.5-fold molar excess of iron (III) sulfate, is a rapid process, with 90 % oxidation to ferrocenium cations taking place in less than 20 minutes. [204] This was reflected in a faster initial release upon the addition of Fe^{3+} and a 13.2 % higher release at 12 hours, over the control. The positively charged corona increases the solubility of the whole complex in PBS, while potentially weakening the physical adsorption of the smart molecules to the surface, exposing the core to the surrounding environment and triggering release. Levelling off takes two hours longer for this complex, than for the COF-API conjugate.

7.5. UV Responsive Release

Unlike the other studies, the beaker for these two release experiments could not be covered by parafilm or glass to limit evaporation of the 100 mL external PBS, as both materials were found to block UV irradiation. Only release values up to 8 hours were considered for the release profile, as during the experiments, PBS evaporation became much more apparent after this point and created erroneous values for the calculated concentrations for time 12 and 24 hours.

Additionally, a different release pattern was observed for the UV sensitive complex, when comparing the release profiles under UV irradiation and control conditions, with the profile for the COF-API carrier (Figure 7.5). Only a 0.9 % decrease in release was recorded for the *trans* conformation **C11** conjugated complex, over the COF-API conjugate. This indicates that this smart molecule did not effectively protect the drug loaded core of the complex from the surrounding environment, resulting in a minimal effect on the release profile.

Upon UV irradiation at 365 nm, the target stimulus, the smart molecule is activated via *trans* to *cis* isomerisation. An 89 % structural change to the *cis* isomer takes places within 3 hours. [185] This was recorded as a continued release up to 4 hours, which had already levelled off under control conditions. A 20.9 % increase in release over the control, is observed at 8 hours. The conformational rearrangement of the **C11** corona could potentially unblock the cages of the framework and expose the loaded core, making it more susceptible to release.

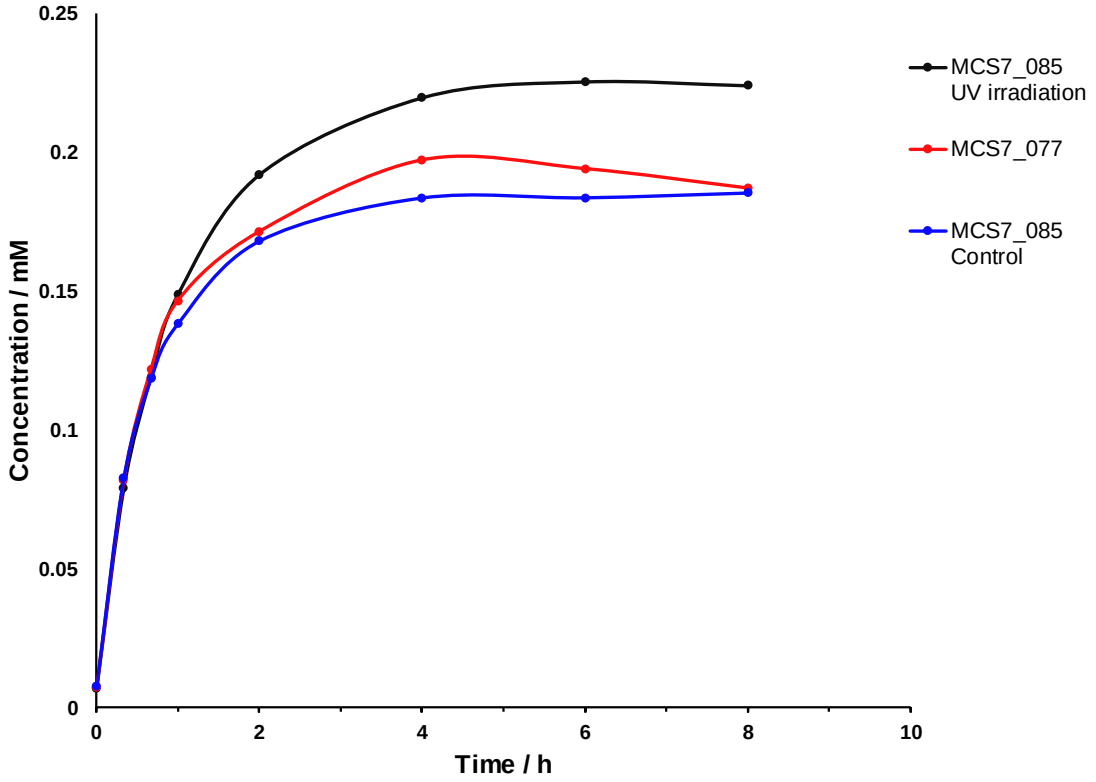

Figure 7.5. Release profiles for MCS7_085, obtained upon loading of **C11** onto MCS7_077, in PBS pH 7.4, without UV irradiation (Control – blue) and under UV irradiation (black), compared with the release profile for MCS7_077 (red), obtained upon loading of **C14** onto MCS7_017, in PBS pH 7.4.

7.6. Concluding Overview

The conjugation of smart stimuli-responsive molecules effectively controlled the drug release and framework degradation of the final complexes, through an improved stability at control conditions and faster and higher release upon application of the target stimulus. The extent of control depends on the identity of the conjugated smart molecule and corresponding stimulus. The pH sensitive smart complex exhibited double the control on the amount released than the electro and UV sensitive complexes, while the electro responsive complex demonstrated a sustained release for longer than the pH and UV sensitive complexes.

One major error which was overlooked during the design of this experimental procedure, was the size of the fragments chosen for release studies. Larger fragments protect the inside bulk for longer, inadvertently affecting the release profile. A maximum

of three fragments, weighing up to 0.005 g in total were used. Nonetheless, the difference in fragment size is unaccounted for.

The application of COF-API-Polymer complexes as drug delivery systems with CRT was demonstrated, with a sustained and/or enhanced release response at the target stimulus. This will add to the contribution to knowledge in a largely unexplored area of COF controlled release systems. An investigation into the rate of release/degradation will be carried out on the dried powder collected from the evaporated aliquots using PXRD and STA. The possibility to collect real time powder diffraction data after adequate adaptation of the experimental conditions will also be explored, to monitor the structural changes taking place upon application of different stimuli. Furthermore, measurement of the zeta potential, specifically before and after activation of the smart pH and electro sensitive coronas, could provide the magnitude of surface charge density.

8. Conclusion and Further Work

The designed COF synthetic reactions, MCS6, MCS7, MCS8, MCS14, yielded twelve crystalline materials with distinctive diffraction patterns, and corresponding FTIR spectroscopy and hot stage microscopy results supporting the formation of new covalent links. The modification of unit cell parameters and atomic coordinates of the fully characterised cage-based imine and ester linked framework, MCS7_017, confirms the loading of the API, 5-fluoro-1H-pyrimidine-2,4-dione, **C14**, and the conjugation of the smart pH, electro and UV sensitive molecules, pyridine-2,6-dicarbaldehyde, **C9**, 1,1'-ferrocenedicarboxaldehyde, **C10**, and 4-[(4-aminophenyl)diazenyl]aniline, **C11**, respectively, into the pores and onto the surface of the new COF structure. Sustained and/or enhanced drug release *in vitro* of the final COF-API-Polymer complexes, MCS7_080, MCS7_082 and MCS7_085, at the target stimulus, demonstrates the application of COFs as stimuli-responsive nanocarriers in drug delivery systems.

This research work has a number of strengths and limitations. The chemical instability of the cage-based crystalline extended network in polar solvents prevented the loading and conjugation of **C14**, and **C9**, **C10** and **C11** respectively, from solvents in which the molecules are highly soluble. The API loading capacity of the framework and the extent of smart molecule conjugation on the COF-API conjugate could not be calculated from the UV-Vis spectra of the supernatant solution before and after loading or conjugation respectively, due to the low solubility of the molecules in hexane and the subsequent use of their oversaturated solutions. Nonetheless, this ensured the highest API loading and smart molecule conjugation possible, under the identified optimal parameters, owing to the large framework:API and conjugate:smart molecule ratios. One notable variable which could not be controlled during the smart polymer conjugation phase of this project, was the potential partial API molecule release from, or displacement by the stimuli-responsive molecules in, the COF-API conjugate.

Framework degradation also significantly restricted the effectiveness of the drug release studies in simulated physiological conditions, speeding up the release of the API, disrupting longer sustained release, and impeding the direct monitoring of the concentration of drug released via UV-Vis spectroscopy. Despite this, a valid quantitative assessment of the final complexes' sensitivity and response to stimuli was still determined from the UV-Vis results, assuming that the release of drug molecules followed the same

profile alongside the framework degradation process. This degradation can be considered beneficial with respect to the application of COFs as nanocarriers in drug delivery systems, as it spares the body from needing to break down the carrier for elimination, in effect limiting the impact on the body as well as the environment and reducing the incidence of immunologic reactions and eco-toxicological risks. Furthermore, the acid-catalysed hydrolysis of imine links in the framework back to the starting monomers, provided an intrinsic degree of pH responsiveness to the COF-API conjugate, even in the absence of conjugated smart polymers.

A major limitation which was not addressed during the investigation of the drug release profile, was the size of the chosen fragments. The number of individual fragments and their total weight were fixed at 3 fragments and 0.005 g respectively. However, since the inside bulk of larger fragments is better protected from the surrounding environment, and this difference in fragment size was unaccounted for, the release profile was inadvertently affected.

The quality of the presented laboratory PXRD data, reflected the challenging crystallisation of frameworks. The new compounds, the COF-API conjugate and the COF-API-Polymer complexes were not characterised using STA and BET pore surface analyser techniques, as instrumentation was installed rather late and the thesis had to be wrapped up and submitted. This led to a limited understanding on the behaviour of the new structures upon heating, and on the extent of solvent and condensation ratio effects.

Additional techniques and the advanced instrumentation at the new solid-state laboratory set up at the Malta Life Sciences Park, including variable temperature PXRD, STA, Raman, BET pore analyser, XRM and SEM, will be used in due time, to fully characterise the new compounds, the COF-API conjugate and its loading capacity, and the COF-API-Polymer complexes and their extent and manner of smart molecule conjugation. Structure solution on the patterns obtained for the COF-API conjugate and the COF-API-Polymer complexes could determine the number of API molecules and smart molecules incorporated within the unit cell, their orientation, and the hydrogen bond and π-π intermolecular interactions physically adsorbing API molecules to each other and to the cage walls, and smart molecules to the pore walls and surface edges. *Ab initio* simulations could further explore the intermolecular interactions involved between loaded/conjugated molecules and the framework, in the synthesised drug loaded structure and final complexes, determining the role that hydrogen bonding and non-covalent interactions play in the assembly and degradation of the smart nanocarrier systems.

Density Functional Theory (DFT) calculations could be used to predict the crystal structures of the new materials and help validate crystal structure solution from experimental data. Docking programs could also be used to predict and simulate interactions between the final complexes and the body.

Only the characterised cage-based structure, was loaded with the API and conjugated with smart molecules. Nonetheless, by proof of concept, this principle can be applied to the other eleven compounds, following their characterisation as porous frameworks through crystal structure determination, and similarly extended to all COF materials. In the same manner, the incorporation of other API molecules of varying molecular size, and of larger smart molecules and polymers responsive to a wider range of stimuli, can be attained.

The aim of the thesis was achieved through the construction of the final complexes and their controlled drug release in simulated physiological conditions. Fine tuning of these final complexes and the synthetic steps to construct them, based on the characterisation results and the obtained knowledge on their interactions, responsiveness and behaviour, could explore the tailor-made synthesis of smart COF nanocarriers with CRT, optimised for specific applications in the field of therapeutics. Investigations *in vivo* on the biocompatibility of the pure COF and the toxicity of the final complexes on different cell lines, would supplement the significant contribution to the limited number of smart COF nanocarrier drug delivery systems. Further conjugation of the final complexes with hydrophilic polymers, such as β-cyclodextrin and PEG, could also be investigated to potentially enhance the loading of hydrophobic drug molecules into the framework and improve the performance of the nanocarrier systems.

9. References

1. Scicluna, M. C.; Vella-Żarb, L. Evolution of nanocarrier drug-delivery systems and recent advancements in covalent organic framework-drug systems. *ACS Appl. Nano Mater.* **2020,** *3* (4), 3097-3115.

2. Logothetidis, S. Nanomedicine: The medicine of tomorrow. In *Nanomedicine and Nanobiotechnology;* Springer-Verlag: Berlin Heidelberg, **2012**; pp 1-26.

3. McNeil, S. E. Nanotechnology for the biologist. *J. Leukoc. Biol.* **2005,** *78* (3), 585-594.

4. Park, K.; Bae, Y. H.; Mrsny, R. J. The missing components today and the new treatments tomorrow. In *Cancer Targeted Drug Delivery: An Elusive Dream;* Springer Science and Business Media: New York, **2013**; pp 689-707.

5. Shi, J.; Votruba, A. R.; Farokhzad, O. C.; Langer, R. Nanotechnology in drug delivery and tissue engineering: From discovery to applications. *Nano Lett.* **2010,** *10* (9), 3223-3230.

6. Bartlett, D. W.; Su, H.; Hildebrandt, I. J.; Weber, W. A.; Davis, M. E. Impact of tumor-specific targeting on the biodistribution and efficacy of siRNA nanoparticles measured by multimodality *in vivo* imaging. *Proc. Natl. Acad. Sci. U.S.A.* **2007,** *104* (39), 15549-15554.

7. Sandanaraj, B. S.; Gremlich, H. U.; Kneuer, R.; Dawson, J.; Wacha, S. Fluorescent nanoprobes as a biomarker for increased vascular permeability: Implications in diagnosis and treatment of cancer and inflammation. *Bioconjugate Chem.* **2010,** *21* (1), 93-101.

8. Brüsewitz, C.; Schendler, A.; Funke, A.; Wagner, T.; Lipp, R. Novel poloxamer-based nanoemulsions to enhance the intestinal absorption of active compounds. *Int. J. Pharm.* **2007,** *329* (1-2), 173-181.

9. Decuzzi, P.; Godin, B.; Tanaka, T.; Lee, S. Y.; Chiappini, C.; Liu, X.; Ferrari, M. Size and shape effects in the biodistribution of intravascularly injected particles. *J. Control. Release* **2010,** *141* (3), 320-327.

10. Serda, R. E.; Gu, J.; Bhavane, R. C.; Liu, X. W.; Chiappini, C.; Decuzzi, P.; Ferrari, M. The association of silicon microparticles with endothelial cells in drug delivery to the vasculature. *Biomaterials* **2009,** *30* (13), 2440-2448.

11. Kreuter, J.; Shamenkov, D.; Petrov, V.; Ramge, P.; Cychutek, K.; Koch-Brandt, C.; Alyautdin, R. Apolipoprotein-mediated transport of nanoparticle-bound drugs across the blood-brain barrier. *J. Drug Target.* **2002,** *10* (4), 317-325.

12. von Maltzahn, G.; Park, J. H.; Lin, K. Y.; Singh, N.; Schwöppe, C.; Mesters, R.; Berdel, W. E.; Ruoslahti, E.; Sailor, M. J.; Bhatia, S. N. Nanoparticles that communicate *in vivo* to amplify tumour targeting. *Nat. Mater.* **2011,** *10* (7), 545-552.

13. Weissleder, R.; Kelly, K.; Sun, E. Y.; Shtatland, T.; Josephson, L. Cell-specific targeting of nanoparticles by multivalent attachment of small molecules. *Nat. Biotechnol.* **2005,** *23* (11), 1418-1423.

14. Hoshino, A.; Fujioka, K.; Oku, T.; Nakamura, S.; Suga, M.; Yamaguchi, Y.; Suzuki, K.; Yasuhara, M.; Yamamoto, K. Quantum dots targeted to the assigned organelle in living cells. *Microbiol. Immunol.* **2004,** *48* (12), 985-994.

15. Hobbs, S. K.; Monsky, W. L.; Yuan, F.; Roberts, W. G.; Griffith, L.; Torchilin, V. P.; Jain, R. K. Regulation of transport pathways in tumor vessels: Role of tumor type and microenvironment. *Proc. Natl. Acad. Sci. U.S.A.* **1998,** *95* (8), 4607-4612.

16. Yuan, F.; Leunig, M.; Huang, S. K.; Berk, D. A.; Papahadjopoulos, D.; Jain, R. K. Microvascular permeability and interstitial penetration of sterically stabilized (stealth) liposomes in a human tumor xenograft. *Cancer Res.* **1994,** *54* (13), 3352-3356.

17. Noguchi, Y.; Wu, J.; Duncan, R.; Strohalm, J.; Ulbrich, K.; Akaike, T.; Maeda, H. Early phase tumor accumulation of macromolecules: A great difference in clearance rate between tumor and normal tissues. *Jpn. J. Cancer Res.* **1998,** *89* (3), 307-314.

18. Schwarz, C.; Mehnert, W. Solid lipid nanoparticles (SLN) for controlled drug delivery II. drug incorporation and physicochemical characterization. *J. Microencapsul.* **1999,** *16* (2), 205-213.

19. Hong, C. R.; Bogle, G.; Wang, J.; Patel, K.; Pruijn, F. B.; Wilson, W. R.; Hicks, K. O. Bystander effects of hypoxia-activated prodrugs: Agent-based modeling using three dimensional cell cultures. *Front. Pharmacol.* **2018,** *9* (1013), 1-16.

20. Russell-Jones, G.; McTavish, K.; McEwan, J.; Thurmond, B. Increasing the tumoricidal activity of daunomycin-pHPMA conjugates using vitamin B_{12} as a targeting agent. *J. Can. Res. Updates* **2012,** *1* (2), 203-211.

21. Yoo, H. S.; Park, T. G. Folate-receptor-targeted delivery of doxorubicin nano-aggregates stabilized by doxorubicin-PEG-folate conjugate. *J. Control. Release* **2004,** *100* (2), 247-256.

22. Peer, D.; Karp, J. M.; Hong, S.; Farokhzad, O. C.; Margalit, R.; Langer, R. Nanocarriers as an emerging platform for cancer therapy. *Nat. Nanotechnol.* **2007,** *2* (12), 751-760.

23. Lu, W.; Xiong, C.; Zhang, R.; Shi, L.; Huang, M.; Zhang, G.; Song, S.; Huang, Q.; Liu, G. Y.; Li, C. Receptor-mediated transcytosis: A mechanism for active extravascular transport of nanoparticles in solid tumors. *J. Control. Release* **2012,** *161* (3), 959-966.

24. Smith, D. M.; Simon, J. K.; Baker Jr, J. R. Applications of nanotechnology for immunology. *Nat. Rev. Immunol.* **2013,** *13* (8), 592-605.

25. Jakoby, J.; Beuschlein, F.; Mentz, S.; Hantel, C.; Süss, R. Liposomal doxorubicin for active targeting: Surface modification of the nanocarrier evaluated *in vitro* and *in vivo* - challenges and prospects. *Oncotarget* **2015,** *6* (41), 43698-43711.

26. Engelberth, S. A.; Hempel, N.; Bergkvist, M. Development of nanoscale approaches for ovarian cancer therapeutics and diagnostics. *Crit. Rev. Oncog.* **2014,** *19* (3-4), 281-315.

27. Vidal, F.; Guzman, L. Dendrimer nanocarriers drug action: Perspective for neuronal pharmacology. *Neural. Regen. Res.* **2015,** *10* (7), 1029-1031.

28. Wu, W.; Wieckowski, S.; Pastorin, G.; Benincasa, M.; Klumpp, C.; Briand, J. P.; Gennaro, R.; Prato, M.; Bianco, A. Targeted delivery of amphotericin B to cells by using functionalized carbon nanotubes. *Angew. Chem.* **2005,** *117* (39), 6515-6520.

29. Liu, Z.; Fan, A. C.; Rakhra, K.; Sherlock, S.; Goodwin, A.; Chen, X.; Yang, Q.; Felsher, D. W.; Dai, H. Supramolecular stacking of doxorubicin on carbon nanotubes for *in vivo* cancer therapy. *Angew. Chem.* **2009,** *121* (41), 7804-7808.

30. Peretz, S.; Regev, O. Carbon nanotubes as nanocarriers in medicine. *Curr. Opin. Colloid Interface Sci.* **2012,** *17* (6), 360-368.

31. Loo, C.; Lowery, A.; Halas, N.; West, J.; Drezek, R. Immunotargeted nanoshells for integrated cancer imaging and therapy. *Nano Lett.* **2005,** *5* (4), 709-711.

32. Lim, Y. T.; Kim, S.; Nakayama, A.; Stott, N. E.; Bawendi, M. G.; Frangioni, J. V. Selection of quantum dot wavelengths for biomedical assays and imaging. *Mol. Imaging* **2003,** *2* (1), 50-64.

33. You, J.; Zhang, G.; Li, C. Exceptionally high payload of doxorubicin in hollow gold nanospheres for near-infrared light-triggered drug release. *ACS Nano* **2010,** *4* (2), 1033-1041.

34. You, J.; Zhang, R.; Zhang, G.; Zhong, M.; Liu, Y.; Van Pelt, C. S.; Liang, D.; Wei, W.; Sood, A. K.; Li, C. Photothermal-chemotherapy with doxorubicin-loaded hollow gold nanospheres: A platform for near-infrared light-trigged drug release. *J. Control. Release* **2012,** *158* (2), 319-328.

35. El-Samaligy, M. S.; Rohdewald, P. Reconstituted collagen nanoparticles, a novel drug carrier delivery system. *J. Pharm. Pharmacol.* **1983,** *35* (8), 537-539.

36. Hrkach, J. S.; Peracchia, M. T.; Domb, A.; Lotan, N.; Langer, R. Nanotechnology for biomaterials engineering: Structural characterization of amphiphilic polymeric nanoparticles by ^{1}H NMR spectroscopy. *Biomaterials* **1997,** *18* (1), 27-30.

37. Butterfield, J. T.; Kim, H.; Knauer, D. J.; Nevala, W. K.; Markovic, S. N. Identification of a peptide-peptide binding motif in the coating of nab-paclitaxel nanoparticles with clinical antibodies: bevacizumab, rituximab, and trastuzumab. *Sci. Rep.* **2017,** *7* (1), 14476.

38. Schmidt, M. M.; Wittrup, K. D. A modeling analysis of the effects of molecular size and binding affinity on tumor targeting. *Mol. Cancer Ther.* **2009,** *8* (10), 2861-2871.

39. Park, K. The controlled drug delivery systems: Past forward and future back. *J. Control. Release* **2014,** *190*, 3-8.

40. Wang, J.; Pelletier, M.; Zhang, H.; Xia, H.; Zhao, Y. High frequency ultrasound-responsive block copolymer micelle. *Langmuir* **2009,** *25* (22), 13201-13205.

41. Bernardos, A.; Mondragón, L.; Aznar, E.; Marcos, M. D.; Martínez-Máñez, R.; Sancenón, F.; Soto, J.; Barat, J. M.; Pérez-Payá, E.; Guillem, C.; Amorós, P. Enzyme-responsive intracellular controlled release using nanometric silica mesoporous supports capped with "saccharides". *ACS Nano* **2010,** *4* (11), 6353-6368.

42. Jeffrey, S. C.; Andreyka, J. B.; Bernhardt, S. X.; Kissler, K. M.; Kline, T.; Lenox, J. S.; Moser, R. F.; Nguyen, M. T.; Okeley, N. M.; Stone, I. J.; Zhang, X.; Senter, P. D. Development and properties of *β*-glucuronide linkers for monoclonal antibody-drug conjugates. *Bioconjugate Chem.* **2006,** *17* (3), 831-840.

43. Burke, P. J.; Senter, P. D.; Meyer, D. W.; Miyamoto, J. B.; Anderson, M.; Toki, B. E.; Manikumar, G.; Wani, M. C.; Kroll, D. J.; Jeffrey, S. C. Design, synthesis, and

biological evaluation of antibody-drug conjugates comprised of potent camptothecin analogues. *Bioconjugate Chem.* **2009,** *20* (6), 1242-1250.

44. DeWit, M. A.; Gillies, E. R. A cascade biodegradable polymer based on alternating cyclization and elimination reactions. *J. Am. Chem. Soc.* **2009,** *131* (51), 18327-18334.

45. Weinstain, R.; Sagi, A.; Karton, N.; Shabat, D. Self-immolative comb-polymers: Multiple-release of side-reporters by a single stimulus event. *Chem.: Eur. J.* **2008,** *14* (23), 6857-6861.

46. Sapra, P.; Stein, R.; Pickett, J.; Qu, Z.; Govindan, S. V.; Cardillo, T. M.; Hansen, H. J.; Horak, I. D.; Griffiths, G. L.; Goldenberg, D. M. Anti-CD74 antibody-doxorubicin conjugate, IMMU-110, in a human multiple myeloma xenograft and in monkeys. *Clin. Cancer Res.* **2005,** *11* (14), 5257-5264.

47. Srinivasarao, M.; Low, P. S. Ligand-targeted drug delivery. *Chem. Rev.* **2017,** *117* (19), 12133-12164.

48. Thomas, M.; Gajda, M.; Naini, C. A.; Franzka, S.; Ulbricht, M.; Hartmann, N. Poly(*N*,*N*-dimethylaminoethyl methacrylate) brushes: pH-dependent switching kinetics of a surface-grafted thermoresponsive polyelectrolyte. *Langmuir* **2015,** *31* (49), 13426-13432.

49. Wang, B.; Xu, X. D.; Wang, Z. C.; Cheng, S. X.; Zhang, X. Z.; Zhuo, R. X. Synthesis and properties of pH and temperature sensitive P(NIPAAm-*co*-DMAEMA) hydrogels. *Colloids Surf. B.* **2008,** *64* (1), 34-41.

50. Kratz, K.; Hellweg, T.; Eimer, W. Structural changes in PNIPAM microgel particles as seen by SANS, DLS, and EM techniques. *Polymer* **2001,** *42* (15), 6631-6639.

51. Natalia, F.; Stoychev, G.; Puretskiy, N.; Leonid, I.; Dmitry, V. Porous thermo-responsive pNIPAM microgels. *Eur. Polym. J.* **2015,** *68,* 650-656.

52. Liu, S. Q.; Tong, Y. W.; Yang, Y. Y. Thermally sensitive micelles self-assembled from poly(*N*-isopropylacrylamide-*co*-*N*,*N*-dimethylacrylamide)-*b*-poly(D,L-lactide-*co*-glycolide) for controlled delivery of paclitaxel. *Mol. BioSyst.* **2005,** *1* (2), 158-165.

53. Cheng, Y.; Doane, T. L.; Chuang, C. H.; Ziady, A.; Burda, C. Near infrared light-triggered drug generation and release from gold nanoparticle carriers for photodynamic therapy. *Small* **2014,** *10* (9), 1799-1804.

54. Shi, D.; Matsusaki, M.; Kaneko, T.; Akashi, M. Photo-cross-linking and cleavage induced reversible size change of bio-based nanoparticles. *Macromolecules* **2008,** *41* (21), 8167-8172.

55. Yuan, Q.; Zhang, Y.; Chen, T.; Lu, D.; Zhao, Z.; Zhang, X.; Li, Z.; Yan, C. H.; Tan, W. Photon-manipulated drug release from a mesoporous nanocontainer controlled by azobenzene-modified nucleic acid. *ACS Nano* **2012,** *6* (7), 6337-6344.

56. Lee, J. H.; Lee, K.; Moon, S. H.; Lee, Y.; Park, T. G.; Cheon, J. All-in-one target-cell-specific magnetic nanoparticles for simulatneous molecular imaging and siRNA delivery. *Angew. Chem. Int. Ed.* **2009,** *48* (23), 4174-4179.

57. Dong, H. F.; Dai, W.; Ju, H.; Lu, H.; Wang, S.; Xu, L.; Zhou, S. F.; Zhang, Y.; Zhang, X. Multifunctional poly(L-lactide)-polyethylene glycol-grafted graphene quantum dots for intracellular microRNA imaging and combined specific-gene-targeting agents delivery for improved therapeutics. *ACS Appl. Mater. Interfaces* **2015,** *7* (20), 11015-11023.

58. Katagiri, K.; Imai, Y.; Koumoto, K.; Kaiden, T.; Kono, K.; Aoshima, S. Magnetoresponsive on-demand release of hybrid liposomes formed from Fe_3O_4 nanoparticles and thermosensitive block copolymers. *Small* **2011,** *7* (12), 1683-1689.

59. Satarkar, N. S.; Hilt, J. Z. Hydrogel nanocomposites as remote-controlled biomaterials. *Acta Biomater.* **2008,** *4* (1), 11-16.

60. Agarwal, A.; Mackey, M. A.; El-Sayed, M. A.; Bellamkonda, R. V. Remote triggered release of doxorubicin in tumors by synergistic application of thermosensitive liposomes and gold nanorods. *ACS Nano* **2011,** *5* (6), 4919-4926.

61. Kohane, D. S.; Langer, R. Biocompatibility and drug delivery systems. *Chem. Sci.* **2010,** *1* (4), 441-446.

62. Redhead, H. M.; Davis, S. S.; Illum, L. Drug delivery in poly(lactide-co-glycolide) nanoparticles surface modified with poloxamer 407 and poloxamine 908: *in vitro* characterisation and *in vivo* evaluation. *J. Control. Release* **2001,** *70* (3), 353-363.

63. Yu, C.; Zhou, M.; Zhang, X.; Wei, W.; Chen, X.; Zhang, X. Smart doxorubicin nanoparticles with high drug payload for enhanced chemotherapy against drug resistance and cancer diagnosis. *Nanoscale* **2015,** *7* (13), 5683-5690.

64. Song, S. W.; Hidajat, K.; Kawi, S. Functionalized SBA-15 materials as carriers for controlled drug delivery: Influence of surface properties on matrix-drug interactions. *Langmuir* **2005,** *21* (21), 9568-9575.

65. Zeng, W.; Qian, X. F.; Zhang, Y. B.; Yin, J.; Zhu, Z. K. Organic modified mesoporous MCM-41 through solvothermal process as drug delivery system. *Mater. Res. Bull.* **2005,** *40* (5), 766-772.

66. Frank, M. M.; Fries, L. F. The role of complement in inflammation and phagocytosis. *Immunol. Today* **1991,** *12* (9), 322-326.

67. Tan, J. S.; Butterfield, D. E.; Voycheck, C. L.; Caldwell, K. D.; Li, J. T. Surface modification of nanoparticles by PEO/PPO block copolymers to minimize interactions with blood components and prolong blood circulation in rats. *Biomaterials* **1993,** *14* (11), 823-833.

68. Allen, C.; Dos Santos, N.; Gallagher, R.; Chiu, G. N. C.; Shu, Y.; Li, W. M.; Johnstone, S. A.; Janoff, A. S.; Mayer, L. D.; Webb, M. S.; Bally, M. B. Controlling the physical behavior and biological performance of liposome formulations through use of surface grafted poly(ethylene glycol). *Biosci. Rep.* **2002,** *22* (2), 225-250.

69. Pain, D.; Das, P. K.; Ghosh, P.; Bachhawat, B. K. Increased circulatory half-life of liposomes after conjunction with dextran. *J. Biosci.* **1984,** *6* (6), 811-816.

70. Cao, Z.; Zhang, L.; Jiang, S. Superhydrophilic zwitterionic polymers stabilize liposomes. *Langmuir* **2012,** *28* (31), 11625-11632.

71. Maruyama, K.; Okuizumi, S.; Ishida, O.; Yamauchi, H.; Kikuchi, H.; Iwatsuru, M. Phosphatidyl polyglycerols prolong liposome circulation *in vivo*. *Int. J. Pharm.* **1994,** *111* (1), 103-107.

72. Hirn, S.; Semmler-Behnke, M.; Schleh, C.; Wenk, A.; Lipka, J.; Schäffler, M.; Takenaka, S.; Möller, W.; Schmid, G.; Simon, U.; Kreyling, W. G. Particle size-dependent and surface charge-dependent biodistribution of gold nanoparticles after intravenous administration. *Eur. J. Pharm. Biopharm.* **2011,** *77* (3), 407-416.

73. Fang, C.; Shi, B.; Pei, Y. Y.; Hong, M. H.; Wu, J.; Chen, H. Z. *In vivo* tumor targeting of tumor necrosis factor-α -loaded stealth nanoparticles: Effect of MePEG molecular weight and particle size. *Eur. J. Pharm. Sci.* **2006,** *27* (1), 27-36.

74. Naahidi, S.; Jafari, M.; Edalat, F.; Raymond, K.; Khademhosseini, A.; Chen, P. Biocompatibility of engineered nanoparticles for drug delivery. *J. Control. Release* **2013,** *166* (2), 182-194.

75. Gref, R.; Minamitake, Y.; Peracchia, M. T.; Trubetskoy, V.; Torchilin, V.; Langer, R. Biodegradable long-circulating polymeric nanospheres. *Science* **1994,** *263* (5153), 1600-1603.

76. Mahapatro, A.; Singh, D. K. Biodegradable nanoparticles are excellent vehicle for site directed *in-vivo* delivery of drugs and vaccines. *J. Nanobiotechnology* **2011,** *9* (1), 55-65.

77. Strebhardt, K.; Ullrich, A. Paul Ehrlich's magic bullet concept: 100 years of progress. *Nat. Rev. Cancer* **2008,** *8* (6), 473-480.

78. Côté, A. P.; Benin, A. I.; Ockwig, N. W.; O'Keeffe, M.; Matzger, A. J.; Yaghi, O. M. Porous, Crystalline, Covalent Organic Frameworks. *Science* **2005,** *310* (5751), 1166-1170.

79. El-Kaderi, H. M.; Hunt, J. R.; Mendoza-Cortés, J. L.; Côté, A. P.; Taylor, R. E.; O'Keeffe, M.; Yaghi, O. M. Designed synthesis of 3D covalent organic frameworks. *Science* **2007,** *316* (5822), 268-272.

80. Kuhn, P.; Antonietti, M.; Thomas, A. Porous, covalent triazine-based frameworks prepared by ionothermal synthesis. *Angew. Chem. Int. Ed.* **2008,** *47* (18), 3450-3453.

81. Bojdys, M. J.; Jeromenok, J.; Thomas, A.; Antonietti, M. Rational extension of the family of layered, covalent, triazine-based frameworks with regular porosity. *Adv. Mater.* **2010,** *22* (19), 2202-2205.

82. Uribe-Romo, F. J.; Doonan, C. J.; Furukawa, H.; Oisaki, K.; Yaghi, O. M. Crystalline covalent organic frameworks with hydrazone linkages. *J. Am. Chem. Soc.* **2011,** *133* (30), 11478–11481.

83. Uribe-Romo, F. J.; Hunt, J. R.; Furukawa, H.; Klöck, C.; O'Keeffe, M.; Yaghi, O. M. A Crystalline imine-linked 3-D porous covalent organic framework. *J. Am. Chem. Soc.* **2009,** *131* (13), 4570-4571.

84. Ding, S. Y.; Wang, W. Covalent organic frameworks (COFs): From design to applications. *Chem. Soc. Rev.* **2013,** *42* (2), 548-568.

85. Colson, J. W.; Woll, A. R.; Mukherjee, A.; Levendorf, M. P.; Spitler, E. L.; Shields, V. B.; Spencer, M. G.; Park, J.; Dichtel, W. R. Oriented 2D covalent organic framework thin films on single-layer graphene. *Science* **2011,** *332* (6026), 228-231.

86. Spitler, E. L.; Koo, B. T.; Novotney, J. L.; Colson, J. W.; Uribe-Romo, F. J.; Gutierrez, G. D.; Clancy, P.; Dichtel, W. R. A 2D covalent organic framework with 4.7-nm pores and insight into its interlayer stacking. *J. Am. Chem. Soc.* **2011,** *133* (48), 19416–19421.

87. Campbell, N. L.; Clowes, R.; Ritchie, L. K.; Cooper, A. I. Rapid microwave synthesis and purification of porous covalent organic frameworks. *Chem. Mater.* **2009,** *21* (2), 204-206.

88. Dogru, M.; Sonnauer, A.; Gavryushin, A.; Knochel, P.; Bein, T. A covalent organic framework with 4 nm open pores. *Chem. Commun.* **2011,** *47* (6), 1707-1709.

89. Yang, S. T.; Kim, J.; Cho, H. Y.; Kim, S.; Ahn, W. S. Facile synthesis of covalent organic frameworks COF-1 and COF-5 by sonochemical method. *R. Soc. Chem. Adv.* **2012,** *2* (27), 10179–10181.

90. Biswal, B. P.; Chandra, S.; Kandambeth, S.; Lukose, B.; Heine, T.; Banjerjee, R. Mechanochemical synthesis of chemically stable isoreticular covalent organic frameworks. *J. Am. Chem. Soc.* **2013,** *135* (14), 5328−5331.

91. Das, G.; Balaji Shinde, D.; Kandambeth, S.; Biswal, B. P.; Banerjee, R. Mechanosynthesis of imine, β-ketoenamine, and hydrogen-bonded imine-linked covalent organic frameworks using liquid-assisted grinding. *Chem. Commun.* **2014,** *50* (84), 12615-12618.

92. Spitler, E. L.; Colson, J. W.; Uribe-Romo, F. J.; Woll, A. R.; Giovino, M. R.; Saldivar, A.; Dichtel, W. R. Lattice expansion of highly oriented 2D phthalocyanine covalent organic framework films. *Angew. Chem. Int. Ed.* **2012,** *51* (11), 2623-2627.

93. Tilford, R. W.; Mugavero III, S. J.; Pellechia, P. J.; Lavigne, J. J. Tailoring microporosity in covalent organic frameworks. *Adv. Mater.* **2008,** *20* (14), 2741-2746.

94. Chen, X.; Huang, N.; Gao, J.; Xu, H.; Xu, F.; Jiang, D. Towards covalent organic frameworks with predesignable and aligned open docking sites. *Chem. Commun.* **2014,** *50* (46), 6161-6163.

95. Bunck, D. N.; Dichtel, W. R. Internal functionalization of three-dimensional covalent organic frameworks. *Angew. Chem. Int. Ed.* **2012,** *51* (8), 1885-1889.

96. Nagai, A.; Guo, Z.; Feng, X.; Jin, S.; Chen, X.; Ding, X.; Jiang, D. Pore surface engineering in covalent organic frameworks. *Nat. Commun.* **2011,** *2* (1), 536.

97. Zhu, Y.; Zhang, W. Reversible tuning of pore size and CO_2 adsorption in azobenzene functionalized porous organic polymers. *Chem. Sci.* **2014,** *5* (12), 4957-4961.

98. Feng, X.; Chen, L.; Dong, Y.; Jiang, D. Porphyrin-based two-dimensional covalent organic frameworks: Synchronized synthetic control of macroscopic structures and pore parameters. *Chem. Commun.* **2011,** *47* (7), 1979-1981.

99. Ding, X.; Guo, J.; Feng, X.; Honsho, Y.; Guo, J.; Seki, S.; Maitarad, P.; Saeki, A.; Nagase, S.; Jiang, D. Synthesis of metallophthalocyanine covalent organic frameworks that exhibit high carrier mobility and photoconductivity. *Angew. Chem. Int. Ed.* **2011,** *50* (6), 1289-1293.

100. Feng, X.; Liu, L.; Honsho, Y.; Saeki, A.; Seki, S.; Irle, S.; Dong, Y.; Nagai, A.; Jiang, D. High-rate charge-carrier transport in porphyrin covalent organic frameworks: Switching from hole to electron to ambipolar conduction. *Angew. Chem. Int. Ed.* **2012,** *51* (11), 2618-2622.

101. Furukawa, H.; Yaghi, O. M. Storage of hydrogen, methane, and carbon dioxide in highly porous covalent organic frameworks for clean energy applications. *J. Am. Chem. Soc.* **2009,** *131* (25), 8875-8883.

102. Yu, J. T.; Chen, Z.; Sun, J.; Huang, Z. T.; Zheng, Q. Y. Cyclotricatechylene based porous crystalline material: Synthesis and applications in gas storage. *J. Mater. Chem.* **2012,** *22* (12), 5369-5373.

103. Ding, S. Y.; Gao, J.; Wang, Q.; Zhang, Y.; Song, W. G.; Su, C. Y.; Wang, W. Construction of covalent organic framework for catalysis: Pd/COF-LZU1 in Suzuki-Miyaura coupling reaction. *J. Am. Chem. Soc.* **2011,** *133* (49), 19816–19822.

104. Li, H.; Eddaoudi, M.; O'Keeffe, M.; Yaghi, O. M. Design and synthesis of an exceptionally stable and highly porous metal-organic framework. *Nature* **1999,** *402* (6759), 276-279.

105. Férey, G.; Serre, C.; Mellot-Draznieks, C.; Millange, F.; Surblé, S.; Dutour, J.; Margiolaki, I. A hybrid solid with giant pores prepared by a combination of targeted chemistry, simulation, and powder diffraction. *Angew. Chem.* **2004,** *116* (46), 6456-6461.

106. Horcajada, P.; Chalati, T.; Serre, C.; Gillet, B.; Sebrie, C.; Baati, T.; Eubank, J. F.; Heurtaux, D.; Clayette, P.; Kreuz, C.; Chang, J. S.; Hwang, Y. K.; Marsaud, V.; Bories, P. N.; Cynober, L.; Gil, S.; Férey, G.; Couvreur, P.; Gref, R. Porous metal-organic framework nanoscale carriers as a potential platform for drug delivery and imaging. *Nat. Mater.* **2010,** *9* (2), 172-178.

107. Horcajada, P.; Serre, C.; Vallet-Regí, M.; Sebban, M.; Taulelle, F.; Férey, G. Metal-organic frameworks as efficient materials for drug delivery. *Angew. Chem.* **2006,** *118* (36), 6120-6124.

108. Bauer, S.; Serre, C.; Devic, T.; Horcajada, P.; Marrot, J.; Férey, G.; Stock, N. High-throughput assisted rationalization of the formation of metal organic frameworks in the iron(III) aminoterephthalate solvothermal system. *Inorg. Chem.* **2008,** *47* (17), 7568-7576.

109. Horcajada, P.; Serre, C.; Maurin, G.; Ramsahye, N. A.; Balas, F.; Vallet-Regí, M.; Sebban, M.; Taulelle, F.; Férey, G. Flexible porous metal-organic frameworks for a controlled drug delivery. *J. Am. Chem. Soc.* **2008,** *130* (21), 6774-6780.

110. An, J.; Geib, S. J.; Rosi, N. L. Cation-triggered drug release from a porous zinc-adeninate metal-organic framework. *J. Am. Chem. Soc.* **2009,** *131* (24), 8376-8377.

111. Devic, T.; Horcajada, P.; Serre, C.; Salles, F.; Maurin, G.; Moulin, B.; Heurtaux, D.; Clet, G.; Vimont, A.; Grenèche, J. M.; Ouay, B. L.; Moreau, F.; Magnier, E.; Filinchuk, Y.; Marrot, J.; Lavalley, J. C.; Daturi, M.; Férey, G. Functionalization in flexible porous solids: Effects on the pore opening and the host-guest interactions. *J. Am. Chem. Soc.* **2010,** *132* (3), 1127-1136.

112. Taylor-Pashow, K. M. L.; Della Rocca, J.; Xie, Z.; Tran, S.; Lin, W. Postsynthetic modifications of iron-carboxylate nanoscale metal-organic frameworks for imaging and drug delivery. *J. Am. Chem. Soc.* **2009,** *131* (40), 14261-14263.

113. Cunha, D.; Yahia, M. B.; Hall, S.; Miller, S. R.; Chevreau, H.; Elkaïm, E.; Maurin, G.; Horcajada, P.; Serre, C. Rationale of drug encapsulation and release from biocompatible porous metal-organic frameworks. *Chem. Mater.* **2013,** *25* (14), 2767-2776.

114. Miller, S. R.; Heurtaux, D.; Baati, T.; Horcajada, P.; Grenèche, J. M.; Serre, C. Biodegradable therapeutic MOFs for the delivery of bioactive molecules. *Chem. Commun.* **2010,** *46* (25), 4526-4528.

115. Chen, L.; Di, J.; Cao, C.; Zhao, Y.; Ma, Y.; Luo, J.; Wen, Y.; Song, W.; Song, Y.; Jiang, L. A pH-driven DNA nanoswitch for responsive controlled release. *Chem. Commun.* **2011,** *47* (10), 2850-2852.

116. Chen, C.; Geng, J.; Pu, F.; Yang, X.; Ren, J.; Qu, X. Polyvalent nucleic acid/mesoporous silica nanoparticle conjugates: Dual stimuli-responsive vehicles for intracellular drug delivery. *Angew. Chem. Int. Ed.* **2011,** *50* (4), 882-886.

117. Zhou, S.; Du, X.; Cui, F.; Zhang, X. Multi-responsive and logic controlled release of DNA-gated mesoporous silica vehicles functionalized with intercalators for multiple delivery. *Small* **2014,** *10* (5), 980-988.

118. Wen, Y.; Xu, L.; Wang, W.; Wang, D.; Du, H.; Zhang, X. Highly efficient remote controlled release system based on light-driven DNA nanomachine functionalized mesoporous silica. *Nanoscale* **2012,** *4* (15), 4473-4476.

119. Chen, W. H.; Yu, X.; Cecconello, A.; Sohn, Y. S.; Nechushtai, R.; Willner, I. Stimuli-responsive nucleic acid-functionalized metal-organic framework nanoparticles using pH- and metal-ion-dependent DNAzymes as locks. *Chem. Sci.* **2017,** *8* (8), 5769-5780.

120. Kahn, J. S.; Freage, L.; Enkin, N.; Aleman Garcia, M. A.; Willner, I. Stimuli-responsive DNA-functionalized metal-organic frameworks (MOFs). *Adv. Mater.* **2017,** *29* (6), 1602782.

121. Chen, W. H.; Liao, W. C.; Sohn, Y. S.; Fadeev, M.; Cecconello, A.; Nechushtai, R.; Willner, I. Stimuli-responsive nucleic acid-based polyacrylamide hydrogel-coated metal-organic framework nanoparticles for controlled drug release. *Adv. Funct. Mater.* **2018,** *28* (8), 1705137.

122. Chen, W. H.; Sohn, Y. S.; Fadeev, M.; Cecconello, A.; Nechushtai, R.; Willner, I. Targeted VEGF-triggered release of an anti-cancer drug from aptamer-functionalized metal-organic framework nanoparticles. *Nanoscale* **2018,** *10* (10), 4650-4657.

123. Zheng, H.; Zhang, Y.; Liu, L.; Wan, W.; Guo, P.; Nyström, A. M.; Zou, X. One-pot synthesis of metal-organic frameworks with encapsulated target molecules and their applications for controlled drug delivery. *J. Am. Chem. Soc.* **2016,** *138* (3), 962-968.

124. Wang, Q.; Sun, Y.; Li, S.; Zhang, P.; Yao, Q. Synthesis and modification of ZIF-8 and its application in drug delivery and tumor therapy. *RSC Adv.* **2020,** *10* (62), 37600-37620.

125. Liang, Z.; Yang, Z.; Yuan, H.; Wang, C.; Qi, J.; Liu, K.; Cao, R.; Zheng, H. A protein@metal-organic framework nanocomposite for pH-triggered anticancer drug delivery. *Dalton Trans.* **2018,** *47* (30), 10223-10228.

126. Wataha, J. C.; Hanks, C. T.; Sun, Z. Effect of cell line on *in vitro* metal ion cytotoxicity. *Dent. Mater* **1994,** *10* (3), 156-161.

127. Zhou, Z.; Liu, X.; Liu, Q.; Liu, L. Evaluation of the potential cytotoxicity of metals associated with implanted biomaterials (I). *Prep. Biochem. Biotech.* **2009,** *39* (1), 81-91.

128. Zhou, Z.; Yi, Q.; Gao, Y.; Liu, Q.; Liu, L.; Zeng, W.; Liu, X. Evaluation of the potential cytotoxicity of metals associated with implanted biomaterials (II). *J. Med. Eng. Technol.* **2010,** *34* (7-8), 455-461.

129. Zhao, H.; Jin, Z.; Su, H.; Jing, X.; Sun, F.; Zhu, G. Targeted synthesis of a 2D ordered porous organic framework for drug release. *Chem. Commun.* **2011,** *47* (22), 6389-6391.

130. Lim, H.; Cha, M. C.; Chang, J. Y. Preparation of microporous polymers based on 1,3,5-triazine units showing high CO_2 adsorption capacity. *Macromol. Chem. Phys.* **2012,** *213* (13), 1385-1390.

131. Rengaraj, A.; Puthiaraj, P.; Haldorai, Y.; Heo, N. S.; Hwang, S. K.; Han, Y. K.; Kwon, S.; Ahn, W. S.; Huh, Y. S. Porous covalent triazine polymer as a potential nanocargo for cancer therapy and imaging. *ACS Appl. Mater. Interfaces* **2016,** *8* (14), 8947-8955.

132. Liu, J.; Zong, E.; Fu, H.; Zheng, S.; Xu, Z.; Zhu, D. Adsorption of aromatic compounds on porous covalent triazine-based framework. *J. Colloid Interface Sci.* **2012,** *372* (1), 99-107.

133. Luo, Y.; Liu, J.; Liu, Y.; Lyu, Y. Porphyrin-based covalent triazine frameworks; Porosity, adsorption performance, and drug delivery. *J. Polym. Sci. A* **2017,** *55* (16), 2594-2600.

134. Vyas, V. S.; Vishwakarma, M.; Moudrakovski, I.; Haase, F.; Savasci, G.; Ochsenfeld, C.; Spatz, J. P.; Lotsch, B. V. Exploiting noncovalent interactions in an imine-based covalent organic framework for quercetin delivery. *Adv. Mater.* **2016,** *28* (39), 8749-8754.

135. Gao, Q.; Bai, L.; Zeng, Y.; Wang, P.; Zhang, X.; Zou, R.; Zhao, Y. Reconstruction of covalent organic frameworks by dynamic equilibrium. *Chem. Eur. J.* **2015,** *21* (47), 16818-16822.

136. Bai, L.; Phua, S. Z. F.; Lim, W. Q.; Jana, A.; Luo, Z.; Tham, H. P.; Zhao, L.; Gao, Q.; Zhao, Y. Nanoscale covalent organic frameworks as smart carriers for drug delivery. *Chem. Commun.* **2016,** *52* (22), 4128-4131.

137. Hashemzadeh, H.; Raissi, H. Covalent organic framework as smart and high efficient carrier for anticancer drug delivery: a DFT calculations and molecular dynamics simulation study. *J. Phys. D: Appl. Phys.* **2018,** *51* (34), 345401.

138. Akyuz, L. An imine based COF as a smart carrier for targeted drug delivery: From synthesis to computational studies. *Microporous Mesoporous Mater.* **2020,** *294,* 109850.

139. Fang, Q.; Wang, J.; Gu, S.; Kaspar, R. B.; Zhuang, Z.; Zheng, J.; Guo, H.; Qiu, S.; Yan, Y. 3D porous crystalline polyimide covalent organic frameworks for drug delivery. *J. Am. Chem. Soc.* **2015,** *137* (26), 8352-8355.

140. Mokhtari, N.; Taymouri, S.; Mirian, M.; Dinari, M. Covalent triazine-based polyimine framework as a biocompatible pH-dependent sustained-release nanocarrier for sorafenib: An *in vitro* approach. *J. Mol. Liq.* **2020,** *297,* 111898.

141. Ma, J. X.; Li, J.; Chen, Y. F.; Ning, R.; Ao, Y. F.; Liu, J. M.; Sun, J.; Wang, D. X.; Wang, Q. Q. Cage based crystalline covalent organic frameworks. *J. Am. Chem. Soc.* **2019,** *141* (9), 3843-3848.

142. Li, M.; Peng, Y.; Yan, F.; Li, C.; He, Y.; Lou, Y.; Ma, D.; Li, Y.; Shi, Z.; Feng, S. A cage-based covalent organic framework for drug delivery. *New J. Chem.* **2021,** *45* (6), 3343-3348.

143. Wang, B.; Liu, X.; Gong, P.; Ge, X.; Liu, Z.; You, J. Fluorescnet COFs with a highly conjugated structure for visual durg loading and responsive release. *Chem. Commun.* **2020,** *56* (4), 519-522.

144. Zhang, L.; Chen, Y.; Shi, R.; Kang, T.; Pang, G.; Wang, B.; Zhao, Y.; Zeng, X.; Zou, C.; Wu, P.; Li, J. Synthesis of hollow nanocages MOF-5 as drug delivery vehicle to solve the load-bearing problem of insoluble antitumor drug oleanolic acid (OA). *Inorg. Chem. Commun.* **2018,** *96,* 20-23.

145. Gao, X.; Hai, X.; Baigude, H.; Guan, W.; Liu, Z. Fabrication of functional hollow microspheres constructed from MOF shells: Promising drug delivery systems with high loading capacity and targeted transport. *Sci. Rep.* **2016,** *6,* 37705.

146. Kandambeth, S.; Venkatesh, V.; Shinde, D. B.; Kumari, S.; Halder, A.; Verma, S.; Banerjee, R. Self-templated chemically stable hollow spherical covalent organic frameworks. *Nat. Commun.* **2015,** *6* (6786), 1-10.

147. Du, Y.; Mao, K.; Kamakoti, P.; Ravikovitch, P.; Paur, C.; Cundy, S.; Li, Q.; Calabro, D. Experimental and computation studies of pyridine-assisted post-synthesis modified air stable covalent-organic frameworks. *Chem. Commun.* **2012,** *48* (38), 4606-4608.

148. Lanni, L. M.; Tilford, R. W.; Bharathy, M.; Lavigne, J. J. Enhanced hydrolytic stability of self-assembling alkylated two-dimensional covalent organic frameworks. *J. Am. Chem. Soc.* **2011,** *133* (35), 13975-13983.

149. Mitra, S.; Sasmal, H. S.; Kundu, T.; Kandambeth, S.; Illath, K.; Díaz Díaz, D.; Banerjee, R. Targeted drug delivery in covalent organic nanosheets (CONs) via sequential postsynthetic modification. *J. Am. Chem. Soc.* **2017,** *139* (12), 4513-4520.

150. Jia, Y.; Zhang, L.; He, B.; Lin, Y.; Wang, J.; Li, M. 8-Hydroxyquinoline functionalized covalent organic framework as a pH sensitive carrier for drug delivery. *Mater. Sci. Eng. C.* **2020,** *117*, 111243.

151. Oliveira, A. D. S.; Rivero-Buceta, E. M.; Vidaurre-Agut, C.; Misturini, A.; Moreno, V.; Jordá, J. L.; Sastre, G.; Pergher, S. B. C.; Botella, P. Sequential pore wall functionalization in covalent organic frameworks and application to stable camptothecin delivery systems. *Mater. Sci. Eng. C.* **2020,** *117*, 111263.

152. Bhanja, P.; Mishra, S.; Manna, K.; Mallick, A.; Saha, K. D.; Bhaumik, A. Covalent organic framework material bearing phloroglucinol building units as a potent anticancer agent. *ACS Appl. Mater. Interfaces* **2017,** *9* (37), 31411-31423.

153. Liu, S.; Hu, C.; Liu, Y.; Zhao, X.; Pang, M.; Lin, J. One-pot synthesis of DOX@Covalent organic framework with enhanced chemotherapeutic efficacy. *Chem. Eur. J.* **2019,** *25* (17), 4315-4319.

154. Shi, X.; Yao, Y.; Xu, Y.; Liu, K.; Zhu, G.; Chi, L.; Lu, G. Imparting catalytic activity to a covalent organic framework material by nanoparticle encapsulation. *ACS Appl. Mater. Interfaces* **2017,** *9* (8), 7481-7488.

155. Das, S. K.; Mishra, S.; Manna, K.; Kayal, U.; Mahapatra, S.; Saha, K. D.; Dalapati, S.; Das, G. P.; Mostafa, A. A.; Bhaumik, A. A new triazine based π-conjugated mesoporous 2D covalent organic framework: Its *in vitro* anticancer activities. *Chem. Commun.* **2018,** *54* (81), 11475-11478.

156. Du, Y.; Calabro, D.; Wooler, B.; Kortunov, P. V.; Li, Q.; Cundy, S.; Mao, K. One step facile synthesis of amine-functionalized COF-1 with enhanced hydro-stability. *Chem. Mater.* **2015,** *27* (5), 1445-1447.

157. Zhang, G.; Li, X.; Liao, Q.; Liu, Y.; Xi, K.; Huang, W.; Jia, X. Water-dispersible PEG-curcumin/amine-functionalized covalent organic framework nanocomposites as smart carriers for *in vivo* drug delivery. *Nat. Commun.* **2018,** *9* (1), 2785.

158. Zhang, G.; Jiang, B.; Wu, C.; Liu, Y.; He, Y.; Huang, X.; Chen, W.; Xi, K.; Guo, H.; Zhao, X.; Jia, X. Thin platelet-like COF nanocomposities for blood brain barrier transport and inhibition of brain metastasis from renal cancer. *J. Mater. Chem. B* **2020,** *8* (20), 4475-4488.

159. Liu, S.; Yang, J.; Guo, R.; Deng, L.; Dong, A.; Zhang, J. Facile fabrication of redox-responsive covalent organic framework nanocarriers for efficiently loading and delivering doxorubicin. *Macromol. Rapid Commun.* **2020,** *41* (4), 1900570.

160. Wang, C.; Liu, H.; Liu, S.; Wang, Z.; Zhang, J. pH and redox dual-sensitive covalent organic framework nanocarriers to resolve the dilemma between extracellular drug loading and intracellular drug release. *Front. Chem.* **2020,** *8,* 488.

161. Anbazhagan, R.; Krishnamoorthi, R.; Kumaresan, S.; Tsai, H. C. Thioether-terminated triazole-bridged covalent organic framework for dual-sensitive drug delivery application. *Mater. Sci. Eng. C.* **2021,** *120,* 111704.

162. Zhang, J.; Wang, L.; Li, N.; Liu, J.; Zhang, W.; Zhang, Z.; Zhou, N.; Zhu, X. A novel azobenzene covalent organic framework. *CrystEngComm* **2014,** *16* (29), 6547-6551.

163. Liu, C.; Zhang, W.; Zeng, Q.; Lei, S. A photoresponsive surface covalent organic framework: Surface-confined synthesis, isomerization, and controlled guest capture and release. *Chem. Eur. J.* **2016,** *22* (20), 6768-6773.

164. Wang, H.; Zhu, W.; Liu, J.; Dong, Z.; Liu, Z. pH-responsive nanoscale covalent organic polymers as a biodegradable drug carrier for combined photodynamic-chemotherapy of cancer. *ACS Appl. Mater. Interfaces* **2018,** *10* (17), 14475-14482.

165. Wang, S. B.; Chen, Z. X.; Gao, F.; Zhang, C.; Zou, M. Z.; Ye, J. J.; Zeng, X.; Zhang, X. Z. Remodeling extracellular matrix based on functional covalent organic framework to enhance tumor photodynamic therapy. *Biomaterials* **2020,** *234,* 119772.

166. Ge, L.; Qiao, C.; Tang, Y.; Zhang, X.; Jiang, X. Light-activated hypoxia-sensitive covalent organic framework for tandem-responsive drug delivery. *Nano Lett.* **2021,** *21* (7), 3218-3224.

167. Gan, S.; Tong, X.; Zhang, Y.; Wu, J.; Hu, Y.; Yuan, A. Covalent organic framework-supported molecularly dispersed near-infrared dyes boost immunogenic phototherapy against tumors. *Adv. Funct. Mater.* **2019,** *29* (46), 1902757.

168. Wang, K.; Zhang, Z.; Lin, L.; Hao, K.; Chen, J.; Tian, H.; Chen, X. Cyanines-assisted exfoliation of covalent organic frameworks into nanocomposites for highly efficient chemo-photothermal tumor therapy. *ACS Appl. Mater. Interfaces* **2019,** *11* (43), 39503-39512.

169. Benyettou, F.; Das, G.; Nair, A. R.; Prakasam, T.; Shinde, D. B.; Sharma, S. K.; Whelan, J.; Lalatonne, Y.; Traboulsi, H.; Pasricha, R.; Abdullah, O.; Jagannathan, R.; Lai, Z.; Motte, L.; Gándara, F.; Sadler, K. C.; Trabolsi, A. Covalent organic framework embedded with magnetic nanoparticles for MRI and chemo-thermotherapy. *J. Am. Chem. Soc.* **2020,** *142* (44), 18782-18794.

170. Zhao, K.; Gong, P.; Huang, J.; Huang, Y.; Wang, D.; Peng, J.; Shen, D.; Zheng, X.; You, J.; Liu, Z. Fluorescence turn-off magnetic COF composite as a novel nanocarrier for drug loading and targeted delivery. *Micropor. Mesopor. Mat.* **2021,** *311*, 110713.

171. Particle Sciences Incorporation. Combination Devices. *Particle Sciences Technical Brief,* **2010**.

172. Food and Drug Administration, Department of Health and Human Services, "Code of Federal Regulations, Title 21 Food and drugs, (D) Drugs for human use, Part 330 Over-the-counter (OTC) human druga which are generally recognized as safe and effective and not misbranded," Office of the Federal Register (OFR) and the Government Publishing Office (GPO), United States, **2019**.

173. Food and Drug Administration, Department of Health and Human Services, "Code of Federal Regulations, Title 21 Food and drugs, (B) Food for human consumption," Office of the Federal Register (OFR) and the Government Publishing Office (GPO), United States, **2019**.

174. Niederberger, M. Nanaqueous sol-gel routes to metal oxide nanoparticles. *Acc. Chem. Res.* **2007,** *40* (9), 793-800.

175. Vestal, C. R.; Zhang, Z. J. Synthesis of $CoCrFeO_4$ nanoparticles using microemulsion methods and size-dependent studies of their magnetic properties. *Chem. Mater.* **2002,** *14* (9), 3817-3822.

176. Vasiliev, P. O.; Faure, B.; Ng, J. B. S.; Bergström, L. Colloidal aspects relating to direct incorporation of TiO_2 nanoparticles into mesoporous spheres by an aerosol-assisted process. *J. Colloid Interface Sci.* **2008,** *319* (1), 144-151.

177. Tilford, R. W.; Gemmill, W. R.; zur Loye, H. C.; Lavigne, J. J. Facile synthesis of a highly crystalline, covalently linked porous boronate network. *Chem. Mater.* **2006,** *18* (22), 5296-5301.

178. Farooq, M. G.; Lokhande, M. V. Synthesis of ferrocene based organometallic compounds and antimicrobial activity. *J. Appl. Chem.* **2014,** *7* (2), 27-32.

179. Scicluna, M. C. *Synthesis and characterisation of new covalent organic framework (COF) materials;* B.Sc. Dissertation, University of Malta: Msida, Malta, **2015**.

180. Scicluna, M. C. *An investigation on the effect of the chemical and physical environments in crystallisation: Pore size tunability of new liquid-assisted grinding (LAG) synthesised covalent organic frameworks (COFs)*; M.Sc. Dissertation, University of Malta: Msida, Malta, **2016**.

181. Scicluna, M. C.; Baisch, U.; Vella-Żarb, L. Rapid and facile one-step microwave synthesis of macrobicyclic cryptands. *Manuscript in preparation*.

182. Scicluna, M. C.; Vella-Żarb, L. *Manuscript in preparation*.

183. Ratemi, E. pH-responsive polymers for drug delivery applications. In *Stimuli Responsive Polymeric Nanocarriers for Drug Delivery Applications, Volume 1;* Woodhead Publishing, Elsevier, **2018**; pp 121-141.

184. Pietschnig, R. Polymers with pendant ferrocenes. *Chem. Soc. Rev.* **2016,** *45* (19), 5216-5231.

185. Merino, E.; Ribagorda, M. Control over molecular motion using the *cis-trans* photoisomerization of the azo group. *Beilstein J. Org. Chem.* **2012,** *8* (1), 1071–1090.

186. Dyadkin, V.; Pattison, P.; Dmitriev, V.; Chernyshov, D. A new multipurpose diffractometer PILATUS@SNBL. *J. Synchrotron Rad.* **2016,** *23* (3), 825-829.

187. Coelho, A. A. TOPAS and TOPAS-Academic: An optimization program integrating computer algebra and crystallographic objects written in C++. *J. Appl. Cryst.* **2018,** *51* (1), 210-218.

188. Rigaku Oxford Diffraction. *CrysAlis PRO;* Rigaku Oxford Diffraction: Yamton, England, **2015**.

189. Sheldrick, G. M. SHELXT - Integrated space-group and crystal-structure determination. *Acta Cryst.* **2015,** *A71* (1), 3-8.

190. Sheldrick, G. M. Crystal structure refinement with SHELXL. *Acta Cryst.* **2015,** *C71* (1), 3-8.

191. Dolomanov, O. V.; Bourhis, L. J.; Gildea, R. J.; Howard, J. A. K.; Puschmann, H. OLEX2: A complete structure solution, refinement and analysis program. *J. Appl. Cryst.* **2009,** *42* (2), 339-341.

192. Furche, F.; Ahlrichs, R.; Hättig, C.; Klopper, W.; Sierka, M.; Weigend, F. Turbomole. *WIREs Comput. Mol. Sci.* **2014,** *4* (2), 91-100.

193. Klamt, A. Conductor-like screening model for real solvents: A new approach to the quantitative calculation of solvation phenomena. *J. Phys. Chem.* **1995,** *99* (7), 2224-2235.

194. Chen, X.; Addicoat, M.; Jin, E.; Xu, H.; Hayashi, T.; Xu, F.; Huang, N.; Irle, S.; Jiang, D. Designed synthesis of double-stage two-dimensional covalent organic frameworks. *Sci. Rep.* **2015,** *5* (14650), 1-19.

195. Spek, A. L. Structure validation in chemical crystallography. *Acta. Cryst.* **2009,** *D65* (2), 148-155.

196. Putz, H.; Brandenburg, K. *Diamond version 4.6.5;* Crystal Impact, GbR: Bonn, Germany, **1999**.

197. Drew, M. G. B.; Marrs, D.; Hunter, J.; Nelson, J. Divergent and convergent forms of a new Schiff-base cryptand; X-ray crystallographic and molecular mechanics investigations. *J. Chem. Soc., Dalton Trans.* **1992,** *0* (1), 11-18.

198. Landini, D.; Maia, A.; Montanari, F.; Tundo, P. Lipophilic [2.2.2] cryptands as phase-transfer catalysts. Activation and nucleophilicty of anions in aqueous-organic two-phase systems and in organic solvents of low polarity. *J. Am. Chem. Soc.* **1979,** *101* (10), 2526-2530.

199. Woodruff, L. A.; Bordunov, A. V.; Pohl, C. A. *Ion exchange cryptands covalently bound to substrates;* Washington, DC: U.S. Patent and Trademark Office, Patent 7,166,266, **2007**.

200. Cai, K.; Lipke, M. C.; Liu, Z.; Nelson, J.; Cheng, T.; Shi, Y.; Cheng, C.; Shen, D.; Han, J. M.; Vemuri, S.; Feng, Y.; Stern, C. L.; Goddard III, W. A.; Wasielewski, M. R.; Fraser Stoddart, J. Molecular russian dolls. *Nat. Commun.* **2018,** *9* (5275), 1-8.

201. Groom, C. R.; Bruno, I. J.; Lightfoot, M. P.; Ward, S. C. The Cambridge Structural Database. *Acta Cryst.* **2016,** *B72* (2), 171-179.

202. STOE. *WinXPOW version 3.12.3;* STOE & Cie GmBH: Darmstadt, Germany, **2004**.

203. Ibrahim, R. A. A.; Suhail, F. S. A.; Al-Hakeim, H. K. Stability of anticancer drug 5-fluorouracil in aqueous solution: An assessment of kinetic behavior. *Nano Biomed. Eng.* **2018**, *10* (3), 224-234.

204. Aytar, B. S.; Muller, J. P. E.; Golan, S.; Kondo, Y.; Talmon, Y.; Abbott, N. L.; Lynn, D. M. Chemical oxidation of a redox-active, ferrocene-containing cationic lipid: Influence on interactions with DNA and characterization in the context of cell transfection. *J. Colloid Interface Sci.* **2012,** *387* (1), 56–64.

10. Appendices

A1. COF Synthesis

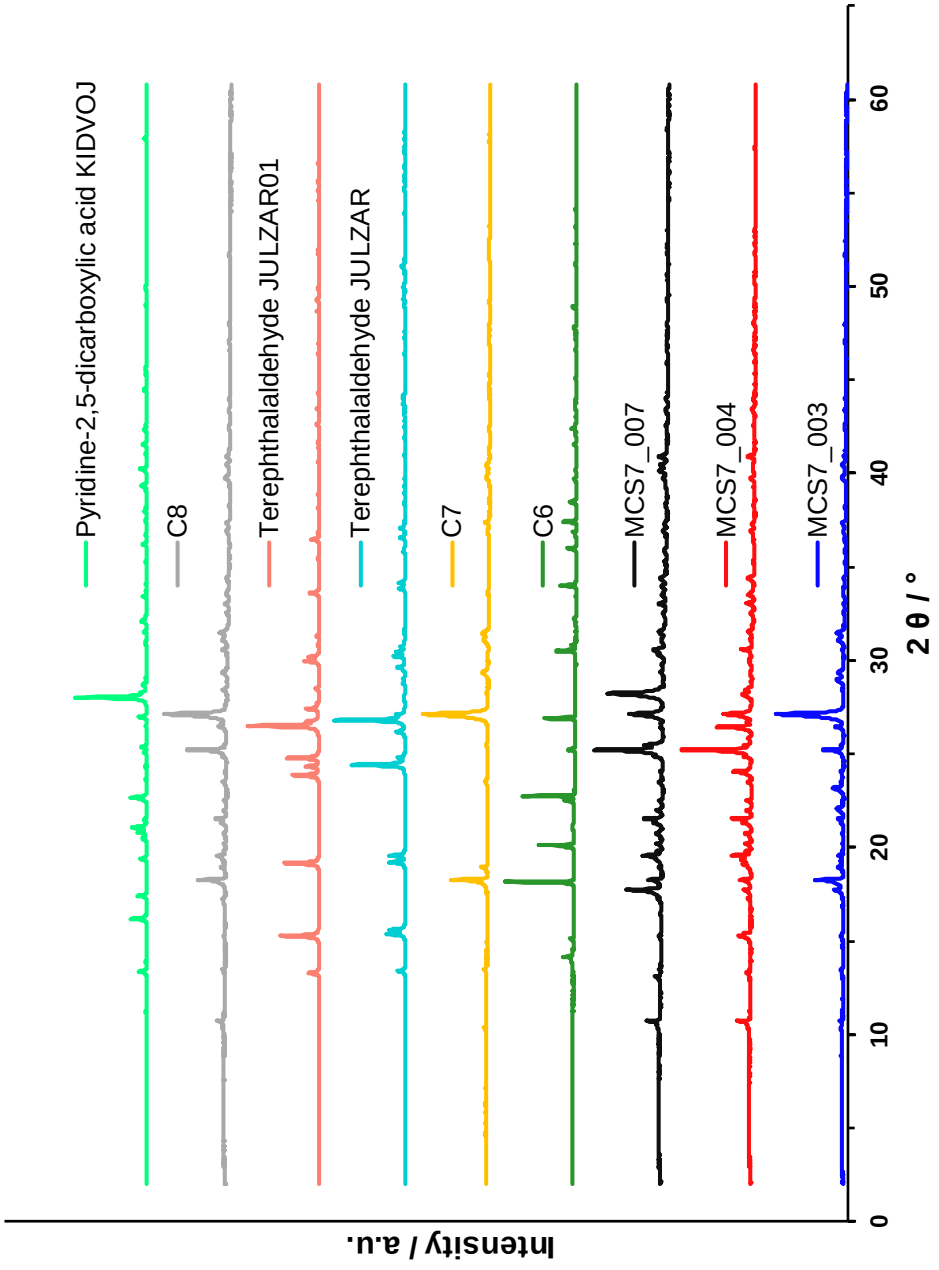

Figure 10.1. Laboratory PXRD patterns for MCS7_003 (blue), MCS7_004 (red) and MCS7_007 (black), obtained from a 2 + 1 + 3 condensation of the monomers via LAG in a catalytic amount of oxolane, benzene, and 1:1 1,4-dioxane:1,3,5-trimethylbenzene, respectively, and for the **C6** (green), **C7** (yellow) and **C8** (grey) monomers at 293 K, and the simulated patterns of the **C7** (JULZAR – turquoise and JULZAR01 – salmon) and **C8** (KIDVOJ – spring green) monomers from the CSD.

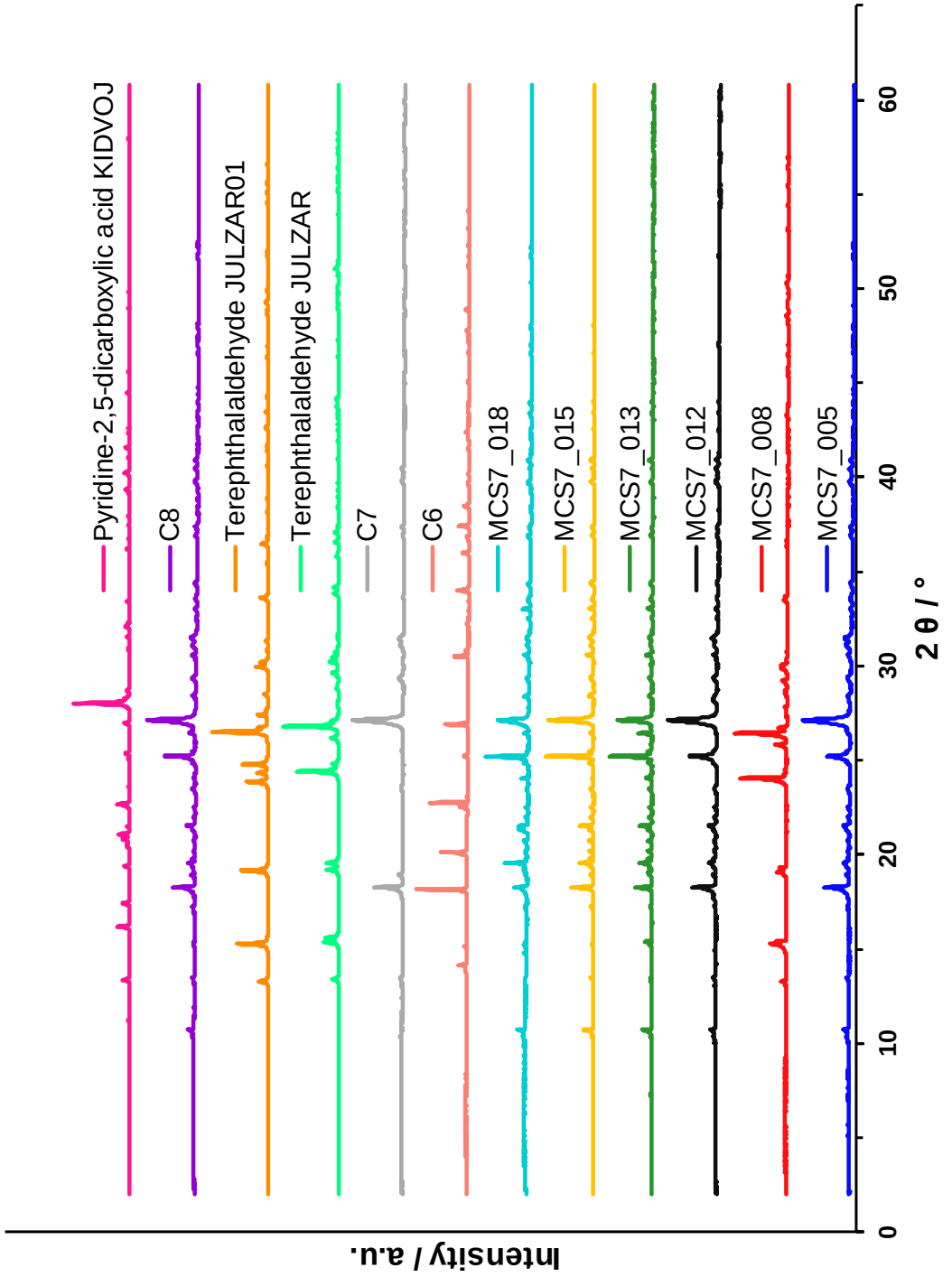

Figure 10.2. Laboratory PXRD patterns for MCS7_005 (blue), MCS7_008 (red), obtained from a 2 + 1 + 3 condensation of the monomers via LAG in a catalytic amount of 5:1 methanol:ethoxyethane, and 1:1 oxolane:methanol, respectively, MCS7_012 (black), MCS7_013 (green), MCS7_015 (yellow) and MCS7_018 (turquoise), obtained from a 4 + 2 + 9 condensation of the monomers via LAG in a catalytic amount of ethanol, oxolane, 5:1 methanol:ethoxyethane, and 1:1 oxolane:methanol, respectively, and for the **C6** (salmon), **C7** (grey) and **C8** (violet) monomers at 293 K, and the simulated patterns of the **C7** (JULZAR – spring green and JULZAR01 – orange) and **C8** (KIDVOJ – pink) monomers from the CSD.

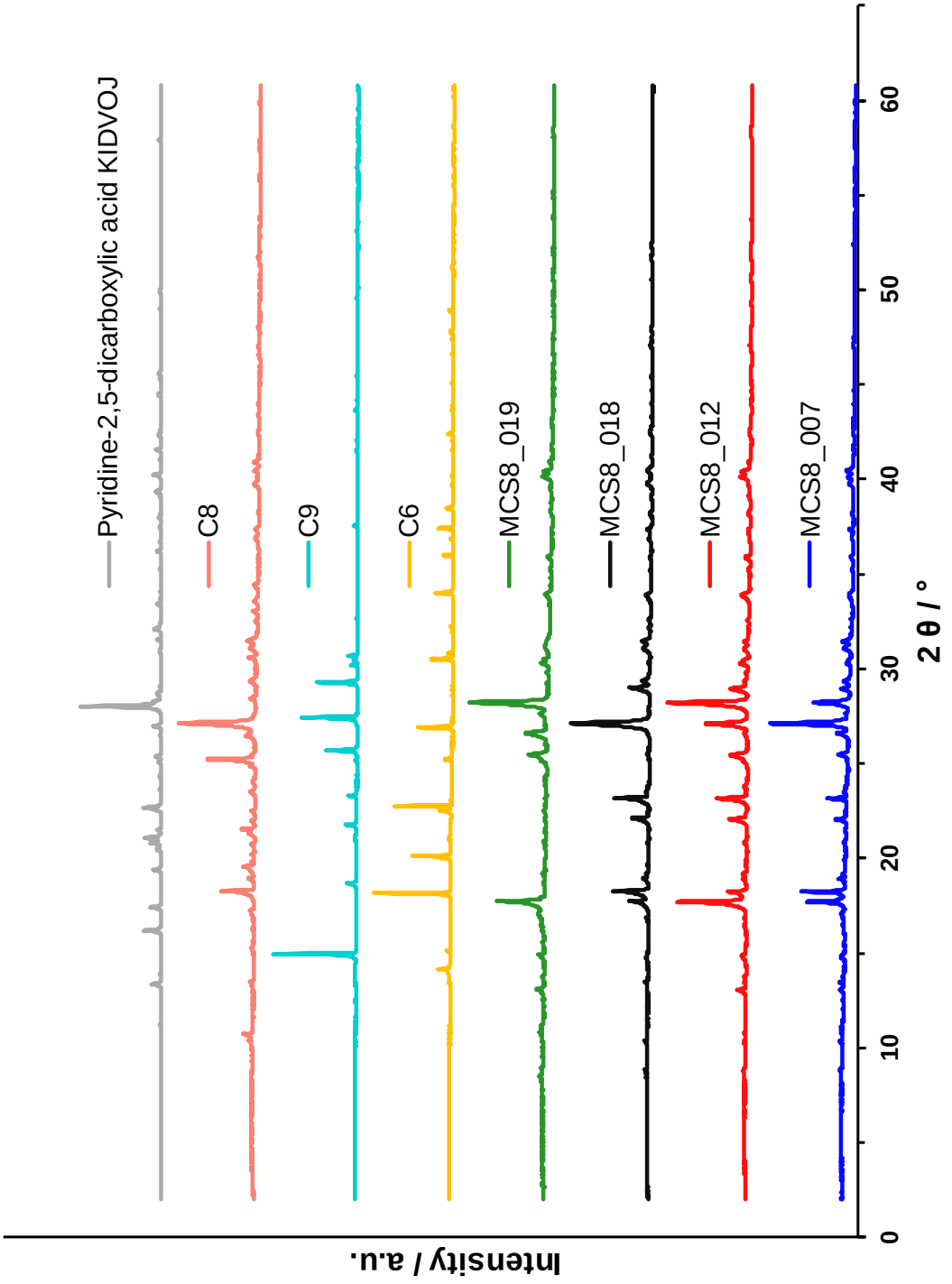

Figure 10.3. Laboratory PXRD patterns for MCS8_007 (blue), obtained from a 2 + 1 + 3 condensation of the monomers via LAG in a catalytic amount of 1:1 1,4-dioxane:1,3,5-trimethylbenzene, MCS8_012 (red), MCS8_018 (black) and MCS8_019 (green), obtained from a 4 + 2 + 9 condensation of the monomers via LAG in a catalytic amount of ethanol, 1:1 oxolane:methanol, and 1:1:0.05 1,4-dioxane:1,3,5-trimethylbenzene:acetic acid (3M), respectively, and for the **C6** (yellow), **C9** (turquoise) and **C8** (salmon) monomers at 293 K, and the simulated pattern of the **C8** (KIDVOJ – grey) monomer from the CSD.

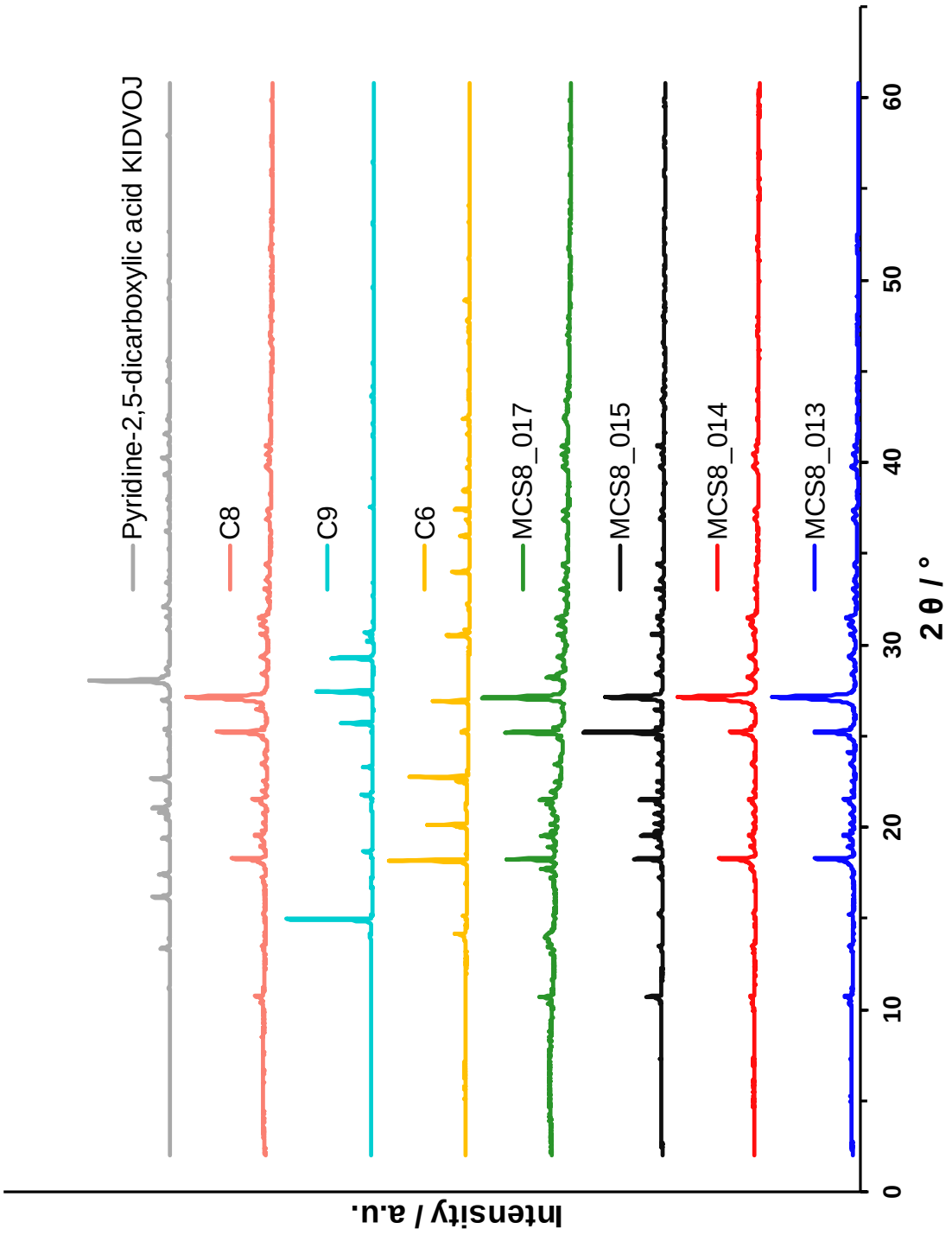

Figure 10.4. Laboratory PXRD patterns for MCS8_013 (blue), MCS8_014 (red), MCS8_015 (black) and MCS8_017 (green), obtained from a 4 + 2 + 9 condensation of the monomers via LAG in a catalytic amount of oxolane, benzene, 5:1 methanol:ethoxyethane, and 1:1 1,4-dioxane:1,3,5-trimethylbenzene, respectively, and for the **C6** (yellow), **C9** (turquoise) and **C8** (salmon) monomers at 293 K, and the simulated pattern of the **C8** (KIDVOJ – grey) monomer from the CSD.

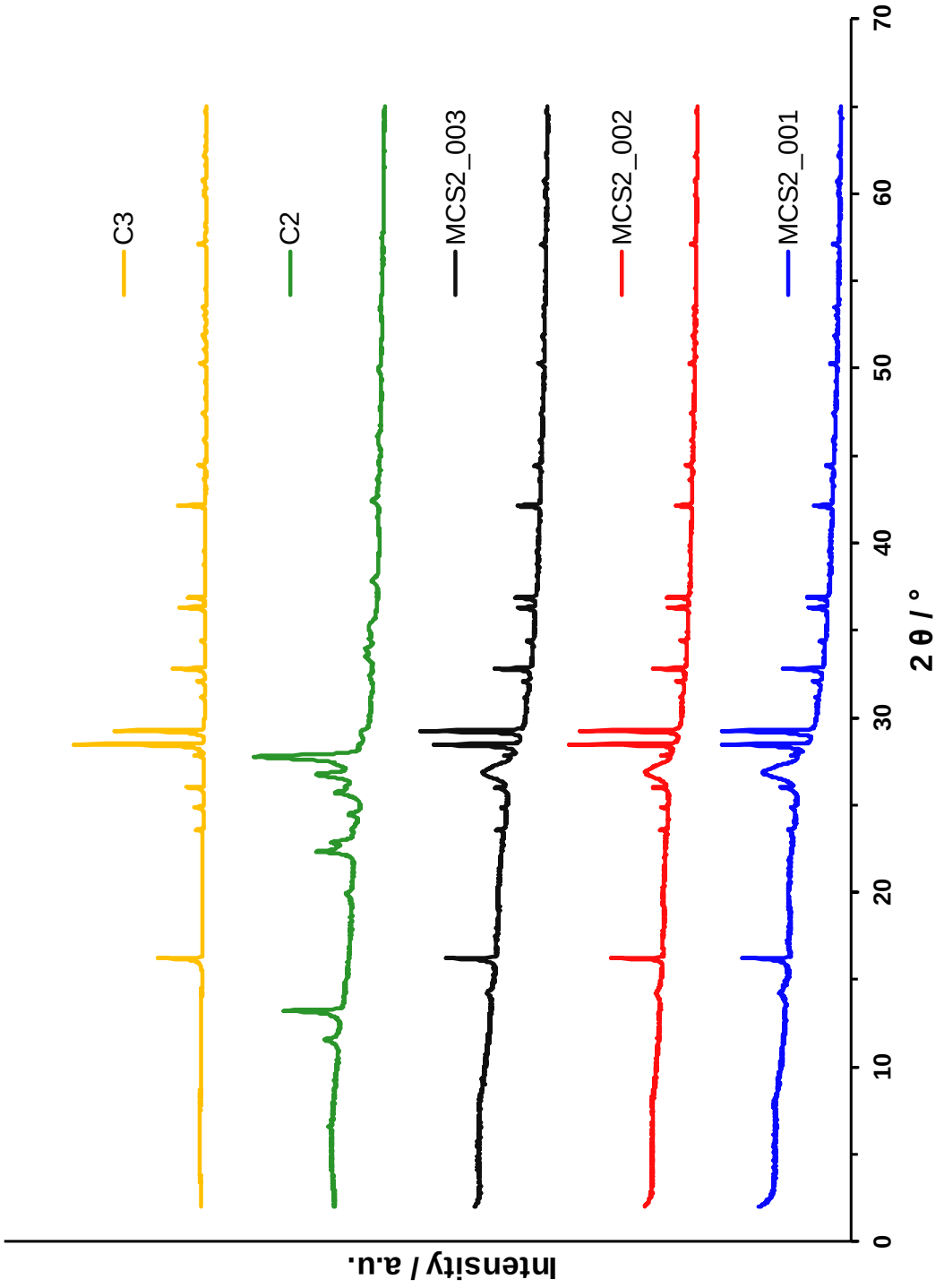

Figure 10.5. Laboratory PXRD patterns for MCS2_001 (blue), MCS2_002 (red) and MCS2_003 (black), obtained from an acetic acid-catalysed 1 + 1 condensation of the monomers via reflux in 1:1 1,4-dioxane:1,3,5-trimethylbenzene, upon washing with oxolane, and subsequent drying under vacuum, respectively, and for the **C2** (green) and **C3** (yellow) monomers at 293 K.

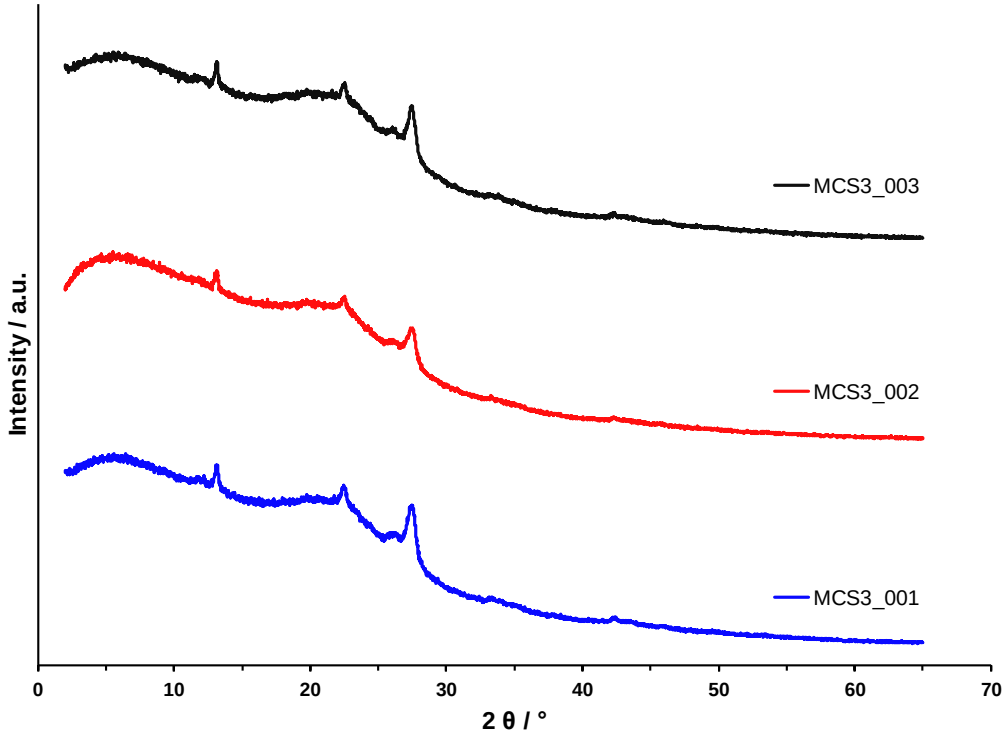

Figure 10.6. Laboratory PXRD patterns for MCS3_001 (blue), MCS3_002 (red) and MCS3_003 (black), obtained from a 3 + 2 condensation of **C2** and **C4** via reflux in 1:1 1,4-dioxane:1,3,5-trimethylbenzene, upon washing with oxolane, and subsequent drying under vacuum, respectively, at 293 K.

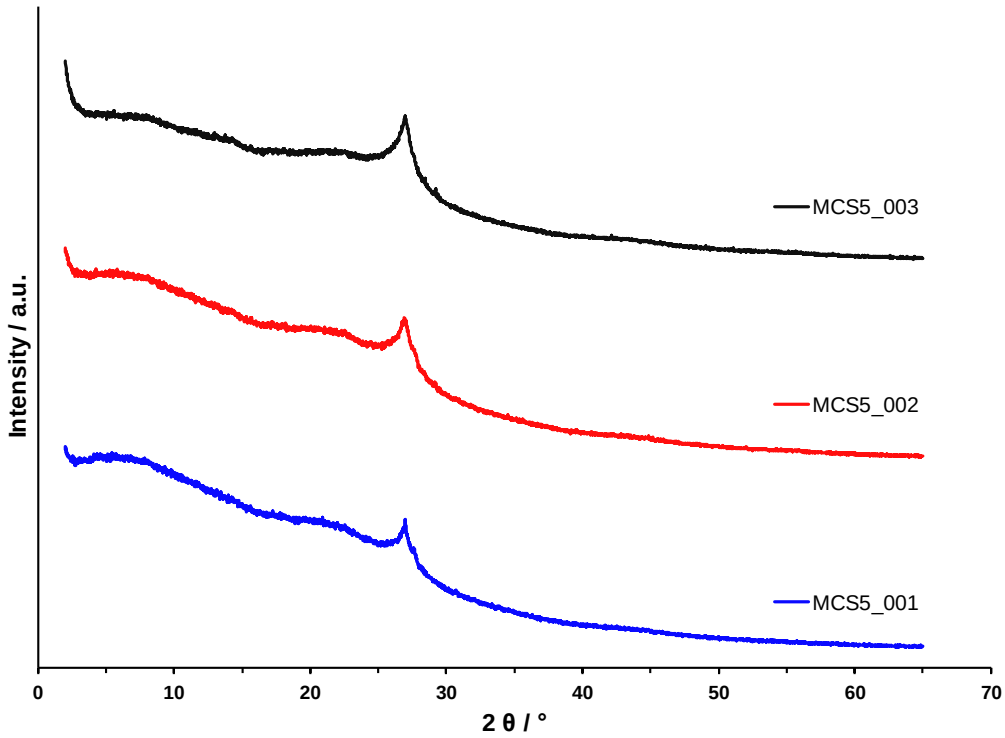

Figure 10.7. Laboratory PXRD patterns for MCS5_001 (blue), MCS5_002 (red) and MCS5_003 (black), obtained from an acetic acid-catalysed 3 + 1 + 3 condensation of **C2**, **C5** and **C3** via reflux in 1:1 1,4-dioxane:1,3,5-trimethylbenzene, upon washing with oxolane, and subsequent drying under vacuum, respectively, at 293 K.

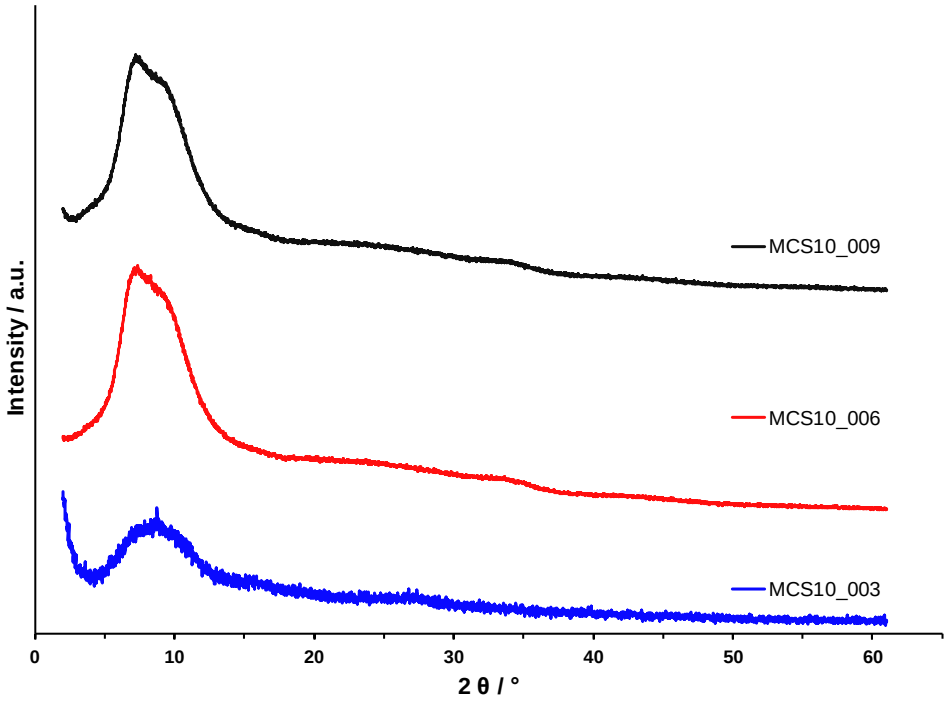

Figure 10.8. Laboratory PXRD patterns for MCS10_003 (blue), obtained from an acetic acid-catalysed 2 + 1 condensation of **C10** and **C4** via reflux in ethanol and upon washing with ethoxyethane, MCS10_006 (red) and MCS10_009 (black), obtained from an acetic acid-catalysed 2 + 1 condensation of the monomers via LAG in a catalytic amount of 5:1 methanol:ethoxyethane, and 1:1 dichloromethane:N,N-dimethylacetamide, respectively, at 293 K.

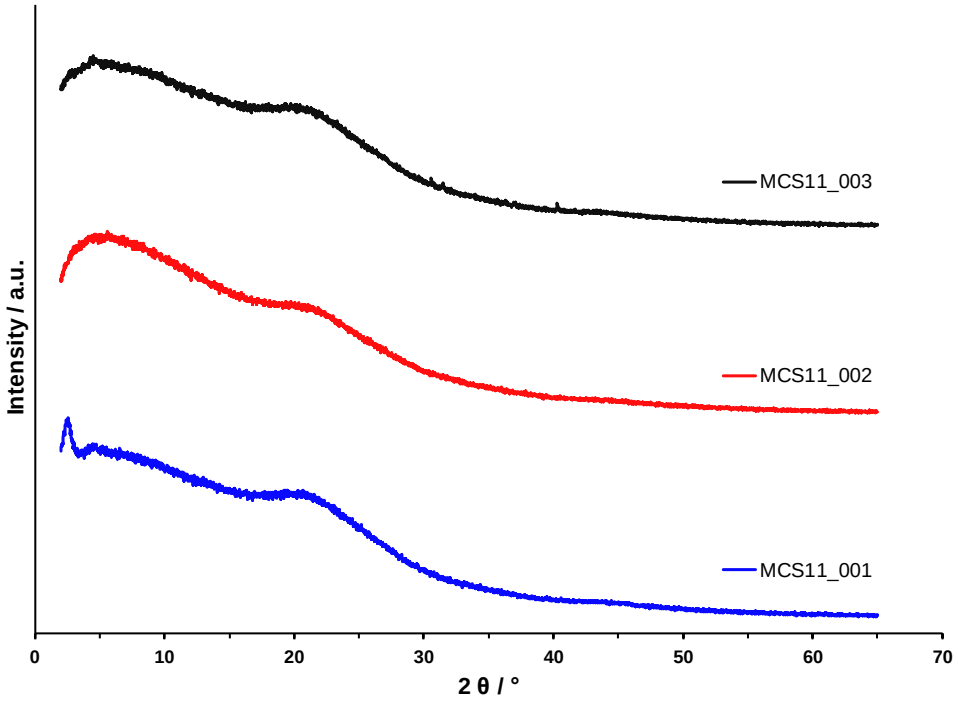

Figure 10.9. Laboratory PXRD patterns for MCS11_001 (blue), MCS11_002 (red) and MCS11_003 (black), obtained from a 1 + 1 condensation of **C11** and **C2** via reflux in 1:1 1,4-dioxane:1,3,5-trimethylbenzene, upon washing with oxolane, and subsequent drying under vacuum, respectively, at 293 K.

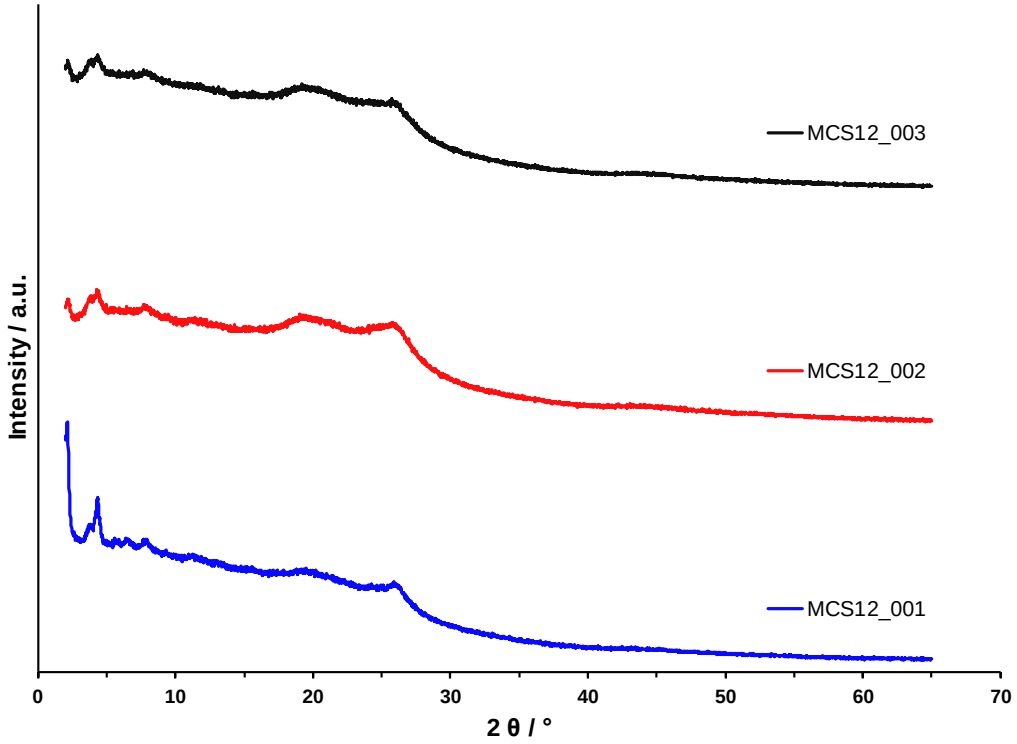

Figure 10.10. Laboratory PXRD patterns for MCS12_001 (blue), MCS12_002 (red) and MCS12_003 (black), obtained from an acetic acid-catalysed 3 + 3 + 1 condensation of **C11**, **C2** and **C5** via reflux in 1:1 1,4-dioxane:1,3,5-trimethylbenzene, upon washing with oxolane, and subsequent drying under vacuum, respectively, at 293 K.

A2. API Loading

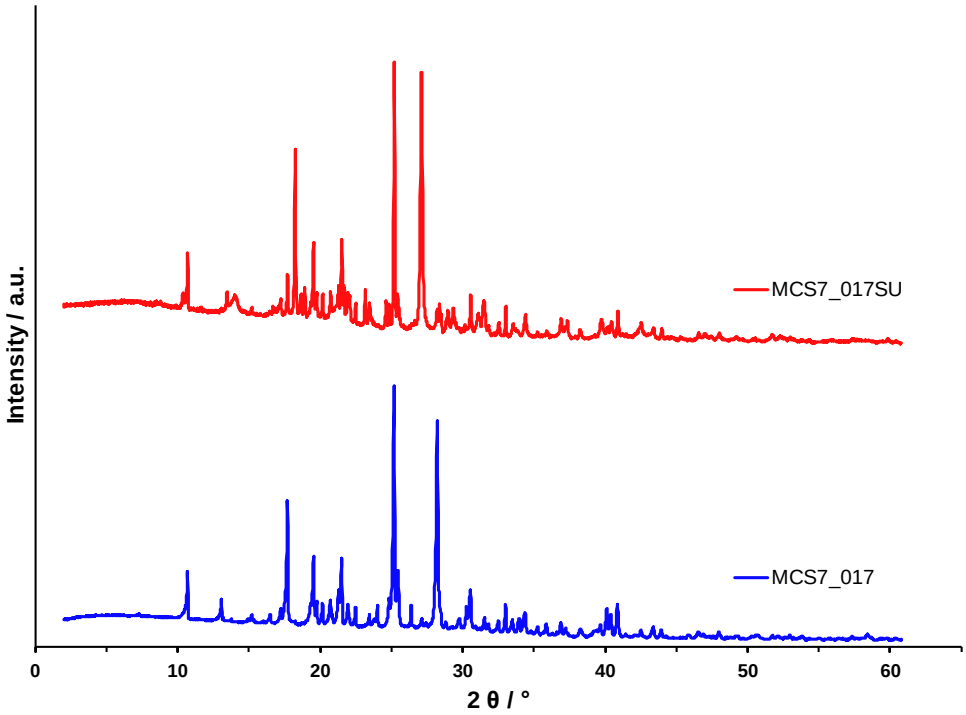

Figure 10.11. Laboratory PXRD patterns for MCS7_017 (blue) and MCS7_017SU (red), obtained from a 4 + 2 + 9 condensation of **C6**, **C7** and **C8**, via LAG in a catalytic amount of 1:1 1,4-dioxane:1,3,5-trimethylbenzene, and scaled-up five times, at 293 K.

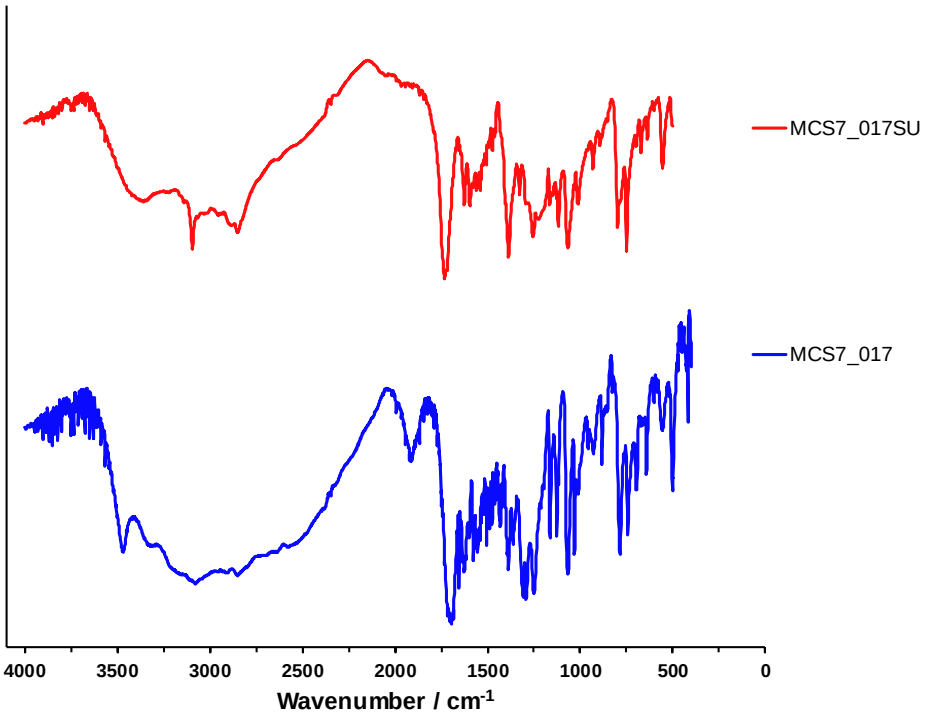

Figure 10.12. FTIR spectra for MCS7_017 (blue) and MCS7_017SU (red), obtained from a 4 + 2 + 9 condensation of **C6**, **C7** and **C8**, via LAG in a catalytic amount of 1:1 1,4-dioxane:1,3,5-trimethylbenzene, and scaled-up five times.

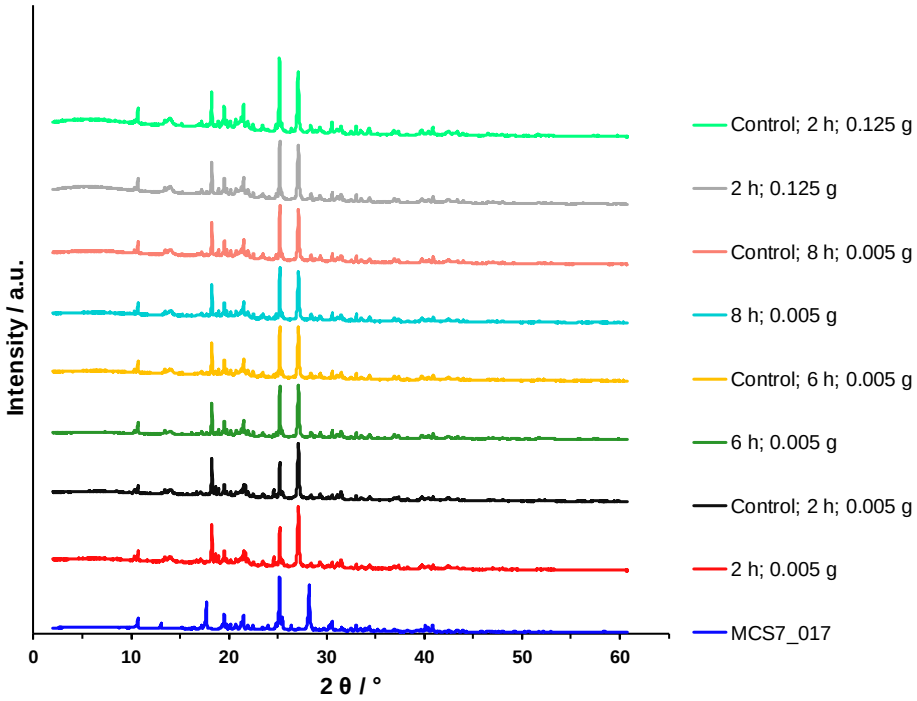

Figure 10.13. Laboratory PXRD patterns for original (blue), obtained from a 4 + 2 + 9 condensation of **C6**, **C7** and **C8**, via LAG in a catalytic amount of 1:1 1,4-dioxane:1,3,5-trimethylbenzene, and **C14** loaded and control MCS7_017, using hexane as solvent, a loading time of 2, 6 and 8 hours, and 0.005 and 0.125 g amounts of the framework, at 293 K.

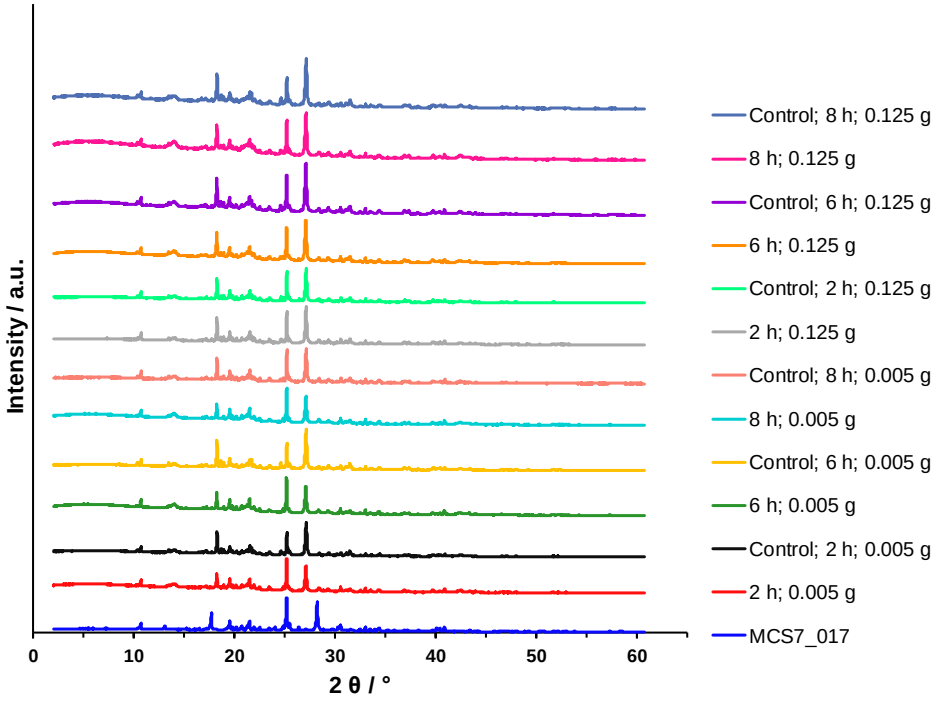

Figure 10.14. Laboratory PXRD patterns for original (blue), obtained from a 4 + 2 + 9 condensation of **C6**, **C7** and **C8**, via LAG in a catalytic amount of 1:1 1,4-dioxane:1,3,5-trimethylbenzene, and **C14** loaded and control MCS7_017, using hexane with oxolane drops as solvent, a loading time of 2, 6 and 8 hours, and 0.005 and 0.125 g amounts of the framework, at 293 K.

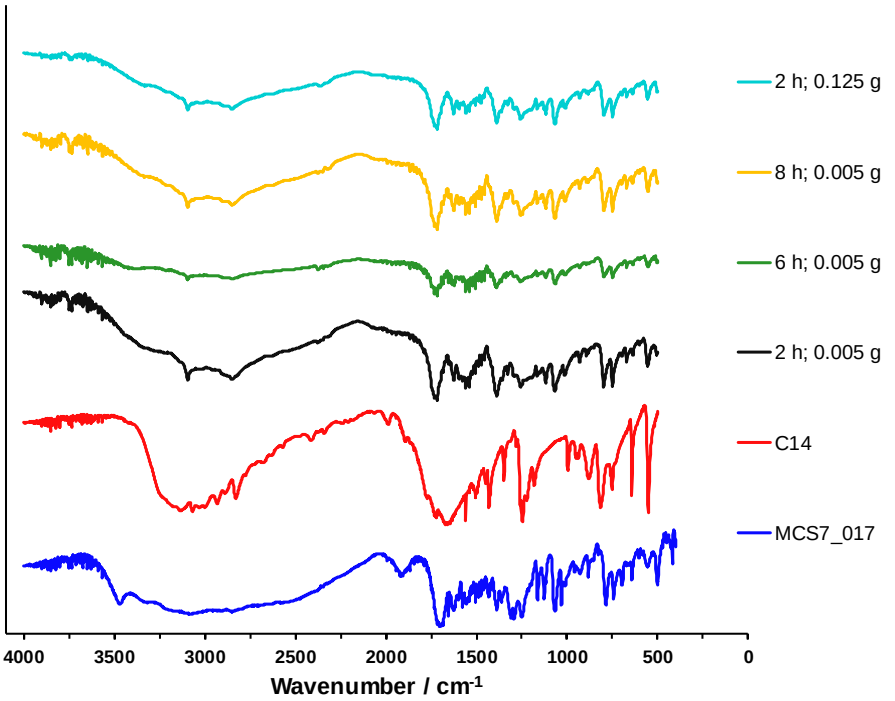

Figure 10.15. FTIR spectra for original (blue), obtained from a 4 + 2 + 9 condensation of **C6**, **C7** and **C8**, via LAG in a catalytic amount of 1:1 1,4-dioxane:1,3,5-trimethylbenzene, and **C14** loaded MCS7_017, using hexane as solvent, a loading time of 2, 6 and 8 hours, and 0.005 and 0.125 g amounts of the framework, and for the API **C14** (red).

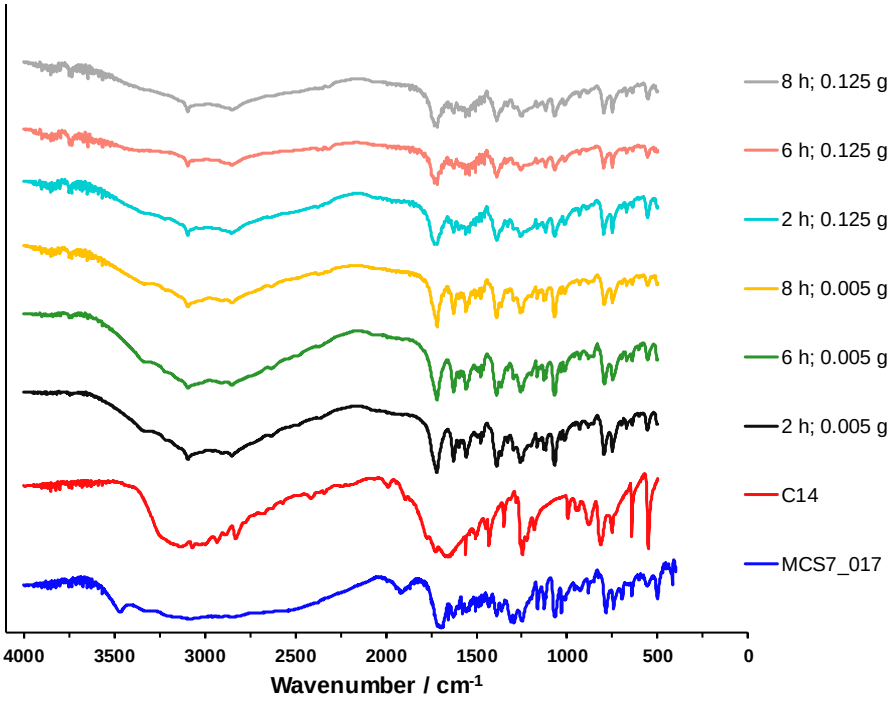

Figure 10.16. FTIR spectra for original (blue), obtained from a 4 + 2 + 9 condensation of **C6**, **C7** and **C8**, via LAG in a catalytic amount of 1:1 1,4-dioxane:1,3,5-trimethylbenzene, and **C14** loaded MCS7_017, using hexane with oxolane drops as solvent, a loading time of 2, 6 and 8 hours, and 0.005 and 0.125 g amounts of the framework, and for the API **C14** (red).

A3. Drug Release Profile

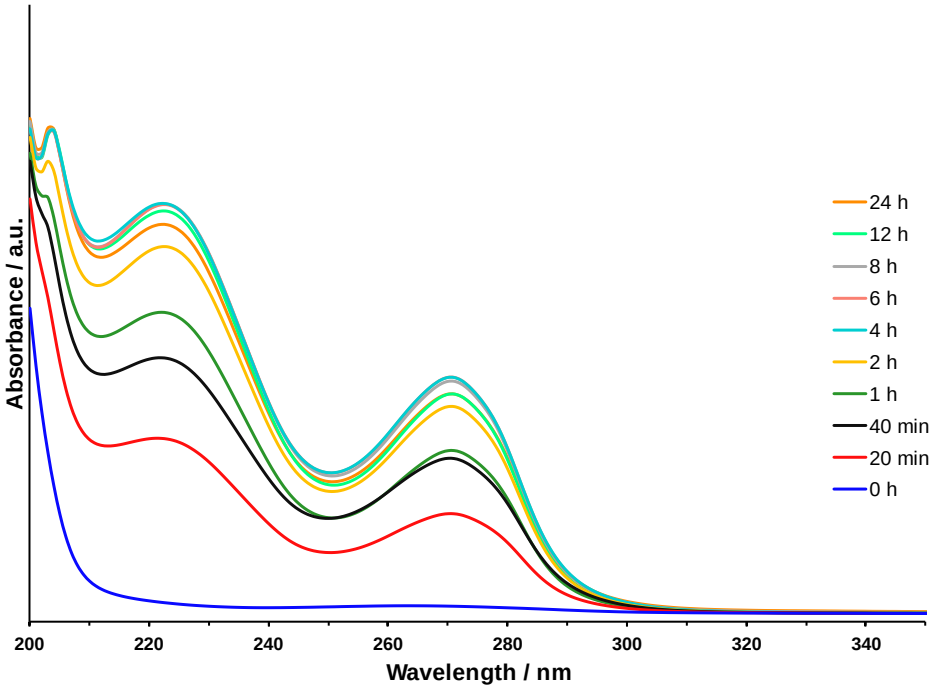

Figure 10.17. UV-Vis spectra for the release study on MCS7_017, obtained from a 4 + 2 + 9 condensation of **C6**, **C7** and **C8**, via LAG in a catalytic amount of 1:1 1,4-dioxane:1,3,5-trimethylbenzene, in PBS pH 7.4, at time 0, 20 min, 40 min, 1, 2, 4, 6, 8, 12 and 24 hours.

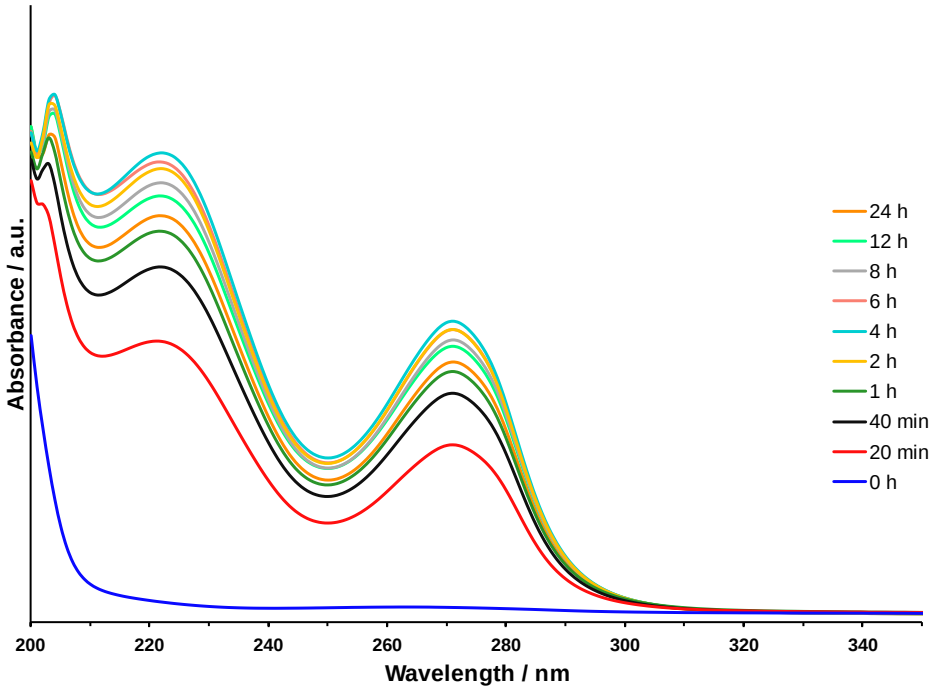

Figure 10.18. UV-Vis spectra for the release study on MCS7_080, obtained upon loading of **C9** onto MCS7_077, in PBS pH 4.9, at time 0, 20 min, 40 min, 1, 2, 4, 6, 8, 12 and 24 hours.

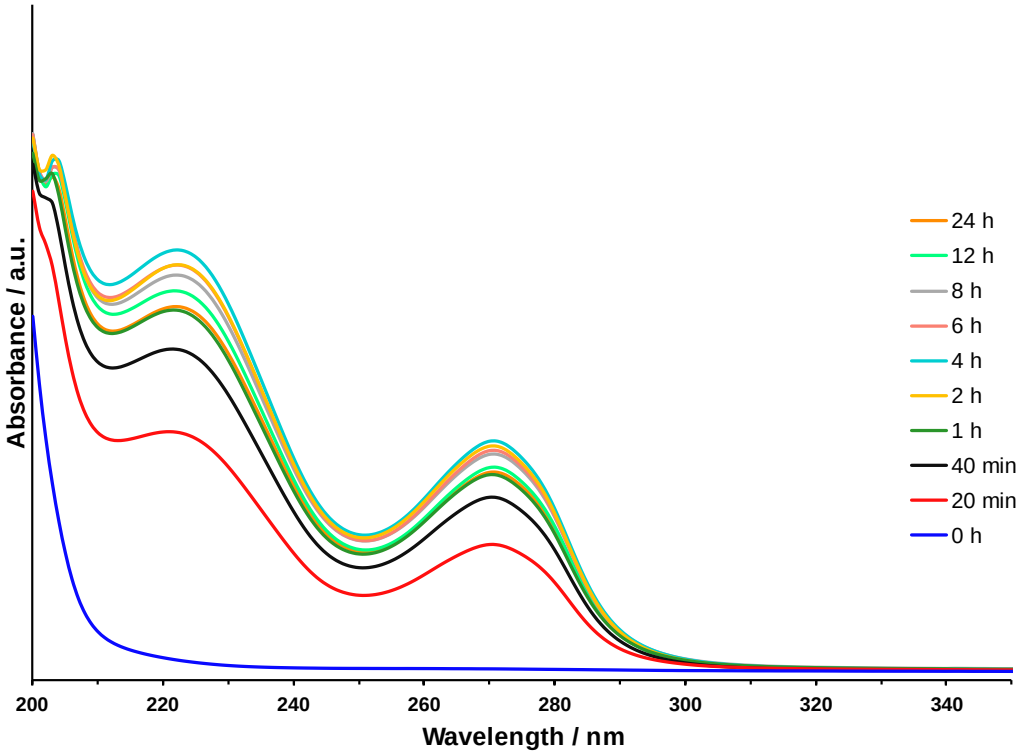

Figure 10.19. UV-Vis spectra for the release study on MCS7_080, obtained upon loading of **C9** onto MCS7_077, in PBS pH 7.4, at time 0, 20 min, 40 min, 1, 2, 4, 6, 8, 12 and 24 hours.

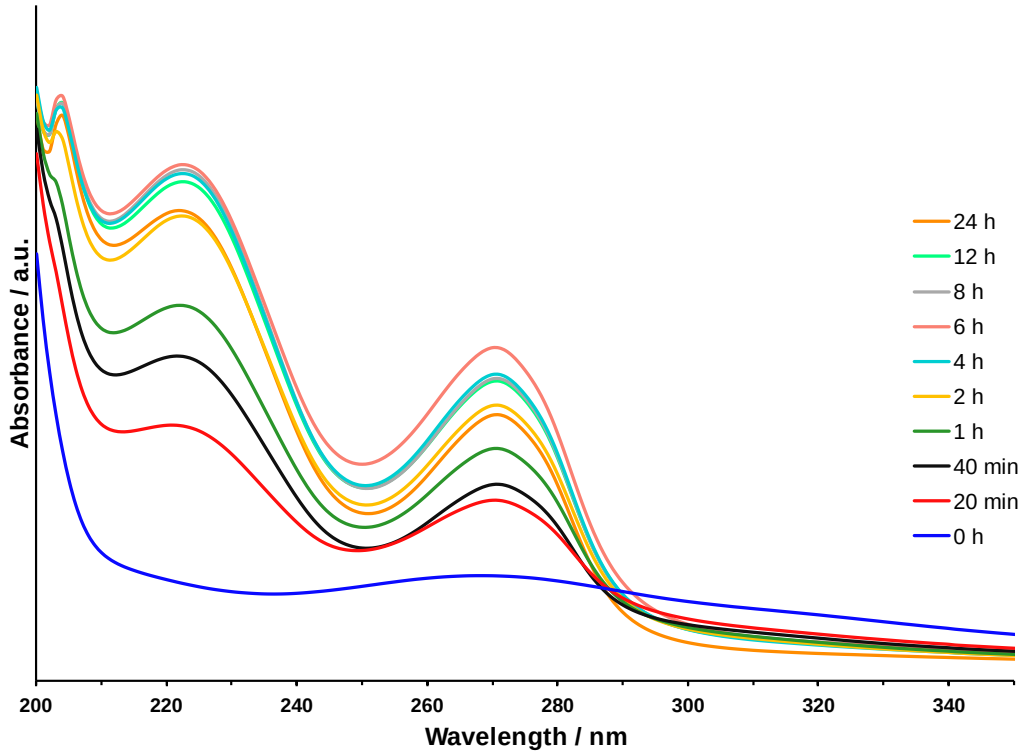

Figure 10.20. UV-Vis spectra for the release study on MCS7_082, obtained upon loading of **C10** onto MCS7_077, in PBS pH 7.4, with addition of Fe^{3+}, at time 0, 20 min, 40 min, 1, 2, 4, 6, 8, 12 and 24 hours.

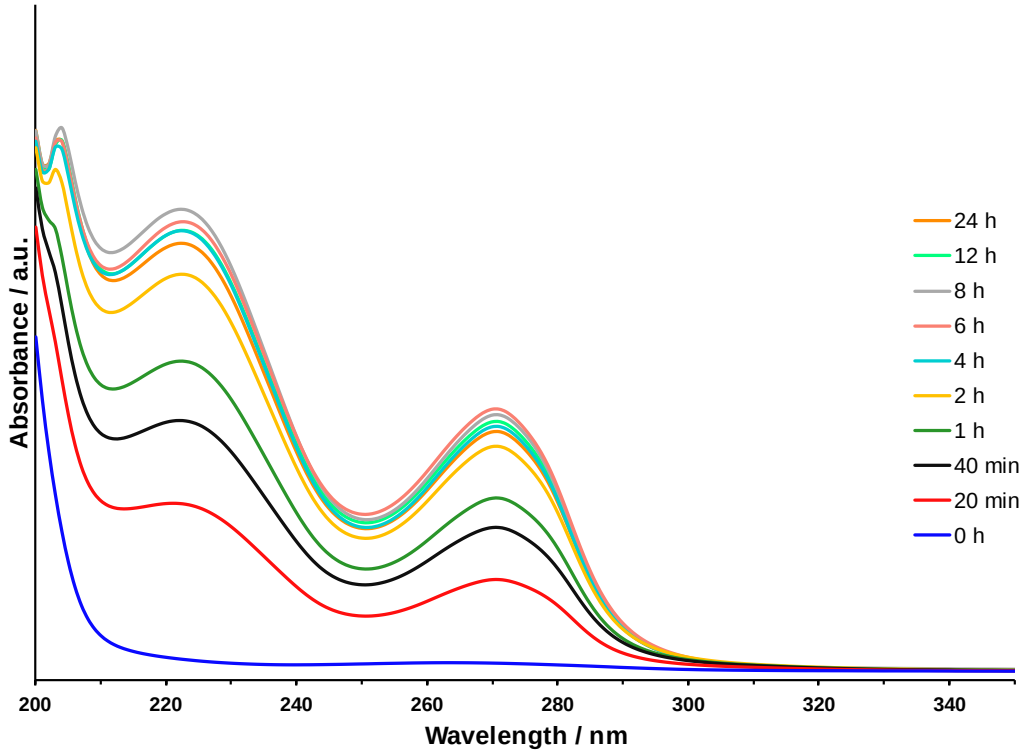

Figure 10.21. UV-Vis spectra for the release study on MCS7_082, obtained upon loading of **C10** onto MCS7_077, in PBS pH 7.4, without addition of Fe^{3+}, at time 0, 20 min, 40 min, 1, 2, 4, 6, 8, 12 and 24 hours.

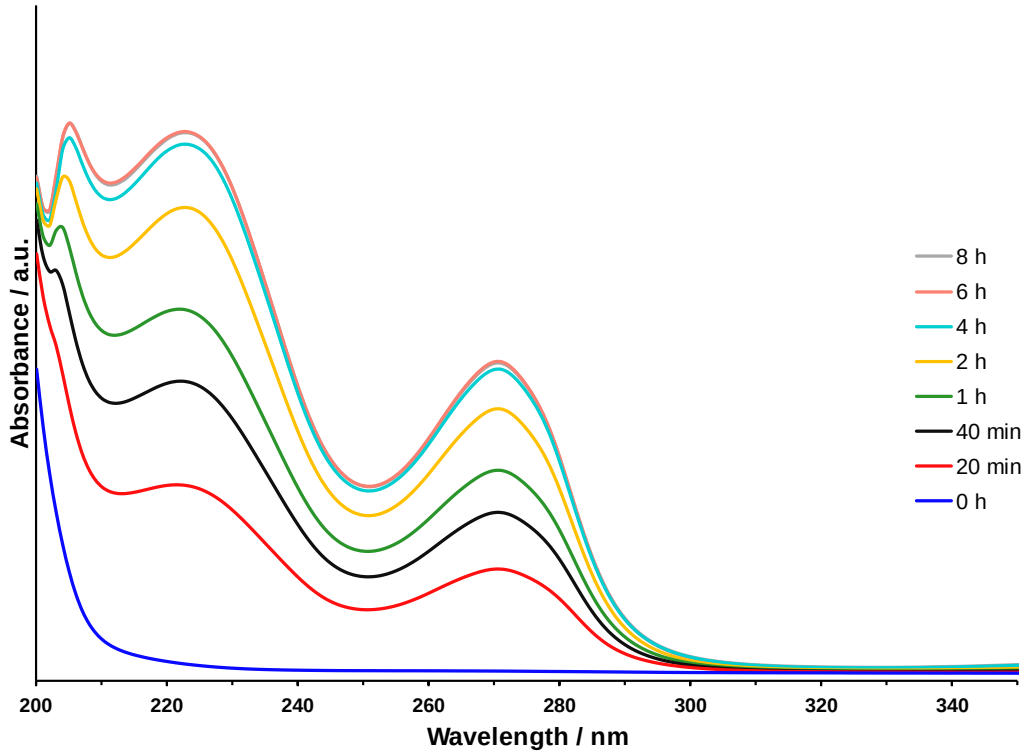

Figure 10.22. UV-Vis spectra for the release study on MCS7_085, obtained upon loading of **C11** onto MCS7_077, in PBS pH 7.4, under UV irradiation, at time 0, 20 min, 40 min, 1, 2, 4, 6 and 8 hours.

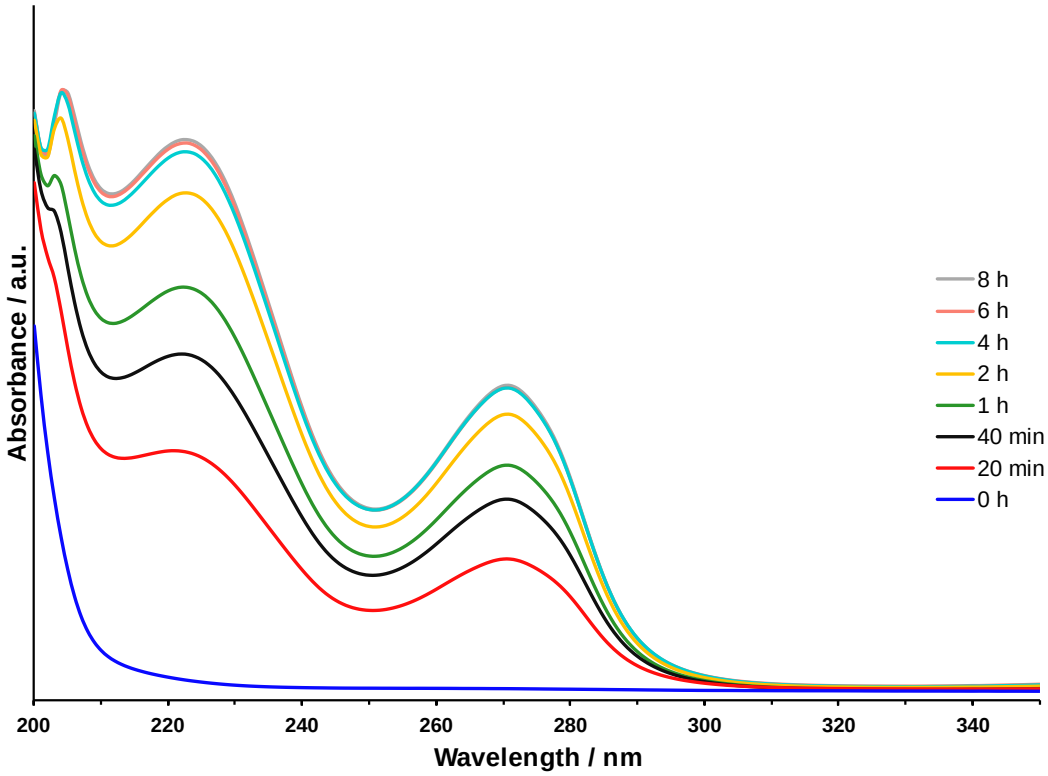

Figure 10.23. UV-Vis spectra for the release study on MCS7_085, obtained upon loading of **C11** onto MCS7_077, in PBS pH 7.4, without UV irradiation, at time 0, 20 min, 40 min, 1, 2, 4, 6 and 8 hours.

A3.1. UV-Vis Calibration for C8

0.240, 0.180, 0.120, 0.060 and 0.030 mM concentrations of **C8** in PBS pH 7.4, were accurately prepared using 5 mL graduated volumetric pipettes, and analysed using UV-Vis spectrophotometry. The absorbance value at λ_{max} of 271 nm was recorded. A calibration curve of absorbance against concentration was plotted, to determine the value of the molar absorptivity, ε, of the **C8** monomer in 1X PBS. The concentration of the monomer in the aliquots from the release studies was calculated using the Beer-Lambert law ($A = \varepsilon cl$), and was then plotted against time, to obtain the release profiles under the tested conditions.

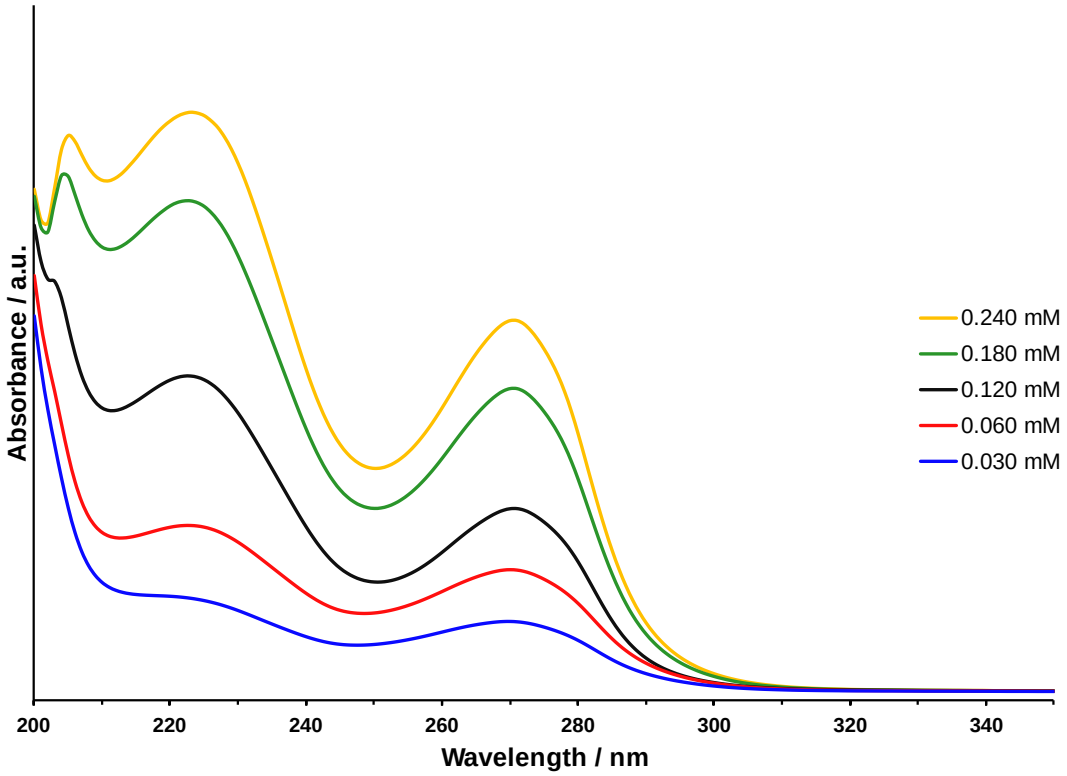

Figure 10.24. UV-Vis spectra for **C8** in PBS pH 7.4, at different concentrations.

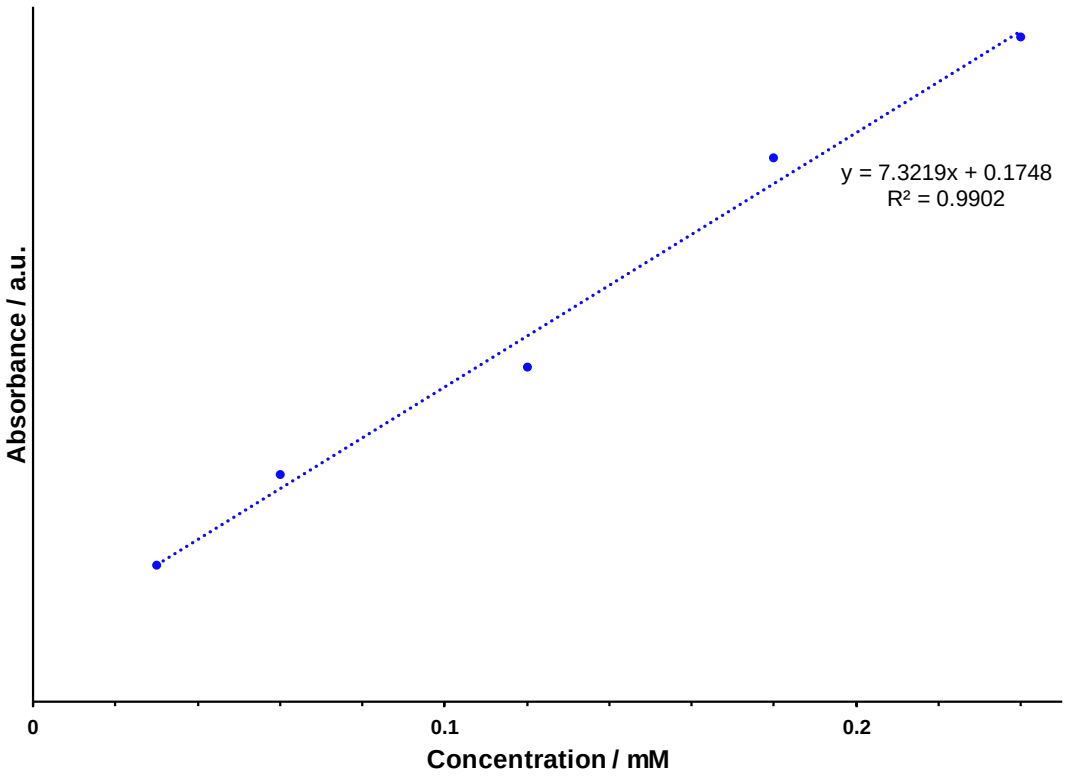

Figure 10.25. Calibration curve for **C8** in 1X PBS pH 7.4.